Marco Magnaterra

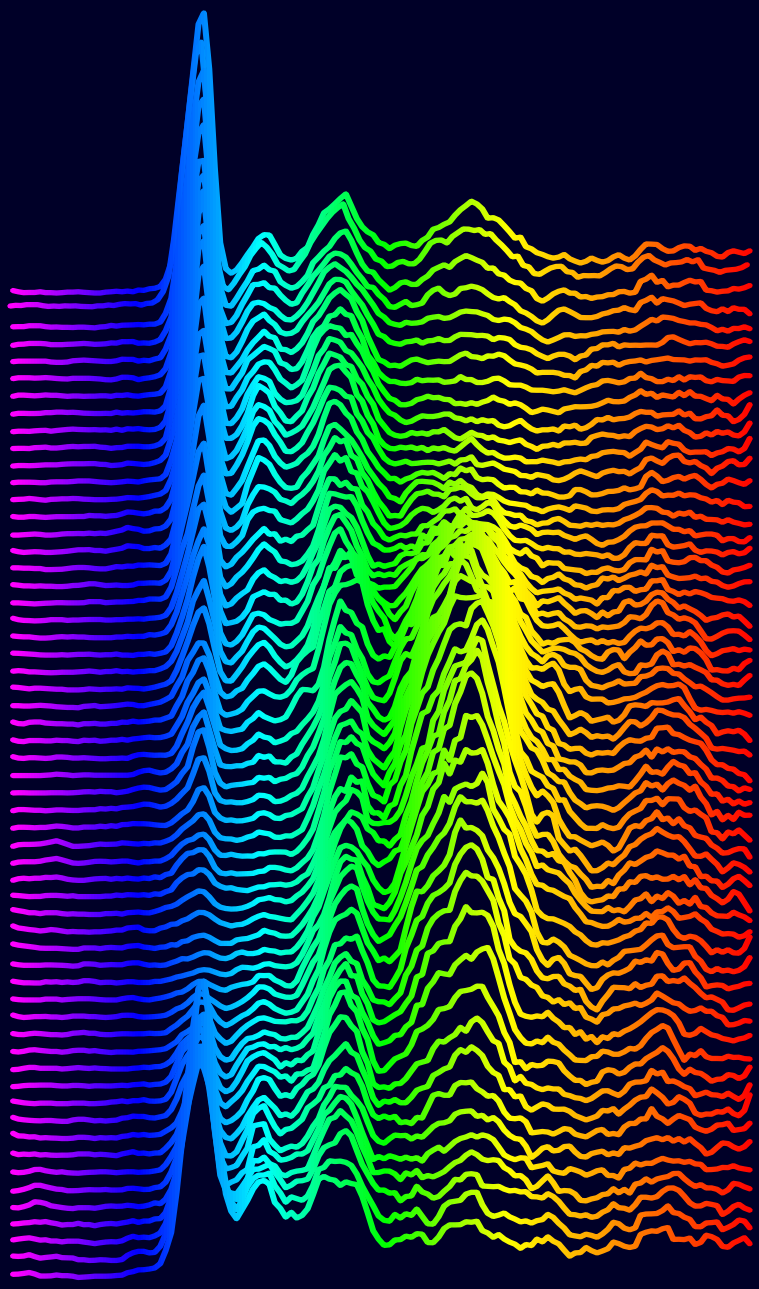

RIXS interference in dimers, trimers, and tetramers:

bond-directional excitations and quasimolecular wavefunctions

RIXS interference in dimers, trimers, and tetramers: bond-directional excitations and quasimolecular wavefunctions

Dissertation

zur

Erlangung des Doktorgrades

der Mathematisch-Naturwissenschaftlichen Fakultät

der Universität zu Köln

vorgelegt von

Marco Magnaterra

angenommen im

Köln 2025

Begutachtung:

Prof. Dr. Markus Grüninger
Prof. Dr. Maurits Haverkort
Prof. Dr. Christian Hess

Abstract

In the quest to realize exotic quantum states of matter, systems with strongly correlated electrons are of particular interest. Such systems may, e.g., form a Mott insulator, with localized magnetic moments. The interactions between these moments depend on the interplay of charge, lattice, orbital, and spin degrees of freedom. Of particular interest are cases where strong spin-orbit coupling leads to spin-orbit entangled $j = 1/2$ magnetic moments, as realized for Ir^{4+} ions within an octahedral ligand cage. These moments can give rise to exotic magnetism. In Kitaev materials with, e.g., a honeycomb lattice of edge-sharing IrO_6 octahedra, theory predicts that exchange interactions between $j = 1/2$ moments predominantly have bond-directional nearest-neighbor character, leading to exchange frustration. Ideally, this results in a quantum spin liquid ground state. Direct evidence for quantum spin liquids and bond-directional interactions remains an open experimental challenge. Another route to realizing exotic quantum states is to search for unusual magnetic moments. We investigate these in cluster Mott insulators, where electrons are delocalized over a cluster, such as a dimer, trimer, or tetramer, forming localized quasimolecular magnetic moments.

To probe the excitations in these systems, we use Resonant Inelastic X-ray Scattering (RIXS). This technique allows us to directly measure the energies of spin and orbital excitations and their dependence on exchanged momentum. When the electrons are delocalized over a cluster, like a dimer, trimer, or tetramer, the RIXS intensity exhibits a characteristic periodic modulation as a function of the exchanged momentum. This modulation arises from interference between the RIXS amplitudes from different sites within the cluster. We show that this modulation contains valuable information about bond-directional excitations in Kitaev materials and the quasimolecular wavefunctions in cluster Mott insulators.

Bond-directional magnetic interactions imply the existence of bond-directional magnetic excitations, spin excitations that render crystallographically equivalent directions magnetically inequivalent. We show how to observe the bond-directional character of the magnetic excitations using RIXS at the Ir L_3 edge in the Kitaev materials Na_2IrO_3 and α-Li_2IrO_3. We identify a low-energy spin-conserving excitation (at 10 meV and 15 meV, respectively) and a high-energy spin-flip excitation (at 45 meV and 35 meV, respectively). By exploiting the polarization and exchanged momentum dependence of the RIXS process, we simultaneously determine the bond direction and the spin operator involved in a given excitation, thus proving the bond-directional character of the magnetic excitations.

In cluster Mott insulators, the quasimolecular character can be probed via the modulation of the RIXS intensity. We study $Ba_4NbIr_3O_{12}$, which contains Ir_3O_{12} trimers, using RIXS at the Ir L_3 edge. This work represents the first RIXS experimental determination of the quasimolecular electronic structure in a quasimolecular trimer cluster compound. We show that the modulation reveals information about the symmetry of the quasimolecular wavefunctions. The lacunar spinel $GaTa_4Se_8$ hosts spin-orbit-entangled quasimolecular wavefunctions on Ta_4 tetrahedra. We study the RIXS modulation at the Ta L_3 edge and find that it is sensitive to the wavefunction composition, particularly to the mixing between bonding and antibonding states. This mixing affects the quasimolecular magnetic moment and renormalizes the effective spin-orbit coupling. Accurate modeling was crucial for correct peak assignment and for understanding the tetrahedral quasimolecular magnetic moment.

Contents

Chapter 1

Introduction

Solid-state physics is a branch of condensed-matter physics that focuses on the study of the physical properties of solids. Often, the atoms in these materials are arranged in a periodic structure, forming a crystal. These atoms and their electrons interact via electromagnetic forces. One might think that solid-state physics could be reduced to particle physics, specifically quantum electrodynamics, which describes the interactions of charged particles via the exchange of photons. However, the large number of particles and the variety of possible symmetries introduce layers of complexity that give rise to emergent phenomena. As Anderson famously stated, "more is different" [10]. New phenomena emerge from the collective behavior of particles that cannot be trivially predicted from the underlying microscopic physical laws. Some of the most fascinating examples are phenomena where the microscopic quantum nature of the particles manifests in macroscopic properties, such as superconductivity and magnetism. The ability to engineer a vast number of different systems with varying symmetries and interactions allows for the realization and study of many unusual phenomena. Exotic emergent quasiparticles can arise, such as Cooper pairs (a bound pair of electrons behaving as a boson), fractional spin or charge excitations (when excitations decay into quasiparticles with fractional quantum numbers), Majorana fermions (fermions that are their own antiparticle), magnetic monopoles (which behave as isolated north or south magnetic poles), magnetic skyrmions (topologically stable vortex-like spin arrangements), and many more. Some of the phenomena related to these quasiparticles are fascinating for the potential technological applications, while others are intriguing because they challenge our fundamental understanding of nature. To study these systems, experimental physicists often use probes such as static electric and magnetic fields, photons, electrons, neutrons, or muons, which have well-understood interactions with the system under investigation. This broad collection of techniques can reveal information about the microscopic structure and interactions within the system. In particular, many of the properties of these systems are determined by the behavior of the valence electrons and how they interact.

In this thesis, we focus on the study of systems with a strong interaction between electrons. In the following, we discuss how this interaction leads to the formation of localized magnetic moments in *Mott insulators*. The interactions between these moments depend on the interplay of charge, orbital, spin, and lattice degrees of freedom. Of particular interest are systems where strong spin-orbit coupling leads to the formation of *spin-orbit entangled magnetic moments*. These moments can give rise to exotic forms of magnetism, such as

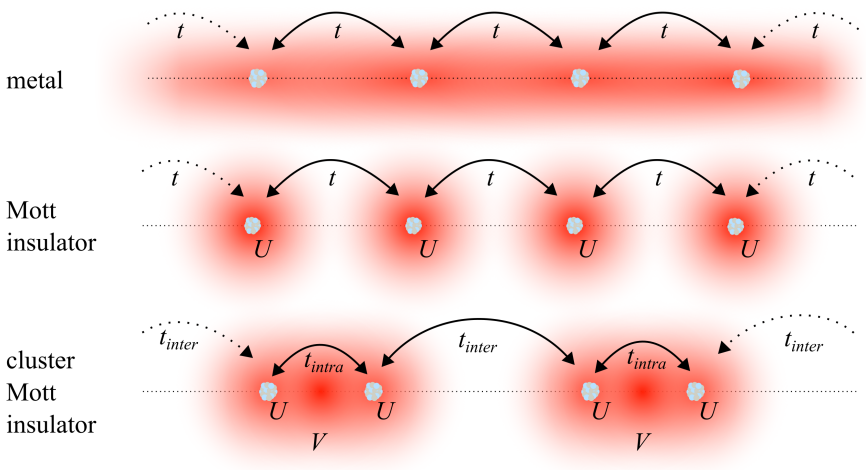

Figure 1.1: Depiction of a linear chain of atoms with one electron and one orbital per site. When hopping t dominates, electrons delocalize, leading to a metallic state. In Mott insulators, Coulomb repulsion U localizes the electrons, creating localized magnetic moments. The last row shows a dimerized chain with one electron per dimer. We can define a hopping t_{intra} inside the dimers and a hopping t_{inter} between different dimers. In cluster Mott insulators, t_{intra} delocalizes electrons within clusters, forming quasimolecular orbitals, while the energy cost V prevents charge fluctuations between different dimers. This leads to the presence of localized quasimolecular magnetic moments.

the *quantum spin liquid* in Kitaev materials. We also discuss how strong hopping between orbital degrees of freedom within clusters of transition metals, such as dimers, trimers, or tetramers, can result in the realization of a *cluster Mott insulator*. In these systems, electrons form localized *quasimolecular magnetic moments*, which may lead to new emergent exotic phenomena. To investigate these systems, we use X-ray photons, which interact with electrons via electromagnetic interactions. This interaction results in an exchange of energy and momentum between the electromagnetic field and the electrons, allowing us to probe the electronic structure of the system. In particular, we use *Resonant Inelastic X-ray Scattering* (RIXS). We show how RIXS can probe the bond-directional nearest-neighbor magnetic excitations in the Kitaev materials Na_2IrO_3 and α-Li_2IrO_3. In cluster Mott insulators, where electrons are delocalized over a cluster, the RIXS intensity exhibits a characteristic periodic modulation that contains valuable information about the cluster wavefunction. We systematically study these systems and discuss the results on the dimer compounds $Ba_3Ti_{3-x}Ir_xO_9$ to explain the potential of the RIXS interferometry technique. We present the studies of the electronic structure of $Ba_4NbIr_3O_{12}$, containing Ir_3O_{12} trimers, and $GaTa_4Se_8$, containing Ta_4 tetramers.

Strongly correlated electrons

A particularly interesting class of materials is those with strong interactions between electrons [11,12]. In such systems, electrons cannot be treated as independent particles but must instead be considered as part of a *strongly correlated electron system*. One of the fascinating consequences of strong electron-electron interactions is the formation of localized magnetic moments in transition-metal compounds. Figure 1.1 illustrates a linear chain of atoms, each with one electron and one orbital per site (half-filling), represented as a density cloud. The overlap between electrons would typically lead to delocalization, resulting in a metallic state. Delocalization reduces the kinetic energy of the electrons by effectively enlarging the

"box" they are confined to. This hopping process can be described in second quantization as $H_t = -t \sum c_{i\sigma}^\dagger c_{j\sigma}$, where $c_{i\sigma}^\dagger$ and $c_{j\sigma}$ denote the creation and annihilation of an electron with spin σ at sites i and j, respectively. However, when an electron moves to a neighboring site already occupied by another electron, they will experience an electrostatic Coulomb repulsion. This interaction is described in second quantization as $H_U = U \sum n_{i\uparrow} n_{i\downarrow}$, where $n_{i\sigma} = c_{i\sigma}^\dagger c_{i\sigma}$ is the number operator for spin σ at site i. The sum of these two terms forms the *Hubbard Hamiltonian* [13, 14]

$$H_H = -t \sum_{\langle i,j \rangle} c_{i\sigma}^\dagger c_{j\sigma} + U \sum_i n_{i\uparrow} n_{i\downarrow}. \tag{1.1}$$

When the hopping term t dominates, electrons delocalize across the crystal, resulting in a metallic state. In contrast, when Coulomb repulsion U dominates, electron delocalization at half-filling is suppressed because moving to a neighboring site is too costly in terms of electrostatic energy. This results in electrons being localized on their atomic sites, forming localized magnetic moments. The system becomes insulating, with electrons confined to their atomic sites, a state known as a *Mott insulator*, depicted in the second row of Fig. 1.1. As a function of t/U, the Hubbard Hamiltonian describes a metal-insulator phase transition [15]. These ideas were proposed by Peierls and Mott in the 1930s, see Appendix A.1 in Ref. [14] for a brief history. They suggested that localized electrons could arise from electron-electron interactions [16]. In particular, this idea was proposed to explain the insulating behavior of materials like NiO, which was predicted to be a metal according to band theory but instead shows a large band gap.

This deceptively simple Hubbard Hamiltonian hides a rich variety of physical phenomena. In a Mott insulator, hopping acts as a perturbation, leading to effective magnetic interactions between the localized magnetic moments. These magnetic interactions determine, e.g., the type of magnetic order (if present) or potentially the properties of a quantum spin liquid. The interactions can vary depending on the characteristics of the magnetic moments. The way localized magnetic moments interact depends on the subtle interplay between different degrees of freedom, such as spin, charge, orbital, and lattice degrees of freedom. For example, the interplay between lattice and orbital degrees of freedom arises because specific lattice distortions can favor particular orbital occupations. Instead, an interplay between spin and orbital degrees of freedom can arise since superexchange depends on the orbital occupation, as discussed in the next paragraph. On top, spin and orbital degrees of freedom may be entangled by spin-orbit coupling.

Orbital physics

The study of the interactions between orbital degrees of freedom and their impact on material properties constitutes the rich field of *orbital physics*. The condition of a Mott insulator is often realized in transition-metal compounds with partially filled valence d shells. In these materials, the transition metal often resides within an octahedral ligand cage, forming ML_6 octahedra in which the metal sits at the center in the ideal, undistorted case. This reduces the symmetry from spherical to cubic (or lower, depending on distortions and the rest of the lattice). This reduction in symmetry gives the orbitals a very specific directionality, as

discussed in Chap. 2.1. In cubic symmetry, orbitals of t_{2g} symmetry are lowered in energy, while those of e_g symmetry are raised. In systems with densely packed transition metals, interactions between orbital degrees of freedom across different sites become important. Orbital degrees of freedom can drastically influence the magnetic properties of a material. The specific geometry and orbital occupation play a crucial role. In practice, how the ML_6 octahedra are connected (whether in a corner-, edge-, or face-sharing geometry) and how many electrons occupy which orbitals determine the effective magnetic Hamiltonian. The description of the hopping between orbitals for the different corner-, edge-, and face-sharing geometries is provided in Chap. 2.2. In some cases, general rules can be formulated to predict the sign of the superexchange interactions (ferro or antiferro), known as the Goodenough-Kanamori rules [17–21]. For a detailed book covering these topics, see Ref. [14]. Orbital physics is a well-established field of research and remains very active. Some reviews covering the development of the field and current hot topics can be found in Refs. [22–25].

An extensively studied topic is the *cooperative Jahn-Teller effect*, which arises from a coupling between the lattice and orbital degrees of freedom. Orbital degeneracy has been shown to be unstable and prone to a spontaneous distortion of the lattice, leading to a reduction in the total energy [26]. This results in one or more orbitals being preferentially occupied in a long-range periodic pattern, a phenomenon known as *orbital ordering* [27]. Orbital ordering can also arise from a purely orbital mechanism coming from the directionality of the orbitals, as described by the Kugel-Khomskii model [28–30]. This model, which contains bond-dependent orbital interactions, is referred to as a compass model and is a source of rich physics [31]. For instance, depending on the parameters this model may yield an orbital liquid state [32].

The directionality of the orbital interactions can lead to the reduction of the dimensionality of the system. In some cases, it can result from the synergy between the directionality of the orbital interactions and an orbital-selective Peierls transition [33]. Many examples are reported in Ref. [24]. Some three-dimensional systems can effectively become one-dimensional by forming chains, or even zero-dimensional by forming, for example, dimers, trimers, or tetramers. A recent example can be found in Ref. [34], where the formation of Ru dimers at low temperature is proposed, suggested also by a drastic change of the RIXS spectra. In the course of this thesis, we study dimers, trimers, and tetramers, focussing on the important information contained in the $\mathbf{q}$ dependence of the RIXS intensity.

Spin-orbit entangled moments

A hot topic of research is the study of systems where spin and orbital degrees of freedom are entangled [35–37]. The spin-orbit coupling entangles orbital and spin degrees of freedom, leading to *spin-orbit entangled magnetic moments*, as discussed in Chap. 2.1.2. Of particular interest is the case of spin-orbit entangled $j = 1/2$ magnetic moments, realized, e.g., for Ir^{4+} with t_{2g}^5 configuration. These moments are a key ingredient for the realization of the Kitaev quantum spin liquid, a subject of extensive research, as discussed below. Spin-orbit coupling can remove orbital degeneracies [38] and induce a Mott insulator state, as observed, e.g., in Sr_2IrO_4 [39, 40], Na_2IrO_3, and α-Li_2IrO_3 [41]. It can also play a role in Jahn-Teller distortions. For example, depending on the electronic configuration, spin-orbit coupling can

quench (t_{2g}^2, t_{2g}^4, and t_{2g}^5), partially suppress (t_{2g}^1), or induce (t_{2g}^3) Jahn-Teller distortions [42].

The way spin-orbit entangled moments interact is non-trivial and can lead to frustrated magnetism [43]. To understand this concept, we start with the case of geometrical frustration, where the lattice geometry itself prevents the simultaneous satisfaction of all magnetic interactions, even if the interactions are isotropic in spin space. A classic example of geometrical frustration is the triangular lattice, where it is impossible to satisfy all antiferromagnetic Heisenberg interactions between nearest-neighbor spins simultaneously. This concept was pointed out by Anderson [44,45], who predicted a spin liquid for this geometry. In contrast, spin-orbit coupling may lead to *exchange frustration*, which arises when the magnetic interactions cannot all be satisfied simultaneously because of anisotropy in spin space, even though the lattice geometry itself is not frustrated. Spin-orbit coupling may cause exchange frustration because the directionality of orbital interactions can translate into anisotropic magnetic interactions.

It was noted in Ref. [46] that when the ML_6 octahedra are arranged in an edge-sharing geometry on a honeycomb lattice, spin-orbit entangled $j = 1/2$ moments lead to anisotropic Ising exchange interactions that are bond-dependent, resulting in exchange frustration. In the ideal case, this realizes the *Kitaev model*, described by

$$H_K = \sum_{\gamma} K\, S_i^{\gamma}\, S_j^{\gamma}, \tag{1.2}$$

where $\gamma = x, y, z$ simultaneously denotes the nearest-neighbor bonds and the component of the spin[1] degree of freedom at sites i and j that are interacting via the Kitaev interaction K. In this model, only a specific spin component interacts along a particular real-space direction. In other words, the model exhibits bond-directional nearest-neighbor spin-spin correlations, having many similarities to the compass model mentioned earlier. Kitaev showed in Ref. [47] that this model has an exactly solvable *quantum spin liquid* (QSL) ground state [48–50]. In a QSL, the system does not exhibit magnetic order even at zero temperature, despite the presence of magnetic interactions. This arises from quantum fluctuations among a massive number of degenerate states, leading to the emergence of a highly entangled many-body quantum state. A fascinating aspect of the Kitaev QSL is the emergence of exotic fractionalized quasiparticle excitations. The spin fractionalizes into a Majorana fermion and a static Z_2 gauge field that hosts vison excitations [47].

Extensive research has been conducted on Kitaev materials to detect signatures of the QSL state. For detailed reviews on the topic, see Refs. [51–55]. In Ref. [46], it was suggested to search for a possible realization of the Kitaev model in Mott insulators with t_{2g}^5 configuration and strong spin-orbit coupling with the honeycomb structure of A_2BO_3. The most extensively studied materials have been the honeycomb materials Na_2IrO_3, α-Li_2IrO_3, and $RuCl_3$ and the hyperhoneycomb material β-Li_2IrO_3. However, they all exhibit magnetic order at low temperatures [54,56]. In contrast, no evidence of long-range magnetic order has been observed in Cu_2IrO_3 [57], $H_3LiIr_2O_6$ [58], and $D_3LiIr_2O_6$ [59]. However, this has been discussed as possibly being caused by disorder [54].

[1] In this context, we refer to the spin-orbit entangled $j = 1/2$ degree of freedom with "spin", because it behaves as a pseudo-spin 1/2 degree of freedom.

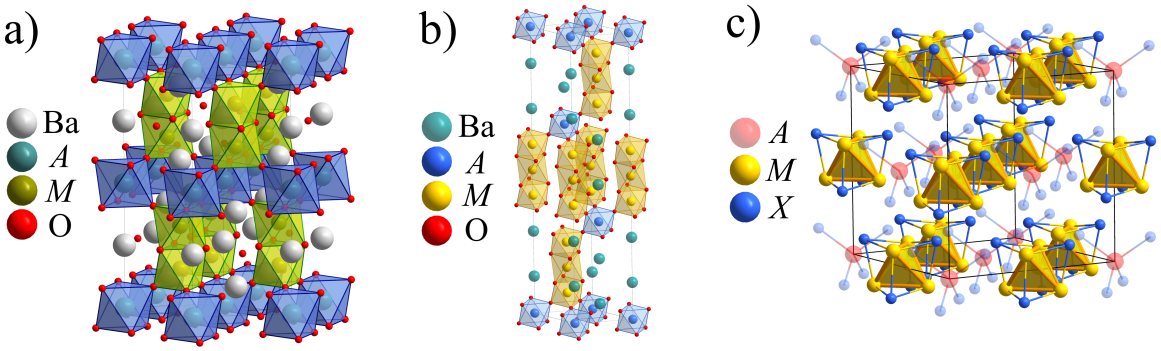

Figure 1.2: Depiction of some structures that can host a cluster Mott insulator state. a) $Ba_3AM_2O_9$ shows M_2O_9 dimers. b) $Ba_4AM_3O_{12}$ hosts M_3O_{12} trimers. c) The lacunar spinels AM_4X_8 contains M_4 tetramers with tetrahedral symmetry.

Cluster Mott insulators

We mentioned how, e.g., the directionality of the orbital interactions can lead to a reduction of dimensionality and the formation of clusters of transition metals. In other cases, the transition-metal atoms are intrinsically arranged in clusters, such as dimers, trimers, or tetramers, due to the specific crystal structure. Many examples of these systems can be found in Refs. [24,60,61]. Some examples of these structures are depicted in Fig. 1.2. In a), the structure of the $Ba_3AM_2O_9$ family is shown. It contains M_2O_9 dimers formed by two face-sharing octahedra. For example, the transition metal M can be Ru [62–66] or Ir [67–72], and the ion A can be another transition metal or a lanthanide. The A ion determines the number of electrons in the dimer. Another system showing dimers that has been investigated is $Ba_5AlIr_2O_{11}$ [73,74]. Figure 1.2b) shows the structure of the $Ba_4AM_3O_{12}$ family, which contains M_3O_{12} trimers formed by three face-sharing MO_6 octahedra. For example, the transition metal M can be Mn [75], Ru [76,77], or Ir [76,78–80], and the ion A can be another transition metal or a lanthanide. The trimers in this structure are detached from each other and can be considered as isolated clusters. In contrast, compounds such as $Ba_4Ir_3O_{10}$ [81,82] and $Ba_7Ir_6O_{19}$ [83] contain trimers that are connected to each other, leading to strong inter-trimer interactions. Not only linear clusters are possible. There are trimers in a planar geometry forming a triangle, as in the breathing kagome lattice $A_xB_yMo_3O_8$ [84–88] and clusters of four atoms in a tetrahedral geometry, as in the lacunar spinel AM_4X_8. Figure 1.2c) shows the structure of the lacunar spinel AM_4X_8, which contains M_4 tetrahedra formed by four edge-sharing MX_6 octahedra. Systems that have been synthesized include the elements M=V, Ti, Mo, Nb, Ta; A=Ga, Ge, Al; and X=S, Se, Te [89–95].

We can imagine that there is strong hopping between orbitals on different sites of a cluster. The distance between the transition-metal ions inside the cluster is sometimes even smaller than the distance they have in the monoatomic metallic crystal. The last row of Fig. 1.1 depicts a dimerized linear chain of atoms in which there is a short distance inside the dimer and a long distance between different dimers. In this case, we have two different hopping terms: a hopping between the orbitals inside the dimer, t_{intra}, and a hopping between the orbitals in different dimers, t_{inter}. Suppose that a strong t_{intra} leads to the delocalization of the electrons inside the cluster, forming bonding and antibonding quasimolecular orbitals. If we consider one electron and one orbital per ion, the system

would result in a conventional insulator even in the absence of electronic correlations (like a band insulator), with both electrons occupying the bonding orbital with opposite spin. Instead, if we consider the case of one electron per dimer, we have a situation of half-filling with one unpaired electron in the bonding orbital. To move one electron from a dimer to another dimer costs an energy $V = E^{\mathrm{dim}}(n-1) + E^{\mathrm{dim}}(n+1) - 2\,E^{\mathrm{dim}}(n)$, where $E^{\mathrm{dim}}(n)$ is the energy of the dimer with n electrons. A *cluster Mott insulator* is realized when t_{inter} is not sufficiently high compared to V to allow charge fluctuations between different dimers. This results in the formation of *localized quasimolecular magnetic moments*. We can write the Hamiltonian as a sum of a cluster Hamiltonian H_c, which depends on t_{intra} and U, and an interaction Hamiltonian $H'_{cc'}$ between different clusters [96]

$$H = \sum_c H_c + \sum_{\langle cc' \rangle} H'_{cc'}. \tag{1.3}$$

The cluster Hamiltonian H_c describes the quasimolecular wavefunctions inside the cluster, while the interaction Hamiltonian $H'_{cc'}$ describes the interaction between the quasimolecular orbitals at different sites and can be treated as a perturbation to H_c. Compared to standard Mott insulators, these systems are more complex. The quasimolecular wavefunctions are determined by internal properties, such as the symmetry of the cluster and the strength of the hopping inside the cluster. The way the clusters interact with each other is determined by the hopping paths between different clusters, which can, in general, have different symmetries and strengths compared to the internal ones. This additional layer of complexity can lead to novel emergent quantum states.

The complexity manifests in the very rich physics of these systems. For example, the dimer $Ba_3AM_2O_9$ and trimer $Ba_4AM_3O_{12}$ compounds are so-called hexagonal perovskites [60] that are proposed as realizations of QSL, as in some cases the clusters are arranged in a triangular lattice, which leads to geometric frustration. In fact, many claims of behavior compatible with a QSL have been made [82, 97–103], including $Ba_3Ti_{3-x}Ir_xO_9$ [104, 105] and $Ba_4NbIr_3O_{12}$ [106–108]. Moreover, $Ba_3AM_2O_9$ and $Ba_4AM_3O_{12}$ systems are versatile since the number of electrons per dimers or trimers can be controlled by the choice of the A ion. For certain electron counts, there can be many low-lying states, which cause the system to undergo phase transitions depending on the subtle balance of the different microscopic interactions [109]. For example, $Ba_3InIr_2O_9$ can change from a $j_{dim} = 1/2$ to a $j_{dim} = 3/2$ ground state depending on the strength of the hopping [6]. Moreover, the transition metal M can be a $3d$, $4d$, or $5d$, allowing to explore different regions of the parameter space.

The planar trimers of the family $A_xB_yMo_3O_8$ are also predicted to exhibit unusual phenomena, such as spin liquids and plaquette charge order [110–112]. Some are, in fact, claimed to be spin liquids [113–115]. These systems show an unusual transition with freezing of the spins [116].

The lacunar spinels exhibit a wide variety of phenomena [94, 95, 117]. For example, they host multiferroic phases and skyrmion lattices with Néel-type skyrmions carrying electric polarization [118–122], (anti-)ferroelectricity with peculiar domain architectures [123, 124], and magnetism tied to polar domain walls [125]. They also have been claimed to exhibit a cluster molecular Jahn-Teller effect [126]. A pressure-induced insulator-to-metal transition followed

by topological superconductivity has been observed [127–131]. The insulator-to-metal transition can also be triggered by a strong electric field [132]. Some of the lacunar spinels, such as $GaTa_4Se_8$, were predicted to be realizations of spin-orbit entangled quasimolecular states [133]. In Pub. [3] and Chap. 6 we prove the spin-orbit entangled quasimolecular nature of the wavefunction. Moreover, we show how the mixing of bonding and antibonding quasimolecular orbitals affects the quasimolecular magnetic moment and renomalizes the effective spin-orbit coupling.

Resonant Inelastic X-ray Scattering

We have described how the properties of strongly correlated electron systems depend on the interplay between different degrees of freedom and interactions. This balance determines the ground state and the properties of the excitations. The energy and momentum dependence of the excitations of spin, charge, orbital, and lattice degrees of freedom are the fingerprints of the underlying interactions. Through measurement and comparison with theoretical models, we can extract the parameters and understand the interactions.

We need a probe that can measure the energy and momentum dependence of these excitations. Scattering techniques can be used to probe the excitations of condensed-matter systems. Examples of such techniques include electron energy loss spectroscopy (EELS), inelastic neutron scattering (INS), non-resonant inelastic x-ray scattering (NIXS) (also called X-ray Raman Scattering (XRS)), and *Resonant Inelastic X-ray Scattering* (*RIXS*). RIXS is the technique used in the experiments discussed in this thesis and is presented in Chap. 3. The RIXS process can be described as a two-step process. In the first step, an incident photon resonantly excites a core electron into an unoccupied state, creating a core hole. This intermediate state is highly unstable and decays as the core hole is filled by an electron from a higher energy level, emitting a photon in the process. An important point in our discussion is that the two steps are coherent, such that all the intermediate state paths are superimposed. The coherence allows the momentum to be conserved in the scattering process, such that the difference in energy and momentum between the incident and emitted photons correspond to the energy and momentum of the excitations created in the material. By measuring these differences, RIXS gives a direct measurement of the energy of the excitations and their dependence on the exchanged momentum.

RIXS is a powerful technique for studying condensed-matter systems [134–136]. Its applications also extend to the fields of chemistry [137], molecular physics [138], and energy materials [139]. RIXS allows for the direct measurement of the energy and momentum dependence of elementary excitations such as phonons, magnons, crystal-field (or *dd*) excitations, charge-transfer excitations, and plasmons. It is capable of covering a large energy range and a wide momentum range simultaneously. In contrast, neutrons are limited in the energy range they can cover and do not couple directly to the electronic charge density. Moreover, neutron experiments require large samples, and some elements, such as Ir, are strong absorbers of neutrons, making such experiments more challenging. However, INS provides better energy resolution for low-energy magnetic excitations, with resolutions in the meV or even µeV range. EELS is instead a surface-sensitive technique, and its analysis is more complex. RIXS, on the other hand, provides a straightforward and direct probe of

bulk unoccupied electronic states. It is polarization-dependent, element- and orbital-specific, and requires only a small sample volume. The use of X-rays allows to exchange a large momentum with the system allowing to cover entirely one or multiple Brillouin zones. Thanks to resonance and polarization dependence, it is sensitive to orbital occupation. A resolution of about 20 meV can be achieved, although the resolution varies significantly depending on the resonance energy of the specific element being studied.

RIXS has proven to be a powerful experimental technique for studying the electronic structure of Mott insulators [140]. The first RIXS experiments on Mott insulators were performed on NiO [141–143]. The focus later shifted to cuprates such as La_2CuO_4 and related doped materials [144–146], with the hope of gaining insights into the mechanism of high-temperature superconductivity [147]. It became evident that RIXS can measure the dispersion of magnetic excitations [148–150], establishing itself as an alternative to INS. Iridates have also emerged as a highly studied class of materials, starting with Sr_2IrO_4 [151–153], which is intriguing due to its link to cuprates and its spin-orbit-assisted Mott insulator state [39]. Additionally, Kitaev materials such as Na_2IrO_3 and α-Li_2IrO_3 have been shown, through RIXS studies of the orbital excitations, to be spin-orbit-assisted Mott insulators [41].

RIXS on Kitaev materials

Clearly determining that a material is a QSL is a difficult task [154, 155]. Thermodynamic measurements, such as magnetic susceptibility and specific heat, can show the presence of frustration and the absence of a transition to a long-range magnetically ordered state or a spin glass state. Local probes, such as muon spin relaxation, can detect the persistence of spin dynamics at low temperatures to exclude the freezing of spins. However, these methods do not clearly identify a spin liquid, as they focus on the negative property of a QSL, the absence of order. The positive attributes that characterize a QSL are long-range entanglement and fractionalized spin excitations. A quantized thermal Hall effect has been predicted to be a signature of fractionalized excitations in certain kinds of QSLs [154, 155].

Spectroscopies, such as INS, Raman, THz, and RIXS, can be used to study the excitations in these materials and hopefully identify the fractionalized excitations. INS is widely used for its ability to directly measure the dynamical spin-spin correlations $S(\mathbf{q}, \omega)$. Examples include studies on Kagome materials [156, 157], the pyrochlore $Yb_2Ti_2O_7$ [158], Co- and V-based honeycomb materials [159–162], and the Ru-based honeycomb Kitaev material α-$RuCl_3$ [163–166]. Among the most cited are the INS studies of α-$RuCl_3$ in Refs. [163, 164], which observed a non-dispersing broad continuum of magnetic excitations persisting up to a temperature much higher than the ordering temperature. They recorded the intensity as a function of the exchanged momentum over a broad range of reciprocal space, which was shown to agree with the Kitaev model.

Measuring INS on iridates is more complicated due to the high neutron absorption of Ir and the small size of the available samples. However, a few studies have been conducted on Na_2IrO_3 [167], α-Li_2IrO_3 [168], β-Li_2IrO_3 [169], and $D_3LiIr_2O_6$ [170]. These studies, however, have been performed on powder crystals, which do not allow to obtain detailed information in reciprocal space.

RIXS can be an alternative technique in these cases, although it has a worse energy resolution. It can also serve as a complementary technique since RIXS has different selection rules compared to INS. For example, in α-$RuCl_3$, even though the resolution at the Ru L_3 edge of $\approx 80\,\text{meV}$ is not high enough to resolve the magnetic excitations, it can still be used to study the orbital excitations [171] (see also Ref. [172] on RuX_3, X = Cl, Br, I), that previously have been observed in optical spectroscopy [173]. The study of the orbital excitations can show wether the system has a $j = 1/2$ ground state [41] or wether it deviates substantially [174]. The orbital excitations in Kitaev materials are also interesting because they show unusual properties [175, 176]. Another advantage of RIXS is its ability to perform experiments under pressure, in the presence of a magnetic field, or using time-resolved pump-probe techniques. $RuCl_3$ has been proposed to exhibit a spin-liquid state induced by a magnetic field [54]. The hope is that with pressure, magnetic field, or optical pumping, we can induce a QSL state in a material that is not a QSL at ambient conditions. The Kitaev materials α-Li_2IrO_3, β-Li_2IrO_3, and Cu_2IrO_3 have been studied with RIXS under pressure [177–179]. The effect of a magnetic field on β-Li_2IrO_3 has been studied with RIXS [180]. Additionally, time-resolved RIXS measurements have been performed on $H_3LiIr_2O_6$ [181].

Theoretically, RIXS has been shown to provide insightful information on the magnetic excitations of Kitaev materials [182–185], which might indicate the fractionalization of the excitations. In the magnetic scattering process, RIXS contains information about the dynamical spin-spin correlations, but this information is mixed with the polarization dependence. While this can pose challenges, it can also be advantageous if the polarization selection rules are properly understood and exploited. Recently, it has been proposed that RIXS can quantify the entanglement in a system, similar to what has been achieved with neutrons [186]; see the review in Ref. [136]. RIXS might provide a measurement of the quantum Fisher information and potentially the quantum entanglement in a QSL.

At the Ir L_3 edge, the resolution of 25 meV is close to the energy of the magnetic excitations in Kitaev honeycomb materials, which have been observed to be in the range of 10-45 meV. In Na_2IrO_3, magnetic excitations have been observed using RIXS at the L_3 edge as a broad continuum [187]. Initially, however, the high-temperature data were interpreted as arising from phonons. In Ref. [188], it was shown via the resonance behavior at the L_3 edge and the comparison between Na_2IrO_3 and α-Li_2IrO_3 that the continuum is due to magnetic excitations persisting up to high temperatures, much higher than the ordering temperature. Phonons, on the other hand, can be studied by measuring RIXS at the ligand edge, in this case the O K edge, as demonstrated in Ref. [189] on α-Li_2IrO_3. In the ordered phase, the observation of magnons and spinons has been claimed in Na_2IrO_3 [190], α-Li_2IrO_3 [191], and β-Li_2IrO_3 [180]. The magnetic excitations of $(H,D)_3LiIr_2O_6$, which do not exhibit magnetic order, have also been investigated [192], revealing a non-dispersing magnetic continuum. These RIXS studies would undoubtedly benefit from improved resolution. A study with a record resolution for the Ir L_3 edge of 12 meV was conducted on Na_2IrO_3 in Ref. [190]. However, the increase in resolving power comes at the cost of significantly lower intensity, resulting in very noisy data.

Despite multiple claims, no observation has yet been able to unequivocally demonstrate

the fractionalization of excitations in Kitaev materials. The idea of a proximate spin liquid has been proposed, where the system is close to a QSL phase, thus showing some of its properties [54]. With RIXS, valuable information about the magnetic interactions in Kitaev materials can be extracted. First of all, the energy of the magnetic excitations gives us information about the strength of the magnetic interactions. In addition, we can detect signatures of dominant bond-directional nearest-neighbor Kitaev interactions, as explained below.

The most widely accepted evidence for the presence of dominant bond-directional interactions comes from the Resonant Elastic X-ray Scattering (REXS) measurements reported in Ref. [193] on Na_2IrO_3. These measurements focused on the diffuse scattering originating from the remnants of the magnetic Bragg peaks above the ordering temperature, where this diffuse scattering is due to the presence of short-range magnetic correlations. By analyzing the polarization dependence of the intensity, the study demonstrated the presence of strong anisotropic bond-directional interactions. However, this approach would be inapplicable in a true QSL, where no magnetic order, and thus no magnetic Bragg peaks, exists. Other studies have attempted to quantify the magnetic interactions by analyzing the particular magnetic order or the dispersion of the magnetic excitations in the ordered phase [180, 190, 191].

We want to identify the fingerprints of bond-directional interactions in the magnetic excitations that are *not* related to the magnetic ordering. In Ref. [188], Revelli *et al.* detected the fingerprints of Kitaev interactions in the magnetic excitations of Na_2IrO_3 and α-Li_2IrO_3 by analyzing the dependence of the RIXS intensity on the exchanged momentum along selected directions. This revealed a periodic sinusoidal modulation of the intensity, which is a signature of the *nearest-neighbor* character of the interactions. These excitations and their modulation persist up to temperatures much higher than the ordering temperature, indicating that they are unrelated to magnetic ordering. In Chap. 4 and Pub. [2], we demonstrate how to probe the *bond-directional* character of the magnetic excitations in Na_2IrO_3 using RIXS. Similar to the INS measurements on $RuCl_3$ [164], we measure the response over a broad range of reciprocal space. But in addition, we employ a geometry specifically designed to exploit the polarization dependence of RIXS. This approach enabled us to disentangle two different excitations: one with spin-conserving character and another with spin-flip character. Moreover, consider the Kitaev model in Eq. (1.2), perturbing the system with the local operator S_i^γ, where $\gamma = x, y, z$, creates a spin-conserving excitation on the γ bond, rendering the three bonds inequivalent and producing *bond-directional excitations* (BDE). The spatial orientation of each bond results in a characteristic periodic sinusoidal modulation of the RIXS intensity as a function of the exchanged momentum, as discussed below and in Chap. 3.2. Instead, the anisotropic Kitaev interactions between spin components lead to a characteristic polarization dependence of the BDE associated with a specific bond. This approach allows us to establish the bond-directional character of the magnetic excitations in Na_2IrO_3 [2], as discussed in Chap. 4.1, and in α-Li_2IrO_3, as presented in Chap. 4.3.

RIXS on cluster Mott insulators

The starting point for the discussion of magnetism in cluster Mott insulators is the determination of the quasimolecular moments. We make full use of the power of RIXS in order to

quantify the interactions within the cluster and determine the quasimolecular wavefunctions. In well-separated clusters as in the structures shown in Fig. 1.2, the quasimolecular orbitals are localized on the cluster, and thus their excitations are generally expected to show little dispersion. In this case, the role of the exchanged momentum in the RIXS process might seem to be negligible. However, it was predicted in Refs. [194,195] that, in the case of molecular orbitals, interference effects as a function of the exchanged momentum are present due to the coherence of the RIXS scattering process [196]. Considering the case of a dimer, in which the electrons are delocalized over the two sites forming quasimolecular orbitals, at the end of the scattering process there is no information on which of the two sites the core hole was created in the intermediate state. This leads to a superposition of the two possible intermediate state paths, which can interfere with each other. This interference effect is the focus of Chap. 3.2.

This phenomenon can be understood through an analogy with Young's double-slit experiment [197], where the slits are analogous to the core holes in the intermediate state. This results in a sinusoidal modulation of the RIXS intensity as a function of the exchanged momentum. The period of the modulation is determined by the distance between the two sites forming the dimer. The first observation of this effect in a solid was reported in Ref. [197] on the dimer compound $Ba_3CeIr_2O_9$. The observation of such a modulation serves as a proof for the formation of quasimolecular orbitals. Interestingly, the modulation contains information about the relative symmetry of the ground state and excited states. This symmetry information can be highly useful for identifying quasimolecular excitations. For instance, an excitation from a quasimolecular bonding state to another bonding state will have a different modulation compared to an excitation from a bonding state to an antibonding state. In other words, in the presence of quasimolecular wavefunctions, the RIXS intensity is proportional to the structure factor of the cluster over which the electrons are delocalized. The phase of the structure factor contains the information about the relative symmetry of the ground state and excited states.

The use of hard X-rays in Ref. [197] allowed the clear measurement of multiple periods of the interference pattern. For soft and tender X-ray regimes, observing a full modulation period is challenging due to the limited momentum transfer [198]. However, this effect must be considered when planning RIXS experiments and analyzing RIXS spectra of cluster Mott insulators, as certain geometries can lead, for example, to the suppression of specific excitations. The study of the modulation of the RIXS intensity arising from interference effects has been named *RIXS interferometry*.

Not many studies have been conducted using RIXS on cluster Mott insulators, and in particular there is a very limited amount of studies using RIXS interferometry. The most extensively studied systems are dimers, as discussed in Refs. [197–203] and Pubs. [1,6]. The first observation of the RIXS modulation in $Ba_3CeIr_2O_9$ [197] demonstrated the potential of this technique to prove the quasimolecular character of the wavefunction. The phase of the modulation was used to identify the relative symmetry of the ground state and excited states, aiding in peak assignment. In $Ba_3InIr_2O_9$ [6], the modulation similarly proved the quasimolecular character and helped identify the ground state. In $Ba_3Ti_{3-x}Ir_xO_9$ [1], the observation of different modulation periods was used to identify the sites on which a

certain excitation is localized. This revealed the important role of Ti-Ir site disorder in these materials. Moreover, it was clearly shown that excitations localized on single atomic sites do not exhibit any modulation. Some of the data published in Pub. [1] are presented in Chap. 3.2 as an example of the RIXS interference effect. In Ref. [202], the RIXS modulation of $Ba_3CeIr_2O_9$ and $Ba_3TaIr_2O_9$ is studied to try to extract the Quantum Fisher information and obtain a measurement of the entanglement in the system. Ru $4d$ dimers have been studied in Ref. [198] using RIXS at the Ru M_3-edge ($E_i \approx 463$ eV). The resonance energy in the soft-X-ray range does not allow to exchange enough momentum to observe the periodic RIXS modulation. However, the formation of quasimolecular orbitals and the consequent RIXS interference effect are considered in the modelling of the RIXS experiments.

The trimer compound $Ba_4Ir_3O_{10}$ was investigated in Ref. [204], although the explanation provided does not explicitly involve quasimolecular orbitals. The first RIXS study addressing the quasimolecular electronic structure of the trimer system $Ba_4NbIr_3O_{12}$ is presented in Pub. [4] and reproduced in Chap. 5. This study is also the first observation of the interference effect in a trimer compound proving that a quasimolecular orbitals picture has to be applied to describe these trimer systems. In a trimer with inversion symmetry, the quasimolecular wavefunctions can be even or odd. The excitations among these states exhibit characteristic modulations depending on their relative symmetry. This signatures are observed in the experimental data and used to identify the excitations and ultimately understand the quasimolecular electronic structure of the trimer.

For the tetramer system $GaTa_4Se_8$, the first RIXS studies were reported in Refs. [205, 206]. However, the interference effect are not considered correctly, leading to a wrong peak assignment. In Pub. [3] we study $GaTa_4Se_8$ using RIXS interferometry at the L_3 edge, representing the first study of the RIXS interference effect on a tetrahedral cluster. The RIXS modulation was found to be sensitive to the composition of the wavefunction, which depends on the competition of different hopping terms that causes a mixing of the corresponding bonding and antibonding orbitals. This mixing determines the shape of the spin-orbit entangled quasimolecular wavefunction and renormalizes the effective spin-orbit coupling. The correct modelling of this effect proved to be crucial to have a correct peak assignment and to understand the quasimolecular electronic structure. These results are reproduced in Chap. 6.1, and in Chaps. 6.2, 6.3, and 6.4, we further explain the modeling of the tetrahedral quasimolecular orbitals and how the RIXS modulation reveals information about them.

In the Kitaev materials Na_2IrO_3 and α-Li_2IrO_3, although they are "simple" Mott insulators, modulations of the RIXS intensity of the magnetic and orbital excitations have been observed by Revelli *et al.* [175,188]. This arises from the bond-directional nearest-neighbor character of the excitations, as explained before. When the excitations are localized on a single bond, the RIXS intensity is modulated similarly to the case of a dimer. We make use of this modulation in Chap. 4 and Pub. [2]. In the ideal case, we decompose the honeycomb lattice into independent dimers and each dimer gives rise to a characteristic modulation and polarization dependence of the RIXS intensity. This is shown to provide a very good description of the RIXS data, see Chap. 4.2.

Thesis outline

In this chapter, we provided an overview of the topics covered in the following of the thesis. We discussed the emergence of phenomena such as Mott insulators, in which Coulomb repulsion between electrons is so strong that it leads to the formation of localized magnetic moments. These localized moments interact with each other in ways that depend on the charge, orbital, spin, and lattice degrees of freedom. We highlighted the importance of orbital degrees of freedom, particularly their directionality. In Chap. 2.1, we will describe the $5d$ orbitals, focusing on the effect of octahedral coordination with a cubic crystal field, as discussed in Chap. 2.1.1. In Chap. 2.1.2, we will explore how spin-orbit coupling leads to the formation of spin-orbit entangled moments, with particular emphasis on the role of the quantization axis. In Chap. 2.1.3, we will model the electron-electron interaction. In Chap. 2.2, we will go beyond the single site and consider two-site clusters in different geometries, such as corner-, edge-, and face-sharing configurations. We will examine how to model the hopping within clusters, which is crucial for describing the quasimolecular orbitals in cluster Mott insulators.

In Chap. 3, we describe the RIXS technique, which is the tool used in this thesis to study the excitations in Kitaev materials and cluster Mott insulators. In Chap. 3.1, we provide a theoretical description of the RIXS process. In Chap. 3.2, we focus on the RIXS interference that arises in clusters with quasimolecular orbitals. We introduce, as an example, the results on the dimer compound $Ba_3Ti_{3-x}Ir_xO_9$ [1]. In Chap. 3.3, we show how to calculate the RIXS amplitude in practice. We see, as an example, how the modulation of the RIXS intensity arises in a dimer and how it contains the information about the relative symmetry of the eigenstates.

In Chap. 4, we present the results of the RIXS study on Kitaev materials. In Chap. 4.1, we reproduce Pub. [2] on Na_2IrO_3. We show how, through the study of the dependence of the RIXS intensity of magnetic excitations on the exchanged momentum and polarization, we can demonstrate the bond-directional character of the excitations. The model used to describe the data is explained in more detail in Chap. 4.2. In Chap. 4.3, we present the results on α-Li_2IrO_3 and compare them with Na_2IrO_3, revealing a common phenomenology of the magnetic excitations in these materials.

In Chap. 5, we reproduce Pub. [4] on the trimer compound $Ba_4NbIr_3O_{12}$. We show that the electrons form quasimolecular orbitals localized on the trimer by measuring the modulation of the RIXS intensity as a function of the exchanged momentum. The symmetry of the wavefunction in this trimer gives rise to characteristic modulations of the RIXS intensity, which we use to identify the excitations.

In Chap. 6, we present our studies on the lacunar spinel $GaTa_4Se_8$, which hosts tetramers arranged in a tetrahedral geometry. In Chap. 6.1, we reproduce Pub. [3], where we study the RIXS interference effect in this system. This allows us to prove the quasimolecular character of the wavefunction and clarify the peak assignment. Moreover, we show how the interference effect is sensitive to the mixing of bonding and antibonding states. This mixing has important consequences for the quasimolecular magnetic moment and the effective spin-orbit splitting. We provide further insights into the tetrahedral quasimolecular orbitals in Chap. 6.2, where we demonstrate how to calculate the quasimolecular wavefunction and the

effect of spin-orbit coupling. In Chap. 6.3, we show how to calculate analytically the single-electron RIXS amplitude in the case of tetrahedral quasimolecular orbitals. In Chap. 6.4, we show how to calculate the quasimolecular orbitals and the RIXS amplitude numerically using the software Quanty. We discuss numerically the effect of electron-electron interaction on the quasimolecular orbitals and the RIXS amplitude.

Finally, in Chap. 7, we summarize the results and discuss the importance for the future research in the field.

Chapter 2

From isolated d orbitals to clusters

In Chapter 1, we discussed how, in Mott insulators, the electron-electron interaction in, e.g., transition-metal compounds leads to the localization of electrons on atomic sites. The properties of these compounds are largely determined by the non-trivial interplay of different degrees of freedom: charge, orbital, spin, and lattice. The hopping acts as a perturbation giving rise to (super-)exchange interactions between the localized magnetic moments. To understand the magnetism in these systems, we need to understand the magnetic moments and their interactions. For the description of the local moments in Mott insulators, it is sufficient to consider a single site, taking into account the crystal field, spin-orbit coupling, and the electron-electron interaction. Instead, in cluster Mott insulators, the hopping between transition-metal ions is not just a perturbation but it leads to the delocalization of electrons and the formation of quasimolecular magnetic moments.

In Chapter 2.1.1, we present how to describe the interaction of the ion with the nearest-neighbor ligand ions using crystal-field theory. We point out the effect of a cubic crystal field on the $5d$ orbitals, which leads to a specific directionality of the orbitals. In Chapter 2.1.2, we discuss how to describe the relativistic effect of spin-orbit coupling, focusing on the role of the quantization axis and the formation of spin-orbit entangled magnetic moments. Then, we describe the electron-electron interaction in Chapter 2.1.3. In Chapter 2.2, we extend the discussion beyond the single-site model to describe the hopping in common geometries of corner-, edge-, and face-sharing octahedra.

2.1 5d orbitals

2.1.1 Crystal field

In the materials presented in this thesis, the transition-metal elements are found inside a roughly octahedral cage of so-called ligand ions, forming MX_6 octahedra with M = Ta and Ir and X = O and Se. The interaction of the transition metal with the ligands can be treated as an effective electrostatic potential, called the crystal field [207, 208]. The presence of the octahedral crystal field has the effect of reducing the symmetry from spherical to cubic O_h. For a single electron, the energy levels of the $5d$ electrons are tenfold degenerate in spherical symmetry. In cubic O_h symmetry, they are split into orbitals of t_{2g} and e_g symmetry. In spherical symmetry, a convenient basis for the angular part of the wavefunctions is the

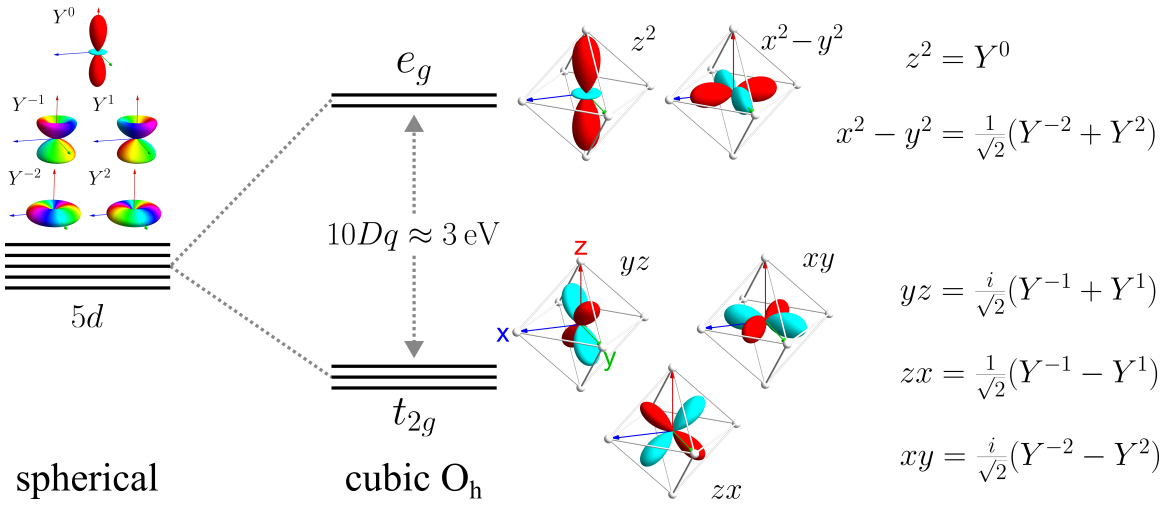

Figure 2.1: Sketch of the single-electron energy levels of the $5d$ shell. The $5d$ electron shell in spherical symmetry is tenfold degenerate. In octahedral coordination, the symmetry is reduced from spherical to cubic O_h. The $5d$ orbitals are split into orbitals of t_{2g} and e_g symmetry. This splitting is $10Dq \approx 3$ eV. On the right, the expressions for the angular parts of the $5d$ cubic orbitals z^2, x^2-y^2, yz, zx, and xy are given as functions of the spherical harmonics with $l = 2$, Y^{m_l}. The angular density is plotted on the left for the spherical harmonics Y^{m_l} and on the right for the cubic harmonics.

spherical harmonics Y^{m_l} with $l = 2$. In cubic symmetry, the cubic harmonics are used, as shown in Fig. 2.1. Their expressions can be represented as a transformation matrix from the spherical harmonics basis [14]

$$\begin{pmatrix} yz \\ zx \\ xy \\ z^2 \\ x^2-y^2 \end{pmatrix} = \begin{pmatrix} 0 & \frac{i}{\sqrt{2}} & 0 & \frac{i}{\sqrt{2}} & 0 \\ 0 & \frac{1}{\sqrt{2}} & 0 & -\frac{1}{\sqrt{2}} & 0 \\ \frac{i}{\sqrt{2}} & 0 & 0 & 0 & -\frac{i}{\sqrt{2}} \\ 0 & 0 & 1 & 0 & 0 \\ \frac{1}{\sqrt{2}} & 0 & 0 & 0 & \frac{1}{\sqrt{2}} \end{pmatrix} \begin{pmatrix} Y^{-2} \\ Y^{-1} \\ Y^0 \\ Y^1 \\ Y^2 \end{pmatrix}. \tag{2.1}$$

In Fig. 2.1, the angular densities of the t_{2g} and e_g orbitals are depicted. The names we use to denote the orbitals (yz, zx, xy, z^2, x^2-y^2) are the actual mathematical expressions for the angular parts of the wavefunctions (where we simplified $3z^2 - r^2$ to z^2). These orbitals have an ellipsoidal shape and a specific orientation in space, which is crucial for many effects. The density of the e_g orbitals (z^2 and x^2-y^2) has lobes pointing toward the ligand atoms, while the t_{2g} orbitals (yz, zx, and xy) point in between ligand atoms. From the angular distribution, we can intuitively expect that the interaction with the ligands is stronger for the e_g orbitals than for the t_{2g} orbitals, leading to a splitting of the energy of the t_{2g} and e_g orbitals. The crystal-field splitting arises from the combined effects of d-p hybridization with the ligands and the electrostatic interaction between the orbitals and the negatively charged ligands. Due to the significant extent of the radial part of the $5d$ orbitals, this results in a splitting of the energy levels, known as $10Dq$, which for $5d$ elements is typically around 3-4 eV [14]. This large splitting results in the electronic configurations $5d^{4,5,6}$ adopting a low-spin state where all electrons occupy the t_{2g} orbitals. For an isolated ion, Hund's rules, which arise from electron-electron interactions, favor the parallel alignment of spins in the

ground state. Considering, e.g., three electrons in octahedral symmetry, these will occupy the t_{2g} with the same alignment of the spin forming $S = 3/2$. For a fourth electron, the Coulomb energy is minimized if it is placed in the e_g orbitals with parallel spin, leading to a high-spin state with $S = 2$. However, it becomes energetically favorable for a fourth electron to occupy the t_{2g} states if $10Dq > 3J_H$, leading to a low-spin ground state. This is true for $5d$ transition metals, where $10Dq$ is about 3-4 eV and J_H amounts to 0.25-0.4 eV, see below. So, in the cases discussed in this thesis, the e_g orbitals will be neglected.

We can make an interesting consideration by calculating the orbital angular momentum of the cubic orbitals starting from the relations

$$L_z \left|Y_l^{m_l}\right\rangle = m_l \hbar \left|Y_l^{m_l}\right\rangle \text{ and } L_\pm \left|Y_l^{m_l}\right\rangle = \hbar\sqrt{(l(l+1) - m_l(m_l \pm 1))}\left|Y_l^{m_l}\right\rangle, \tag{2.2}$$

which lead to the following matrices in the cubic basis $\{yz,\ zx,\ xy,\ z^2,\ x^2 - y^2\}$:

$$L_x = \left(\begin{array}{ccc|cc} 0 & 0 & 0 & -i\sqrt{3} & -i \\ 0 & 0 & i & 0 & 0 \\ 0 & -i & 0 & 0 & 0 \\ \hline i\sqrt{3} & 0 & 0 & 0 & 0 \\ i & 0 & 0 & 0 & 0 \end{array}\right), \quad L_y = \left(\begin{array}{ccc|cc} 0 & 0 & -i & 0 & 0 \\ 0 & 0 & 0 & i\sqrt{3} & -i \\ i & 0 & 0 & 0 & 0 \\ \hline 0 & -i\sqrt{3} & 0 & 0 & 0 \\ 0 & i & 0 & 0 & 0 \end{array}\right),$$
$$\text{and} \quad L_z = \left(\begin{array}{ccc|cc} 0 & i & 0 & 0 & 0 \\ -i & 0 & 0 & 0 & 0 \\ 0 & 0 & 0 & 0 & 2i \\ \hline 0 & 0 & 0 & 0 & 0 \\ 0 & 0 & -2i & 0 & 0 \end{array}\right). \tag{2.3}$$

From these matrices, we observe that the orbital angular momentum in the e_g orbital sector is fully quenched (i.e., it is zero). Instead, the orbital angular momentum of the t_{2g} shell is only partially quenched, as it is equivalent to a p shell with an effective angular momentum $l_{\text{eff}} = -1$. In fact, the same 3×3 matrices, multiplied by -1, are obtained using the expressions in Eq. (2.2) with $l = 1$ and the p orbitals $\{x, y, z\}$ defined as

$$\begin{pmatrix} x \\ y \\ z \end{pmatrix} = \begin{pmatrix} \frac{i}{\sqrt{2}} & 0 & -\frac{i}{\sqrt{2}} \\ \frac{1}{\sqrt{2}} & 0 & \frac{1}{\sqrt{2}} \\ 0 & 1 & 0 \end{pmatrix} \begin{pmatrix} Y^{-1} \\ Y^0 \\ Y^1 \end{pmatrix}. \tag{2.4}$$

Thus, when restricted to the t_{2g} orbitals, the system can be effectively treated as having an orbital angular momentum $l_{\text{eff}} = -1$. Note that some authors adopt a convention with $l_{\text{eff}} = +1$, while the sign of the spin-orbit coupling parameter is inverted.

A distortion of the octahedral ligand cage gives rise to deviations from cubic symmetry, leading to a further splitting of the orbitals. There are different possible distortions [14,209]. For our discussion, we consider a trigonal distortion as obtained for compression or elongation along one of the four equivalent [111] axes perpendicular to the faces. This yields a single C_3 symmetry axis, and the symmetry is reduced to D_{3d}. The t_{2g} orbitals split into an a_{1g} singlet and an e_g^π doublet with an energy difference of Δ. In the basis $\{yz, zx, xy\}$, for a

distortion along [111], the trigonal crystal-field Hamiltonian can be written as [210]

$$H_{trig} = -\frac{\Delta}{3}\begin{pmatrix} 0 & 1 & 1 \\ 1 & 0 & 1 \\ 1 & 1 & 0 \end{pmatrix}, \tag{2.5}$$

where a positive Δ reduces the energy of the a_{1g} state by $-\frac{2}{3}\Delta$ and increases the energy of the e_g^π states by $\frac{1}{3}\Delta$. The trigonal orbitals can be written as a real combination of the t_{2g} orbitals

$$\begin{pmatrix} a_{1g} \\ e_{g,a}^\pi \\ e_{g,b}^\pi \end{pmatrix} = \begin{pmatrix} \frac{1}{\sqrt{3}} & \frac{1}{\sqrt{3}} & \frac{1}{\sqrt{3}} \\ \frac{1}{\sqrt{2}} & -\frac{1}{\sqrt{2}} & 0 \\ -\frac{1}{\sqrt{6}} & -\frac{1}{\sqrt{6}} & \frac{2}{\sqrt{6}} \end{pmatrix} \begin{pmatrix} yz \\ zx \\ xy \end{pmatrix} \tag{2.6}$$

or as a complex combination

$$\begin{pmatrix} a_{1g} \\ e_{g,a}^\pi \\ e_{g,b}^\pi \end{pmatrix} = \frac{1}{\sqrt{3}} \begin{pmatrix} 1 & 1 & 1 \\ e^{-2\pi i/3} & e^{i\,2\pi/3} & 1 \\ -e^{2\pi i/3} & -e^{-i\,2\pi/3} & -1 \end{pmatrix} \begin{pmatrix} yz \\ zx \\ xy \end{pmatrix}. \tag{2.7}$$

2.1.2 Spin-orbit coupling

The spin-orbit coupling is a relativistic effect that couples the orbital and spin angular momentum of electrons. The spin-orbit Hamiltonian can be written as

$$H_{so} = \zeta \sum_i \mathbf{l}_i \cdot \mathbf{s}_i, \tag{2.8}$$

where $\mathbf{l}_i$ and $\mathbf{s}_i$ are the orbital and spin angular momentum operators of the single electron i, and ζ is a parameter that describes the strength of the spin-orbit coupling. This parameter can be calculated as

$$\zeta = \langle R(r)| \frac{1}{2m^2c^2} \frac{1}{r} \frac{\mathrm{d}V(r)}{\mathrm{d}r} |R(r)\rangle, \tag{2.9}$$

where $R(r)$ is the radial part of the atomic wavefunction and $V(r)$ is the atomic potential.

For a many-body system in LS coupling, the spin-orbit coupling can be written as

$$H_{so} = \lambda\, \mathbf{L}\cdot\mathbf{S} = \lambda \left(L_z S_z + \frac{1}{2}(L^+S^- + L^-S^+) \right) = \lambda \left(L_x S_x + L_y S_y + L_z S_z \right), \tag{2.10}$$

where $\mathbf{L}$ and $\mathbf{S}$ are the *total* orbital and spin angular momentum operators, respectively, and $\lambda = \pm\zeta/(2S)$, with the "+" sign for less-than-half-filled shells and the "−" sign for more-than-half-filled shells.

We calculate the spin-orbit coupling matrix starting from the L_x, L_y, and L_z matrices in Eq. (2.3) and the Pauli matrices

$$\sigma_x = \begin{pmatrix} 0 & 1 \\ 1 & 0 \end{pmatrix} \frac{1}{2}, \quad \sigma_y = \begin{pmatrix} 0 & -i \\ i & 0 \end{pmatrix} \frac{1}{2}, \quad \sigma_z = \begin{pmatrix} 1 & 0 \\ 0 & -1 \end{pmatrix} \frac{1}{2}. \tag{2.11}$$

We aim to derive the spin-orbit coupling Hamiltonian for a generic spin direction in the t_{2g} basis. The spin quantization axis is important in the calculation of the RIXS intensity, as

explained, for example, in Ref. [211]. We calculate the spin-orbit coupling by keeping the definition of the orbital operators in the local basis but rotating the local spin operators to the global spin quantization axis. For a generic spin direction, obtained by rotating the local reference frame with the rotation matrix $R_z(\phi) \cdot R_y(\theta)$, where θ is the polar angle and ϕ is the azimuthal angle, we can rewrite Eq. (2.10) as

$$\begin{aligned} H_{so}(\theta,\phi) = \lambda[&L_x\left(\cos(\theta)\cos(\phi)S_x + \sin(\theta)\cos(\phi)S_y - \sin(\phi)S_z\right) \\ &+L_y\left(\cos(\theta)\sin(\phi)S_x + \cos(\phi)S_y + \sin(\theta)\sin(\phi)S_z\right) \\ &+L_z\left(-\sin(\theta)S_x + \cos(\theta)S_z\right)]. \end{aligned} \tag{2.12}$$

Using the expressions in Eq. (2.3) and (2.11), we obtain a matrix that describes the spin-orbit interaction in the t_{2g} basis $\{yz\uparrow, yz\downarrow, zx\uparrow, zx\downarrow, xy\uparrow, xy\downarrow\}$ as a function of the angles θ and ϕ

$$H_{so}(\theta,\phi) = \frac{\lambda}{2}\begin{pmatrix} 0 & 0 & i\mathrm{c}_\theta & -i\mathrm{s}_\theta & -i\mathrm{s}_\theta\mathrm{s}_\phi & -\mathrm{c}_\phi - i\mathrm{c}_\theta\mathrm{s}_\phi \\ 0 & 0 & -i\mathrm{s}_\theta & -i\mathrm{c}_\theta & \mathrm{c}_\phi - i\mathrm{c}_\theta\mathrm{s}_\phi & i\mathrm{s}_\theta\mathrm{s}_\phi \\ -i\mathrm{c}_\theta & i\mathrm{s}_\theta & 0 & 0 & i\mathrm{s}_\theta\mathrm{c}_\phi & -\mathrm{s}_\phi + i\mathrm{c}_\theta\mathrm{c}_\phi \\ i\mathrm{s}_\theta & i\mathrm{c}_\theta & 0 & 0 & \mathrm{s}_\phi + i\mathrm{c}_\theta\mathrm{c}_\phi & -i\mathrm{s}_\theta\mathrm{c}_\phi \\ i\mathrm{s}_\theta\mathrm{s}_\phi & \mathrm{c}_\phi + i\mathrm{c}_\theta\mathrm{s}_\phi & -i\mathrm{s}_\theta\mathrm{c}_\phi & \mathrm{s}_\phi - i\mathrm{c}_\theta\mathrm{c}_\phi & 0 & 0 \\ -\mathrm{c}_\phi + i\mathrm{c}_\theta\mathrm{s}_\phi & -i\mathrm{s}_\theta\mathrm{s}_\phi & -\mathrm{s}_\phi - i\mathrm{c}_\theta\mathrm{c}_\phi & i\mathrm{s}_\theta\mathrm{c}_\phi & 0 & 0 \end{pmatrix}, \tag{2.13}$$

where we defined, for brevity, $\mathrm{c}_x := \cos(x)$ and $\mathrm{s}_x := \sin(x)$.

An alternative way to derive the same spin-orbit coupling Hamiltonian follows a discussion similar to Ref. [212]. The spin matrix for a generic spin direction can be written as

$$\sigma = \sigma_x \sin(\theta)\cos(\phi) + \sigma_y \sin(\theta)\sin(\phi) + \sigma_z \cos(\theta), \tag{2.14}$$

where θ is the polar angle and ϕ is the azimuthal angle. The eigenvectors $\sigma\,|\pm\rangle = \pm 1\,|\pm\rangle$ can be written as

$$\begin{aligned} |+\rangle &= \begin{pmatrix}\alpha_+\\ \beta_+\end{pmatrix} = \begin{pmatrix} e^{-i\phi}\cos(\theta/2)\\ \sin(\theta/2)\end{pmatrix}, \\ |-\rangle &= \begin{pmatrix}\alpha_-\\ \beta_-\end{pmatrix} = \begin{pmatrix} -e^{-i\phi}\sin(\theta/2)\\ \cos(\theta/2)\end{pmatrix}. \end{aligned} \tag{2.15}$$

We can write a transformation that changes the spin quantization from the z axis to the direction described by the polar angle θ and the azimuthal angle ϕ as

$$R_{so}(\theta,\phi) = \begin{pmatrix} \alpha_+ & \beta_+ & 0 & 0 & 0 & 0 \\ \alpha_- & \beta_- & 0 & 0 & 0 & 0 \\ 0 & 0 & \alpha_+ & \beta_+ & 0 & 0 \\ 0 & 0 & \alpha_- & \beta_- & 0 & 0 \\ 0 & 0 & 0 & 0 & \alpha_+ & \beta_+ \\ 0 & 0 & 0 & 0 & \alpha_- & \beta_- \end{pmatrix}. \tag{2.16}$$

By applying this change of basis to the spin-orbit coupling Hamiltonian of Eq. (2.10) as $R^*_{so} \cdot H_{so} \cdot R^T_{so}$, we obtain the same matrix as in Eq. (2.13).

The standard convention for the spin quantization axis is along the z axis. In this case,

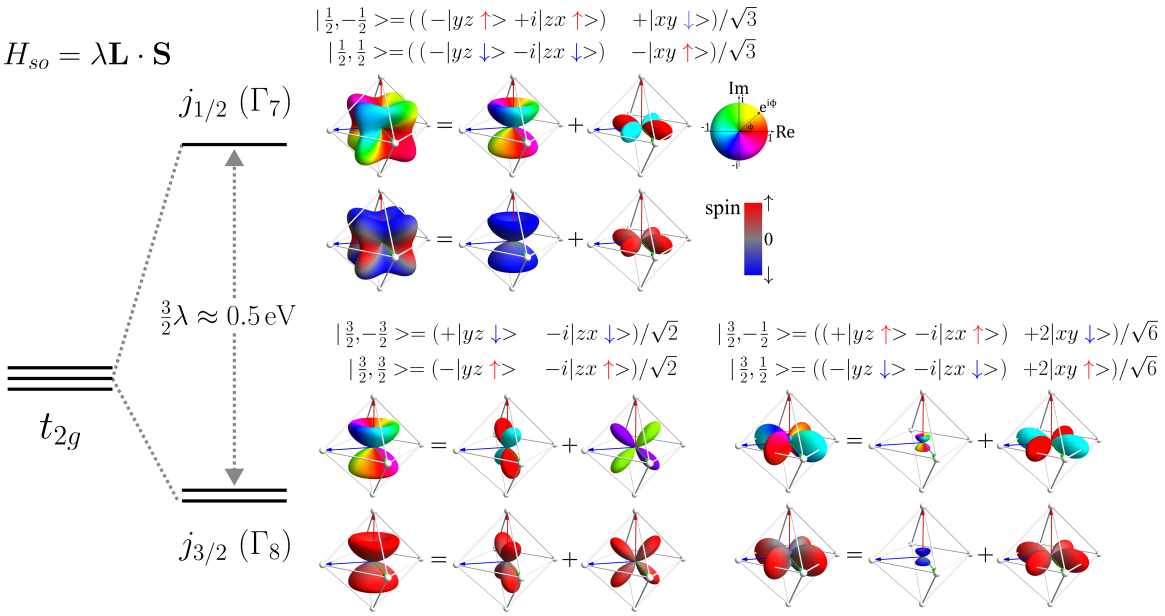

Figure 2.2: For a t_{2g}^1 configuration (or t_{2g}^5), the spin-orbit coupling $H_{so} = \lambda \mathbf{L} \cdot \mathbf{S}$ lifts the degeneracy of the t_{2g} states and splits them into a quartet and a doublet with $j = \frac{3}{2}$ and $j = \frac{1}{2}$, respectively. The splitting is $\frac{3}{2}\lambda$, which for $5d$ transition metals is approximately 0.5 eV. The expressions for the eigenstates $|j, j_z\rangle$ of the spin-orbit Hamiltonian are provided. Spin-orbit coupling mixes t_{2g} orbitals with different spins, leading to spin-orbit entangled wavefunctions with anisotropic spin distribution. This is illustrated in the plot of the density of the angular part of the wavefunctions, shown here for $|j, +j_z\rangle$. The color represents the phase on the top and the spin direction on the bottom.

we have $\theta = \phi = 0$, and the spin-orbit coupling Hamiltonian matrix is [213]

$$H_{so}^z = \begin{pmatrix} 0 & 0 & i & 0 & 0 & -1 \\ 0 & 0 & 0 & -i & 1 & 0 \\ -i & 0 & 0 & 0 & 0 & i \\ 0 & i & 0 & 0 & i & 0 \\ 0 & 1 & 0 & -i & 0 & 0 \\ -1 & 0 & -i & 0 & 0 & 0 \end{pmatrix} \frac{\lambda}{2}. \tag{2.17}$$

The spin-orbit interaction lifts the degeneracy of the t_{2g} orbitals and splits them according to their value of j. Since the t_{2g} electrons have an *effective* orbital angular momentum $l_{\text{eff}} = -1$, the levels split into an *effective* total angular momentum $j_{\text{eff}} = 3/2$ quartet and a $j_{\text{eff}} = 1/2$ doublet, as shown in Fig. 2.2. In the following, we omit the subscript "eff" for simplicity. As shown by Eq. (2.9), the spin-orbit coupling parameter ζ changes from ion to ion. For example, for $5d$ ions like Ta^{4+} and Ir^{4+}, the spin-orbit coupling leads to a splitting of the t_{2g} orbitals of $\approx$ 0.4 eV [214] and $\approx$ 0.6 eV [9] [215], respectively. The eigenstates of the spin-orbit coupling Hamiltonian are denoted by their values of j and j_z as $|j, j_z\rangle$: $(|\frac{1}{2}, +\frac{1}{2}\rangle, |\frac{1}{2}, -\frac{1}{2}\rangle, |\frac{3}{2}, +\frac{3}{2}\rangle, |\frac{3}{2}, -\frac{3}{2}\rangle, |\frac{3}{2}, +\frac{1}{2}\rangle, |\frac{3}{2}, -\frac{1}{2}\rangle)$. In the basis of the cubic states

$\{yz\uparrow, yz\downarrow, zx\uparrow, zx\downarrow, xy\uparrow, xy\downarrow\}$, they can be written as [216]

$$\begin{pmatrix} |\frac{1}{2},+\frac{1}{2}\rangle \\ |\frac{1}{2},-\frac{1}{2}\rangle \\ |\frac{3}{2},+\frac{3}{2}\rangle \\ |\frac{3}{2},-\frac{3}{2}\rangle \\ |\frac{3}{2},+\frac{1}{2}\rangle \\ |\frac{3}{2},-\frac{1}{2}\rangle \end{pmatrix} = \begin{pmatrix} 0 & -\frac{1}{\sqrt{3}} & 0 & -\frac{i}{\sqrt{3}} & -\frac{1}{\sqrt{3}} & 0 \\ -\frac{1}{\sqrt{3}} & 0 & \frac{i}{\sqrt{3}} & 0 & 0 & \frac{1}{\sqrt{3}} \\ -\frac{1}{\sqrt{2}} & 0 & -\frac{i}{\sqrt{2}} & 0 & 0 & 0 \\ 0 & \frac{1}{\sqrt{2}} & 0 & -\frac{i}{\sqrt{2}} & 0 & 0 \\ 0 & -\frac{1}{\sqrt{6}} & 0 & -\frac{i}{\sqrt{6}} & \sqrt{\frac{2}{3}} & 0 \\ \frac{1}{\sqrt{6}} & 0 & -\frac{i}{\sqrt{6}} & 0 & 0 & \sqrt{\frac{2}{3}} \end{pmatrix} \begin{pmatrix} |yz\uparrow\rangle \\ |yz\downarrow\rangle \\ |zx\uparrow\rangle \\ |zx\downarrow\rangle \\ |xy\uparrow\rangle \\ |xy\downarrow\rangle \end{pmatrix}. \tag{2.18}$$

In Fig. 2.2, the angular densities of the eigenstates are shown. Spin-orbit coupling mixes t_{2g} orbitals with different spins, leading to spin-orbit entangled wavefunctions with anisotropic spin distribution. For example, the state

$$|\frac{1}{2},+\frac{1}{2}\rangle = (-|yz\downarrow\rangle - i\,|zx\downarrow\rangle - |xy\uparrow\rangle)/\sqrt{3} \tag{2.19}$$

is composed of a spin-up $xy\uparrow$ and spin-down $yz\downarrow$ and $zx\downarrow$ states. This means that the spin direction is tied to a certain orbital component, and since the t_{2g} orbitals have a definite spatial orientation, this can lead to anisotropic magnetic interactions. In systems with an electronic configuration t_{2g}^5, such as Ir^{4+}, the ground state can be described as a single hole in the $j = 1/2$ doublet. This state can be represented as a pseudo-spin $\frac{1}{2}$ state. However, it shows unusual properties due to the spin-orbit entangled nature of the wavefunction. For example, the calculation of the expectation values for the spin, orbital, and total angular momentum of the $|j, +j_z\rangle$ wavefunctions gives [212]

	S_z	L_z	J_z
$\|\frac{1}{2},+\frac{1}{2}\rangle$	$-\frac{1}{6}$	$-\frac{2}{3}$	$-\frac{5}{6}$
$\|\frac{3}{2},+\frac{3}{2}\rangle$	$+\frac{1}{2}$	-1	$-\frac{1}{2}$
$\|\frac{3}{2},+\frac{1}{2}\rangle$	$+\frac{1}{6}$	$-\frac{1}{3}$	$-\frac{1}{6}$

(2.20)

and opposite signs for the $|j, -j_z\rangle$ wavefunctions.

Instead, if the magnetic moment points along the y direction, for example, we have $\theta = \phi = 90°$, and the spin-orbit Hamiltonian is

$$H_{so}^{y} = \begin{pmatrix} 0 & 0 & 0 & -i & -i & 0 \\ 0 & 0 & -i & 0 & 0 & i \\ 0 & i & 0 & 0 & 0 & -1 \\ i & 0 & 0 & 0 & 1 & 0 \\ i & 0 & 0 & 1 & 0 & 0 \\ 0 & -i & -1 & 0 & 0 & 0 \end{pmatrix} \frac{\lambda}{2}. \tag{2.21}$$

To understand the consequences, we take as an example the $j = 1/2$ wavefunction. When the quantization is along y, the wavefunction becomes

$$|\frac{1}{2},+\frac{1}{2}\rangle_y = (-i\,|yz\downarrow_y\rangle + |zx\uparrow_y\rangle + |xy\downarrow_y\rangle)/\sqrt{3}, \tag{2.22}$$

where the subscript $\uparrow_y$ indicates the quantization axis. By comparing Eq. (2.22) with the expression for the quantization axis along z in Eq. (2.19), one can see that the orbital with spin-up component is different. Since the spin and orbital degrees of freedom are entangled, the spin distribution is different. This results in different magnetic interactions and a different polarization dependence in the RIXS process.

2.1.3 Electron-electron interaction

We saw in Chap. 1 how the electron-electron (e-e) interaction is very important and leads to the formation of interesting strongly correlated electron systems. Here, we see how to model the e-e interaction considering a single site. This is important for the multiplet structure of the energy levels [217], and we will observe its significance when modeling clusters.

Electrons interact via the Coulomb interaction $H_{e\text{-}e} = \frac{1}{2}\sum_{i\neq j}\frac{e^2}{|r_i - r_j|}$, where r_i is the position of the i-th electron interacting with the j-th electron at position r_j. The e-e interaction can be treated as a scattering process mediated by the electrostatic force. Two electrons with quantum numbers τ_3 and τ_4 scatter into the states with the quantum numbers τ_1 and τ_2 where $\tau_i : n, l, m_i, \sigma_i$. For the scattering of electrons occupying the same shell, we have $n_1 = n_2 = n_3 = n_4$ and $l_1 = l_2 = l_3 = l_4$. The Hamiltonian in second quantization can be written as

$$H_{e\text{-}e} = \sum_{\tau_1\tau_2\tau_3\tau_4} U_{\tau_1\tau_2\tau_3\tau_4} a^\dagger_{\tau_1} a^\dagger_{\tau_2} a_{\tau_3} a_{\tau_4}. \tag{2.23}$$

By expressing the wavefunctions in terms of a radial and an angular part, we can calculate the coefficients as an integral over the radial part and one over the angular part. The integral over the angular part determines which integrals over the radial parts are relevant, known as the Slater integrals F^k. The conservation of angular momentum restricts the number of parameters such that $|l_f - l_i| \leq k \leq |l_f + l_i|$ and k is even. For a d shell with $l = 2$, this results in three terms: F^0, F^2, and F^4.

Kanamori proposed a simplification of the full e-e Hamiltonian [218] based on the approximation that the interaction terms depend only on whether the electrons occupy the same or a different orbital. When the calculation is restricted to the t_{2g} shell, the approximation is exact. The e-e interaction Hamiltonian can then be written in the so-called Kanamori scheme as follows [216, 219]:

$$\begin{aligned} H_C = U \sum_{\alpha} n_{\alpha\uparrow} n_{\alpha\downarrow} + \frac{1}{2}(U - 3J_H) \sum_{\sigma,\alpha\neq\alpha'} n_{\alpha\sigma} n_{\alpha'\sigma} + (U - 2J_H) \sum_{\alpha\neq\alpha'} n_{\alpha\uparrow} n_{\alpha'\downarrow} \\ + J_H \sum_{\alpha\neq\alpha'} \left(c^\dagger_{\alpha\uparrow} c^\dagger_{\alpha\downarrow} c_{\alpha'\downarrow} c_{\alpha'\uparrow} - c^\dagger_{\alpha\uparrow} c_{\alpha\downarrow} c^\dagger_{\alpha'\downarrow} c_{\alpha'\uparrow} \right), \end{aligned} \tag{2.24}$$

where $c^\dagger_{\alpha\sigma}$ ($c_{\alpha\sigma}$) creates (annihilates) an electron of orbital type α with spin $\sigma =\uparrow,\downarrow$, and $n_{\alpha\sigma} = c^\dagger_{\alpha\sigma} c_{\alpha\sigma}$ is the number operator. The intraorbital Coulomb repulsion is given by U, and J_H denotes Hund's coupling [14].

As mentioned, when restricted to the t_{2g} orbitals, the Kanamori Hamiltonian and the full e-e interaction Hamiltonian are equivalent. We can then write a relationship between

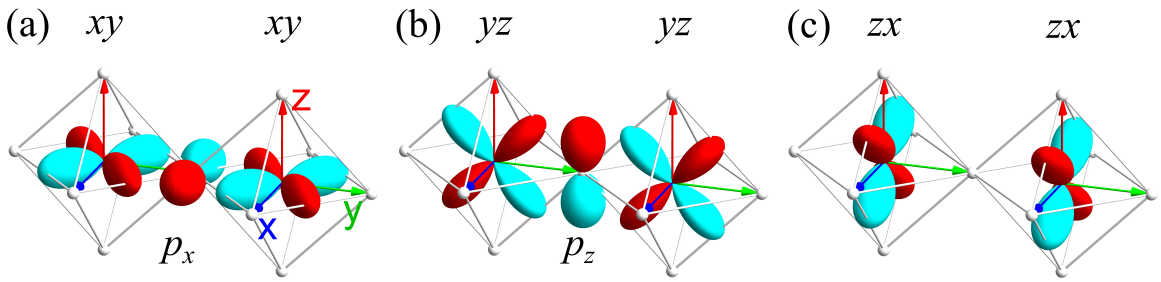

Figure 2.3: Sketch of the corner-sharing geometry showing the allowed hopping paths for the ideal M-L-M bond angle of 180°. With reference to the local $\{x, y, z\}$ coordinate frame as defined in (a), the hopping paths are: (a) hopping between xy and xy orbitals; (b) yz and yz; (c) zx and zx. (a) and (b) are hoppings via the p orbitals of the ligands. See the hopping matrix in Eq. (2.26).

the Slater integrals F^0, F^2, and F^4 and the parameters U and J_H [217,219],

$$\begin{aligned} U &= F^0 + \frac{4}{49}F^2 + \frac{4}{49}F^4, \\ J_H &= \frac{3}{49}F^2 + \frac{20}{441}F^4. \end{aligned} \tag{2.25}$$

To complete the conversion, we need to assume a certain ratio F^4/F^2. Their values can be calculated using Hartree-Fock calculations [217, 220], which indicate a ratio of about $F^4/F^2 \approx 5/8$. Typical values of J_H for $5d$ transition metals are in the range 0.25-0.4 eV, while U is in the range 1.5-2.5 eV. For example, optical spectroscopy and RIXS studies on the $5d^4$ system K_2OsCl_6 and the $5d^3$ system K_2ReCl_6 report values of $J_H = 0.28$ eV and $J_H = 0.34$ eV, respectively [7, 8]. For $5d^4$ iridates, RIXS studies find J_H in the range 0.25-0.4 eV [221–224].

2.2 Corner-, edge-, and face-sharing octahedra

In the following chapter we briefly discuss how the orbitals of the MO_6 octahedra interact with each other in the corner-, edge-, and face-sharing geometries. More detailed discussions can be found in Refs. [14, 22–25]. When the hopping is relatively small ($t/U \ll 1$), it can typically be treated as a perturbation to the local single-site wavefunctions giving rise to (super-)exchange interactions. The resulting interactions depend on the geometry, the available hopping paths, and the orbital occupation. Instead, when the hopping is large, the local single-site wavefunctions are no longer a good starting point, and the quasimolecular bonding and antibonding states formed by their superposition must be considered.

2.2.1 Corner-sharing octahedra

In the geometry depicted in Fig. 2.3, neighboring octahedra share one corner along the y axis. It is the most commonly studied configuration, found in systems such as perovskites, post-perovskites, colossal magnetoresistance (CMR) manganites, high-temperature cuprate superconductors like $(La,Sr)_2CuO_4$, and also in the layered iridate Sr_2IrO_4. In the ideal case, the metal-ligand-metal (M-L-M) bond angle is 180° and the hopping matrix in the

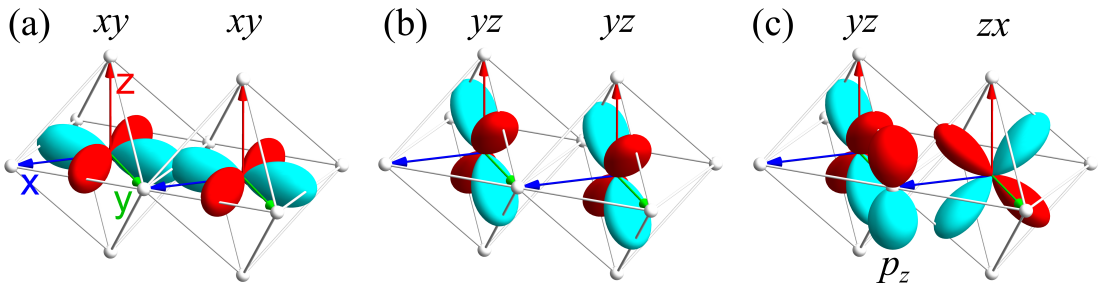

Figure 2.4: Sketch of the edge-sharing geometry showing the allowed hopping paths. With reference to the local $\{x, y, z\}$ coordinate frame as defined in (a), the hopping paths are: (a) hopping between xy and xy orbitals; (b) yz and yz; (c) yz and zx. See the hopping matrix in Eq. (2.27).

t_{2g} orbital basis $\{yz, zx, xy\}$ is

$$T_{corner} = c_2^\dagger \begin{pmatrix} t_1 & 0 & 0 \\ 0 & t_2 & 0 \\ 0 & 0 & t_1 \end{pmatrix} c_1 + \text{c.c.}, \tag{2.26}$$

where $c_1 = (c_{yz_1}, c_{zx_1}, c_{xy_1})$ are the annihilation operators on site 1, and $c_2^\dagger = (c_{yz_2}^\dagger, c_{zx_2}^\dagger, c_{xy_2}^\dagger)$ are the creation operators on site 2. The hopping matrix is diagonal, with the hopping parameter t_1 between xy and xy, and between yz and yz orbitals, and t_2 between zx and zx orbitals. As shown in Fig. 2.3, t_1 involves the hopping via the p orbitals of the ligands, while t_2 is a direct hopping between the d orbitals. Small deviations of the bond angle allow other off-diagonal terms to be finite but these do not play a significant role. However, large deviations, such as those found in post-perovskites, can have a substantial impact. For example, values of t_1 in Sr_2IrO_4 are calculated to be around 0.2 eV [225] and dependent on the M-L-M bond angle. The hopping is not very large and can be treated as a perturbation in t/U leading to effective magnetic (super-)exchange interactions. A general conclusion derived from studies of $3d$ compounds, where spin-orbit coupling is negligible, is that ferro-orbital ordering leads to antiferromagnetic spin ordering, while antiferro-orbital ordering leads to ferromagnetic spin exchange. In $5d^5$ systems with strong spin-orbit coupling like Sr_2IrO_4, the spin-orbit entangled $j = 1/2$ ground state is often a good starting point and the hopping in corner-sharing geometry usually leads to antiferromagnetic interactions.

2.2.2 Edge-sharing octahedra

Figure 2.4 shows two octahedra sharing an edge in the x-y plane, more precisely along $(1, 1, 0)$. This configuration is found, for example, in the battery material $LiCoO_2$, in spinels and lacunar spinels, and in Kitaev materials. The hopping channels in the ideal geometry are shown in Fig. 2.4, and the hopping matrix in the t_{2g} orbital basis $\{yz, zx, xy\}$ is [226]

$$T_{edge} = c_2^\dagger \begin{pmatrix} t_1 & t_2 & 0 \\ t_2 & t_1 & 0 \\ 0 & 0 & t_3 \end{pmatrix} c_1 + \text{c.c.}. \tag{2.27}$$

The diagonal hopping channels t_1 and t_3 are direct hopping between the d orbitals, with t_3 involving orbitals that point directly toward each other, as shown in Fig. 2.4(a). The

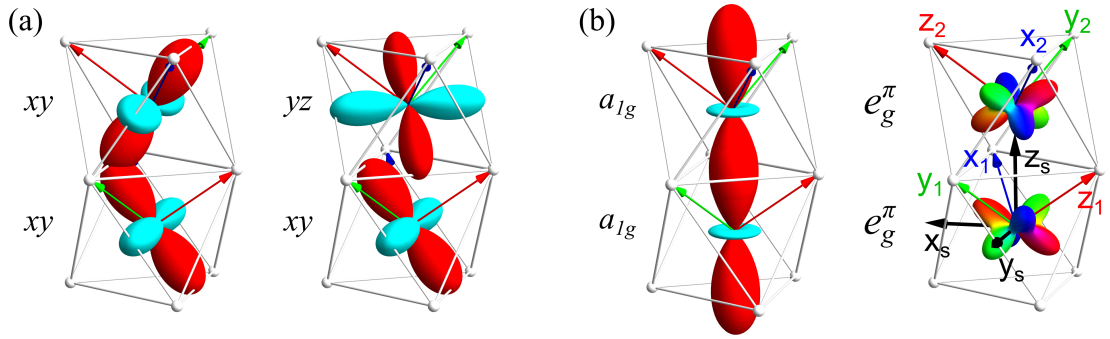

Figure 2.5: Sketch of the face-sharing geometry showing the possible hopping paths. (a) Hopping paths in the t_{2g} basis: the diagonal hopping t_1 (shown for xy-xy) and the off-diagonal hopping t_2 (shown for xy-yz). (b) Hopping paths in the trigonal orbital basis, where the hopping matrix is diagonal: t_σ between a_{1g}-a_{1g} orbitals and t_π between e_g^π-e_g^π orbitals. Note that the local reference frames $\{x_1, y_1, z_1\}$ and $\{x_2, y_2, z_2\}$ are rotated by 180° with respect to each other around the common $\{1, 1, 1\}$ axis. as shown in (b). A global coordinate system $\{x_s, y_s, z_s\}$ is defined. The color represent the phase of the wavefunction, according to the same color code as in Fig. 2.2.

off-diagonal t_2 has a direct hopping component but, importantly, it has a ligand-mediated hopping component that scales as t_{pd}^2/Δ_{CT}, where t_{pd} is the hopping between the transition metal d and the ligand p orbitals, and Δ_{CT} is the charge-transfer energy. For certain deviations from this idealized geometry, the other off-diagonal hopping t_4 becomes finite as well,

$$T_{edge} = c_2^\dagger \begin{pmatrix} t_1 & t_2 & t_4 \\ t_2 & t_1 & t_4 \\ t_4 & t_4 & t_3 \end{pmatrix} c_1 + \text{c.c.}. \tag{2.28}$$

In this geometry, deviations from the ideal 90° M-L-M angle have important consequences on the values of the hopping integrals, as shown by Fig. 4.1 in Chap. 4.2. In Na_2IrO_3, for example, the angle is almost 100°, and the hopping parameter t_2 is calculated to be the largest at about 250 meV, dominated by the hopping via the ligands. The other hopping parameters, t_1 and t_3, are calculated to be only about 10-30 meV [226–229]. In contrast, in $GaTa_4Se_8$, the bond angle is around 72°, and the direct hopping t_3 becomes dominant and quite large, being about 1 eV [133] [3]. As a consequence, the two cases are very different. In Na_2IrO_3, the small hopping can be treated as a perturbation to the local $j = 1/2$ wavefunction, which leads to effective magnetic exchange interactions, explained in more detail in Chap. 4.2. Instead, in $GaTa_4Se_8$, the large hopping drastically affects the wavefunction giving rise to bonding and antibonding quasimolecular orbitals, more details are provided in Chap. 6.2.

2.2.3 Face-sharing octahedra

The face-sharing geometry is the least studied geometry. It is found, for example, in the family of compounds $Ba_3AM_2O_9$ and $Ba_4AM_3O_{12}$ [60], shown in Fig. 1.2 of Chap. 1, which contain M_2O_9 face-sharing dimers and M_3O_{12} face-sharing trimers, respectively. In Fig. 2.5(a), the hopping channels in the t_{2g} basis $\{yz, zx, xy\}$ are shown, and the hopping matrix

is [109,230]

$$T_{face} = -c_2^\dagger \begin{pmatrix} t_1 & t_2 & t_2 \\ t_2 & t_1 & t_2 \\ t_2 & t_2 & t_1 \end{pmatrix} c_1 + \text{c.c.}. \tag{2.29}$$

A more convenient basis for this geometry is the trigonal basis $\{a_{1g}, e^\pi_{g,a}, e^\pi_{g,b}\}$, see Fig. 2.5(b) and Eq. 2.7, on which the hopping matrix is diagonal

$$T_{face} = -c_2^\dagger \begin{pmatrix} t_\sigma & 0 & 0 \\ 0 & t_\pi & 0 \\ 0 & 0 & t_\pi \end{pmatrix} c_1 + \text{c.c.}. \tag{2.30}$$

The relationship between the hopping parameters in the two bases is

$$t_\sigma = t_1 + 2\,t_2, \quad t_\pi = t_1 - t_2. \tag{2.31}$$

Based on *ab-initio* calculations [109] on $5d$ transition metals, t_2 is expected to be about 0.2-0.4 eV, and $t_2 \gg |t_1|$. This means that $t_\sigma \approx 2\,t_2 \approx 0.4$-$0.8$ eV and $f = t_\pi/t_\sigma \approx -1/2$. So, in this geometry for $5d$ elements we expect a strong hopping that gives rise to the formation of bonding and antibonding states.

We can perform the calculations using for the orbitals the local reference frames $\{x_1, y_1, z_1\}$ and $\{x_2, y_2, z_2\}$, as shown in Fig. 2.5. The spin-orbit coupling has to be expressed using a global spin quantization axis, as done in [109]. We introduce a global spin quantization reference frame $\{x_s, y_s, z_s\}$ as in Fig. 2.5(b). The angles θ and ϕ that bring the local frames $\{x_1, y_1, z_1\}$ and $\{x_2, y_2, z_2\}$ into the global frame are, respectively, $(\theta_1, \phi_1) = (\arccos(\frac{1}{\sqrt{3}}), \frac{\pi}{4})$ and $(\theta_2, \phi_2) = (-\arccos(\frac{1}{\sqrt{3}}), -\frac{3\pi}{4})$, where $\arccos(\frac{1}{\sqrt{3}}) \approx 54.74°$. We thus have two different spin-orbit coupling matrices for the two sites, which, by using Eq. 2.13, are given by:

$$H_{so}(\theta_1, \phi_1) = \frac{\lambda}{2} \begin{pmatrix} 0 & 0 & \frac{i}{\sqrt{3}} & -i\sqrt{\frac{2}{3}} & -\frac{i}{\sqrt{3}} & -\frac{1}{\sqrt{2}} - \frac{i}{\sqrt{6}} \\ 0 & 0 & -i\sqrt{\frac{2}{3}} & -\frac{i}{\sqrt{3}} & \frac{1}{\sqrt{2}} - \frac{i}{\sqrt{6}} & \frac{i}{\sqrt{3}} \\ -\frac{i}{\sqrt{3}} & i\sqrt{\frac{2}{3}} & 0 & 0 & \frac{i}{\sqrt{3}} & -\frac{1}{\sqrt{2}} + \frac{i}{\sqrt{6}} \\ i\sqrt{\frac{2}{3}} & \frac{i}{\sqrt{3}} & 0 & 0 & \frac{1}{\sqrt{2}} + \frac{i}{\sqrt{6}} & -\frac{i}{\sqrt{3}} \\ \frac{i}{\sqrt{3}} & \frac{1}{\sqrt{2}} + \frac{i}{\sqrt{6}} & -\frac{i}{\sqrt{3}} & \frac{1}{\sqrt{2}} - \frac{i}{\sqrt{6}} & 0 & 0 \\ -\frac{1}{\sqrt{2}} + \frac{i}{\sqrt{6}} & -\frac{i}{\sqrt{3}} & -\frac{1}{\sqrt{2}} - \frac{i}{\sqrt{6}} & \frac{i}{\sqrt{3}} & 0 & 0 \end{pmatrix} \tag{2.32}$$

and

$$H_{so}(\theta_2, \phi_2) = \frac{\lambda}{2} \begin{pmatrix} 0 & 0 & \frac{i}{\sqrt{3}} & i\sqrt{\frac{2}{3}} & -\frac{i}{\sqrt{3}} & \frac{1}{\sqrt{2}} + \frac{i}{\sqrt{6}} \\ 0 & 0 & i\sqrt{\frac{2}{3}} & -\frac{i}{\sqrt{3}} & -\frac{1}{\sqrt{2}} + \frac{i}{\sqrt{6}} & \frac{i}{\sqrt{3}} \\ -\frac{i}{\sqrt{3}} & -i\sqrt{\frac{2}{3}} & 0 & 0 & \frac{i}{\sqrt{3}} & \frac{1}{\sqrt{2}} - \frac{i}{\sqrt{6}} \\ -i\sqrt{\frac{2}{3}} & \frac{i}{\sqrt{3}} & 0 & 0 & -\frac{1}{\sqrt{2}} - \frac{i}{\sqrt{6}} & -\frac{i}{\sqrt{3}} \\ \frac{i}{\sqrt{3}} & -\frac{1}{\sqrt{2}} - \frac{i}{\sqrt{6}} & -\frac{i}{\sqrt{3}} & -\frac{1}{\sqrt{2}} + \frac{i}{\sqrt{6}} & 0 & 0 \\ \frac{1}{\sqrt{2}} - \frac{i}{\sqrt{6}} & -\frac{i}{\sqrt{3}} & \frac{1}{\sqrt{2}} + \frac{i}{\sqrt{6}} & \frac{i}{\sqrt{3}} & 0 & 0 \end{pmatrix}. \tag{2.33}$$

The spin-orbit coupling matrices for a dimer given in Ref. [109] differ from the ones above because of a different choice of the direction of the global frame. We have chosen the global axis along $(0, 0, 1)_s$ in the global frame, which is equivalent to $(1, 1, 1)_i$ in the local frames

$i = 1, 2$. In contrast, the opposite orientation of the global axis is chosen in Ref. [109], such that the global $(0, 0, 1)_s$ axis corresponds to $(-1, -1, -1)_i$ in the local frames. The spin-orbit coupling matrices D_1 and D_2 given in Ref. [109] can be reproduced by adding π to θ_1 and θ_2.

Chapter 3

Resonant Inelastic X-ray Scattering on correlated clusters in solids

The technique we used to investigate the electronic excitations in cluster Mott insulators and Kitaev materials is Resonant Inelastic X-ray Scattering (RIXS). The popularity of RIXS has grown over the last 30 years thanks to technological, experimental, and theoretical advances, and it is now a well-established technique [134–139,231–234]. RIXS is an inelastic photon-in, photon-out spectroscopy technique in which the system under investigation is irradiated with monochromatic X-ray radiation, and the energy and momentum of the scattered X-rays are measured. We are interested in observing those scattering processes in which a part of the energy and momentum is transferred from the X-rays to the system, causing it to transition to an excited state. The amount of energy and momentum transferred to the system is determined via energy and momentum conservation by measuring the change in the energy and direction of the scattered X-rays, which are analyzed through an X-ray spectrometer.

The peculiarity of the RIXS technique lies in the choice of the incident energy, which is chosen to be in resonance with the excitation energy of a core electron into the valence shell. In other words, the incident energy is in resonance with an X-ray absorption edge. The energy of the X-ray absorption edges is characteristic of each element, making RIXS an element-selective technique. RIXS is denoted by the core-hole excitation, for example, "RIXS at the L_3 edge of Ir^{4+}" means that the incident energy is in resonance with the excitation of a $2p_{\frac{3}{2}}$ electron. In the symbol X_y, the letter $X = (K, L, M, N, \dots)$ denotes the principal quantum number $n = (1, 2, 3, 4, \dots)$ of the core shell, while the number $y = (1, 2, 3, \dots)$ specifies the subshell corresponding to $(s, p_{1/2}, p_{3/2}, \dots)$. For $5d$ transition metals like Ta and Ir, the L_3 absorption edge is in the *hard* X-ray range, respectively at about 9.88 keV and 11.215 keV [235]. The *direct valence* RIXS process can be described as a two-step process. First, there is a resonant absorption of the X-ray photon that excites a core electron into the valence shell, bringing the system into an intermediate state with a very unstable core hole. The core hole has a very short lifetime, for example, for $2p$ in $5d$ transition metals it is of the order of 1 fs. An electron from the valence shell fills the core hole and an X-ray photon is emitted. The energy of the outgoing X-ray depends on which final state is reached. An important aspect for our work is that the absorption and emission processes are coherent. This means that all the intermediate states paths are summed coherently, leading

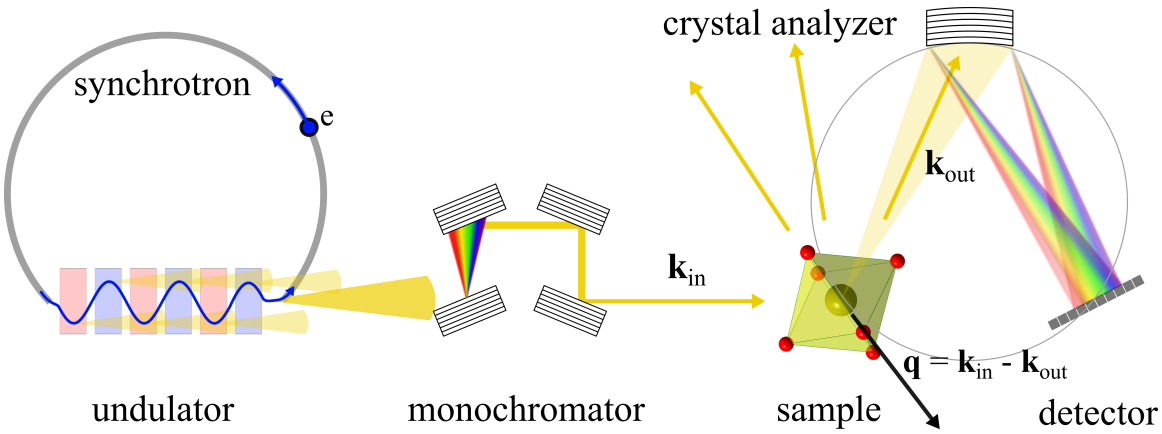

Figure 3.1: A simplified schematic of a RIXS experiment. In a RIXS experiment, X-rays are generated in a synchrotron using an undulator. The incident energy is selected by a monochromator. The X-rays are then focused onto the sample under investigation. The scattered X-rays are diffracted and dispersed by a crystal analyzer. In the Rowland circle geometry, the sample, crystal analyzer, and detector all lie on the circumference of a circle.

to interference effects in the RIXS intensity. The consequences of this coherence are central to our work and are explained later in the chapter.

A broad variety of excitations can be observed with RIXS: phonons, magnetic excitations, crystal field and orbital excitations, and charge-transfer excitations [134–136]. In this thesis we focus on magnetic and orbital excitations of the electrons. As seen in the previous chapter, the energy scale of the orbital excitations is from few meV to several eV. This scale is determined by parameters such as spin-orbit coupling, crystal field, J_H, and hopping. Instead, magnetic excitations have lower energies, up to a few hundred meV, determined by magnetic interactions. The study of these excitations with RIXS allows us to understand the electronic structure of the material and quantify the parameters of the hamiltonian. Resonance enhances the scattering cross section of these excitations and leads to specific polarization selection rules that depend on the RIXS edge. For example, the strong spin-orbit coupling of the $2p$ shell allows to probe spin-flip excitations at the L_3 edge of $5d$ transition metals [236]. However, even in resonance, the fluorescence decay competes with other decay channels [231], making the RIXS scattering cross section very small. This requires a very bright incident X-ray beam for a successful RIXS experiment. For this reason, the experiments are performed in synchrotrons, and the technique became viable with the advent of 3rd generation synchrotrons. Figure 3.1 shows a simplified schematic of a RIXS experiment. A detailed discussion of synchrotron physics and technology can be found in Refs. [237–239]. In a synchrotron, a beam of electrons travels in a circular particle accelerator with energies ranging from 0.1 to 10 GeV. Magnets are used to deviate the electron beam, causing it to emit electromagnetic radiation. Due to the high kinetic energy, the electron velocity is very close to the speed of light, resulting in a significant Doppler shift and the emission of photons with very short wavelengths in the direction parallel to the velocity [237]. In RIXS, we require a highly intense X-ray beam at a specific resonance energy. Undulators are used to achieve high brilliance peaking at certain photon energies [237]. An array of alternating magnetic dipoles creates an alternating magnetic field perpendicular to the electron path, causing the electrons to oscillate in the synchrotron

plane. The X-rays emitted along the axis of the undulator add coherently, resulting in constructive or destructive interference depending on the wavelength of the emitted X-ray. Which wavelength adds coherently depends on the undulator period and the magnetic field strength. The photons generated in this way naturally have a linear polarization parallel to the synchrotron plane. X-ray monochromators are used to select the resonance energy of the beam with momentum $\mathbf{k}_{in}$ incident on the sample. In Fig. 3.1 a four-bounce monochromator is depicted. In the hard X-ray regime monochromators are based on Bragg diffraction from a crystal. The beam is focused on the sample by a system of X-ray focusing mirrors [240] down to a spot size of $\approx 10\,\mu\text{m} \times 10\,\mu\text{m}$. This allows the measurement of small single crystals.

The radiation scattered from the sample is diffracted and dispersed by a crystal analyzer exploiting again a Bragg reflection. By positioning the crystal analyzer at a specific scattering angle 2θ, we can measure the X-rays that transferred a momentum $\mathbf{q} = \mathbf{k}_{in} - \mathbf{k}_{out}(2\theta)$ to the sample. Most RIXS spectrometers employ a Rowland circle geometry [241], where the sample, crystal analyzer, and detector lie on a circle of radius R. If the crystal analyzer is of the Johann type [242], meaning it is spherically bent with a radius of curvature of 2R, all the diffracted X-rays with the same energy are imaged on the detector at the same point. To achieve the highest resolution, diced spherical analyzers [243] are used to avoid the strain caused by bending the crystal to the required curvature. Each RIXS edge usually requires a different crystal analyzer or the exploitation of a different reflection of the same crystal analyzer, to adapt to the different resonance energies. So, the energy resolution that can be achieved changes from element to element. For example, for the Ir L_3 edge ($\approx$11.2145 keV) the energy resolution is $\approx 25\,\text{meV}$ using a Si(844) backscattering channel cut monochromator and the Si(884) spherical diced crystal analyzer on a 2 m length spectrometer. Instead, for Ta L_3 (9.8 keV) an energy resolution of $\approx 80\,\text{meV}$ can be achieved using a Si(440) four-bounce monochromator and a $R = 2\,\text{m}$ Si(066) spherical diced crystal analyzer. The number of scattered X-rays are then commonly measured with position-sensitive detectors [244,245], such as a CCD array [246].

So, performing a RIXS experiment requires advanced instrumentation, and a list of synchrotrons with beamlines where RIXS experiments can be conducted can be found in Ref. [135].

3.1 Theoretical formulation of RIXS

The interaction between X-rays and matter has been studied for a long time and is well understood. A detailed derivation and discussion can be found for example in Ref. [134, 232–234]. For our discussion, we summarize the relevant parts of Ref. [134, 234], where the full Hamiltonian describing the interaction between a system of N electrons and an electromagnetic field is derived. The essential part involves applying a low energy approximation, a non-relativistic approximation, and neglecting magnetic interactions. In these approximations the Hamiltonian can be split in an electronic and photon-field part H_0 and a perturbation part H' which describes the electromagnetic interaction between the electrons

and the photons. The interaction Hamiltonian we want to discuss is

$$H' = \sum_{i=1}^{N} \left[\frac{e}{m} \mathbf{A}(\mathbf{r}_i) \cdot \mathbf{p}_i + \frac{e^2}{2m} \mathbf{A}^2(\mathbf{r}_i) \right], \tag{3.1}$$

where $\mathbf{p}_i$ is the momentum of the electron i and the sum is over all N electrons in the system and $\mathbf{A}$ is the vector potential written in second quantization as

$$\mathbf{A}(\mathbf{r}) = \sum_{\mathbf{k},\boldsymbol{\epsilon}} \sqrt{\frac{\hbar}{2V\epsilon_0\omega_{\mathbf{k}}}} (\boldsymbol{\epsilon}\, a_{\mathbf{k}\epsilon}\, e^{i\mathbf{k}\cdot\mathbf{r}} + \boldsymbol{\epsilon}^*\, a^\dagger_{\mathbf{k}\epsilon}\, e^{-i\mathbf{k}\cdot\mathbf{r}}), \tag{3.2}$$

with $a_{\mathbf{k}\epsilon}$ and $a^\dagger_{\mathbf{k}\epsilon}$ being the annihilation and creation operators of a photon with momentum $\mathbf{k}$ and polarization $\boldsymbol{\epsilon}$, $\omega_{\mathbf{k}}$ the frequency of the photon, V the volume of the system, and ϵ_0 the vacuum permittivity. In the previously mentioned approximations H' can be treated as a perturbation to H_0. Fermi's Golden Rule to the second order describes the transition rate w for a scattering process where the system transitions from an initial state $|\mathtt{g}\rangle = |g, \mathbf{k}\boldsymbol{\epsilon}\rangle$ with energy $E_\mathtt{g}$ to a final state $|\mathtt{f}\rangle = |f, \mathbf{k}'\boldsymbol{\epsilon}'\rangle$ with energy $E_\mathtt{f}$. Here, $|g\rangle$ and $|f\rangle$ are eigenstates of the electronic part of H_0, and $\mathbf{k}$ and $\mathbf{k}'$ are the momenta of the incoming and outgoing photons. In the scattering process, a momentum $\mathbf{q} = \mathbf{k} - \mathbf{k}'$ and an energy $\hbar\omega = \hbar\omega_{\mathbf{k}} - \hbar\omega_{\mathbf{k}'}$ are transferred from the electromagnetic field to the electrons. The transition rate w is given by

$$w = \frac{2\pi}{\hbar} \sum_{\mathtt{f}} \left| \langle \mathtt{f}|H'|\mathtt{g}\rangle + \sum_n \frac{\langle \mathtt{f}|H'|n\rangle \langle n|H'|\mathtt{g}\rangle}{E_\mathtt{g} - E_n} \right|^2 \delta(E_\mathtt{f} - E_\mathtt{g}), \tag{3.3}$$

where $|n\rangle$ are eigenstates of the electronic part of H_0 with energy E_n.

The first term $\mathbf{A}\cdot\mathbf{p}$ of Eq. (3.1) is proportional to $a_{\mathbf{k}\epsilon}$ and $a^\dagger_{\mathbf{k}\epsilon}$ and at the first order in Eq. (3.3) it describes absorption and fluorescence processes. The second term $\mathbf{A}^2$ of Eq. (3.1) at the first order in Eq. (3.3) describes instead a two photon process since it is proportional to $a_{\mathbf{k}\epsilon}a^\dagger_{\mathbf{k}'\epsilon'}$ and $a^\dagger_{\mathbf{k}'\epsilon'}a_{\mathbf{k}\epsilon}$. This term describes the Thomson scattering as well as the Non-resonant Inelastic X-ray Scattering. The scattering amplitude is proportional to

$$A^{non\text{-}res} \propto \langle \mathtt{f}| \sum_i \mathbf{A}^2(\mathbf{r}_i) |\mathtt{g}\rangle \propto \boldsymbol{\epsilon}'^* \cdot \boldsymbol{\epsilon} \langle f| \sum_i e^{i\mathbf{q}\cdot\mathbf{r}_i} |g\rangle . \tag{3.4}$$

At zero energy transfer, this gives rise to the Bragg peaks intensity and to non-resonant elastic scattering. This scattering process is minimized when $\boldsymbol{\epsilon}'$ and $\boldsymbol{\epsilon}$ are perpendicular. When the incident energy is much larger than any resonance of the material the inelastic scattering is dominated by this term.

Instead, the second order processes in Eq. (3.3) are dominant when the denominator is very small. This happens when $E_g + \hbar\omega_{\mathbf{k}} - E_n + i\Gamma_n$ is very small, that is, when the incoming X-rays are in *resonance* with an excitation in the material, where we introduced the lifetime broadening of the intermediate state Γ_n. The first term $\mathbf{A}\cdot\mathbf{p}$ of Eq. (3.1) at the second order in Eq. (3.3) leads to the Kramers-Heisenberg equation

$$w^{res} \propto \left| \sum_n \sum_{i,j=1}^{N} \frac{\langle f|\, e^{-i\mathbf{k}'\cdot\mathbf{r}_i}\ \boldsymbol{\epsilon}'^* \cdot \mathbf{p}_i\, |n\rangle \langle n|\, e^{i\mathbf{k}\cdot\mathbf{r}_j}\ \boldsymbol{\epsilon} \cdot \mathbf{p}_j\, |g\rangle}{E_g + \hbar\omega_{\mathbf{k}} - E_n + i\Gamma_n} \right|^2 . \tag{3.5}$$

This equation describes a process in which a photon with polarization $\boldsymbol{\epsilon}$ and momentum $\mathbf{k}$ is absorbed by the electrons at position $\mathbf{r}_j$ with momentum $\mathbf{p}_j$ and the system transitions from the ground state $|g\rangle$ to an intermediate state $|n\rangle$. The system then relaxes from the intermediate state $|n\rangle$ to the final state $|f\rangle$ through spontaneous emission of a photon with polarization $\boldsymbol{\epsilon}'$ and momentum $\mathbf{k}'$ by deexciting the electrons at position $\mathbf{r}_i$ with momentum $\mathbf{p}_i$. The amplitude is summed coherently over all the intermediate states and the denominator determines the weight of a certain intermediate state. The amplitude is also summed coherently over all the electrons at positions $\mathbf{r}_{i,j}$ that participate in the excitation and deexcitation.

The core states are very much localized having a very small radial wavefunction and being screened by many higher energy shells which leads to a negligible interaction with the neighboring atoms. This means that we can assume that the core electron is excited into high energy states of the same ion. For the same reasons, the core hole does not propagate to the neighboring atoms in the intermediate state, which means that the core hole is created and annihilated at the same site.

We can rewrite Eq. (3.5) as

$$w^{res} \propto \left| \langle f | \, \mathcal{D}'^{\dagger} \, G \, \mathcal{D} \, | g \rangle \right|^2 , \tag{3.6}$$

where we introduced the transition operators $\mathcal{D} = \sum_{j=1}^{N} e^{i\mathbf{k}\cdot\mathbf{r}_j} \; \boldsymbol{\epsilon} \cdot \mathbf{r}_j$ and $\mathcal{D}'$ (by exploiting the commutation relations, we replaced the momentum operator with the position operator) and the propagator of the core hole in the intermediate state $G = \sum_n \frac{|n\rangle\langle n|}{E_g + \hbar\omega_{\mathbf{k}} - E_n + i\Gamma_n}$. In the dipole approximation it is assumed that $e^{i\mathbf{k}\cdot\mathbf{r}_j}$ is approximately constant over the length scale of the atomic wavefunctions, so that $e^{i\mathbf{k}\cdot\mathbf{r}_j} \approx e^{i\mathbf{k}\cdot\mathbf{R}_j}$ where $\mathbf{R}_j$ is not an operator but a vector pointing to the nucleus of the atom to which the electron j is bound. Since the $2p$ radial wavefunction of the core hole in $5d$ transition metals has a very small extent of the order of $0.1\,\text{Å}$, this is a good approximation even for photon with energies of $\approx 10\,\text{keV}$ which carry a momentum of $\approx 5\,\text{Å}^{-1}$. With this approximation we can rewrite the transition operator as

$$\mathcal{D} = \sum_j e^{i\mathbf{k}\cdot\mathbf{R}_j} D_j , \tag{3.7}$$

with $D_j = \boldsymbol{\epsilon} \cdot \mathbf{r}_j$. With the assumption introduced previously that the core hole is created and annihilated at the same site, we can rewrite the amplitude of Eq. (3.6) as:

$$\begin{aligned} A^{RIXS} &\propto \langle f | \sum_{i,j=1}^{N} e^{i(\mathbf{k}\cdot\mathbf{R}_j - \mathbf{k}'\cdot\mathbf{R}_i)} D_i'^{\dagger} \, G \, D_j \, | g \rangle \\ &= \langle f | \sum_{j=1}^{N} e^{i\mathbf{q}\cdot\mathbf{R}_j} D_j'^{\dagger} \, G \, D_j \, | g \rangle \\ &= \langle f | \sum_{j=1}^{N} e^{i\mathbf{q}\cdot\mathbf{R}_j} M_j \, | g \rangle , \end{aligned} \tag{3.8}$$

where we used the exchanged momentum $\mathbf{q} = \mathbf{k} - \mathbf{k}'$, defined the local RIXS operator $M_j = D_j'^{\dagger} \, G \, D_j$, and the sum now runs over all the atomic sites j at position $\mathbf{R}_j$ that

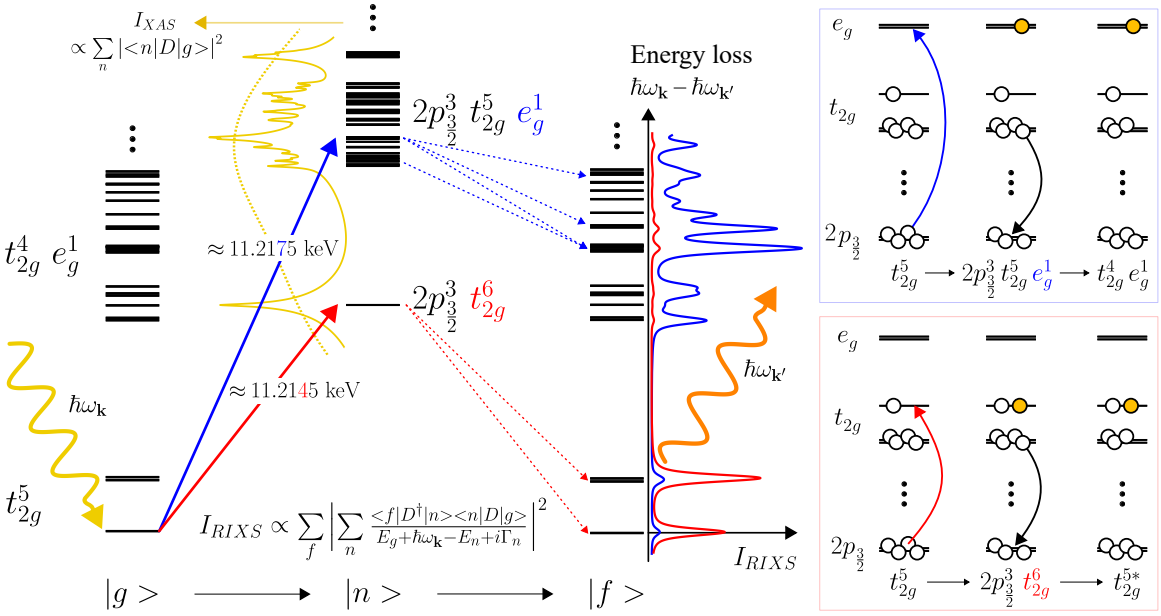

Figure 3.2: Schematic representation of the two-step RIXS process for the L_3 edge of Ir^{4+}. The energies of the many-body eigenstates are represented as horizontal lines. Depending on the resonance energy, different intermediate states can be reached. At approximately 11.2145 keV, the intermediate states with the configuration $2p_{\frac{3}{2}}^3\ t_{2g}^6$ are predominantly reached. If the resonance energy is increased by $10Dq \approx 3$ eV to approximately 11.2175 keV, the intermediate states with the configuration $2p_{\frac{3}{2}}^3\ t_{2g}^5\ e_g^1$ dominate. These two processes are illustrated on the right using a single-electron picture. Resonance with the t_{2g} states enhances the RIXS intensity of the intra-t_{2g} excitations, while resonance with the e_g states boosts the intensity of the $t_{2g}^4\ e_g^1$ excitations. The energy levels and spectra were calculated using Quanty [247].

contribute coherently to the scattering process.

Figure 3.2 shows the RIXS process for the L_3 edge of Ir^{4+}. The energy levels of the many-body eigenstates of the initial and final $2p^6\ 5d^5$ configuration and of the intermediate $2p^5\ 5d^6$ configuration are represented as horizontal lines. In the ground state $|g\rangle$ of Ir^{4+}, five electrons occupy the t_{2g} states. Spin-orbit coupling splits the t_{2g}^5 configuration into a $j = 1/2$ ground state and $j = 3/2$ excited states, as discussed in Chap. 2.1.2. The two steps of the RIXS process are represented. The first step is the resonant absorption of the incoming X-ray with energy $\hbar\omega_{\mathbf{k}}$, which excites the system from the ground state $|g\rangle$ to the intermediate states $|n\rangle$. The $2p$ orbitals are split by a strong spin-orbit coupling into a lower lying $2p_{\frac{1}{2}}$ and upper lying $2p_{\frac{3}{2}}$ multiplets, with a splitting of 1.6 keV. We are going to consider the intermediate states in which a core hole is created in the $2p_{\frac{3}{2}}$ states, leading to an intermediate state configuration $2p_{\frac{3}{2}}^3\ 5d^6$. The second step is the deexcitation from the intermediate state $|n\rangle$ to the final state $|f\rangle$, via the spontaneous emission of an X-ray photon with energy $\hbar\omega_{\mathbf{k}'}$. In an experiment, the RIXS intensity (I_{RIXS}) is measured as a function of the energy loss: $\hbar\omega_{\mathbf{k}} - \hbar\omega_{\mathbf{k}'}$. The incident energy is chosen to resonate with the excitation of an electron from the core $2p_{\frac{3}{2}}$ states into the valence shell. The weight of different intermediate states depends on the resonance energy as shown by the denominator of Eq. (3.5) and on the matrix element $\langle n|\, D\, |g\rangle$. The square of this matrix element gives the X-ray absorption spectrum. This is plotted in Fig. 3.2 as a function of the incident energy, with a narrow linewidth (solid line) to highlight the individual contributions and with a realistic linewidth (dotted line) of about 5 eV [248]. For example, at approximately

11.2145 keV, the intermediate states with the configuration $2p^3_{\frac{3}{2}}\, t^6_{2g}$ have more weight. If the resonance energy is increased by approximately $10Dq \approx 3\,\text{eV}$, the intermediate states with the configuration $2p^3_{\frac{3}{2}}\, t^5_{2g}\, e^1_g$ have more weight. These processes are depicted on the right in a single-electron picture representing the electronic configurations of ground, intermediate, and final states. All the intermediate states that can be reached contribute coherently to the scattering process but the weight determines which excitation path dominates. Different resonance energies enhance the RIXS intensity of different final states. Resonance with the t_{2g} states boosts the intensity of intra-t_{2g} excitations, while resonance with the e_g states boosts the intensity of final states with the configuration $t^4_{2g}\, e^1_g$. This is represented by the calculated RIXS spectra plot in Fig. 3.2.

3.2 Interference effects in RIXS

In Eq. (3.8) we showed that the RIXS amplitude in dipole approximation contains a summation over all the ions that contribute coherently to the scattering process. In case of excitations of isolated single ions the summation contains only one site and the RIXS amplitude can be written simply as $\langle f|\, M\, |g\rangle$. Instead, in the case of molecular orbitals the summation runs over all the ions over which the initial and final states are delocalized [194, 195, 197]. In fact, in this case, at the end of the scattering process the information on which atomic site the core hole was created in the intermediate state is lost. The excitation paths that involve the creation of the core hole on each site are summed coherently which gives rise to constructive and destructive interference effects.

To explain the RIXS measurements and the RIXS interference effects in a practical way we present here RIXS measurements on $Ba_3Ti_{3-x}Ir_xO_9$ as an example. These results have been published in Ref. [1] and introduced in [175]. This material was studied as a function of the Ir concentration $x \in \{0.3, 0.5, 1.5, 1.8\}$. The study of the RIXS interference, which means the study of the RIXS intensity as a function of the exchanged momentum $\mathbf{q}$, allowed to determine that the physics is dominated by strong site disorder, see Fig. 3.3. These results highlight the unusual kind of disorder in this material which modifies the magnetic moment, changing the character from the localized spin-orbit entangled $j = 1/2$ moments to quasimolecular singlet states on Ir_2O_9 dimers.

The crystal structure of $Ba_3Ti_{3-x}Ir_xO_9$ is shown in Fig. 3.3. It belongs to the family of the hexagonal iridate family $Ba_3AIr_2O_9$. If the structure is perfectly ordered, for $x = 2$ the Ir occupies all the 4f sites forming Ir_2O_9 face-sharing dimers and Ti the $2a$ sites, but, as we are going to see, this material shows a strong Ir-Ti site disorder. This leads to the coexistence in the crystal of single-site isolated Ir^{4+} $j = 1/2$ moments, face-sharing dimers, and corner-sharing dimers.

We performed RIXS measurements at the Ir L_3 edge at beamline ID20 at the European Synchrotron Radiation Facility (ESRF) [249, 250]. First, we studied the resonance behavior by measuring RIXS spectra as a function of the incident energy E_{in} from 11.213 to 11.222 keV on the sample with $x = 1.8$ with a low-resolution (0.4 eV). The result is shown in the resonance map in Fig. 3.4(a). The energy loss of the inelastic features is independent of the incident energy while the RIXS intensity shows a strong resonance behavior. Two main

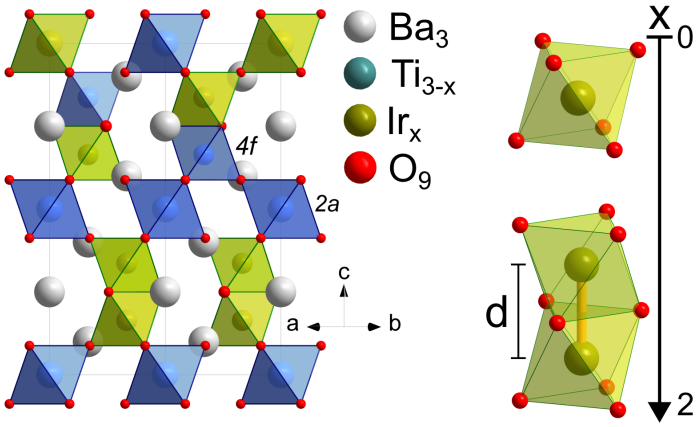

Figure 3.3: Crystal structure of $Ba_3Ti_{3-x}Ir_xO_9$ which highlights the effect of site disorder. In the fully ordered structure Ir occupies the $4f$ sites and Ti the $2a$ sites. Using RIXS interferometry we observed the presence of site disorder. As a function of increasing concentration of Ir x, the system changes from being dominated by localized single-site Ir $j = 1/2$ moments to showing the formation of dimers hosting quasimolecular orbitals. Our results reveal the coexistence of dimers formed by both face-sharing and corner-sharing geometries, in which the Ir atoms occupy the $4f$-$4f$ and $4f$-$2a$ sites, respectively.

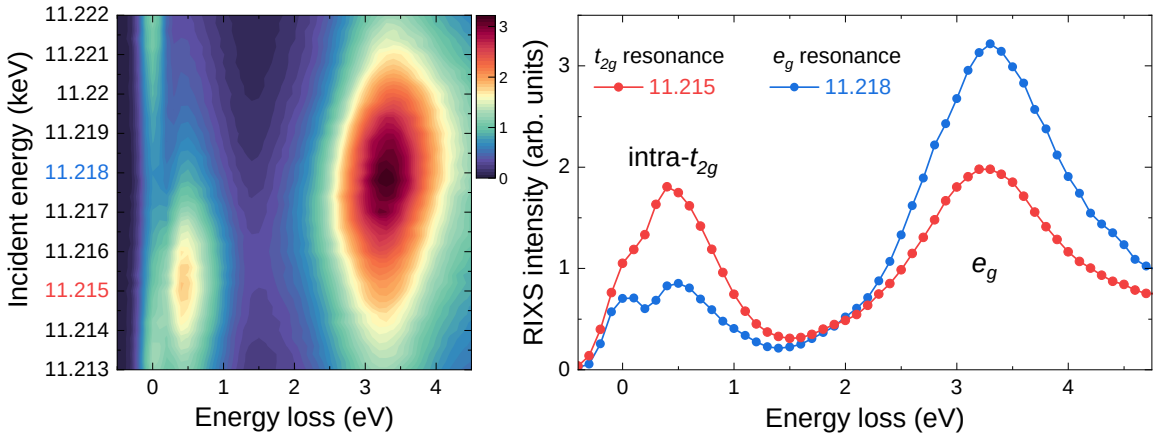

Figure 3.4: Resonance map of $Ba_3Ti_{3-x}Ir_xO_9$ for $x = 1.8$. The RIXS intensity is shown as a color map as a function of energy loss and incident energy. Two spectra are shown, acquired at the maxima of the t_{2g} (red) and e_g (blue) resonances.

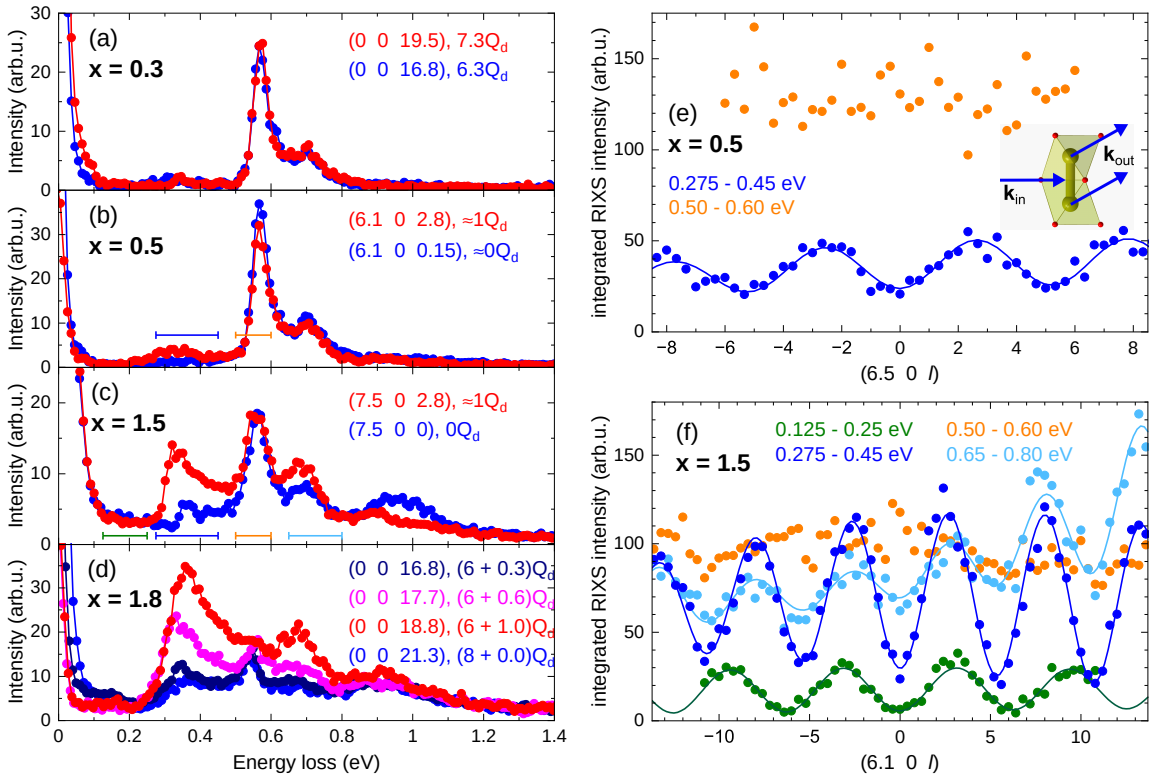

Figure 3.5: (a)-(d) RIXS spectra of $Ba_3Ti_{3-x}Ir_xO_9$ at $T = 20$K for $x = 0.3, 0.5, 1.5, 1.8$ showing single-site and dimer excitations. At small x, the spin-orbit exciton dominates, indicating single-site $j = 1/2$ moments. At large x, broad features above 0.2 eV indicate quasimolecular excitations on Ir_2 dimers, as shown by the $\sin^2(q_c d/2)$ modulation with period $2Q_d = 2\pi/d$. (e) and (f) show the integrals of the RIXS intensity. The single-site spin-orbit exciton at 0.57 eV (orange) is constant, while the 0.35 eV peak (dark blue) shows a $\sin^2(q_c d/2)$ modulation, proving the dimer character. The larger period below 0.25 eV for $x = 1.5$ (dark green) indicates a different origin related to Ir ions on $2a$ sites. Figure reproduced from Ref. [1].

inelastic features can be identified: one peaking at about 0.5 eV and one at 3.25 eV. The two features show a different dependence of the RIXS intensity on the incident energy. The 0.5 eV feature is maximized for an incident energy of about 11.215 keV, while the 3.25 eV feature at 11.218 keV, see Fig. 3.4(b). The differences in energy loss and resonance energy are both about 3 eV, which agrees with the value of $10Dq$ expected for the t_{2g}-e_g splitting. In fact, the 0.5 eV feature can be identified as intra-t_{2g} excitations while the 3.25 eV feature with t_{2g}-e_g excitations. As explained in Chap. 3.1, the intensity is maximized when we resonate with certain intermediate states. The resonance behavior allows to identify the character of certain excitations and to maximize the intensity measured during the experiment. In this experiment (as well as in the rest of the thesis) we focused on the intra-t_{2g} excitations and choose accordingly a $E_{in} = 11.215$ keV. Notice that the exact value of the resonance energy can change from material to material. We now analyze how the RIXS spectra of $Ba_3Ti_{3-x}Ir_xO_9$ change as a function of the Ir concentration $x \in \{0.3, 0.5, 1.5, 1.8\}$. In Fig. 3.5(a) and (b), we can see the spectra for $x = 0.3$ and 0.5. The spectra are dominated by the so-called spin-orbit exciton at 0.57 and 0.70 eV, which are excitations of the Ir^{4+} ion from the $j = 1/2$ ground state to the $j = 3/2$ states split by a trigonal crystal field. This reflects the presence of mainly isolated IrO_6 octahedra at low concentrations. As we move to higher concentrations, from Fig. 3.5(a) to (d), the spectra change and show many more

features. This is because the occupation of neighboring $4f$ sites becomes more likely, leading to the formation of dimers. The strong interaction inside the dimers leads to the formation of bonding and antibonding orbitals, which increases the number of possible excited states and results in a much richer spectrum. At $x = 1.8$, the spectra are dominated by dimer excitations, with the most intense in the range 0.275-0.45 eV and less intense ones in the ranges 0.125-0.25 eV, 0.65-0.80 eV, and 0.85-1.15 eV. These excitations can also be seen with lower intensity for $x = 1.5$, while only the most intense in the range 0.275-0.45 eV can be identified for $x = 0.5$. In the panels Fig. 3.5(a)-(d), spectra acquired at different exchanged momentum $\mathbf{q}$ for different values of l are plotted. The single-site excitations at 0.57 and 0.70 eV do not show any $\mathbf{q}$ dependence, reflecting their localized single-site nature. Instead, the dimer excitations show a pronounced dependence of their intensity on l. We can see this dependence in more detail by plotting the integral of the RIXS intensity as a function of l, as shown in Fig. 3.5(e)-(f) for $x = 0.5$ and $x = 1.5$, respectively. The dimer excitations show a pronounced sinusoidal modulation. The modulation of the strongest dimer excitation can be well described by

$$I_f(q_c) = (a_0 + a_1 q_c + a_2 q_c^2)\sin^2(q_c d/2) + c_0 + c_1 q_c, \tag{3.9}$$

where q_c is the projection of exchanged momentum $\mathbf{q}$ along the c axis, and d is the distance between two Ir ions occupying the $4f$ sites, and the fit parameters a_i and c_i describe the modulation amplitude and the offset. From the fit we obtain the period of the sinusoidal part $\sin^2(q_c d/2)$ equal to $2Q_d = (5.34 \pm 0.04)2\pi/c = 2\pi/d$, from which we can obtain the distance $d = (2.66 \pm 0.02)$ Å at 20 K knowing that $c = 14.1516$ Å. The presence of this modulation allows us to determine that this excitation involves quasimolecular orbitals that are delocalized over Ir ions at a distance d. This distance agrees with the value of 2.65 Å reported in Ref. [251] from X-ray diffraction for the distance inside the Ir_2O_9 dimers at the $4f$ position. In Fig. 3.5(f) we can see that the integral in the range 0.65-0.80 eV is also modulated with the same period but a lower amplitude. The lower amplitude reflects the overlap in this region of dimer and single-site excitations. Something very interesting is observed by integrating in the range 0.125-0.25 eV. The period observed is about 17% larger, pointing to a different origin of the excitations, in particular pointing to a smaller distance in real space. Further details will be discussed below. The modulation arises from the coherent scattering over the two sites of the dimer as sketched in the inset in Fig. 3.5(e). When the wavefunction is delocalized over multiple sites, at the end of the scattering process there is no information about the site on which the core hole was created in the intermediate state. In addition to summing over all the intermediate states that can be reached, we sum over all the sites over which the initial and final states are delocalized. This means that the RIXS scattering amplitude has to be summed coherently for the two excitation paths which leads to interference terms. The amplitude can be written as:

$$A_f(\mathbf{q}) \propto \langle f| \sum_{j=1,2} e^{i\mathbf{q}\mathbf{R}_j} M_j |g\rangle\,, \tag{3.10}$$

where M_j is the local dipole matrix element for the RIXS process at site $\mathbf{R}_j$ and $e^{i\mathbf{q}\mathbf{R}_j}$ the

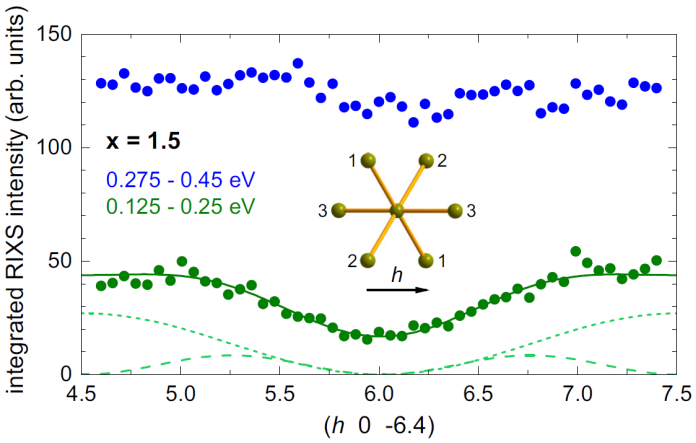

Figure 3.6: RIXS interference patterns of $Ba_3Ti_{3-x}Ir_xO_9$ for $x = 1.5$ as a function of h. The dominant dimer peak at 0.35 eV, integrated from 0.275 to 0.45 eV (blue), does not depend on h since the dimer axis is parallel to c. In contrast, the 0.15 eV (dark green) shows a modulation with two different periods along h. The solid line is the total fit, while the light green lines show the two contributions with periods 3 and 3/2 in h. Figure reproduced from Ref. [1].

phase factor. For a dimer with inversion symmetry, the matrix elements on the two sites have the same modulus but can have different sign which yields

$$A_f^{inv}(\mathbf{q}) \propto (e^{iq_c d/2} \pm e^{-iq_c d/2}) \ \langle f| M |g\rangle \,. \tag{3.11}$$

The RIXS intensity is proportional to the square of the modulus of the amplitude. So, we obtain a sinusoidal modulation of the RIXS intensity equal to either $\cos^2(q_c d/2)$ or $\sin^2(q_c d/2)$, depending on the $\pm$ sign.

The excitation observed at 0.15 eV shows a modulation period of $2Q_{2a} = (6.27 \pm 0.08)2\pi/c$, larger than for the other dimer excitations. This corresponds to a distance of $d_{2a} = 2.26 \pm 0.03$ Å, that agrees with the projection along c of the distance between the $4f$ and $2a$ sites. The vector connecting the atoms inside a $4f$-$2a$ dimer is not only parallel to the c axis but it has a component perpendicular to c. In Fig. 3.6 is plotted the integrated RIXS intensity for $x = 1.5$ as a function of h, so for a direction of Δq perpendicular to the c axis. The integrals of the dominant dimer peak at 0.35 eV and of the 0.15 eV feature are shown. We can see that while the integral of the first does not depend on h, the second shows a certain modulation that can be fit using two contributions with periods of 3 and 3/2 in h. In the inset of Fig. 3.6 is plotted the projection of the six possible Ir^{2a}-O-Ir^{4f} bonds onto the ab plane. We can see that the scalar product between the exchanged momentum and the bonds will lead to two different projections for the bonds labeled 1 and 2 and for the bonds labeled 3. This results in two different periods of the modulation that can be observed in the data. These Ir^{2a}-O-Ir^{4f} bonds are in a corner-sharing geometry which is in agreement with the large exchange energy observed.

By measuring the RIXS modulation we were able to prove the quasimolecular character and determine to which crystallographic sites the excitations belong through the analysis of the modulation period.

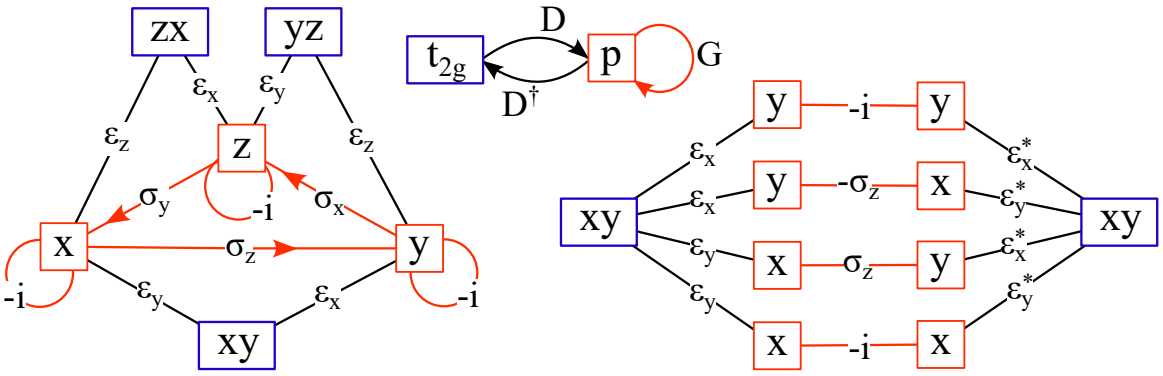

Figure 3.7: Graphical representation of the RIXS transition operator $M = D'^{\dagger}\, G\, D$ for the L_3 edge with a single hole in the t_{2g} shell. Reproduced from [252] with focus on the t_{2g} orbitals.

3.3 RIXS matrix elements for the t_{2g} shell at the L_3 edge

We calculate in the following chapter the RIXS amplitude at the L_3 edge for an excitation within the t_{2g} orbitals in a single-hole picture. We start by considering a single site and then extend the calculation to the case of a dimer where interference effects arise. A visual representation of the RIXS operator $M = D'^{\dagger}\, G\, D$ for the t_{2g} shell is shown in Fig. 3.7. The first step of the RIXS process is a dipole transition that excites the hole from the t_{2g} shell into the core $2p$ shell. We can write it as a matrix in the basis $\{x\uparrow, x\downarrow, y\uparrow, y\downarrow, z\uparrow, z\downarrow\}$ for the p orbitals and $\{yz\uparrow, yz\downarrow, zx\uparrow, zx\downarrow, xy\uparrow, xy\downarrow\}$ (sometimes denoted as $\{X\uparrow, X\downarrow, Y\uparrow, Y\downarrow, Z\uparrow, Z\downarrow\}$) for the t_{2g} orbitals as

$$D = \begin{pmatrix} 0 & 0 & \epsilon_z & 0 & \epsilon_y & 0 \\ 0 & 0 & 0 & \epsilon_z & 0 & \epsilon_y \\ \epsilon_z & 0 & 0 & 0 & \epsilon_x & 0 \\ 0 & \epsilon_z & 0 & 0 & 0 & \epsilon_x \\ \epsilon_y & 0 & \epsilon_x & 0 & 0 & 0 \\ 0 & \epsilon_y & 0 & \epsilon_x & 0 & 0 \end{pmatrix}, \tag{3.12}$$

where ϵ_i are the components of the incident polarization. In the intermediate state the core hole propagates due to the strong spin-orbit coupling. The propagation matrix for the L_3 edge can be written as [253]

$$G = -i(\mathrm{Id} + \mathbf{L}\cdot\mathbf{S}) = \begin{pmatrix} -i\,\mathrm{Id} & -\sigma_z & \sigma_y \\ \sigma_z & -i\,\mathrm{Id} & -\sigma_x \\ -\sigma_y & \sigma_x & -i\,\mathrm{Id} \end{pmatrix}, \tag{3.13}$$

where Id is the identity matrix and $\mathbf{L}\cdot\mathbf{S}$ is the spin-orbit coupling operator acting on the p shell. We employ the z axis as the spin quantization axis. When the spin quantization axis is different from the z axis, $\mathbf{L}\cdot\mathbf{S}$ can be calculated using the procedure explained in Chap. 2.1.2. In Fig. 3.7, a propagation opposite to the arrow direction introduces a minus sign. After the propagation, we reach the final state through the emission of a photon, which can be described by $D'^{\dagger}$, coinciding with Eq. (3.12) but with the outgoing polarization $\epsilon_i'^{\dagger}$. In our experiments, the polarization of the outgoing beam could not be resolved, so we decompose the outgoing polarization into horizontal (parallel to the scattering plane) and

vertical (perpendicular to the scattering plane) outgoing linear polarization ϵ_i'. Being linear, the polarization is real, and we drop the †. So, we can write a matrix that describes the single-hole, single-site RIXS transition operator as $M = D' \cdot G \cdot D$:

$$M = \begin{pmatrix} -2i\,(yy' + zz') & zy' - yz' & zz' - 2ixy' \\ zy' - yz' & -2i\,(yy' + zz') & -xz' - izy' \\ -zz' - 2iyx' & zx' - iyz' & -2i\,(xx' + zz') \\ zx' + iyz' & zz' - 2iyx' & i\,(xz' - zx') \\ -zy' - 2izx' & -y\,(x' + iy') & z\,(x' - 2iy') \\ -y\,(x' - iy') & z\,(y' - 2ix') & -x\,(x' - iy') \end{pmatrix} \begin{pmatrix} -xz' + izy' & (y - 2ix)z' & (x + iy)y' \\ -zz' - 2ixy' & (x - iy)y' & (-y - 2ix)z' \\ i\,(zx' - xz') & -((x + 2iy)z') & (x + iy)x' \\ -2i\,(xx' + zz') & (x - iy)x' & (x - 2iy)z' \\ -x\,(x' + iy') & (y - 2ix)x' - (x + 2iy)y' & 0 \\ -z\,(x' + 2iy') & 0 & (-y - 2ix)x' + (x - 2iy)y' \end{pmatrix} \tag{3.14}$$

where I simplified ϵ_i as x, y, z for the incident polarization and ϵ_i' as x', y', z' for the outgoing polarization. Note that, in the matrix connecting the xy orbitals, the off-diagonal terms are zero. This is because, as shown in Fig. 3.7, the xy orbitals are connected only via $-i$ and σ_z when the spin quantization axis is along the z axis. As a result, spin-flip transitions of the xy orbitals are forbidden. In contrast, spin-flip transitions are allowed for the other orbitals (yz and zx). Changing the spin-orbit quantization axis changes the matrix elements. For example, when the quantization axis is along x (y), the spin-flip transitions that are forbidden are those of the yz (zx) orbitals.

Consider two eigenstates Ψ_i and Ψ_f as vectors defined in the $\{yz\uparrow, yz\downarrow, zx\uparrow, zx\downarrow, xy\uparrow, xy\downarrow\}$ t_{2g} basis. We can calculate the RIXS scattering amplitude for the excitation from Ψ_i to Ψ_f as $\Psi_f^* \cdot M \cdot \Psi_i$. Alternatively, we can calculate it as the sum of all the elements of the matrix obtained as $M \odot (\Psi_f^* \otimes \Psi_i)$. As an example, we calculate the transitions between the $j = 1/2$ states of Eq. (2.18) [234,254]. We have the wavefunctions

$$\begin{aligned} |\tfrac{1}{2}, +\tfrac{1}{2}\rangle &= -\frac{1}{\sqrt{3}}\,|yz\downarrow\rangle - \frac{i}{\sqrt{3}}\,|zx\downarrow\rangle - \frac{1}{\sqrt{3}}\,|xy\uparrow\rangle \\ |\tfrac{1}{2}, -\tfrac{1}{2}\rangle &= -\frac{1}{\sqrt{3}}\,|yz\uparrow\rangle + \frac{i}{\sqrt{3}}\,|zx\uparrow\rangle + \frac{1}{\sqrt{3}}\,|xy\downarrow\rangle \end{aligned} \tag{3.15}$$

and we want to calculate the 4 transition amplitudes for the spin-conserving $\langle \frac{1}{2}, \pm\frac{1}{2}|\, M\, |\frac{1}{2}, \pm\frac{1}{2}\rangle$ and the spin-flip $\langle \frac{1}{2}, \mp\frac{1}{2}|\, M\, |\frac{1}{2}, \pm\frac{1}{2}\rangle$ excitations. Consider the excitation $\langle \frac{1}{2}, +\frac{1}{2}|\, M\, |\frac{1}{2}, +\frac{1}{2}\rangle$.

Calculating $\langle \frac{1}{2}, +\frac{1}{2}| \otimes |\frac{1}{2}, +\frac{1}{2}\rangle$ allows us too see which transition paths are possible,

$$\frac{1}{3}\begin{pmatrix} 0 & 0 & 0 & 0 & 0 & 0 \\ 0 & 1 & 0 & i & 1 & 0 \\ 0 & 0 & 0 & 0 & 0 & 0 \\ 0 & -i & 0 & 1 & -i & 0 \\ 0 & 1 & 0 & i & 1 & 0 \\ 0 & 0 & 0 & 0 & 0 & 0 \end{pmatrix}. \tag{3.16}$$

There are 9 possible transition paths

$$\begin{aligned} &\langle yz\downarrow| M |yz\downarrow\rangle\,,\ \langle zx\downarrow| M |yz\downarrow\rangle\,,\ \langle xy\uparrow| M |yz\downarrow\rangle\,, \\ &\langle yz\downarrow| M |zx\downarrow\rangle\,,\ \langle zx\downarrow| M |zx\downarrow\rangle\,,\ \langle xy\uparrow| M |zx\downarrow\rangle\,, \\ &\langle yz\downarrow| M |xy\uparrow\rangle\,,\ \langle zx\downarrow| M |xy\uparrow\rangle\,,\ \langle xy\uparrow| M |xy\uparrow\rangle\,, \end{aligned} \tag{3.17}$$

that are summed coherently in amplitude. Each path can be walked in multiple ways, for example, the excitation path $\langle xy\uparrow| M |xy\uparrow\rangle$, shown in Fig. 3.7, can go through the creation of the intermediate state core hole in a x or y orbital of the p shell. The final state can then be reached from the same orbitals (gaining a phase $-i$) or the core hole can propagate from x to y due to spin-orbit coupling (trough σ_z). Instead, for the excitation $\langle \frac{1}{2}, -\frac{1}{2}| M |\frac{1}{2}, +\frac{1}{2}\rangle$ we have the excitation paths

$$\begin{aligned} &\langle yz\uparrow| M |yz\downarrow\rangle\,,\ \langle zx\uparrow| M |yz\downarrow\rangle\,,\ \langle xy\downarrow| M |yz\downarrow\rangle\,, \\ &\langle yz\uparrow| M |zx\downarrow\rangle\,,\ \langle zx\downarrow| M |zx\downarrow\rangle\,,\ \langle xy\downarrow| M |zx\downarrow\rangle\,, \\ &\langle yz\uparrow| M |xy\uparrow\rangle\,,\ \langle zx\uparrow| M |xy\uparrow\rangle\,,\ \cancel{\langle xy\downarrow| M |xy\uparrow\rangle}. \end{aligned} \tag{3.18}$$

We notice again that, for spin-quantization along the z axis, the matrix element $\langle xy\downarrow| M |xy\uparrow\rangle$ is zero. By summing the matrix elements in amplitude and with the correct factors we obtain the expressions

$$\begin{aligned} \langle \frac{1}{2}, +\frac{1}{2}| M |\frac{1}{2}, +\frac{1}{2}\rangle &= A^z_{\uparrow\uparrow} = -i(x'x + y'y + z'z) - (x'y - y'x)/2 \\ \langle \frac{1}{2}, -\frac{1}{2}| M |\frac{1}{2}, -\frac{1}{2}\rangle &= A^z_{\downarrow\downarrow} = -i(x'x + y'y + z'z) + (x'y - y'x)/2 \\ \langle \frac{1}{2}, -\frac{1}{2}| M |\frac{1}{2}, +\frac{1}{2}\rangle &= A^z_{\uparrow\downarrow} = (-(y'z - z'y) - i(z'x - x'z))/2 \\ \langle \frac{1}{2}, +\frac{1}{2}| M |\frac{1}{2}, -\frac{1}{2}\rangle &= A^z_{\downarrow\uparrow} = (-(y'z - z'y) + i(z'x - x'z))/2, \end{aligned} \tag{3.19}$$

where we introduced the RIXS scattering amplitudes $A^z_{\sigma\sigma'}$ within the $j = 1/2$ sector for spin quantization along z.

RIXS interference in a dimer

We show now how to calculate the RIXS intensity in the case of more than one site considering the simple case of a dimer formed by 2 ions at positions $R_1 = (0, 0, 0)$ and $R_2 = (0, 0, d)$. To simplify the calculations, but also to prepare for the calculations performed in Chap. 4.2, we restrict to the $j = 1/2$ wavefunctions. To calculate the RIXS intensity we have to

calculate $\langle\Psi_f|\sum_{j=1,2} e^{i\mathbf{q}\cdot\mathbf{R}_j} M_j\,|\Psi_i\rangle$. We consider the wavefunctions

$$\begin{aligned}
|\Psi_0\rangle &= \left|(\tfrac{1}{2},+\tfrac{1}{2})_1,(\tfrac{1}{2},+\tfrac{1}{2})_2\right\rangle = |\uparrow\uparrow\rangle \\
|\Psi_1\rangle &= \left|(\tfrac{1}{2},-\tfrac{1}{2})_1,(\tfrac{1}{2},-\tfrac{1}{2})_2\right\rangle = |\downarrow\downarrow\rangle \\
|\Psi_2\rangle &= \left(\left|(\tfrac{1}{2},-\tfrac{1}{2})_1,(\tfrac{1}{2},+\tfrac{1}{2})_2\right\rangle - \left|(\tfrac{1}{2},+\tfrac{1}{2})_1,(\tfrac{1}{2},-\tfrac{1}{2})_2\right\rangle\right)/\sqrt{2} = (|\downarrow\uparrow\rangle - |\uparrow\downarrow\rangle)/\sqrt{2} \\
|\Psi_3\rangle &= \left(\left|(\tfrac{1}{2},-\tfrac{1}{2})_1,(\tfrac{1}{2},+\tfrac{1}{2})_2\right\rangle + \left|(\tfrac{1}{2},+\tfrac{1}{2})_1,(\tfrac{1}{2},-\tfrac{1}{2})_2\right\rangle\right)/\sqrt{2} = (|\downarrow\uparrow\rangle + |\uparrow\downarrow\rangle)/\sqrt{2},
\end{aligned} \tag{3.20}$$

where we denoted for simplicity the wavefunction $|j,\pm j_z\rangle_i$ of site i with the (pseudo)spin direction. We calculate as an exercise the excitations from Ψ_0 to Ψ_i with $i = 0,1,2,3$. The elastic excitation from Ψ_0 to Ψ_0 can be reached in 2 different ways: a spin-conserving transition either on site 1 or on site 2. The RIXS intensity can be calculated as:

$$\begin{aligned}
I_{00} &= |\,\langle\uparrow\uparrow|\sum_{j=1,2} e^{i\mathbf{q}\cdot\mathbf{R}_j} M_j\,|\uparrow\uparrow\rangle\,|^2 \\
&= |A^z_{\uparrow\uparrow}\,e^{i\mathbf{q}\cdot\mathbf{R}_1} + A^z_{\uparrow\uparrow}\,e^{i\mathbf{q}\cdot\mathbf{R}_2}|^2 \\
&= |A^z_{\uparrow\uparrow}\,(1+e^{i\mathbf{q}\cdot\Delta\mathbf{R}})|^2 \\
&= |A^z_{\uparrow\uparrow}|^2\,|e^{i\mathbf{q}\cdot\Delta\mathbf{R}/2}(e^{-i\mathbf{q}\cdot\Delta\mathbf{R}/2} + e^{i\mathbf{q}\cdot\Delta\mathbf{R}/2})|^2 \\
&= |A^z_{\uparrow\uparrow}|^2\,4\cos^2(q_z d/2),
\end{aligned} \tag{3.21}$$

where we defined $\Delta\mathbf{R} = \mathbf{R}_2 - \mathbf{R}_1$. With the single-site RIXS amplitude being the same, it can be collected and the complex exponentials interfere giving rise to a $\cos^2(q_z d/2)$ sinusoidal modulation with a period as function of q_z related to the distance d inside the dimer.

The excitation from $|\uparrow\uparrow\rangle$ to $|\downarrow\downarrow\rangle$ cannot be reached. As discussed in Chap. 3.1, because the core holes are very deep, the RIXS operator is local, meaning it involves the excitation and deexcitation of the electrons at the same site. So, we cannot excite two sites simultaneously.

The other two excitations we compute here are $(\langle\uparrow\downarrow| \pm \langle\downarrow\uparrow|)\sum_{j=1,2} e^{i\mathbf{q}\cdot\mathbf{R}_j} M_j\,|\uparrow\uparrow\rangle$. This excitation can be reached in 2 ways: by flipping the spin on the first site with amplitude $A^z_{\uparrow\downarrow}$ and phase $\pm e^0 = \pm 1$ depending on the sign of the final state, or equivalently flipping the spin on the second site with the same amplitude but with exponent $e^{i\mathbf{q}\cdot\mathbf{R}_2}$. The RIXS intensity can be calculated as:

$$\begin{aligned}
I_{02/3} &= |(\langle\uparrow\downarrow| \pm \langle\downarrow\uparrow|)\sum_{j=1,2} e^{i\mathbf{q}\cdot\mathbf{R}_j} M_j\,|\uparrow\uparrow\rangle\,|^2 \\
&= |\pm A^z_{\uparrow\downarrow}\,e^{i\mathbf{q}\cdot\mathbf{R}_1} + A^z_{\uparrow\downarrow}\,e^{i\mathbf{q}\cdot\mathbf{R}_2}|^2 \\
&= |A^z_{\uparrow\downarrow}\,(\pm 1 + e^{i\mathbf{q}\cdot\Delta\mathbf{R}})|^2 \\
&= |A^z_{\uparrow\downarrow}|^2\,(2 \pm 2\cos(q_z d)) \\
&= |A^z_{\uparrow\downarrow}|^2\,4\cos^2(q_z d/2 + (1\mp 1)\pi/4),
\end{aligned} \tag{3.22}$$

which shows that, depending on the phase of the wavefunction, whether $+$ or $-$, gives rise to a $\cos^2(q_z d/2)$ or a $\sin^2(q_z d/2)$ modulation. So, the modulation contains the information

about the relative phase of the ground state and final state wavefunctions. However, this information is mixed with the polarization dependence given by the matrix elements.

Chapter 4

Bond-directional excitations in Kitaev materials

4.1 RIXS observation of bond-directional nearest-neighbor excitations in the Kitaev material Na_2IrO_3

At the basis of the Kitaev model is the bond-directional nearest-neighbor character of the exchange interactions. In Ref. [188], Revelli *et al.* observed in the Kitaev materials Na_2IrO_3 and α-Li_2IrO_3 a nearest-neighbor modulation of the RIXS intensity similar to the one observed in dimer systems [197] [1,6]. Experimentally, it is very challenging to collect evidence for the bond-directional character of the exchange interactions, as discussed in Chap. 1. In the following chapter, we address this issue via the magnetic excitations. A bond-directional character of exchange interactions implies a corresponding bond-directional nature of the magnetic excitations, and we show how RIXS can be used to identify the corresponding signatures. In particular, the task is to show that, e.g., a spin-conserving excitation involving the spin operator S^z creates an excitation only on the z bond. We therefore have to find a way to simultaneously determine the bond direction and the spin operator involved. We have solved this by making efficient use of the nearest-neighbor or two-site character of the spin correlations and the RIXS polarization dependence. Altogether, this provides the first observation of bond-directional excitations, validating the Kitaev character of exchange interactions in the Kitaev materials Na_2IrO_3 and α-Li_2IrO_3. The results on Na_2IrO_3 are published in Pub. [2], which we reproduce in the following. In Chap. 4.2, we add an extended discussion on the model used to describe the data. At the end, in Chap. 4.3, we show that in α-Li_2IrO_3 we observe a similar bond-directional behavior of the magnetic excitations as in Na_2IrO_3.

Contribution

M. Magnaterra and M. Grüninger conceived the experiment. M. Magnaterra, M. Moretti Sala, A. Revelli, M. H. Upton, Jungho Kim, P. H. M. van Loosdrecht, and M. Grüninger carried out a proof-of-principles RIXS study at beamline 27-ID at APS. M. Magnaterra, K. Hopfer, Ch. J. Sahle, M. Moretti Sala, G. Monaco, and M. Grüninger performed the RIXS experiments at beamline ID20 of the ESRF. M. Magnaterra analyzed the data. I.-M. Pietsch, F. Breitner, and P. Gegenwart provided and synthesized the single crystals used for the measurements. M. Magnaterra and M. Grüninger performed the theoretical calculations with support from J. Attig, C. Hickey, S. Trebst, and J. van den Brink. M. Magnaterra, M. Grüninger, S. Trebst, and J. van den Brink wrote the manuscript with input from all authors.

RIXS observation of bond-directional nearest-neighbor excitations in the Kitaev material Na_2IrO_3

M. Magnaterra,[1] K. Hopfer,[1] Ch. J. Sahle,[2] M. Moretti Sala,[3] G. Monaco,[4] J. Attig,[5] C. Hickey,[5] I.-M. Pietsch,[6] F. Breitner,[6] P. Gegenwart,[6] M. H. Upton,[7] Jungho Kim,[7] S. Trebst,[5] P. H. M. van Loosdrecht,[1] J. van den Brink,[8,9] and M. Grüninger[1]

[1]*Institute of Physics II, University of Cologne, 50937 Cologne, Germany*
[2]*ESRF, The European Synchrotron, 71 Avenue des Martyrs, CS40220, 38043 Grenoble Cedex 9, France*
[3]*Dipartimento di Fisica, Politecnico di Milano, I-20133 Milano, Italy*
[4]*Dipartimento di Fisica e Astronomia "Galileo Galilei", Università di Padova, Padova, Italy*
[5]*Institute for Theoretical Physics, University of Cologne, 50937 Cologne, Germany*
[6]*Experimental Physics VI, Center for Electronic Correlations and Magnetism, University of Augsburg, 86159 Augsburg, Germany*
[7]*Advanced Photon Source, Argonne National Laboratory, Argonne, Illinois 60439, USA*
[8]*Institute for Theoretical Solid State Physics, IFW Dresden, 01069 Dresden, Germany*
[9]*Institute for Theoretical Physics and Würzburg-Dresden Cluster of Excellence ct.qmat, Technische Universität Dresden, 01069 Dresden, Germany*

(Dated: January 19, 2023)

Spin-orbit coupling locks spin direction and spatial orientation and generates, in semi-classical magnets, a local spin easy-axis and associated ordering. Quantum spin-1/2's defy this fate: rather than spins becoming locally anisotropic, the spin-spin interactions do. Consequently interactions become dependent on the spatial orientation of bonds between spins, prime theoretical examples of which are Kitaev magnets. Bond-directional interactions imply the existence of bond-directional magnetic modes, predicted spin excitations that render crystallographically equivalent bonds magnetically inequivalent, which yet have remained elusive experimentally. Here we show that resonant inelastic x-ray scattering allows us to explicitly probe the bond-directional character of magnetic excitations. To do so, we use a scattering plane spanned by one bond and the corresponding spin component and scan a range of momentum transfer that encompasses multiple Brillouin zones. Applying this approach to Na_2IrO_3 we establish the different bond-directional characters of magnetic excitations at ~ 10 meV and ~ 45 meV. Combined with the observation of spin-spin correlations that are confined to a single bond, this experimentally validates the Kitaev character of exchange interactions long proposed for this material.

The physics of quantum magnets with bond-directional interactions can be captured by so-called compass models [1], quantum theories of matter in which the couplings between different spin components are inherently spatially (typically, direction) dependent. Theoretically, this class of models harbors a range of interesting emergent physical phenomena, including the frustration of (semi-)classical ordered states on unfrustrated lattices, and a boost of quantum effects, prompting, in certain cases, the appearance of quantum spin liquids [2–4] – Kitaev spin liquids are well-known examples [5, 6]. In spin-1/2 materials, spin-orbit coupling naturally induces bond-directional spin-spin interactions. These can dominate when spin-orbit coupling becomes large, e.g., in $4d$ and $5d$ transition metal compounds [7–9]. However it has remained a principal challenge to experimentally identify the fingerprints of bond-directional magnetic interactions [10] and to establish methods to systematically explore their consequences for elementary magnetic properties.

Here we show that bond-directional *excitations* (BDE) – spin excitations that render crystallographically equivalent directions magnetically inequivalent – are a hallmark of bond-directional magnetic *interactions* and demonstrate how to use resonant inelastic x-ray scattering (RIXS) to directly probe these BDE. The challenge to resolving the bond-directional character of magnetic modes is that it requires simultaneous knowledge of both the spin operator creating the excitation and the direction of the bond involved. We introduce a RIXS geometry that yields the former via the polarization dependence and the latter by measuring across *multiple* Brillouin zones. Using this method on Na_2IrO_3, a Kitaev material exhibiting a proximate spin liquid regime [11–13], we establish the different bond-directional characters of spin-conserving and spin-flip excitations at ~ 10 meV and ~ 45 meV, respectively.

Resolving BDE with RIXS on Na_2IrO_3 is based on polarization selection rules but a polarization analysis of the scattered x-rays is not available at the commonly used Ir L edge. We have solved this problem by exploiting a *tilted* sample geometry which highlights polarization effects over the large range of $\mathbf{q}$ space that can be covered with hard x-rays, see Fig. 1. Tilting the sample puts the spin-orbit entangled j^z component of the local pseudo-spin $j = 1/2$ moments into the scattering plane. This allows us to disentangle excitations of j^z from those of j^x or j^y. The anisotropy in j space translates into a characteristic $\mathbf{q}$ dependence of the intensity that provides a direct signature of bond-directional behavior.

Bond-directional character: To illustrate the conceptual relation between bond-directional interactions and BDE we consider a central spin on site i surrounded by sites j, connected by bonds $\gamma_{\langle ij\rangle}$ along crystallographically equivalent directions. When exchange interactions are bond-directional, the magnetic Hamiltonian H_γ for two spins on bond γ has the property that in general $H_\gamma \neq H_{\gamma'}$ even if bonds γ and γ' are equivalent from a structural point of view. When one now creates a magnetic excitation by perturbing the central spin by operator $\hat{O}_i$, the commutator $\left[H_{\gamma\langle ij\rangle}, O_i\right]$ in general depends on γ. As a consequence this magnetic excitation distributes *unevenly* over the crystallographically equivalent bonds, breaking lattice symmetry.

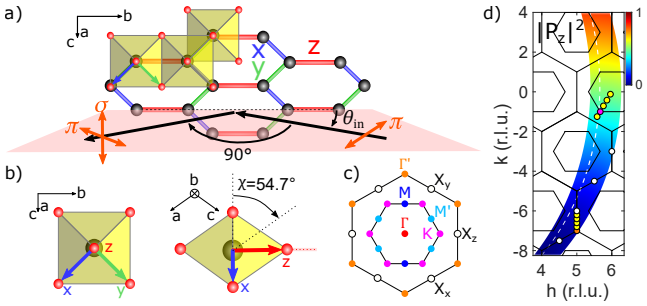

FIG. 1. **(a) Sketch of scattering geometry with tilted sample.** We use incident π polarization while the RIXS intensity is summed over outgoing π and σ polarizations. (b) Front and side views of a single IrO_6 octahedron. For a tilt angle χ=54.7°, j^z lies in the scattering plane. (c) 2D high-symmetry points in the first and second Brillouin zones around Γ. A Γ point occurs for $h+k$ even and $k=3m$ with integer m and h, see (d). BDE are most evident around X_γ. (d) Polarization factor $|P^z(\mathbf{q})|^2$ across the covered $\mathbf{q}$ range. The dashed line corresponds to scanning $\theta_{\rm in}$ from 5° to 65° for $\chi=54.7°$ and scattering angle $2\theta=90°$. Experimentally, we vary χ between 52° and 64°. Symbols mark the $\mathbf{q}$ points addressed in Fig. 2. For the high-symmetry points, symbol colors refer to the sketch in c).

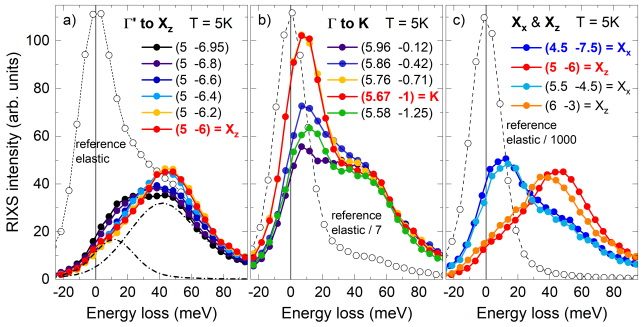

FIG. 2. **RIXS spectra at 5 K at selected q points.** (a) Γ' to X_z, (b) Γ to K, (c) X_x and X_z, cf. Fig. 1. The spectra show two peaks at about 10 meV and 45 meV which we attribute to predominantly local nearest-neighbor excitations. Dash-dotted lines in (a) distinguish the two peaks at (5 -6.95). Reference spectra recorded with $2\theta\neq90°$ and a corresponding large elastic line mark zero energy loss (open symbols, scaled down as indicated). In (c), the different intensities of the two peaks at X_x and X_z provide direct evidence of BDE.

An elementary example in which BDE emerge is the honeycomb Kitaev model with $H_\gamma = K\,S_i^\gamma S_j^\gamma$ where $\gamma=x,y,z$ simultaneously denotes the three nearest-neighbor bonds *and* the three spin components, signifying the bond-directional character of the interaction. A local operator S_i^x commutes with H_x but not with H_y and H_z on the other two bonds, so that perturbing the system by S_i^x renders the three crystallographic bonds inequivalent and produces BDE. In particular S_i^x creates localized flux excitations on the two hexagons that share the x bond, while the third hexagon connected to site i remains unaffected, manifestly breaking the three-fold rotational symmetry of the flux distribution and consequently the Majorana modes scattered by the fluxes.

Single crystals of Na_2IrO_3 were grown following the procedure described in [14] with 10 % extra Ir at 1323 K for 14 days. To establish the presence of BDE we measured RIXS at the Ir L_3 edge at beamline ID20 at the ESRF [15, 16]. The incident energy $E_{\rm in}=11.2145$ keV resonantly enhances magnetic excitations of the $j=1/2$ moments. The sample surface is parallel to the honeycomb plane, i.e., the ab plane. The b axis contains the z bond and lies in the horizontal scattering plane such that the incident beam is parallel to b for a vanishing angle of incidence $\theta_{\rm in}$, see Fig. 1. With a tilt of the sample of $\chi=54.7°$ around b, where χ is the angle between the vertical and the honeycomb ab plane, j^z is lying in the scattering plane. The elastic contribution due to Thomson scattering is almost fully suppressed by strictly using a scattering angle $2\theta=90°$, where all outgoing polarization contributions are perpendicular to the incident π polarization. The resolution $\delta\mathbf{q}$ of the transferred momentum equals about $(\pm0.05\ \pm0.1\ \pm0.05)$ reciprocal lattice units (r.l.u.) using a 60 mm iris on the $R=2$ m Si(844) spherical diced analyzer. The energy resolution is $\delta E=25$ meV. All RIXS data were corrected for self-absorption [17].

RIXS spectra measured at 5 K at selected $\mathbf{q}$ points show two inelastic features peaking around 10 meV and 45 meV, see Fig. 2. Their magnetic character is demonstrated by the resonance behavior measured at 30 K, i.e., above the 3D ordering temperature $T_N=15$ K, see *Supplementary Information* [18]. Our focus is on the bond-directional character of excitations expected for a Kitaev material, not on low-energy magnons of the ordered state. In previous RIXS studies, the broad continuum peaking around 45 meV has been established as a generic, quasi-2D magnetic excitation of the $j=1/2$ honeycomb iridates which persists up to 300 K [13, 19–21]. A similar continuum has been observed in the $j=1/2$ honeycomb compound α-$RuCl_3$ [22, 23]. The 10 meV peak is particularly pronounced at the K point, which agrees with first RIXS results collected with improved energy resolution $\delta E=12$ meV [19]. Observation of the 10 meV feature with $\delta E=25$ meV requires excellent suppression of elastic Thomson scattering which we achieve by using $2\theta=90°$. For comparison, reference spectra (open symbols) measured with $2\theta\neq90°$ are peaking at zero energy loss.

In general, RIXS spectra as a function of energy loss are appropriate to study dispersive modes. However, for both inelastic features the peak energies hardly depend on $\mathbf{q}$, see Fig. 2. The key to a microscopic understanding of the two predominantly local excitations is the $\mathbf{q}$-dependent intensity $I(\mathbf{q},\omega)$. This is most evident from the astounding behavior at X_x and X_z, see Fig. 2c). These $\mathbf{q}$ points are fully equivalent for the honeycomb lattice but probe different bond directions in the case of nearest-neighbor excitations, as argued below. We will show that a small value of the polarization factor $|P^z(\mathbf{q})|^2$ depicted in Fig. 1d) suppresses j^z-conserving excitations and enhances j^z-flip modes. This suppresses the spin-conserving 10 meV feature and enhances the 45 meV spin-flip mode at X_z but not at X_x, i.e., on z bonds but not on x bonds. Hence $I(\mathbf{q},\omega)$ demonstrates that the magnetic honeycomb lattice of Na_2IrO_3 hosts BDE that have spin-flip or spin-conserving character.

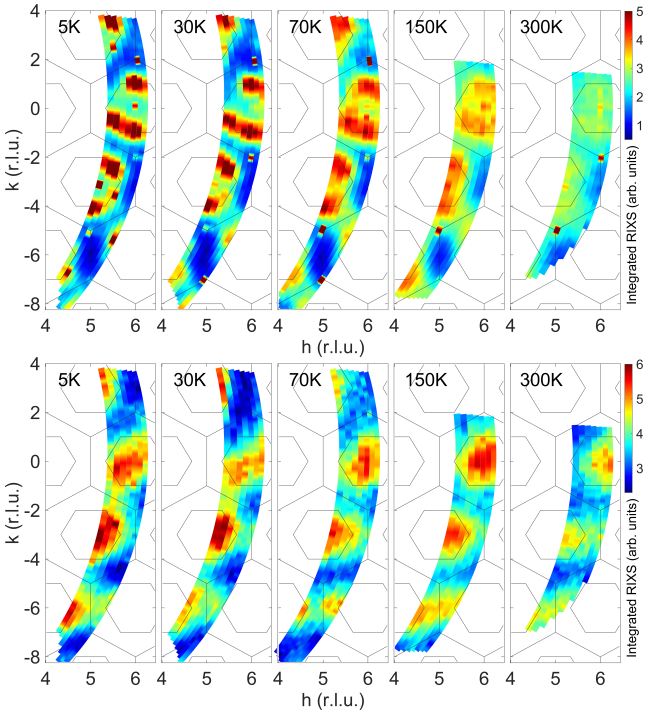

FIG. 3. **RIXS intensity maps at different temperatures,** integrated from -15 to 15 meV (top) and from 45 to 125 meV (bottom), focusing on the behavior of the two peaks shown in the spectra, cf. Fig. 2. At low energy, the narrow spots for integer h and k such as at (6 2) correspond to tails of structural Bragg peaks.

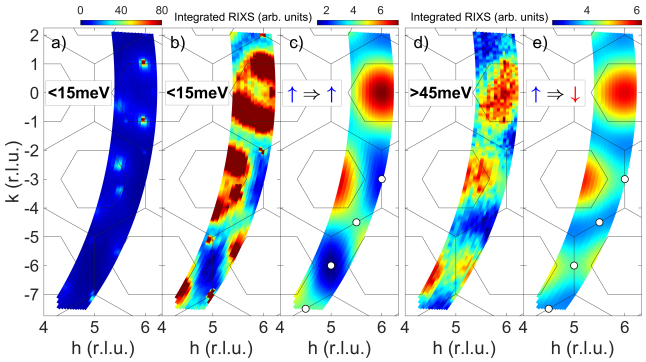

FIG. 4. **Maps of the RIXS intensity** at 5 K integrated from -15 to 15 meV ((a), (b)) and from 45 to 125 meV (d). Compared to Fig. 3, the data were measured on a finer mesh in $\mathbf{q}$ space. Panels (a) and (b) show the same data on different color scales. The bond-directional character is apparent from polarization-related differences of the RIXS intensity at, e.g., the X_γ points (white circles). (c), (e): Predictions of a simple bond model for BDE with spin-conserving and spin-flip character, respectively, see Eqs. (1) and (2). Excitations are restricted to either an x, y, or z bond with corresponding correlations of j^x, j^y, or j^z, respectively. The calculated modulation pattern reflects nearest-neighbor correlations, cf. Fig. 5.

RIXS intensity maps: Figure 3 depicts 2D $\mathbf{q}$-space maps of $I(\mathbf{q})$ integrated below 15 meV and above 45 meV, respectively. The integration ranges have been chosen to disentangle the different behavior of the two peaks observed in the spectra. For the continuum peaking around 45 meV, the quasi-2D character is supported by the gradual evolution with temperature T, see bottom panels in Fig. 3. This insensitivity to T and in particular to T_N agrees with previous RIXS results [13] for selected values of $\mathbf{q}$. The overall behavior with a broad peak centered at Γ can be described by nearest-neighbor correlations (see below).

To study the 10 meV peak, we have to cope with the fact that the dominant contribution to the low-energy intensity below T_N stems from elastic magnetic Bragg scattering with the 3D ordering wave vector $\mathbf{Q}_0 = (0\ 1\ 1/2)$ [24, 25] and from low-energy magnons that are expected to emerge from there. In the 2D (h k) maps, the magnetic Bragg spots are not hit perfectly since the value of l is adapted to achieve $2\theta = 90°$. Nevertheless we find pronounced maxima at $M = \Gamma \pm (0\ 1)$ and enhanced intensity at M', cf. Fig. 1c). The narrow features at M and M' are evident in Fig. 4a), which shows the same 5 K data as panel b) but on another color scale. Chun *et al.* [10] analyzed the elastic scattering at M and M' to derive the existence of dominant Kitaev exchange interactions in Na_2IrO_3. In contrast, we focus on the inelastic response not too close to M and M'.

With decreasing temperature, the low-energy maps in the top panels of Fig. 3 show the building up of intensity close to M, reflecting the evolution of longer-range 3D correlations. However, central to our study is the behavior in $\mathbf{q}$ ranges not too close to M such as around the four X_γ points marked by white symbols in Fig. 4b). There, also the low-energy maps are insensitive to T, and the data at 5 K and 30 K $\approx 2T_N$ are very similar. In agreement with the spectra, cf. Fig. 2c), the low-energy maps show extended ranges of low intensity around $X_z = (5\ {-6})$ and $X_z = (6\ {-3})$ but larger intensity around $X_x = (4.5\ {-7.5})$ and $X_x = (5.5\ {-4.5})$. The opposite behavior is observed for the 45 meV continuum in the high-energy maps, again in agreement with the spectra. The tilted sample geometry of our experiment has been designed to address this particular behavior via the polarization factors, revealing a clear signature of bond-directional behavior, as we will show below.

Below T_N, magnetic order breaks the three-fold rotational symmetry of the honeycomb lattice. However, immediately above T_N short-range zigzag correlations of all three domains were observed with equal strength [10]. Therefore, the inequivalence of X_x and X_z above T_N and the corresponding breaking of rotational symmetry cannot be attributed to long-range magnetic order. Furthermore, the RIXS intensity at X_γ is insensitive to l, and the intensity maps measured at 5 K on two different magnetic domains are very similar, see *Supplementary Information* [18]. All of these results firmly establish the quasi-2D character of the studied excitations.

Nearest-neighbor correlations: From the RIXS intensity maps we now establish the predominance of nearest-neighbor correlations, which will allow us to, e.g., identify the response at X_γ with the γ bond. A magnetically ordered state is characterized by long-range spin-spin correlations. Above the ordering temperature T_N, thermal fluctuations yield a strong decrease of the correlation length. In quasi-2D com-

pounds, short-range correlations typically survive at temperatures much higher than T_N [26]. The Kitaev model describes a very different case in which spin-spin correlations are strictly restricted to two nearest neighbors on a single bond.

This unusual scenario of nearest-neighbor correlations leaves clear fingerprints in the $\mathbf{q}$ dependence of the RIXS intensity [13]. The dynamical structure factor of two sites has sinusoidal shape, i.e., the two-site scattering problem is equivalent to an inelastic incarnation of Young's double-slit experiment [27]. Summing over the three different bonds one finds

$$I_{\rm nn}(\mathbf{q}) = I_0 + \sum_\gamma I_\gamma(\mathbf{q})\, \cos^2(\mathbf{q}\cdot\Delta\mathbf{R}_\gamma/2)\,, \qquad (1)$$

where $\Delta\mathbf{R}_\gamma = \mathbf{R}_2 - \mathbf{R}_1$ denotes a γ bond with two correlated nearest-neighbor Ir sites, I_0 is a background intensity, and I_γ depends on the polarization. Such sinusoidal behavior has been observed for the continuum in the Kitaev material α-$RuCl_3$ in inelastic neutron scattering [23]. In RIXS on the honeycomb iridates, Eq. (1) has been found to describe the integrated intensity of the continuum along Γ-M-Γ' and Γ-K-X [13], treating I_0 and I_γ as empirical fit parameters. In Fig. 5, we visualize the sinusoidal intensity modulation of each bond for $I_\gamma = 1$ and $I_0 = 0$. The sum $I_{\rm nn}(\mathbf{q})$ in the right panel yields broad maxima at Γ and reduced intensity at Γ'. Comparing $I_{\rm nn}(\mathbf{q})$ with the high-energy maps in the bottom panels of Fig. 3 demonstrates that already this simple picture of individual bonds describes the behavior of the continuum surprisingly well. For integration below 15 meV, the RIXS intensity in the first Brillouin zone is dominated, at low temperature, by longer-range correlations of zigzag type, as discussed above. For $\mathbf{q}$ points not too close to M and M', a convincing description in terms of the nearest-neighbor model requires considering the polarization-dependent matrix elements, as done in Fig. 4c) and discussed below.

In such a nearest-neighbor scenario with two-site structure factors $F_\gamma = \cos^2(\mathbf{q}\cdot\Delta\mathbf{R}_\gamma/2)$, the data at X_γ selectively probe the response of the γ bond. For instance $X_z = (5\ {-6})$ hosts a maximum of F_z with vanishing contributions from x and y bonds, see Fig. 5, while $X_x = (4.5\ {-7.5})$ shows a maximum of F_x with $F_y = F_z = 0$.

Bond-directional excitations: With this information on the bond direction, we utilize polarization selection rules to address bond-directional behavior, i.e., whether the application of, e.g., the local operator S_i^x creates an excitation connected to a specific bond. In the Kitaev model, a RIXS excitation on the γ bond requires to apply $P^\gamma S_i^\gamma$ [28, 29] with the polarization factor $\mathbf{P} = i\varepsilon' \times \varepsilon$ and the incident and outgoing polarizations ε and ε', respectively. As shown below, this describes the behavior of the 10 meV feature but disagrees with the different polarization properties of the 45 meV continuum. Therefore, we employ a complementary microscopic approach and start from the RIXS matrix element for magnetic excitations of a $j = 1/2$ moment at site $\mathbf{R}_i$ [30]. With the outgoing π and σ polarizations being perpendicular to the incident polarization, see Fig. 1, this matrix element is proportional to $\mathbf{P}\cdot\mathbf{S_i}$, where $\mathbf{S_i}$ operates within the $j = 1/2$ subspace. For the two sites of, e.g., a z bond, we consider that S_i^z creates a spin-conserving (sc) excitation while S_i^x or S_i^y yield a spin flip (sf) of the z component. For $I_\gamma(\mathbf{q})$ in Eq. (1) this yields

$$I_z^{\rm sc}(\mathbf{q}) \propto |P^z(\mathbf{q})|^2 \ \text{ and } \ I_z^{\rm sf}(\mathbf{q}) \propto |P^x(\mathbf{q})|^2 + |P^y(\mathbf{q})|^2 \quad (2)$$

and equivalent expressions for x and y bonds. We have chosen the experimental geometry with the aim to strongly suppress $|P^z(\mathbf{q})|^2$ in the lower parts of the maps, see Fig. 1d). More precisely, $|P^z|^2 \propto \sin^2(\theta_{\rm in})$, and the angle of incidence $\theta_{\rm in}$ is varied from about 5° to 65°. This corresponds to an $(h\ k)$ range where k roughly runs from -8 to 4 and depends roughly linearly on $\theta_{\rm in}$. In contrast, $|P^x(\mathbf{q})|^2$ and $|P^y(\mathbf{q})|^2$ are nearly constant and large, see *Supplementary Information* [18]. In the bond-directional scenario described by Eq. (2), the suppression of $|P^z|^2$ switches off spin-conserving excitations on z bonds while it reduces the intensity of spin-flip excitations on x or y bonds by about a factor 2. This explains the stunning difference of the spectra measured at X_z and X_x, see Fig. 2c), if we attribute the peaks at 10 and 45 meV to spin-conserving and spin-flip excitations, respectively, and identify X_γ with the γ bond, as appropriate for nearest-neighbor correlations.

Finally, we calculate maps of the RIXS intensity $I_{\rm nn}(\mathbf{q})$ expected for BDE, see Eq. (1). This combines the sinusoidal structure factors F_γ of the nearest-neighbor model, containing information on the bond direction, with the polarization-dependent $I_\gamma(\mathbf{q})$ given in Eq. (2), reflecting the involved spin component. Figures 4c) and 4e) plot $I_{\rm nn}(\mathbf{q})$ for spin-conserving and spin-flip excitations, respectively. The excellent agreement with the RIXS data in panels b) and d) corroborates the above assignment of spin-conserving and spin-flip excitations at low and high energies, respectively. The continuum, integrated above 45 meV, is described very well over the entire range of $\mathbf{q}$ and for all studied temperatures. For integration below 15 meV, our nearest-neighbor model represents the RIXS data very well at high T such as 70 K or 150 K. At 5 K, it still captures the behavior not too close to M, while the response in the vicinity of M reflects longer-range correlations. Altogether, bond-directional behavior is most evident around X_γ points. For instance X_x and X_z are equivalent on the honeycomb lattice and within the nearest-neighbor model for

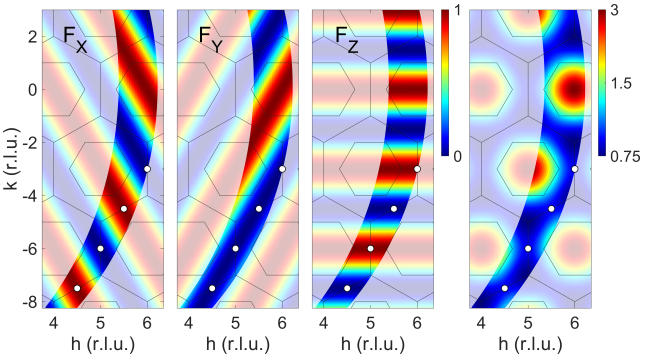

FIG. 5. **Sinusoidal two-site modulation patterns.** The three panels on the left depict the structure factor $F_\gamma = \cos^2(\mathbf{q}\cdot\Delta\mathbf{R}_\gamma/2)$ for individual γ bonds with $\gamma = x, y, z$, see Eq. (1). The measured $\mathbf{q}$ range is highlighted, cf. Fig. 3. Right: Sum over x, y, and z bonds. White circles mark X_x and X_z points, these are relevant for the discussion of the bond-directional character, see Fig. 2c).

isotropic $I_\gamma = 1$, see Fig. 5. The anisotropic, bond-directional character of the magnetic excitations in Na_2IrO_3 yields very different RIXS intensities around X_x and X_z as well as different behavior at low and high energy.

Outlook: In the quest to identify Kitaev materials, the observation of bond-directional excitations via our advanced RIXS scheme can play a decisive role in validating, for a given compound, the presence of bond-directional interactions. These are appreciated as a source of frustration beyond the geometric frustration of non-bipartite lattices and key to the emergence of non-conventional forms of magnetism (such as recently discussed for fcc $j = 1/2$ Ba_2CeIrO_6 [31]) and potentially spin liquid ground states (as hypothesized [32] for $j = 1/2$ pyrochlore $Yb_2Ti_2O_7$). A first step in this direction might be to apply our approach to other honeycomb Kitaev materials, but also to $j = 1/2$ systems which have not attracted primary interest for bond-directional exchanges such as Sr_2IrO_4. In further developing our experimental approach a natural next step is to validate other forms of bond-directional interactions, such as dominating off-diagonal Γ-interactions [8, 9], and their manifestation in bond-directional excitations.

ACKNOWLEDGMENTS

We thank A. Revelli for experimental support and useful discussions. We gratefully acknowledge the European Synchrotron Radiation Facility (ESRF) and the Advanced Photon Source (APS) for providing beam time and technical support. Prior to the measurements at ESRF shown here, we had performed a proof-of-principles RIXS study at beamline 27-ID at APS for the feasibility of this measurement geometry with a large sample tilt angle χ. APS is a U.S. Department of Energy (DOE) Office of Science user facility operated for the DOE Office of Science by Argonne National Laboratory under Contract No. DE-AC02-06CH11357. Furthermore, we acknowledge funding from the Deutsche Forschungsgemeinschaft (DFG, German Research Foundation) via Project numbers 277146847 (CRC 1238, projects B03, C03), 247310070 (CRC 1143, project A05), and 107745057 (TRR 80).

[1] Z. Nussinov and J. van den Brink, Compass models: Theory and physical motivations, Rev. Mod. Phys. **87**, 1 (2015).
[2] C. Broholm, R. J. Cava, S. A. Kivelson, D. G. Nocera, M. R. Norman, and T. Senthil, Quantum spin liquids, Science **367**, eaay0668 (2020).
[3] L. Savary and L. Balents, Quantum spin liquids: a review, Reports on Progress in Physics **80**, 016502 (2016).
[4] J. Knolle and R. Moessner, A Field Guide to Spin Liquids, Annual Review of Condensed Matter Physics **10**, 451 (2019).
[5] A. Kitaev, Anyons in an exactly solved model and beyond, Annals of Physics **321**, 2 (2006).
[6] M. Hermanns, I. Kimchi, and J. Knolle, Physics of the Kitaev Model: Fractionalization, Dynamic Correlations, and Material Connections, Annual Review of Condensed Matter Physics **9**, 17 (2018).
[7] G. Jackeli and G. Khaliullin, Mott Insulators in the Strong Spin-Orbit Coupling Limit: From Heisenberg to a Quantum Compass and Kitaev Models, Phys. Rev. Lett. **102**, 017205 (2009).
[8] J. G. Rau, E. K.-H. Lee, and H.-Y. Kee, Spin-Orbit Physics Giving Rise to Novel Phases in Correlated Systems: Iridates and Related Materials, Annual Review of Condensed Matter Physics **7**, 195 (2016).
[9] S. Trebst and C. Hickey, Kitaev materials, Physics Reports **950**, 1 (2022).
[10] S. H. Chun, J.-W. Kim, J. Kim, H. Zheng, C. C. Stoumpos, C. D. Malliakas, J. F. Mitchell, K. Mehlawat, Y. Singh, Y. Choi, T. Gog, A. Al-Zein, M. Moretti Sala, M. Krisch, J. Chaloupka, G. Jackeli, G. Khaliullin, and B. J. Kim, Direct evidence for dominant bond-directional interactions in a honeycomb lattice iridate Na_2IrO_3, Nature Physics **11**, 462 (2015).
[11] A. Banerjee, C. A. Bridges, J. Q. Yan, A. A. Aczel, L. Li, M. B. Stone, G. E. Granroth, M. D. Lumsden, Y. Yiu, J. Knolle, S. Bhattacharjee, D. L. Kovrizhin, R. Moessner, D. A. Tennant, D. G. Mandrus, and S. E. Nagler, Proximate Kitaev quantum spin liquid behaviour in a honeycomb magnet, Nature Materials **15**, 733 (2016).
[12] K. Mehlawat, A. Thamizhavel, and Y. Singh, Heat capacity evidence for proximity to the Kitaev quantum spin liquid in A_2IrO_3 ($A = Na$, Li), Phys. Rev. B **95**, 144406 (2017).
[13] A. Revelli, M. Moretti Sala, G. Monaco, C. Hickey, P. Becker, F. Freund, A. Jesche, P. Gegenwart, T. Eschmann, F. L. Buessen, S. Trebst, P. H. M. van Loosdrecht, J. van den Brink, and M. Grüninger, Fingerprints of Kitaev physics in the magnetic excitations of honeycomb iridates, Phys. Rev. Research **2**, 043094 (2020).
[14] Y. Singh and P. Gegenwart, Antiferromagnetic Mott insulating state in single crystals of the honeycomb lattice material Na_2IrO_3, Phys. Rev. B **82**, 064412 (2010).
[15] M. Moretti Sala, C. Henriquet, L. Simonelli, R. Verbeni, and G. Monaco, High energy-resolution set-up for Ir L_3 edge RIXS experiments, Journal of Electron Spectroscopy and Related Phenomena **188**, 150 (2013).
[16] M. Moretti Sala, K. Martel, C. Henriquet, A. Al Zein, L. Simonelli, C. J. Sahle, H. Gonzalez, M.-C. Lagier, C. Ponchut, S. Huotari, R. Verbeni, M. Krisch, and G. Monaco, A high-energy-resolution resonant inelastic X-ray scattering spectrometer at ID20 of the European Synchrotron Radiation Facility, Journal of Synchrotron Radiation **25**, 580 (2018).
[17] M. Minola, G. Dellea, H. Gretarsson, Y. Y. Peng, Y. Lu, J. Porras, T. Loew, F. Yakhou, N. B. Brookes, Y. B. Huang, J. Pelliciari, T. Schmitt, G. Ghiringhelli, B. Keimer, L. Braicovich, and M. Le Tacon, Collective nature of spin excitations in superconducting cuprates probed by resonant inelastic x-ray scattering, Phys. Rev. Lett. **114**, 217003 (2015).
[18] The *Supplementary Information* discusses the resonance behavior, the insensitivity to l and to magnetic domains, and the full polarization factors.
[19] J. Kim, J. Chaloupka, Y. Singh, J. W. Kim, B. J. Kim, D. Casa, A. Said, X. Huang, and T. Gog, Dynamic Spin Correlations in the Honeycomb Lattice Na_2IrO_3 Measured by Resonant Inelastic x-Ray Scattering, Phys. Rev. X **10**, 021034 (2020).
[20] S. H. Chun, P. P. Stavropoulos, H.-Y. Kee, M. Moretti Sala, J. Kim, J.-W. Kim, B. J. Kim, J. F. Mitchell, and Y.-J. Kim, Optical magnons with dominant bond-directional exchange inter-

actions in the honeycomb lattice iridate α-Li_2IrO_3, Phys. Rev. B **103**, L020410 (2021).
[21] J. Kim, H. Zhao, and G. Cao, Resolution of zigzag magnetic correlations in Na-deficient Na_xIrO_3 without long-range ordering, Phys. Rev. B **106**, 075157 (2022).
[22] H. Suzuki, H. Liu, J. Bertinshaw, K. Ueda, H. Kim, S. Laha, D. Weber, Z. Yang, L. Wang, H. Takahashi, K. Fürsich, M. Minola, B. V. Lotsch, B. J. Kim, H. Yavaş, M. Daghofer, J. Chaloupka, G. Khaliullin, H. Gretarsson, and B. Keimer, Proximate ferromagnetic state in the Kitaev model material $\alpha - RuCl_3$, Nature Communications **12**, 4512 (2021).
[23] A. Banerjee, J. Yan, J. Knolle, C. A. Bridges, M. B. Stone, M. D. Lumsden, D. G. Mandrus, D. A. Tennant, R. Moessner, and S. E. Nagler, Neutron scattering in the proximate quantum spin liquid $\alpha - RuCl_3$, Science **356**, 1055 (2017).
[24] F. Ye, S. Chi, H. Cao, B. C. Chakoumakos, J. A. Fernandez-Baca, R. Custelcean, T. F. Qi, O. B. Korneta, and G. Cao, Direct evidence of a zigzag spin-chain structure in the honeycomb lattice: A neutron and x-ray diffraction investigation of single-crystal Na_2IrO_3, Phys. Rev. B **85**, 180403(R) (2012).
[25] S. K. Choi, R. Coldea, A. N. Kolmogorov, T. Lancaster, I. I. Mazin, S. J. Blundell, P. G. Radaelli, Y. Singh, P. Gegenwart, K. R. Choi, S.-W. Cheong, P. J. Baker, C. Stock, and J. Taylor, Spin Waves and Revised Crystal Structure of Honeycomb Iridate Na_2IrO_3, Phys. Rev. Lett. **108**, 127204 (2012).
[26] H. M. Rønnow, D. F. McMorrow, and A. Harrison, High-Temperature Magnetic Correlations in the 2D $S = 1/2$ Antiferromagnet Copper Formate Tetradeuterate, Phys. Rev. Lett. **82**, 3152 (1999).
[27] A. Revelli, M. M. Sala, G. Monaco, P. Becker, L. Bohatý, M. Hermanns, T. C. Koethe, T. Fröhlich, P. Warzanowski, T. Lorenz, S. V. Streltsov, P. H. M. van Loosdrecht, D. I. Khomskii, J. van den Brink, and M. Grüninger, Resonant inelastic x-ray incarnation of Young's double-slit experiment, Science Advances **5**, eaav4020 (2019).
[28] G. B. Halász, N. B. Perkins, and J. van den Brink, Resonant Inelastic X-Ray Scattering Response of the Kitaev Honeycomb Model, Phys. Rev. Lett. **117**, 127203 (2016).
[29] Reference [28] distinguishes spin-conserving and non-spin-conserving channels, refering to the spin of an electron in the RIXS process. We measure the non-spin-conserving channel in direct RIXS, which in terms of the local $j = 1/2$ moments contains both j^γ-flip and j^γ-conserving excitations.
[30] L. J. P. Ament, G. Khaliullin, and J. van den Brink, Theory of resonant inelastic x-ray scattering in iridium oxide compounds: Probing spin-orbit-entangled ground states and excitations, Phys. Rev. B **84**, 020403(R) (2011).
[31] A. Revelli, C. C. Loo, D. Kiese, P. Becker, T. Fröhlich, T. Lorenz, M. Moretti Sala, G. Monaco, F. L. Buessen, J. Attig, M. Hermanns, S. V. Streltsov, D. I. Khomskii, J. van den Brink, M. Braden, P. H. M. van Loosdrecht, S. Trebst, A. Paramekanti, and M. Grüninger, Spin-orbit entangled $j = \frac{1}{2}$ moments in Ba_2CeIrO_6: A frustrated fcc quantum magnet, Phys. Rev. B **100**, 085139 (2019).
[32] J. D. Thompson, P. A. McClarty, D. Prabhakaran, I. Cabrera, T. Guidi, and R. Coldea, Quasiparticle Breakdown and Spin Hamiltonian of the Frustrated Quantum Pyrochlore $Yb_2Ti_2O_7$ in a Magnetic Field, Phys. Rev. Lett. **119**, 057203 (2017).

Supplementary Information
RIXS observation of bond-directional nearest-neighbor excitations in the Kitaev material Na_2IrO_3

M. Magnaterra,[1] K. Hopfer,[1] Ch. J. Sahle,[2] M. Moretti Sala,[3] G. Monaco,[4] J. Attig,[5] C. Hickey,[5] I.-M. Pietsch,[6] F. Breitner,[6] P. Gegenwart,[6] M. H. Upton,[7] Jungho Kim,[7] S. Trebst,[5] P. H. M. van Loosdrecht,[1] J. van den Brink,[8,9] and M. Grüninger[1]

[1]*Institute of Physics II, University of Cologne, 50937 Cologne, Germany*
[2]*ESRF, The European Synchrotron, 71 Avenue des Martyrs, CS40220, 38043 Grenoble Cedex 9, France*
[3]*Dipartimento di Fisica, Politecnico di Milano, I-20133 Milano, Italy*
[4]*Dipartimento di Fisica e Astronomia "Galileo Galilei", Università di Padova, Padova, Italy*
[5]*Institute for Theoretical Physics, University of Cologne, 50937 Cologne, Germany*
[6]*Experimental Physics VI, Center for Electronic Correlations and Magnetism, University of Augsburg, 86159 Augsburg, Germany*
[7]*Advanced Photon Source, Argonne National Laboratory, Argonne, Illinois 60439, USA*
[8]*Institute for Theoretical Solid State Physics, IFW Dresden, 01069 Dresden, Germany*
[9]*Institute for Theoretical Physics and Würzburg-Dresden Cluster of Excellence ct.qmat, Technische Universität Dresden, 01069 Dresden, Germany*

(Dated: January 19, 2023)

I. RESONANCE BEHAVIOR

The resonance behavior at the Ir L_3 edge provides an unambiguous proof of the magnetic nature of the excitations at about 10 meV and 45 meV. For Ir^{4+} ions, magnetic excitations within the $j = 1/2$ subspace are resonantly enhanced in a direct RIXS process that involves the promotion of a $2p$ core electron to the t_{2g} orbitals [1]. For Na_2IrO_3, this t_{2g} resonance occurs for an incident energy $E_{\rm in} = 11.2145$ keV [2]. For comparison, the RIXS intensity of excitations to e_g orbitals in the iridates is maximized by choosing a 3 to 4 eV larger value of $E_{\rm in}$ [3]. We observe pronounced t_{2g} resonance behavior both around 10 meV and around 45 meV, see Fig. 1. The right panel shows a resonance map measured at (5 -5.9 -5) where the 45 meV continuum is pronounced while the 10 meV peak is suppressed, as demonstrated by the RIXS spectra in Fig. 2c) of the main text. In contrast, the data in the left panel of Fig. 1 were measured at (4.5 -7.1 -4.7) and show a dominant contribution of the 10 meV feature. The common t_{2g} resonance behavior firmly corroborates the magnetic character of both excitations.

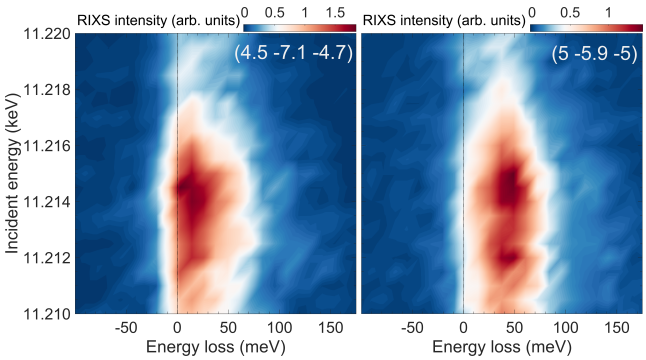

FIG. 1. **Resonance maps** of the magnetic excitations at 30 K. The 10 meV peak dominates for transferred momentum (4.5 -7.1 -4.7) (left), while the 45 meV continuum prevails at (5 -5.9 -5) (right). Both features show t_{2g} resonance at $E_{\rm in} = 11.2145$ keV (vertical scale). There is no evidence for an e_g resonance at $E_{\rm in} = 11.218$ keV. The elastic line at zero loss (solid black line) is suppressed by using a scattering angle $2\theta = 90^\circ$.

In contrast, the excitation of phonons corresponds to an *indirect* RIXS process that is boosted if e_g orbitals are involved [4]. However, phonons have not been detected in L_3 edge RIXS data of Mott-insulating $5d^5$ iridates with Ir^{4+} ions, see, e.g., Refs. [2, 3, 5–11]. The suppression of the phonon contribution can be explained by the well-screened and short-lived intermediate state Ir $2p^5\ t_{2g}^6$ at the L_3 edge. This has to be distinguished from the case of RIXS at the O K edge with $E_{\rm in} \approx 0.53$ keV, where the observation of phonon features in α-Li_2IrO_3 [12] can be attributed to the very different, long-lived intermediate state.

II. 2D CHARACTER OF EXCITATIONS AND INSENSITIVITY TO MAGNETIC DOMAINS

A. l dependence

Below the Néel temperature $T_N = 15$ K, Na_2IrO_3 hosts long-range magnetic order with the 3D propagation vector $\mathbf{Q}_0 = (0\ 1\ 1/2)$ [13, 14]. In the 3D ordered state, low-energy magnons are expected to emerge from $\mathbf{Q}_0$ and to show a dispersion as a function of the transferred momentum $\mathbf{q}$. However, we focus on the magnetic excitations at about 10 meV and 45 meV that cannot be described as magnons of the long-range ordered phase. These features persist to temperatures far above T_N, see Fig. 3 of the main text, which provides strong evidence for a predominantly 2D character. Our study highlights the RIXS intensity of these 2D excitations in $(h\ k)$ space not too close to $M = (0\ \pm 1)$ and $M' = (\pm 1/2\ \pm 1/2)$, cf. Fig. 1c) in the main text. In the $(h\ k)$ range relevant to us, the RIXS intensity is insensitive to l even at 5 K, which is demonstrated in Fig. 2, using $X_z = (5\ {-6})$, $X_x = (5.5\ {-4.5})$, and $K = (5.66\ {-3})$ as examples. Panels a) and b) show data as a function of l for integration of the RIXS intensity below 15 meV and above 45 meV. In the latter case, the RIXS intensity is roughly constant as a function of l. In particular, the intensity of the 45 meV feature is significantly lower at

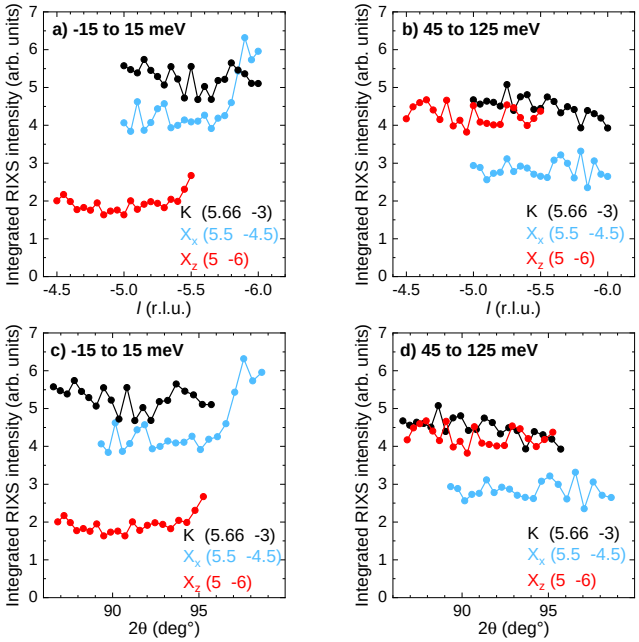

FIG. 2. **2D character of magnetic excitations.** Panels a) and b) depict the RIXS intensity at (5.66 -3 l), (5.5 -4.5 l), and (5 -6 l) for integration below 15 meV and above 45 meV, respectively. The data have been collected at 5 K. Panels c) and d) show the same data plotted as a function of the scattering angle 2θ. At low energy, the contribution of the elastic line is suppressed for $2\theta = 90°$.

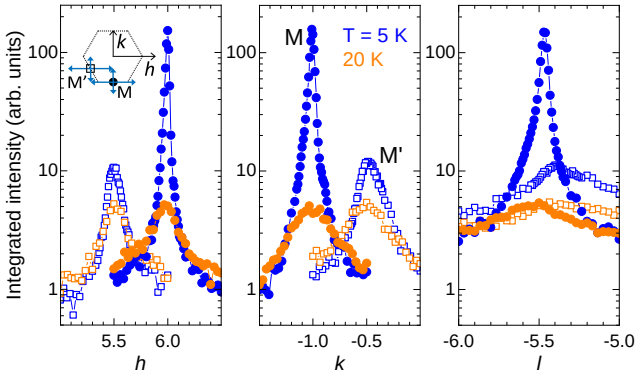

FIG. 3. **Quasielastic scans across a magnetic Bragg peak.** The scattered intensity was integrated from -15 meV to +15 meV. Full and open symbols show data across (6 -1 -5.5) and (5.5 -0.5 -5.5), respectively. At 20 K, above T_N, both **q** points show the same intensity. At 5 K, (6 -1 -5.5) hosts a magnetic Bragg peak.

X_x than at X_z for all studied values of l. The 15 meV shows the opposite behavior, the RIXS intensity is higher at X_x than at X_z, again for all l. For integration from -15 to 15 meV, the contribution of the elastic line has to be considered. In the data shown in Figs. 2, 3, and 4 of the main text, the elastic line has been suppressed by choosing a scattering angle $2\theta = 90°$. This, however, fixes l for a given (h k) point. Measuring the l dependence requires to change 2θ away from 90°. Therefore, we replot the same data in panels c) and d) as a function of 2θ. Close to 90°, the RIXS intensity is roughly constant also for integration below 15 meV, which strongly corroborates the 2D character. The increase of the low-energy intensity for 2θ further away from 90° arises from the increasing elastic contribution of Thomson scattering.

B. 3D magnetic domains

The 2D character is further supported by the insensitivity of our results to 3D magnetic domains. The ideal 2D honeycomb lattice exhibits threefold rotational symmetry, such that the M points (0 ±1) and the M' points (±1/2 ±1/2) all are equivalent. However, the 3D crystal structure of Na_2IrO_3 shows a small monoclinic distortion, hence (0 ±1 1/2) and (±1/2 ±1/2 1/2) are not equivalent. With the 3D propagation vector $\mathbf{Q}_0 = (0\ 1\ 1/2)$ of long-range magnetic order [13, 14], the orientation of the zigzag ordering pattern is tied to the crystal structure.

Laue diffraction of our samples indicates structural 120° twinning in the honeycomb plane. The structural twins dictate the formation of corresponding magnetic domains. The cross section of the incident x-ray beam of roughly $(15 \times 15)\ \mu m^2$ allows us to select the measurement spot such that a given twin domain dominates the response, as demonstrated by scans across $M_{3D} = (6\ -1\ -5.5)$ and $M'_{3D} = (5.5\ -0.5\ -5.5)$ for zero energy loss, see Fig. 3. At 20 K, i.e., above T_N, we observe clear peaks of the elastically scattered intensity along h and k but a broad intensity distribution along l. Furthermore, the intensity is very similar at M_{3D} and M'_{3D}. This suggests the coexistence of short-range 2D zigzag fragments running along three equivalent directions, in agreement with the results of Chun *et al.* [15]. At 5 K, we find a magnetic Bragg peak at M_{3D} that is characterized by a pronounced peak as a function of l. In contrast, the intensity at M'_{3D} is much lower and the peak still is very broad as a function of l. This demonstrates that the measurement predominantly probes a single magnetic domain.

In Fig. 4 we compare (h k) maps of the RIXS intensity measured at 5 K on two different spots of the sample that correspond to two different twin domains rotated by 120°. For each spot, we study the intensity integrated from -15 to 15 meV and from 45 to 125 meV. The intensity maps for the two different domains are very similar. In particular, the distinct behavior at different X_γ points is observed equivalently. This result corroborates that the different intensities at X_x and X_z cannot be attributed to small differences arising from the 3D crystal structure but reflect bond-directional excitations that are detected based on the polarization dependence. Note that the unambiguous determination of the character of a specific domain requires to address specific (h k l) points, the domain character cannot be read from (h k) maps measured with $2\theta = 90°$.

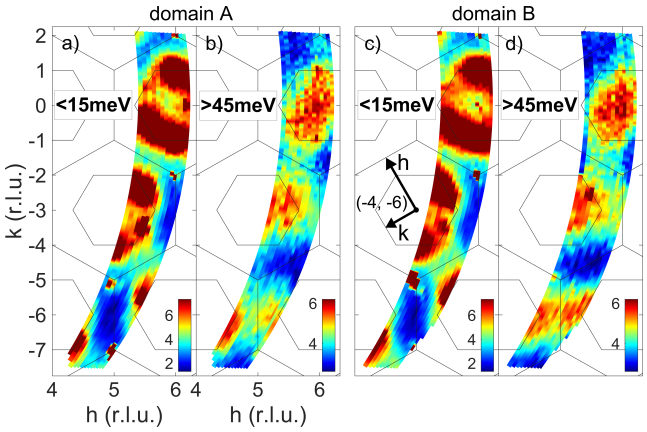

FIG. 4. **Maps of the RIXS intensity of two twin domains** measured at 5 K. Domain B is rotated by 120° with respect to domain A, as indicated by the coordinate frame in panel c). The intensity has been integrated from -15 to 15 meV and from 45 to 125 meV. The data agree on the bond-directional character of the magnetic excitations.

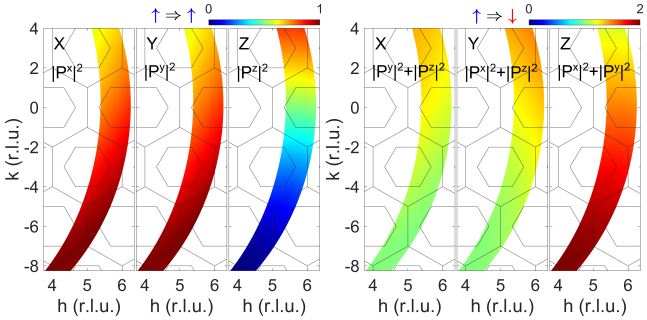

FIG. 5. **Polarization factors** of the three bonds. Left: $|P^\gamma(\mathbf{q})|^2$, applicable to spin-conserving excitations on a γ bond, as observed at 10 meV, cf. Eq. (5). The central feature is the suppression of $|P^z(\mathbf{q})|^2$ in the lower part of the map, while $|P^x|^2$ and $|P^y|^2$ do not vary strongly with $\mathbf{q}$. Right: The panel for the z bond depicts $|P^x(\mathbf{q})|^2 + |P^y(\mathbf{q})|^2$, which is applicable to spin-flip excitations on the z bond, cf. Eq. (7). The other panels show equivalent expressions for x and y bonds. This describes the behavior of the 45 meV feature.

III. POLARIZATION FACTORS

At the Ir L edge, the RIXS intensity $I(\mathbf{q},\omega)$ for excitations from the ground state $|0\rangle$ to a final state $|f\rangle$ is given by a coherent sum of scattering processes localized on individual sites. The sum is running over all sites $\mathbf{R}_i$ at which a given final state $|f\rangle$ can be reached, i.e., over which $|f\rangle$ is delocalized. In dipole approximation one finds [1]

$$I(\mathbf{q},\omega) = \sum_f \left| \langle f| \sum_i e^{i\mathbf{q}\cdot\mathbf{R}_i} \left[D^\dagger D\right]_{\mathbf{R}_i} |0\rangle \right|^2 \delta(\hbar\omega - E_f) \tag{1}$$

where E_f denotes the excitation energy and D is the local dipole operator. In general, magnetic excitations can be generated via different polarization channels [16]. We use $2\theta = 90°$ for the scattering angle, hence the outgoing vertical and horizontal polarizations ε'_σ and ε'_π are perpendicular to the linear incident polarization ε. In this case, the single-site RIXS matrix elements for magnetic excitations within the $j = 1/2$ manifold at site $\mathbf{R}_i$ are given by [17]

$$\left[D^\dagger D\right]_{\mathbf{R}_i} = \frac{2}{3}\mathbf{P}\cdot\mathbf{S}_i \tag{2}$$

with the polarization factor $\mathbf{P} = i\varepsilon' \times \varepsilon$, and $\mathbf{S}_i$ operates within the $j = 1/2$ subspace. In the employed experimental geometry with $2\theta = 90°$, see Fig. 1 of the main text, the polarization factor mainly depends on the angle of incidence θ_{in}, which translates to a $\mathbf{q}$ dependence of the polarization factor.

In terms of the diagonal components of the dynamical spin structure factor $S(\mathbf{q},\omega)$,

$$S^{\gamma\gamma}(\mathbf{q},\omega) = \sum_f \left| \langle f| \sum_i e^{i\mathbf{q}\cdot\mathbf{R}_i} S_i^\gamma |0\rangle \right|^2 \delta(\hbar\omega - E_f)\,, \tag{3}$$

the RIXS intensity can be written as

$$I(\mathbf{q},\omega) \propto \sum_{\gamma\in\{x,y,z\}} |P^\gamma(\mathbf{q})|^2 S^{\gamma\gamma}(\mathbf{q},\omega)\,, \tag{4}$$

where, as usual, we neglect the off-diagonal components of $S(\mathbf{q},\omega)$. In this form, the RIXS intensity thus measures the sum of the dynamical spin structure factor components weighted by their respective momentum-dependent polarization factors. We have chosen the experimental geometry such that $|P^z(\mathbf{q})|^2$ strongly differs from the other components, see Fig. 5. By varying $\mathbf{q}$, one can thus vary the weighting of the different components of $S(\mathbf{q},\omega)$, e.g. suppressing the contribution of $S^{zz}(\mathbf{q},\omega)$.

Considering only nearest-neighbor correlations, the $\mathbf{q}$ dependence of the dynamical structure factor is captured using only $\cos^2(\mathbf{q}\cdot\mathbf{\Delta R}_\gamma/2)$ terms. For the 10 meV peak (spin-conserving excitations), the total intensity is well described by

$$I^{\text{sc}}_{\text{nn}}(\mathbf{q}) = \sum_\gamma |P^\gamma(\mathbf{q})|^2 \cos^2(\mathbf{q}\cdot\mathbf{\Delta R}_\gamma/2)\,, \tag{5}$$

where the $\mathbf{q}$ dependence of the structure factor is given by

$$S^{\gamma\gamma}(\mathbf{q}, 10\,\text{meV}) \propto \cos^2(\mathbf{q}\cdot\mathbf{\Delta R}_\gamma/2)\,, \tag{6}$$

meaning that j^γ correlations dominate on γ bonds. For the 45 meV peak (spin-flip excitations), our data agree with

$$\begin{aligned} I^{\text{sf}}_{\text{nn}}(\mathbf{q}) &= \sum_\gamma \left[\sum_{\gamma'\neq\gamma} |P^{\gamma'}(\mathbf{q})|^2\right] \cos^2(\mathbf{q}\cdot\mathbf{\Delta R}_\gamma/2) \\ &= \sum_\gamma |P^\gamma(\mathbf{q})|^2 \left[\sum_{\gamma'\neq\gamma} \cos^2(\mathbf{q}\cdot\mathbf{\Delta R}_{\gamma'}/2)\right], \end{aligned} \tag{7}$$

which yields

$$S^{\gamma\gamma}(\mathbf{q}, 45\,\text{meV}) \propto \sum_{\gamma'\neq\gamma} \cos^2(\mathbf{q}\cdot\mathbf{\Delta R}_{\gamma'}/2)\,. \tag{8}$$

This means that, e.g., application of S_i^x creates a spin flip on either a y bond or a z bond. From Eqns. (5) and (7) one can read off I^{sc}_γ and I^{sf}_γ used in Eqns. (1) and (2) of the main text.

[1] L. J. P. Ament, M. van Veenendaal, T. P. Devereaux, J. P. Hill, and J. van den Brink, Resonant inelastic x-ray scattering studies of elementary excitations, Rev. Mod. Phys. **83**, 705 (2011).

[2] A. Revelli, M. Moretti Sala, G. Monaco, C. Hickey, P. Becker, F. Freund, A. Jesche, P. Gegenwart, T. Eschmann, F. L. Buessen, S. Trebst, P. H. M. van Loosdrecht, J. van den Brink, and M. Grüninger, Fingerprints of Kitaev physics in the magnetic excitations of honeycomb iridates, Phys. Rev. Research **2**, 043094 (2020).

[3] E. Lefrançois, A.-M. Pradipto, M. Moretti Sala, L. C. Chapon, V. Simonet, S. Picozzi, P. Lejay, S. Petit, and R. Ballou, Anisotropic interactions opposing magnetocrystalline anisotropy in Sr_3NiIrO_6, Phys. Rev. B **93**, 224401 (2016).

[4] S. Moser, S. Fatale, P. Krüger, H. Berger, P. Bugnon, A. Magrez, H. Niwa, J. Miyawaki, Y. Harada, and M. Grioni, Electron-Phonon Coupling in the Bulk of Anatase TiO_2 Measured by Resonant Inelastic X-Ray Spectroscopy, Phys. Rev. Lett. **115**, 096404 (2015).

[5] J. Kim, M. Daghofer, A. H. Said, T. Gog, J. van den Brink, G. Khaliullin, and B. J. Kim, Excitonic quasiparticles in a spin–orbit Mott insulator, Nature Communications **5**, 4453 (2014).

[6] M. Moretti Sala, V. Schnells, S. Boseggia, L. Simonelli, A. Al-Zein, J. G. Vale, L. Paolasini, E. C. Hunter, R. S. Perry, D. Prabhakaran, A. T. Boothroyd, M. Krisch, G. Monaco, H. M. Rønnow, D. F. McMorrow, and F. Mila, Evidence of quantum dimer excitations in $Sr_3Ir_2O_7$, Phys. Rev. B **92**, 024405 (2015).

[7] X. Lu, D. E. McNally, M. Moretti Sala, J. Terzic, M. H. Upton, D. Casa, G. Ingold, G. Cao, and T. Schmitt, Doping Evolution of Magnetic Order and Magnetic Excitations in $(Sr_{1-x}La_x)_3Ir_2O_7$, Phys. Rev. Lett. **118**, 027202 (2017).

[8] M. Rossi, M. Retegan, C. Giacobbe, R. Fumagalli, A. Efimenko, T. Kulka, K. Wohlfeld, A. I. Gubanov, and M. Moretti Sala, Possibility to realize spin-orbit-induced correlated physics in iridium fluorides, Phys. Rev. B **95**, 235161 (2017).

[9] A. Revelli, C. C. Loo, D. Kiese, P. Becker, T. Fröhlich, T. Lorenz, M. Moretti Sala, G. Monaco, F. L. Buessen, J. Attig, M. Hermanns, S. V. Streltsov, D. I. Khomskii, J. van den Brink, M. Braden, P. H. M. van Loosdrecht, S. Trebst, A. Paramekanti, and M. Grüninger, Spin-orbit entangled $j = \frac{1}{2}$ moments in Ba_2CeIrO_6: A frustrated fcc quantum magnet, Phys. Rev. B **100**, 085139 (2019).

[10] J. Kim, J. Chaloupka, Y. Singh, J. W. Kim, B. J. Kim, D. Casa, A. Said, X. Huang, and T. Gog, Dynamic Spin Correlations in the Honeycomb Lattice Na_2IrO_3 Measured by Resonant Inelastic x-Ray Scattering, Phys. Rev. X **10**, 021034 (2020).

[11] S. H. Chun, P. P. Stavropoulos, H.-Y. Kee, M. Moretti Sala, J. Kim, J.-W. Kim, B. J. Kim, J. F. Mitchell, and Y.-J. Kim, Optical magnons with dominant bond-directional exchange interactions in the honeycomb lattice iridate α-Li_2IrO_3, Phys. Rev. B **103**, L020410 (2021).

[12] J. G. Vale, C. D. Dashwood, E. Paris, L. S. I. Veiga, M. Garcia-Fernandez, A. Nag, A. Walters, K.-J. Zhou, I.-M. Pietsch, A. Jesche, P. Gegenwart, R. Coldea, T. Schmitt, and D. F. McMorrow, High-resolution resonant inelastic x-ray scattering study of the electron-phonon coupling in honeycomb $\alpha - Li_2IrO_3$, Phys. Rev. B **100**, 224303 (2019).

[13] F. Ye, S. Chi, H. Cao, B. C. Chakoumakos, J. A. Fernandez-Baca, R. Custelcean, T. F. Qi, O. B. Korneta, and G. Cao, Direct evidence of a zigzag spin-chain structure in the honeycomb lattice: A neutron and x-ray diffraction investigation of single-crystal Na_2IrO_3, Phys. Rev. B **85**, 180403 (2012).

[14] S. K. Choi, R. Coldea, A. N. Kolmogorov, T. Lancaster, I. I. Mazin, S. J. Blundell, P. G. Radaelli, Y. Singh, P. Gegenwart, K. R. Choi, S.-W. Cheong, P. J. Baker, C. Stock, and J. Taylor, Spin Waves and Revised Crystal Structure of Honeycomb Iridate Na_2IrO_3, Phys. Rev. Lett. **108**, 127204 (2012).

[15] S. H. Chun, J.-W. Kim, J. Kim, H. Zheng, C. C. Stoumpos, C. D. Malliakas, J. F. Mitchell, K. Mehlawat, Y. Singh, Y. Choi, T. Gog, A. Al-Zein, M. Moretti Sala, M. Krisch, J. Chaloupka, G. Jackeli, G. Khaliullin, and B. J. Kim, Direct evidence for dominant bond-directional interactions in a honeycomb lattice iridate Na_2IrO_3, Nature Physics **11**, 462 (2015).

[16] M. W. Haverkort, Theory of Resonant Inelastic X-Ray Scattering by Collective Magnetic Excitations, Phys. Rev. Lett. **105**, 167404 (2010).

[17] L. J. P. Ament, G. Khaliullin, and J. van den Brink, Theory of resonant inelastic x-ray scattering in iridium oxide compounds: Probing spin-orbit-entangled ground states and excitations, Phys. Rev. B **84**, 020403 (2011).

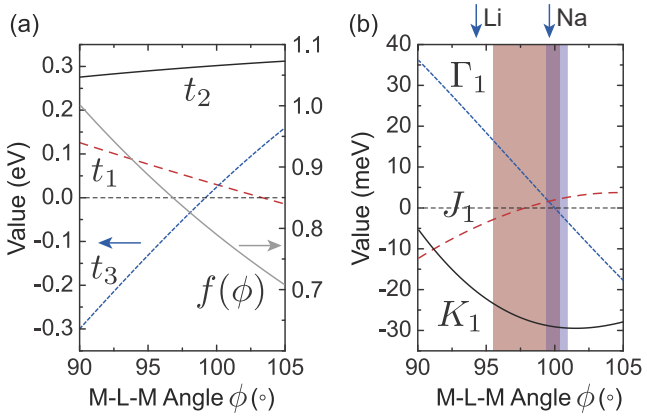

Figure 4.1: (a) Dependence for A_2IrO_3 of the hopping integrals t_1, t_2, and t_3 and of the empirical damping factor $f(\phi)$ on the M-L-M bond angle ϕ. (b) Resulting magnetic interactions J, K, and Γ obtained using the expressions in Eq. (4.6). Figure reproduced from Fig. 10 of Ref. [226].

4.2 Dimer model for the microscopic description of Kitaev materials

We present here a simple microscopic model to describe the honeycomb Kitaev materials, which has proven to be very effective in describing the RIXS measurements. We use a straightforward single-bond model in which each x, y, and z bond is treated as an independent dimer and described by the $JK\Gamma\Gamma'$ Hamiltonian. This model is justified for describing local excitations if only the nearest-neighbor Kitaev interaction is present. Consider the Kitaev model

$$H_K = \sum_{\gamma} K\, S_i^{\gamma}\, S_j^{\gamma}, \tag{4.1}$$

and a spin-conserving excitation. The application of the S_i^{γ} operator, where $\gamma = x, y, z$, would create an excitation on the γ bond, while the other bonds would remain unperturbed. The materials investigated here exhibit magnetic order, indicating the presence of additional magnetic interactions (non-Kitaev interactions and longer-range ones). However, we employ this model because of the surprising number of features in the RIXS data that it can successfully describe. Also, being simple, it gives us valuable insights into the fundamental physics of the magnetic excitations in these materials.

Na_2IrO_3 and α-Li_2IrO_3 contain IrO_6 octahedra in an edge-sharing geometry like the one described in Chap. 2.2.2 and depicted in Fig. 2.4. Iridium is found in a 4+ valence state, which leads to a t_{2g}^5 electronic configuration. With strong spin-orbit coupling, this results in a $j = 1/2$ ground state. We wrote down the most general hopping matrix in Eq. (2.27). In this case, the metal-ligand-metal angle is important and affects the values of the hopping terms, see Fig. 4.1 reproduced from Ref. [226]. Theoretical calculations show, in Na_2IrO_3 for example, that t_2 is about 250 meV while the moduli of t_1, t_3, and t_4 are about 10-30 meV [226–229]. The direct hopping is suppressed and the hopping though the ligands t_2 becomes the dominant one. The hopping describes the interaction between the orbital degrees of freedom of the two different sites. However, since spin-orbit coupling mixes the spin and orbital degrees of freedom, in the $|j, j_z\rangle$ basis, the hopping between states with different j_z becomes possible. By expanding the basis of the hopping matrix in Eq. (2.27) to include the spin and

changing the basis to the $|j, j_z\rangle$ states $\{|\frac{1}{2}, +\frac{1}{2}\rangle, |\frac{1}{2}, -\frac{1}{2}\rangle, |\frac{3}{2}, +\frac{3}{2}\rangle, |\frac{3}{2}, -\frac{3}{2}\rangle, |\frac{3}{2}, +\frac{1}{2}\rangle, |\frac{3}{2}, -\frac{1}{2}\rangle\}$ using the definitions in Eq. (2.18) we obtain

$$T^j_{edge} = \left(\begin{array}{cc|cccc} \frac{1}{3}(2t_1+t_3) & 0 & \frac{(1+i)}{\sqrt{6}}t_4 & i\sqrt{\frac{2}{3}}t_2 & \frac{\sqrt{2}}{3}(t_1-t_3) & -\frac{(1-i)}{\sqrt{2}}t_4 \\ 0 & \frac{1}{3}(2t_1+t_3) & i\sqrt{\frac{2}{3}}t_2 & \frac{(1-i)}{\sqrt{6}}t_4 & -\frac{(1+i)}{\sqrt{2}}t_4 & \frac{\sqrt{2}}{3}(t_3-t_1) \\ \hline \frac{(1-i)}{\sqrt{6}}t_4 & -i\sqrt{\frac{2}{3}}t_2 & t_1 & 0 & -\frac{(1-i)}{\sqrt{3}}t_4 & \frac{i}{\sqrt{3}}t_2 \\ -i\sqrt{\frac{2}{3}}t_2 & \frac{(1+i)}{\sqrt{6}}t_4 & 0 & t_1 & -\frac{i}{\sqrt{3}}t_2 & \frac{(1+i)}{\sqrt{3}}t_4 \\ \frac{\sqrt{2}}{3}(t_1-t_3) & -\frac{(1-i)}{\sqrt{2}}t_4 & -\frac{(1+i)}{\sqrt{3}}t_4 & \frac{i}{\sqrt{3}}t_2 & \frac{1}{3}(t_1+2t_3) & 0 \\ -\frac{(1+i)}{\sqrt{2}}t_4 & \frac{\sqrt{2}}{3}(t_3-t_1) & -\frac{i}{\sqrt{3}}t_2 & \frac{(1-i)}{\sqrt{3}}t_4 & 0 & \frac{1}{3}(t_1+2t_3) \end{array}\right) \tag{4.2}$$

which, when only t_2 is present and $t_1 = t_3 = t_4 = 0$, becomes

$$T^j_{edge} = \left(\begin{array}{cc|cccc} 0 & 0 & 0 & i\sqrt{\frac{2}{3}}t_2 & 0 & 0 \\ 0 & 0 & i\sqrt{\frac{2}{3}}t_2 & 0 & 0 & 0 \\ \hline 0 & -i\sqrt{\frac{2}{3}}t_2 & 0 & 0 & 0 & \frac{i}{\sqrt{3}}t_2 \\ -i\sqrt{\frac{2}{3}}t_2 & 0 & 0 & 0 & -\frac{i}{\sqrt{3}}t_2 & 0 \\ 0 & 0 & 0 & \frac{i}{\sqrt{3}}t_2 & 0 & 0 \\ 0 & 0 & -\frac{i}{\sqrt{3}}t_2 & 0 & 0 & 0 \end{array}\right). \tag{4.3}$$

We can see that the hopping between the $j = 1/2$ states is zero. The only non-zero hopping channels are $|1/2, \pm 1/2\rangle \rightarrow |3/2, \mp 3/2\rangle$ and $|3/2, \pm 3/2\rangle \rightarrow |3/2, \mp 1/2\rangle$. The hopping is between states with opposite j_z direction. However, the expectation value for the spin operator of both the $|1/2, +1/2\rangle$ and the $|3/2, -3/2\rangle$ wavefunctions is negative, as shown in Table (2.20). This is a consequence of the spin-orbit coupling that mixes the spin and orbital degrees of freedom. Via the hopping t_2, the $j = 1/2$ hole can jump to the neighboring site into the $j = 3/2$ quartet yielding a d^4d^6 electronic configuration. To reach this configuration, however, costs electrostatic repulsion U. But at the same time J_H acts on the d^4d^6 intermediate state lowering the energy of the configurations with the electrons with parallel spin. The hole can then jump back to its original site. This ultimately leads to a ferromagnetic Ising-type interaction $\propto \frac{t_2^2 J_H}{U^2}$ [24, 51, 255]. By restricting to the $j = 1/2$ sector, this hopping matrix gives rise to an effective magnetic interaction Hamiltonian, as derived explicitly by Winter *et al.* in Ref. [226], that can be written as

$$H^z_{JK\Gamma} = J\vec{S}_1 \cdot \vec{S}_2 + KS^z_1 S^z_2 + \Gamma(S^x_1 S^y_2 + S^y_1 S^x_2), \tag{4.4}$$

where we consider only two sites 1 and 2 of a given z bond. When the symmetry deviates from the ideal one, an additional interaction related to t_4 becomes possible

$$H^z_{\Gamma'} = \Gamma'(S^x_1 S^z_2 + S^z_1 S^x_2 + S^y_1 S^z_2 + S^z_1 S^y_2). \tag{4.5}$$

The parameters describing the magnetic interactions J, K, Γ, and Γ' are related to the

hoppings t_1, t_2, t_3, and t_4 through the expressions [226]

$$\begin{aligned} J =& \frac{4\mathbb{A}}{9}(2t_1+t_3)^2 - \frac{8\mathbb{B}}{9}[9t_4^2+2(t_1-t_3)^2] \\ K =& \frac{4\mathbb{B}}{3}[(t_1-t_3)^2+3t_4^2-3t_2^2] \\ \Gamma =& \frac{8\mathbb{B}}{3}[3t_4^2+2t_2(t_1-t_3)] \\ \Gamma' =& \frac{8\mathbb{B}}{3}[t_4(3t_2+t_3-t_1)], \end{aligned} \tag{4.6}$$

where the parameters are

$$\begin{aligned} \mathbb{A} =& -\frac{1}{3}[\frac{J_H+3(U+3\lambda)}{6J_H^2-U(U+3\lambda)+J_H(U+4\lambda)}] \\ \mathbb{B} =& \frac{4}{3}[\frac{3J_H-U-3\lambda}{6J_H-2U-3\lambda}\eta] \\ \eta =& J_H/[6J_H^2-J_H(8U+17\lambda)+(2U+3\lambda)(U+3\lambda)], \end{aligned} \tag{4.7}$$

where intraband processes, i.e., hopping of holes between $j=1/2$ states, are proportional to $\mathbb{A}$ while interband processes, i.e., hopping between $j=1/2$ and $j=3/2$ states, are proportional to $\mathbb{B}$. Note that if J_H is zero, $\mathbb{B}=0$ and the only term that remains is the isotropic Heisenberg exchange $J=\frac{4}{9}\frac{(2t_1+t_3)^2}{U}$, arising from the direct hopping between $j=1/2$ states, see Eq. (4.2). So, the Hund's coupling J_H, which acts on the virtual d^4d^6 configurations, is essential for the presence of the Kitaev interaction. We can also see that when $t_1=t_3=t_4=0$ and $t_2\neq 0$, only K is non-zero.

In the basis $(|\uparrow\uparrow\rangle, |\uparrow\downarrow\rangle, |\downarrow\uparrow\rangle, |\downarrow\downarrow\rangle)$ the Hamiltonians in Eq. (4.4) and (4.5) describing the magnetic interactions for the z bond can be written as

$$H^z_{JK\Gamma\Gamma'} = \frac{1}{4}\begin{pmatrix} J+K & (1-i)\Gamma' & (1-i)\Gamma' & -2i\Gamma \\ (1+i)\Gamma' & -J-K & 2J & (-1+i)\Gamma' \\ (1+i)\Gamma' & 2J & -J-K & (-1+i)\Gamma' \\ 2i\Gamma & (-1-i)\Gamma' & (-1-i)\Gamma' & J+K \end{pmatrix}, \tag{4.8}$$

by using the definitions of the Pauli matrices in Eq. (2.11). If only K is non-zero, the matrix is diagonal and the eigenstates split into two doublets $|0\rangle_a = |\uparrow\uparrow\rangle$ and $|0\rangle_b = |\downarrow\downarrow\rangle$ with energy $+K/4$ and $|1\rangle_{a,b} = |\uparrow\downarrow\rangle \pm |\downarrow\uparrow\rangle$ at $-K/4$. A negative K favors a ferromagnetic alignment of the spins. By introducing also J and Γ, the doublets split into

$$\begin{aligned} |0\rangle =& \ (i|\uparrow\uparrow\rangle + |\downarrow\downarrow\rangle)/\sqrt{2}; & E_0 =& (-2\Gamma+J+K)/4 \\ |1\rangle =& \ (-i|\uparrow\uparrow\rangle + |\downarrow\downarrow\rangle)/\sqrt{2}; & E_1 =& (2\Gamma+J+K)/4 \\ |2\rangle =& \ (|\downarrow\uparrow\rangle - |\uparrow\downarrow\rangle)/\sqrt{2}; & E_2 =& (-3J-K)/4 \\ |3\rangle =& \ (|\downarrow\uparrow\rangle + |\uparrow\downarrow\rangle)/\sqrt{2}; & E_3 =& (J-K)/4 \end{aligned}, \tag{4.9}$$

where the $|1\rangle_{a,b}$ levels are split by J and $|0\rangle_{a,b}$ are mixed and split by Γ. For positive Γ the ground state is $|0\rangle$ and for negative Γ it is $|1\rangle$. A positive (negative) J leads to the energy of $|2\rangle$ being lower (higher) than $|3\rangle$. By considering also the Γ' term, $|0\rangle$ and $|3\rangle$ are mixed

leading to the eigenstates

$$\begin{aligned} |0'\rangle =&(|0\rangle + \gamma\, e^{-i\pi/4}\,|3\rangle)/\sqrt{1+\gamma^2} \\ |3'\rangle =&(\gamma\,|0\rangle - e^{-i\pi/4}\,|3\rangle)/\sqrt{1+\gamma^2} \end{aligned} \tag{4.10}$$

with eigenvalues

$$\begin{aligned} E_{0'} =&(J-\Gamma-\sqrt{8\Gamma'^2+(\Gamma-K)^2})/4 \\ E_{3'} =&(J-\Gamma+\sqrt{8\Gamma'^2+(\Gamma-K)^2})/4 \end{aligned} \tag{4.11}$$

where

$$\gamma = \frac{K-\Gamma+\sqrt{8\Gamma'^2+(\Gamma-K)^2}}{\sqrt{8}\,\Gamma'}. \tag{4.12}$$

The other 2 eigenstates are not affected by Γ'.

We show in the following how these states can be distinguished based on the RIXS polarization dependence. For this we need the RIXS amplitudes calculated in Eq. (3.19) for the excitations within the $j = 1/2$ doublet, that we report and rewrite here by introducing the polarization factors

$$\begin{aligned} P_x &= i(y'z - z'y) \\ P_y &= i(z'x - x'z) \\ P_z &= i(x'y - y'x) \\ P_{\parallel} &= x'x + y'y + z'z, \end{aligned} \tag{4.13}$$

so that

$$\begin{aligned} A^z_{\uparrow\uparrow} =& -i(x'x + y'y + z'z) - (x'y - y'x)/2 = -i\,P_{\parallel} + i\,P_z/2 \\ A^z_{\downarrow\downarrow} =& -i(x'x + y'y + z'z) + (x'y - y'x)/2 = -i\,P_{\parallel} - i\,P_z/2 \\ A^z_{\uparrow\downarrow} =&(-(y'z - z'y) - i(z'x - x'z))/2 = (i\,P_x - P_y)/2 \\ A^z_{\downarrow\uparrow} =&(-(y'z - z'y) + i(z'x - x'z))/2 = (i\,P_x + P_y)/2. \end{aligned} \tag{4.14}$$

We performed the experiments with a scattering angle of $2\theta = 90°$ to suppress the elastic scattering, which means $P_{\parallel} = 0$. In case only the Kitaev interaction is present, we have the eigenstates $|0\rangle_{a,b}$ and $|1\rangle_{a,b}$ introduced previously. The calculation of the RIXS amplitude for the excitations from $|0\rangle_a$ to the excited states has already been discussed in Chap. 3.3 in Eq. (3.20), (3.21), and (3.22). The calculation here is the same but we use the definitions of the polarization factors of Eq. (4.13) and define the position of the two sites forming the z bond as $\mathbf{R}_0 = (0,0,0)$ and $\mathbf{R}_z = (0, b/3, 0)$ where b is the lattice constant, such that for the z bond the ions are connected by the vector $\Delta\mathbf{R}_z = \mathbf{R}_z - \mathbf{R}_0$. So, the scattering amplitude for the spin conserving excitation $|\uparrow\uparrow\rangle$ to $|\uparrow\uparrow\rangle$ is

$$A^z_{\uparrow\uparrow}(1 + e^{i\mathbf{q}\cdot\Delta\mathbf{R}_z}) = \frac{i}{2}P_z(1 + e^{i\mathbf{q}\cdot\Delta\mathbf{R}_z}) \tag{4.15}$$

and the intensity is proportional to

$$I^z_{\uparrow\uparrow} = P_z^2 \cos^2(kb/6). \tag{4.16}$$

The same intensity is obtained for the scattering from $|\downarrow\downarrow\rangle$ to $|\downarrow\downarrow\rangle$ but the amplitude differs for a minus sign, see Eq. (4.14). Instead, the scattering from $|\uparrow\uparrow\rangle$ to $|\downarrow\downarrow\rangle$ is not possible as explained in Chap. 3.3. The states $|2\rangle$ and $|3\rangle$ can be reached from the $|0\rangle$ state with a spin-flip excitation, the amplitude of which can be written as

$$A^z_{\uparrow\downarrow}(\pm 1 + e^{i\mathbf{q}\cdot\Delta\mathbf{R}_z}) = \frac{1}{2}(iP_x - P_y)(\pm 1 + e^{i\mathbf{q}\cdot\Delta\mathbf{R}_z}) \tag{4.17}$$

and the intensity as

$$I^z_{\uparrow\downarrow} = (P_x^2 + P_y^2)\cos^2(kb/6 + (1 \mp 1)\pi/4). \tag{4.18}$$

The modulation depends on the phase of the final state. We find a $\sin^2(kb/6)$ for the excitation to $|2\rangle = (-|\uparrow\downarrow\rangle + |\uparrow\downarrow\rangle)/\sqrt{2}$ and a $\cos^2(kb/6)$ for $|3\rangle = (|\uparrow\downarrow\rangle + |\uparrow\downarrow\rangle)/\sqrt{2}$. Instead the spin-flip scattering amplitude from the $|\downarrow\downarrow\rangle$ state is

$$A^z_{\downarrow\uparrow}(\pm 1 + e^{i\mathbf{q}\cdot\Delta\mathbf{R}_z}) = \frac{1}{2}(iP_x + P_y)(\pm 1 + e^{i\mathbf{q}\cdot\Delta\mathbf{R}_z}) \tag{4.19}$$

and the intensity is

$$I^z_{\downarrow\uparrow} = (P_x^2 + P_y^2)\cos^2(kb/6 + (1 \mp 1)\pi/4). \tag{4.20}$$

So, the RIXS spin-flip scattering intensity from $|\uparrow\uparrow\rangle$ and from $|\downarrow\downarrow\rangle$ is the same but the amplitudes differ in phase.

So far, the calculation is valid when the spin-quantization axis is defined along the z axis, i.e. for the z bond. An important assumption of our model is that for each bond we need to calculate the RIXS amplitude assuming the spin-quantization axis along the axis of the Kitaev interaction for that bond. In RIXS, the scattering intensity depends on the direction of the quantization axis as discussed in Chap. 3.3. In Na_2IrO_3 and $RuCl_3$, for example, the polarization dependence of the REXS intensity has been used to determine the direction of the magnetic moment in the ordered phase [193, 256]. As I am going to argue in the following, the fact that each bond x, y, and z has to be treated as if it has its own quantization axis is the characteristic of bond-directional excitations. To calculate the RIXS intensity for the other bonds in this case we can permute cyclically the polarization as $xyz \to zxy \to yzx$ to calculate the $z \to y \to x$ bonds and use the same expressions above for the amplitude. The other bonds are defined to be at positions $\Delta\mathbf{R}_x = (-a/2, -b/6, 0)$ and $\Delta\mathbf{R}_y = (a/2, -b/6, 0)$. So, for the y and x bonds we have the intensities

$$\begin{aligned}
I^y_{\uparrow\uparrow} &= (P_y^2)\ \cos^2(h_a a/4 - kb/12), \\
I^y_{\uparrow\downarrow} &= (P_z^2 + P_x^2)\ \cos^2(h_a a/4 - kb/12), \\
&\text{and} \\
I^x_{\uparrow\uparrow} &= (P_x^2)\ \cos^2(-h_a a/4 - kb/12), \\
I^x_{\uparrow\downarrow} &= (P_y^2 + P_z^2)\ \cos^2(-h_a a/4 - kb/12),
\end{aligned} \tag{4.21}$$

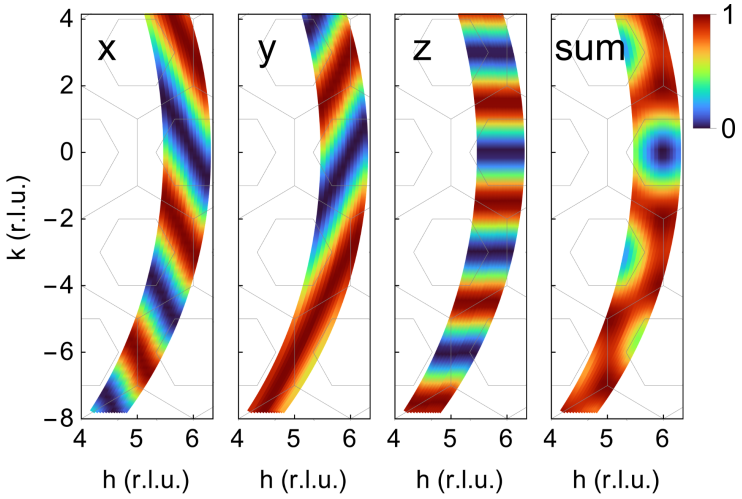

Figure 4.2: Colormaps for the $\sin^2$ modulation for the x, y, and z bond and their sum.

where $h_a = \cos(19.034°)h$ is the projection of the exchanged momentum along the crystallographic **a** axis which lies in the honeycomb plane. These expressions give rise to the modulation plot in Fig. 5 of Chap. 4.1. The polarization factors are plotted as colormaps in Fig. 5 of the Supplementary Information of Chap. 4.1. As depicted in Fig. 1 of Chap. 4.1, in the experimental geometry used in the experiments, a small incident angle θ (for negative and large k) results in the incident polarization ϵ being almost parallel to the local z axis. Consequently, the x and y components of the incident polarization are negligible. This implies that the polarization factor P_z (see Eq. (4.13)) is nearly zero for small θ but increases as θ grows, see Fig. 1(d) of Chap. 4.1. Therefore, spin-conserving scattering on the z bond is suppressed in the lower part of the map. In contrast, spin-flip scattering, which is proportional to $P_x^2 + P_y^2$, remains allowed for the z bond in the lower part of the map. To generate the maps shown in Fig. 4 of Chap. 4.1, we calculate the RIXS intensities for the three bonds (x, y, and z) independently and sum them incoherently. This approach treats each bond as a distinct and independent scattering channel. In a pure Kitaev model, where only the K term is non-zero, the interaction is purely bond-directional. For example, consider a spin-conserving process. Perturbing the z component of the spin affects only the other ion belonging to the z bond as their S^z components interact. The other bonds x and y do not feel the perturbation as they do not interact with the S^z component. The same reasoning applies to the x and y bonds for a perturbation of the S^x and S^y components of the spin. This bond-specific nature of the excitations is what defines bond-directional excitations.

Opposite to the $\cos^2$ modulation, the $\sin^2$ modulation of the x bond, for example, has a maximum at the X_y and X_z points but a minimum at the X_x points. The resulting colormaps of the $\sin^2$ modulations are shown in Fig. 4.2. Overall, the sum of the modulation of the three bonds gives rise to minima at the Γ points and maxima at the Γ' points. When $|2\rangle$ is the ground state, the magnetic excitations show a $\sin^2$ modulation with minima at the Γ points. This modulation is not observed in the data of Na_2IrO_3, see Fig. 3 and 4 of Chap. 4.1. This means that we can exclude that $|2\rangle$ is the ground state. So, for the moment we neglect the $|2\rangle$ state, but we will come back to it in the discussion of the data of α-Li_2IrO_3.

We consider now the effect of the Γ term. As said, Γ mixes and splits the $|\uparrow\uparrow\rangle$ and $|\downarrow\downarrow\rangle$

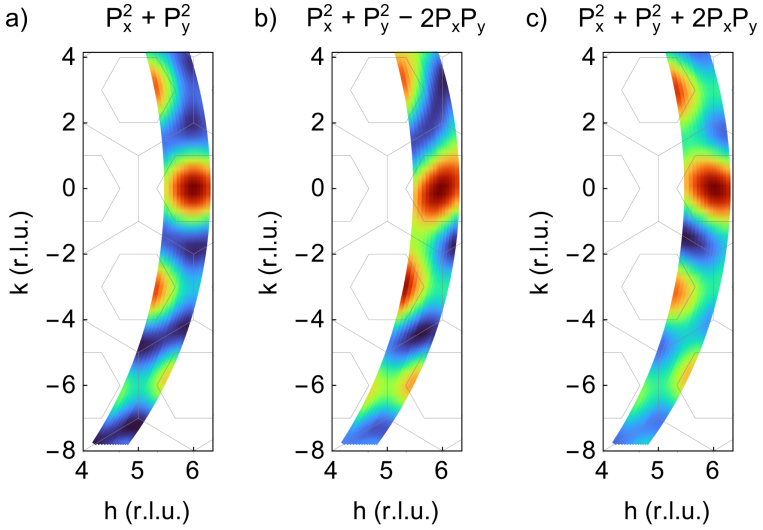

Figure 4.3: Maps for the spin-flip excitation for different ground states, $|0\rangle_a = |\uparrow\uparrow\rangle$ or $|0\rangle_b = |\downarrow\downarrow\rangle$ in a), $|0\rangle = i|\uparrow\uparrow\rangle + |\downarrow\downarrow\rangle$ in b), and $|1\rangle = -i|\uparrow\uparrow\rangle + |\downarrow\downarrow\rangle$ in c).

states giving rise to $|0\rangle = (i|\uparrow\uparrow\rangle + |\downarrow\downarrow\rangle)/\sqrt{2}$ and $|1\rangle = (-i|\uparrow\uparrow\rangle + |\downarrow\downarrow\rangle)/\sqrt{2}$ with an energy splitting of Γ. In this simple model, the ground state depends on the sign of Γ. We show in the following how the two states can be distinguished based on the RIXS polarization dependence. Consider first the excitation within those two states $\langle 1|\sum_{j=0,z} e^{i\mathbf{q}\cdot\mathbf{R}_j} M_j |0\rangle$. We have to sum in amplitude the two excitation paths $i|\uparrow\uparrow\rangle$ to $i\langle\uparrow\uparrow|$ (note the complex conjugate of $-i$) and $|\downarrow\downarrow\rangle$ to $\langle\downarrow\downarrow|$. This gives

$$(-A^z_{\uparrow\uparrow} + A^z_{\downarrow\downarrow})(1 + e^{i\mathbf{q}\cdot\Delta\mathbf{R}_z}) = (-\frac{i}{2}P_z - \frac{i}{2}P_z)(1 + e^{i\mathbf{q}\cdot\Delta\mathbf{R}_z}) \tag{4.22}$$

leading to an intensity identical to $I^z_{\uparrow\uparrow}$ and to $I^z_{\downarrow\downarrow}$

$$I^z_{01} = I^z_{10} = P_z^2 \cos^2(kb/6). \tag{4.23}$$

Instead, the spin-flip excitations depend on which is the ground state. We calculate the amplitude

$$\begin{aligned}(\langle\downarrow\uparrow| + \langle\uparrow\downarrow|) \sum_{j=0,z} e^{i\mathbf{q}\cdot\mathbf{R}_j} M_j (\pm i|\uparrow\uparrow\rangle + |\downarrow\downarrow\rangle) \\ = (\pm i A^z_{\uparrow\downarrow} + A^z_{\downarrow\uparrow})(1 + e^{i\mathbf{q}\cdot\Delta\mathbf{R}_z}) \\ = (\pm i(iP_x - P_y) + (iP_x + P_y))/2(1 + e^{i\mathbf{q}\cdot\Delta\mathbf{R}_z}) \\ = (i \mp 1)(P_x \mp P_y)/2(1 + e^{i\mathbf{q}\cdot\Delta\mathbf{R}_z}),\end{aligned} \tag{4.24}$$

which, when squared to obtain the intensity, gives rise to an interference term

$$I^z_{\substack{0\\1}3} = (P_x^2 + P_y^2 \mp 2P_xP_y)\cos^2(kb/6). \tag{4.25}$$

The sign of the interference term $2P_xP_y$ depends on the sign of Γ, such that it is negative (positive) for positive (negative) Γ. The effect of this interference term can be observed in Fig. 4.3 where we compare the maps for polarization dependence $P_x^2 + P_y^2$ in a), $P_x^2 + P_y^2 - 2P_xP_y$ in b) and $P_x^2 + P_y^2 + 2P_xP_y$ in c). Remember that this polarization dependence

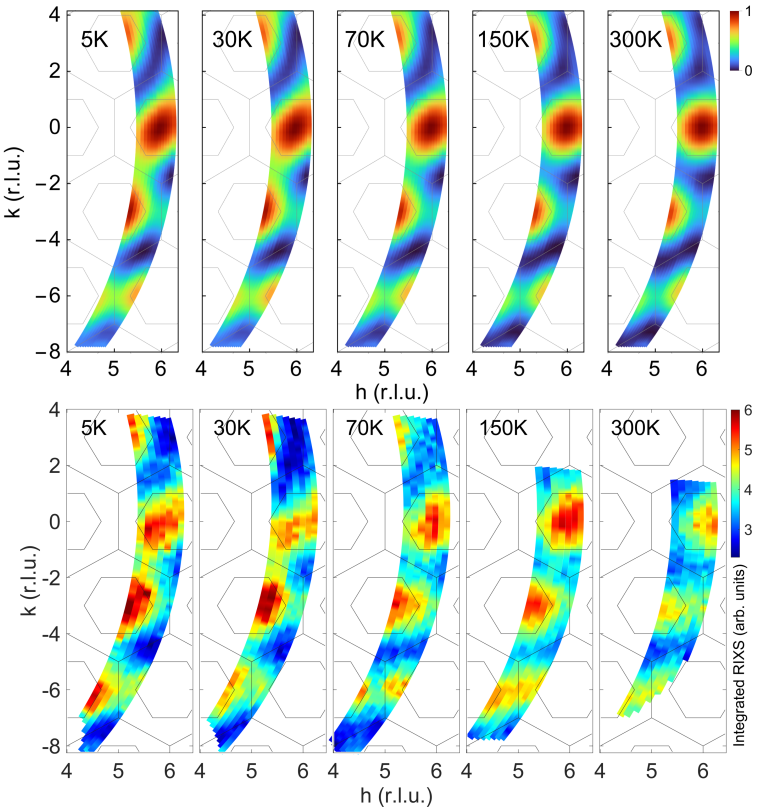

Figure 4.4: Maps for the spin-flip excitation as a function of the temperature. The top row shows the maps calculated supposing $|0\rangle$ as the ground state and an excited state $|1\rangle$ at 10 meV thermally populated according to the Bose factor. The bottom row shows the experimental data on Na_2IrO_3. As the temperature increases, the intensity at the $(5.5\ -1.5)$ point decreases, aspect that is qualitatively reproduced by the calculations.

is for the z bond and the polarization dependence of the other bonds can be obtained via permutations of x, y, and z. The maps correspond respectively to the ground states $|0\rangle_a = |\uparrow\uparrow\rangle$ and $|0\rangle_b = |\downarrow\downarrow\rangle$ in a), $|0\rangle = i\,|\uparrow\uparrow\rangle + |\downarrow\downarrow\rangle$ in b), and $|1\rangle = -i\,|\uparrow\uparrow\rangle + |\downarrow\downarrow\rangle$ in c). As described in Chap. 4.1, $P_x^2 + P_y^2$ overall describes the data very well, in particular at the X_x and X_z points where the bond directional behavior is most clear. However, the polarization dependence $P_x^2 + P_y^2 - 2P_xP_y$ that arises from a ground state $|0\rangle = +i\,|\uparrow\uparrow\rangle + |\downarrow\downarrow\rangle$, describes some aspects better than the simple spin-flip model. The difference is most clear at the X_y point at $(5.5\ -1.5)$. At this point the calculated map b) has a relatively high intensity compared to c), while a) is in between. By comparing with the data at the bottom of Fig. 3 and Fig. 4d) of Chap. 4.1, we see that the data at low temperature are best described by the map b) of Fig. 4.3.

Another aspect that the ground state $|0\rangle$ reproduces better is the temperature evolution of the intensity at $(5.5\ -1.5)$. In fact, the high temperature data at the bottom of Fig. 3 of Chap. 4.1 are reproduced better by the map a). We can describe this temperature evolution by supposing a ground state $|0\rangle$ and the thermal population of the excited state $|1\rangle$ lying 10 meV higher. This means summing in intensity the maps b) and c) of Fig. 4.3, weighting c) by the Bose factor $e^{-E_1/(k_bT)}$, where E_1 is the energy of $|1\rangle$ relative to the ground state, k_b the Boltzmann factor, and T the temperature. This sum can be seen in Fig. 4.4 where the calculations at the top are compared to the data at the bottom. By increasing the temperature, the intensity at $(5.5\ -1.5)$ decreases and tends to the intensity of the map a).

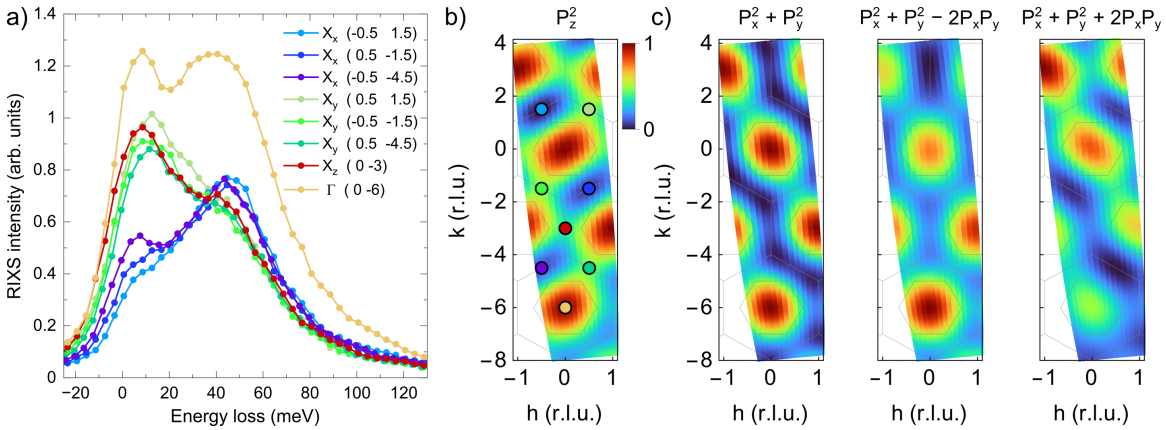

Figure 4.5: a) RIXS spectra acquired at the X_x, X_y, X_z, and Γ points on a Na_2IrO_3 sample oriented with the (010) and (001) directions in the scattering plane at 30 K. b) Calculated RIXS intensity map for spin-conserving transitions described by the polarization factor P_z^2. c) Calculated RIXS intensity maps for spin-flip transitions with different ground states $|0\rangle_a = |\uparrow\uparrow\rangle$ or $|0\rangle_b = |\downarrow\downarrow\rangle$ in (i), $|0\rangle = i\,|\uparrow\uparrow\rangle + |\downarrow\downarrow\rangle$ in (ii), and $|1\rangle = -i\,|\uparrow\uparrow\rangle + |\downarrow\downarrow\rangle$ in (iii).

This reproduces qualitatively the behavior observed in the experimental data. So, we have seen how from this simple single-bond $JK\Gamma\Gamma'$ model we would conclude that the ground state is the $|0\rangle = i\,|\uparrow\uparrow\rangle + |\downarrow\downarrow\rangle$ state.

This conclusion is further supported by the data obtained from the sample in a different orientation. The spectra in Fig. 4.5a) are acquired at the X_x, X_y, X_z, and Γ points on the same Na_2IrO_3 sample measured in Chap. 4.1 but oriented with the (010) and (001) directions in the scattering plane. Accordingly, the honeycomb planes are perpendicular to the scattering plane. Two excitations can be distinguished at 10 and 45 meV. The low energy excitation shows a high intensity at X_y and a low intensity at the X_x points. This behavior can be described by the map in Fig. 4.5b) which shows the calculation for a spin-conserving transition described for the z bond by the polarization factor P_z^2. On top of the map are marked the points at which the spectra have been acquired. The map reproduces the lower intensity at the X_x points compared to the X_y points and that the intensity is maximum at the Γ point. Remarkably, it even reproduces the relative intensity at different X_x points. The intensity is minimum at $(-0.5\ 1.5)$, then it gradually increases moving to $(0.5\ -1.5)$ and $(-0.5\ -4.5)$. The high-energy excitation instead shows a small difference in intensity between X points, but a much higher intensity at Γ. Panel c) shows different calculations that suppose different ground states like in Fig. 4.3. One can see that both $P_x^2 + P_y^2$ and $P_x^2 + P_y^2 + 2P_xP_y$ predict a strong difference between the X_x and X_y points, while $P_x^2 + P_y^2 - 2P_xP_y$ correctly predicts that the intensity at the X_x and X_y is similar. In conclusion, the data acquired in this orientation support the conclusion that the ground state in this bond model is $|0\rangle = i\,|\uparrow\uparrow\rangle + |\downarrow\downarrow\rangle$.

In the simple model presented, the sign of Γ determines the ground state, suggesting that Γ must be positive. However, we can consider Γ as an effective parameter that encapsulates the complexity of the real material, where interactions are not strictly limited to nearest-neighbors. For instance, Ref. [226] demonstrates that the parameters of the $JK\Gamma\Gamma'$ model depend on the number of sites considered in the calculations and whether crystal field splitting is included.

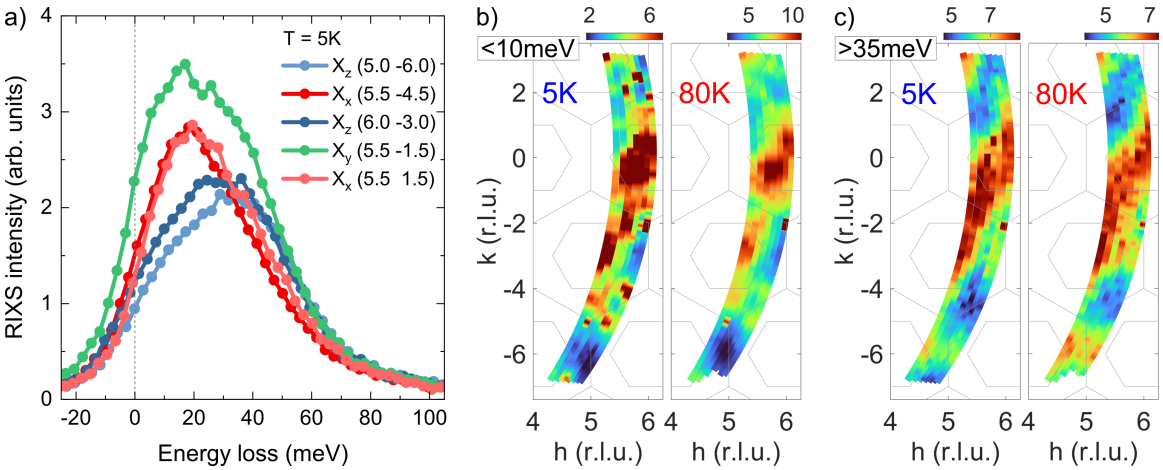

Figure 4.6: a) Spectra of α-Li_2IrO_3 acquired at 5 K at X_x, X_y, and X_z points showing the bond-directional behavior of the excitations. b) and c) maps of the RIXS integrated intensity of α-Li_2IrO_3 in a wide range of reciprocal space, measured above (80 K) and below (5 K) the Néel temperature of 15 K. The spectra are integrated below 10 meV in b) and above 35 meV in c).

It can be shown that Γ' has no effect on the polarization dependence of the RIXS intensity of the spin-flip excitation when the ground state is $|0'\rangle$. Instead the Γ' term has an effect on the spin-conserving excitation from $|0'\rangle$ to $|1\rangle$. However, it is shown in Fig. 4a) and b) of Chap. 4.1 that the magnetic Bragg peaks overlap with the magnetic excitations, making a quantitative analysis hard.

4.3 Common phenomenology of the Kitaev materials Na_2IrO_3 and α-Li_2IrO_3

In Ref. [188], Revelli *et al.* studied the similar phenomenology of the magnetic excitations in Na_2IrO_3 and α-Li_2IrO_3, showing a nearest-neighbor character of the continuum. The electronic excitations also exhibit a similar behavior in the Kitaev materials [175, 176, 188]. To observe the bond-directional character of the excitations, we measured α-Li_2IrO_3 using the same experimental setup as for Na_2IrO_3 at ID20 of the ESRF, employing the same tilted sample geometry. The different sizes of Li and Na result in different lattice constants. In order to cover the same range of hk reciprocal space at $2\theta = 90°$, the sample tilt angle required for α-Li_2IrO_3 was approximately 2° larger than for Na_2IrO_3. We thus measured the RIXS intensity of the magnetic excitations over a large range of reciprocal space. As with Na_2IrO_3, the spectra of α-Li_2IrO_3 at the X points, shown in Fig. 4.6(a), show most clearly the bond-directional behavior. In α-Li_2IrO_3, we also identify two distinct features in the magnetic excitations exhibiting different behavior. However, the energy scale is smaller than in Na_2IrO_3, with a low-energy feature peaking at about 15 meV and a high-energy feature at around 35 meV. With a resolution of 25 meV, the two features do not show as clearly separated peaks as in Na_2IrO_3. Nevertheless, they can be distinguished based on their different RIXS polarization dependencies. Figures 4.6(b) and (c) show the integrated RIXS intensity of the regions below 10 meV and above 35 meV, respectively, measured both below and above the Néel temperature of 15 K [257], at 5 K and 80 K. Comparing the maps of Na_2IrO_3 and α-Li_2IrO_3, the main difference in the low-energy map at low temperature is

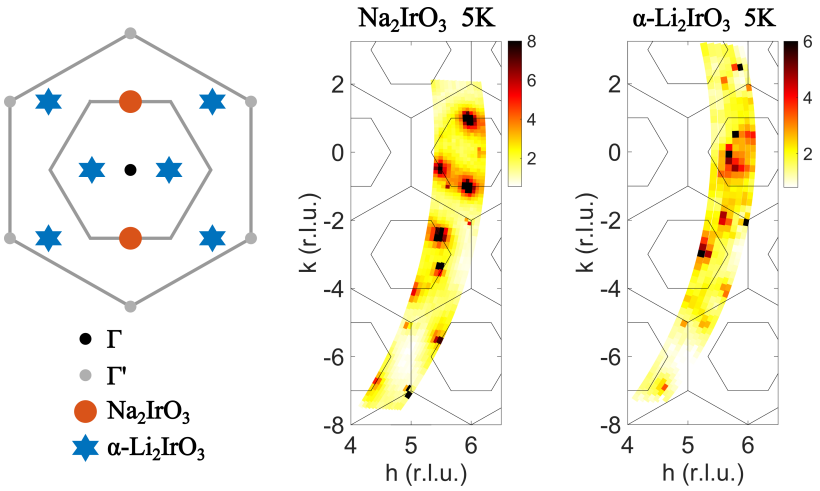

Figure 4.7: Comparison of the RIXS intensity maps of the low energy loss part of Na_2IrO_3 and α-Li_2IrO_3 at 5 K. The position of the magnetic Bragg peaks inside the extended Brillouin zone of Na_2IrO_3 and α-Li_2IrO_3 are shown in the inset. The presence of different domains rotated by 120° gives rise to additional Bragg peaks.

that different magnetic Bragg peaks arise from their different magnetic ordering patterns. In α-Li_2IrO_3, with a magnetic propagation vector of (0.32 0 0) [51,257], magnetic Bragg peaks appear around the Γ and Γ' points, as shown in the sketch in Fig. 4.7. Instead, Na_2IrO_3 has a magnetic propagation vector (0 1 0.5) [167,258] which results in magnetic Bragg peaks at the M points as in Fig. 4.7. Due to the presence of twin domains rotated by 120°, three domains are observed simultaneously, resulting in six magnetic Bragg peaks around each Γ and Γ' point. This can be observed in the maps of the low-energy part of the magnetic excitations in Fig. 4.7. Instead, in the map in Fig. 4.6(b) acquired at 80 K, above the Néel temperature, the intensity of the magnetic Bragg peaks becomes broader in q space. This broadening reveals the underlying behavior of the low-energy excitations more clearly. The behavior is particularly evident at the X points, as shown by the spectra. Around the X_z points, the low-energy intensity is low, while at the X_x points, the intensity is higher. As for Na_2IrO_3, the behavior of the low-energy excitation can be reproduced by the spin-conserving excitation, as shown by the calculated map in Fig. 4.8(a).

In the maps of the high-energy part of the magnetic excitations, the most notable difference between α-Li_2IrO_3 and Na_2IrO_3 is the higher intensity at the $X_y = (5.5\ {-1.5})$ point in α-Li_2IrO_3, compare Fig. 4.6(c) with the bottom of Fig. 4.4. The high intensity at $X_y = (5.5\ {-1.5})$ can be explained by the overlap of the excitation from the ground state $|0\rangle = i\,|{\uparrow\uparrow}\rangle + |{\downarrow\downarrow}\rangle$ to $|2\rangle = |{\downarrow\uparrow}\rangle - |{\uparrow\downarrow}\rangle$ and to $|3\rangle = |{\downarrow\uparrow}\rangle + |{\uparrow\downarrow}\rangle$. The calculated maps are shown in Fig 4.8(a), (b), and (c) for the excitations from $|0\rangle$ to $|1\rangle$, $|2\rangle$, and $|3\rangle$ respectively. As explained, these correspond to a spin-conserving excitation, a spin-flip excitation with a change of phase that gives rise to a $\sin^2$ modulation, and a spin-flip excitation with the same phase. Different from the case of Na_2IrO_3, in α-Li_2IrO_3 the map (c) cannot fully describe the experimental data of the high energy part of the magnetic excitations. However, it still correctly reproduces the complementary and alternating intensity at the X_x and X_z points shown by the spectra in Fig. 4.6(a). Figure 4.8(d), (e), (f), and (g) depict the maps obtained by summing to the map (c) the map (b) weighted by a factor 0.2, 0.4, 0.6, and 0.8 respectively. The excitation to $|2\rangle$ shows a maximum at $X_y = (5.5\ {-1.5})$, and thus as the

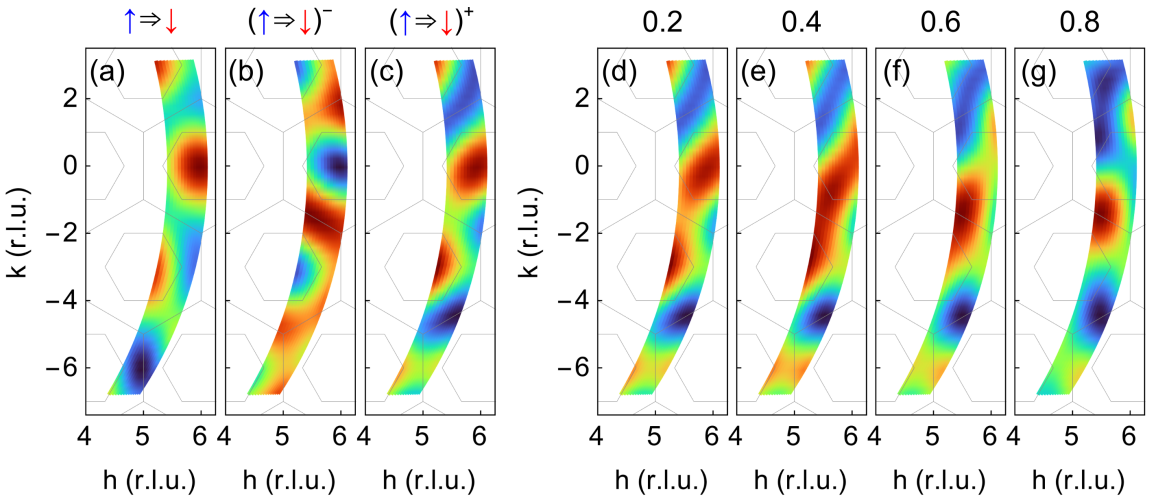

Figure 4.8: (a), (b), (c) Calculated RIXS intensity maps for α-Li_2IrO_3 from the $|0\rangle$ ground state to the $|1\rangle$, $|2\rangle$, and $|3\rangle$ states, respectively. These excitations correspond to a spin-conserving transition (a) and two spin-flip transitions (b) and (c), with (b) showing a $\sin^2$ modulation. (d), (e), (f), (g) Sum of the intensity of map (c) with increasing contributions from map (b).

admixture increases the intensity at the X_y increases, such that a factor of 0.4 reproduces the experimental map, compare Fig. 4.6(c) and Fig. 4.8(e).

Through the study of the RIXS modulation and polarization dependence we were able to determine that the magnetic excitations in α-Li_2IrO_3 hide three different bond-directional excitations. Even though the resolution was not sufficient to resolve the three excitations, the polarization dependence of the RIXS intensity allows us to distinguish them. A very simple single bond dimer model proved to be sufficient to describe the RIXS intensity of the magnetic excitations in Na_2IrO_3 and α-Li_2IrO_3. The model is based on the $JK\Gamma\Gamma'$ Hamiltonian and gives us insight into what kind of excitations are present. We identify in Na_2IrO_3 and α-Li_2IrO_3 a low-energy (peaking at approximately 10 meV and 15 meV) spin-conserving excitation and a high-energy (peaking at approximately 45 meV and 35 meV) spin-flip excitation. In Na_2IrO_3 the high-energy excitation can be described by a spin-flip excitation from $|0\rangle$ to $|3\rangle$. Instead in α-Li_2IrO_3 the high-energy excitation can be described by the overlap of the spin-flip excitations from $|0\rangle$ to $|2\rangle$ and $|3\rangle$. In both materials the ground state is best described by $|0\rangle = i|\uparrow\uparrow\rangle + |\downarrow\downarrow\rangle$, obtained by a positive Γ parameter. The presence of the excitation to $|2\rangle$ could not be observed in Na_2IrO_3. This observation is missing a clear explanation but we can make some speculations. The parameters of the $JK\Gamma\Gamma'$ Hamiltonian are expected to be different in Na_2IrO_3 and α-Li_2IrO_3. As shown in Fig. 4.1, the parameters of the $JK\Gamma\Gamma'$ Hamiltonian depend, for example, on the M-L-M angle. The angles are known to be different in Na_2IrO_3 and α-Li_2IrO_3 due to the different sizes of the ions. Experimentally, the magnetic order in the two materials is different and the energy of the magnetic excitations observed is different, which also points toward different values of the parameters. We can speculate that the observation of the excitation to the state $|2\rangle$ in α-Li_2IrO_3 and not in Na_2IrO_3 is related to the different sign of J in the two materials. If J is negative, see Eq. (4.9), the energy of $|2\rangle$ is higher than that of $|3\rangle$. This would place the excitation to $|2\rangle$ at higher energy, where it may become observable. Instead, if J is positive, the energy of $|2\rangle$ is lower than that of $|3\rangle$, and the excitation to $|2\rangle$ would

be in between the other two excitations, making it more difficult to detect. This would be in agreement with the results of Ref. [226], where the sign of J is positive for Na_2IrO_3 and negative for α-Li_2IrO_3, see Fig. 4.1. Other estimates for the parameters are reported in the literature from the analysis of the magnetic excitations in terms of magnon dispersion, such as in α-Li_2IrO_3 in Ref. [191] and in Na_2IrO_3 in Ref. [190]. Both suggest positive Γ and J for both compounds. However, our results show that the magnetic excitations, far from the magnetic Bragg peaks, exhibit a very similar nearest-neighbor local behavior both above and below the magnetic phase transition. This result suggests that these excitations are not related to the magnetic order. An analysis in terms of dispersion might therefore not be reliable. For example, the spectra acquired at equivalent X points shows that the main effect as a function of the exchanged momentum is a change in the intensity of the excitations, while the energy of the excitations remains approximately constant.

Chapter 5

Trimers in $Ba_4NbIr_3O_{12}$

5.1 Quasimolecular electronic structure of the trimer iridate $Ba_4NbIr_3O_{12}$

The trimer compound $Ba_4NbIr_3O_{12}$ has attracted attention due to claims of behavior compatible with a spin-liquid ground state [106–108]. However, *ab-initio* calculations have instead proposed a quasimolecular $J_{\text{trimer}} = 0$ state [259]. In this chapter, we present the results of RIXS measurements at the Ir L_3 edge on the trimer compound $Ba_4NbIr_3O_{12}$. These results are published in Pub. [4], which we reproduce in the following. The observation of the modulation of the RIXS intensity demonstrates the quasimolecular character of the wavefunctions. The calculations show that the $J_{\text{trimer}} = 0$ ground state is in agreement with the experimental data. This RIXS study is the first experimental determination of the quasimolecular electronic structure of a quasimolecular trimer cluster compound. In the theoretical analysis, we discuss the general features of the trimer quasimolecular wavefunctions and the resulting RIXS modulation. In particular, the different symmetries of the trimer eigenstates result in a characteristic RIXS modulation pattern observable in the experimental data. This will serve as a solid basis for future studies of the electronic structure of trimer quasimolecular wavefunctions.

Contribution

M. Magnaterra and M. Grüninger conceived the experiment. M. Magnaterra, P. Warzanowski, L. Pätzold, E. Bergamasco, Ch. J. Sahle, B. Detlefs, K. Ruotsalainen, M. Moretti Sala, G. Monaco, and M. Grüninger carried out the experiment at beamline ID20 of the ESRF. M. Magnaterra analyzed the data. H. Schilling and P. Becker synthesized and characterized the single crystal "A" used in the experiments. G. S. Thakur, Q. Faure, M. Songvilay, and C. Felser provided the single crystal "B" used in the experiments. A. Sandberg and M. Hermanns performed the theoretical analysis and calculations with support from M. Magnaterra, M. Grüninger, P. H. M. van Loosdrecht, and J. van den Brink. M. Magnaterra, A. Sandberg, M. Hermanns, and M. Grüninger wrote the manuscript with input from all authors.

Editors' Suggestion

Quasimolecular electronic structure of the trimer iridate $Ba_4NbIr_3O_{12}$

M. Magnaterra [1], A. Sandberg [2], H. Schilling [3], P. Warzanowski [1], L. Pätzold [1], E. Bergamasco [1], Ch. J. Sahle [4], B. Detlefs [4], K. Ruotsalainen [4], M. Moretti Sala [5], G. Monaco [6], P. Becker [3], Q. Faure [7], G. S. Thakur [8,9], M. Songvilay [10], C. Felser [9], P. H. M. van Loosdrecht [1], J. van den Brink [11,12], M. Hermanns [2,13] and M. Grüninger [1]

[1] *Institute of Physics II, University of Cologne, 50937 Cologne, Germany*

[2] *Department of Physics, Stockholm University, AlbaNova University Center, SE-106 91 Stockholm, Sweden*

[3] *Sect. Crystallography, Institute of Geology and Mineralogy, University of Cologne, 50674 Cologne, Germany*

[4] *European Synchrotron Radiation Facility, BP 220, F-38043 Grenoble Cedex, France*

[5] *Dipartimento di Fisica, Politecnico di Milano, I-20133 Milano, Italy*

[6] *Dipartimento di Fisica e Astronomia "Galileo Galilei", Università di Padova, I-35131 Padova, Italy*

[7] *Laboratoire Léon Brillouin, CEA, CNRS, Université Paris-Saclay, CEA-Saclay, 91191 Gif-sur-Yvette, France*

[8] *Department of Chemical Sciences, Indian Institute of Science Education and Research, Berhampur, Odisha 760003, India*

[9] *Max Planck Institute for Chemical Physics of Solids, 01187 Dresden, Germany*

[10] *Université Grenoble Alpes, CNRS, Institut Néel, 38042 Grenoble, France*

[11] *Institute for Theoretical Solid State Physics, IFW Dresden, 01069 Dresden, Germany*

[12] *Institute for Theoretical Physics and Würzburg-Dresden Cluster of Excellence ct.qmat, Technische Universität Dresden, 01069 Dresden, Germany*

[13] *Stockholm University, SE-106 91 Stockholm, Sweden*

(Received 31 October 2024; revised 21 January 2025; accepted 24 January 2025; published 10 February 2025)

The insulating mixed-valent $Ir^{+3.66}$ compound $Ba_4NbIr_3O_{12}$ hosts two holes per Ir_3O_{12} trimer unit. We address the electronic structure via resonant inelastic x-ray scattering (RIXS) at the Ir L_3 edge and exact diagonalization. The holes occupy quasimolecular orbitals that are delocalized over a trimer. This gives rise to a rich intra-t_{2g} excitation spectrum that extends from 0.5 eV to energies larger than 2 eV. Furthermore, it yields a strong modulation of the RIXS intensity as a function of the transferred momentum $\mathbf{q}$. A clear fingerprint of the quasimolecular trimer character is the observation of two modulation periods, $2\pi/d$ and $2\pi/2d$, where d and $2d$ denote the intratrimer Ir-Ir distances. We discuss how the specific modulation reflects the character of the wave function of an excited state. Our quantitative analysis shows that spin-orbit coupling λ of about 0.4 eV is decisive for the character of the electronic states, despite a large hopping $t_{a_{1g}}$ of about 0.8 eV. The ground state of a single trimer is described very well by both holes occupying the bonding $j = \frac{1}{2}$ orbital, forming a vanishing quasimolecular moment with $J = 0$.

DOI: 10.1103/PhysRevB.111.085122

I. INTRODUCTION

In the pursuit of discovering novel magnetic phases, particularly quantum spin liquids, a promising approach is the engineering of unusual interactions between neighboring magnetic moments. An intriguing way to achieve this is through first engineering the character of the local moments themselves. This is possible in cluster Mott insulators, a novel class of transition-metal compounds where electronic degrees of freedom are delocalized only over individual, small clusters such as dimers, trimers, or tetramers [1–12]. The characteristics of the emerging quasimolecular magnetic moments are determined by a complex interplay of spin and orbital degrees of freedom, Coulomb interactions, and intracluster hopping that depends on the cluster shape. For instance, the magnetic moments were predicted to be effectively temperature dependent and in particular anisotropic in iridate dimers [13]. In general, the unconventional quasimolecular character of the moments is expected to enable magnetic exchange between neighboring clusters that significantly deviates from the conventional Heisenberg exchange, notably permitting bond-direction-dependent exchange interactions.

In a similar fashion, different types of exchange interactions have been realized in, e.g., $5d^5$ iridates with t_{2g}^5 configuration, where spin-orbit entangled $j = \frac{1}{2}$ moments emerge due to strong spin-orbit coupling. In fact, exchange couplings depend strongly on the bonding geometry of, e.g., IrO_6 octahedra. They vary from isotropic Heisenberg exchange for 180° bonds in corner-sharing configuration to Ising coupling on 90° bonds in edge-sharing geometry [14]. The latter allows for the realization of bond-directional Kitaev exchange on tricoordinated lattices [14,15]. Bond-directional magnetic excitations are a hallmark of bond-directional exchange and have been observed in Na_2IrO_3 in resonant inelastic x-ray scattering (RIXS) [16].

Face-sharing IrO_6 octahedra, however, feature a very short Ir-Ir distance of roughly 2.5–2.7 Å [17–19]. This yields much larger hopping t, reaching values of the order of 1 eV [7,20]. Accordingly, the existence of exchange-coupled local moments is questionable [7,13,21]. Metallic behavior but also a metal-insulator transition have been observed in, e.g., different polytypes of $BaIrO_3$ with face-sharing octahedra [22–25]. Insulators are found in the $Ba_3MIr_2O_9$ family hosting Ir_2O_9

dimers. The Ir valence and hence the number of holes per dimer depends on the choice of the M ions. RIXS data for $M = Ce^{4+}$, Ti^{4+}, and In^{3+} [7–9] demonstrate that the holes occupy quasimolecular orbitals and are fully delocalized over a given dimer.

Spin-orbit coupling has been found to be decisive for the character of these quasimolecular dimer orbitals [7,8,13]. For example, with three holes per dimer in face-sharing geometry, the magnetic moment changes from $J_{\mathrm{dim}} = \frac{1}{2}$ to $\frac{3}{2}$ with increasing intradimer hopping [13], and the spin-liquid candidate $Ba_3InIr_2O_9$ [26] has been found to be close to this transition [8]. Another example for the versatile character of the novel quasimolecular moments in cluster Mott insulators is found in the lacunar spinel $GaTa_4Se_8$ [10,27,28]. RIXS data show that the Ta_4 tetrahedra host quasimolecular $J_{\mathrm{tet}} = \frac{3}{2}$ moments for which the actual wave function is governed by spin-orbit coupling and the competition of different intratetrahedral hopping channels [10].

RIXS is the ideal tool to unravel the quasimolecular electronic structure of cluster Mott insulators [7–10,28–31]. In the fast-collision approximation [32–35], the RIXS intensity $I(\mathbf{q})$ of an electronic intracluster excitation at energy $\hbar\omega_0$ reflects the dynamical structure factor $S(\mathbf{q}, \omega_0)$, where $\mathbf{q}$ denotes the transferred momentum. The modulation of $I(\mathbf{q})$ is equivalent to an interference pattern that arises due to coherent scattering on all sites of a cluster. Such RIXS interferometry allows us to probe the quasimolecular wave function and to uncover the symmetry and character of the electronic states, as successfully demonstrated for dimers and tetrahedra [7–10]. A corresponding modulation of the RIXS intensity can also be studied for, e.g., homonuclear diatomic molecules [29,30,36,37], bilayer compounds [38], or the Kitaev magnets Na_2IrO_3 and α-Li_2IrO_3 with nearest-neighbor spin-spin correlations [16,39]. Furthermore, it has been discussed in the context of witnessing entanglement, using iridate dimers as a model system [40]. For the interpretation of the RIXS data, it is useful to remember that trimers built from face-sharing IrO_6 octahedra exhibit inversion symmetry, in contrast to, e.g., face-sharing dimers or tetrahedra. The middle site M_2 acts as the center of inversion [see Fig. 1(b)]. All electronic states of a trimer can be classified by their parity. Upon inversion, even states are invariant while odd states acquire an overall minus sign. The inversion eigenvalue plays a pivotal role for many observables, also for the RIXS intensity $I(\mathbf{q})$. We show that $I(\mathbf{q})$ of a trimer behaves qualitatively different for transitions that flip the inversion eigenvalue compared to those that do not. As such, RIXS interferometry gives an unambiguous fingerprint of the symmetry of the eigenstates.

Trimer compounds such as $Ba_4NbM_3O_{12}$ have been reported for $3d$, $4d$, and $5d$ transition-metal ions $M = $ Mn, Ru, Rh, and Ir [41–47], and a gradual transition from localized electrons for $M = $ Mn to quasimolecular orbitals for $M = $ Ir has been discussed based on *ab initio* calculations [21]. For instance $Ba_4NbIr_3O_{12}$ adopts a hexagonal-perovskite structure with well-separated Ir_3O_{12} trimers that form triangular layers [see Fig. 1(a)]. Particularly rich physics ranging from a quantum spin liquid to heavy-fermion strange metal behavior has been claimed for $Ba_4Nb_{1-x}Ru_{3+x}O_{12}$ [47]. Iridate trimers have been reported with different crystal structures

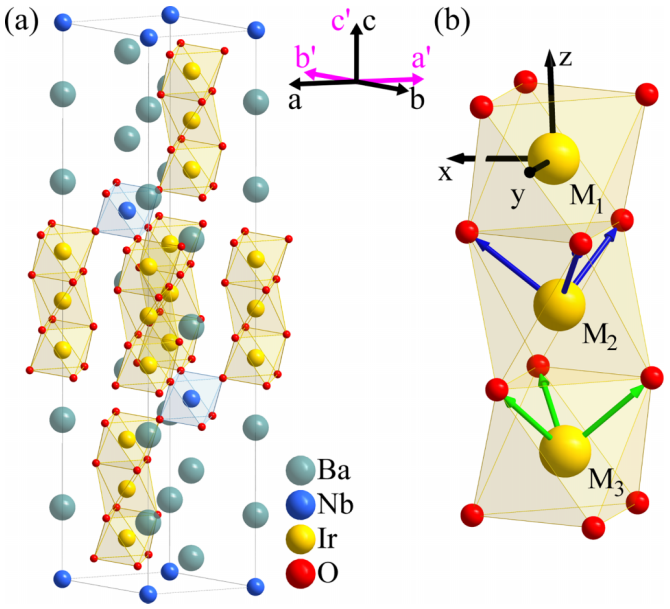

FIG. 1. (a) Sketch of the trigonal crystal structure ($R\bar{3}m$) of $Ba_4NbIr_3O_{12}$ with face-sharing IrO_6 octahedra forming well-separated Ir_3O_{12} trimer units. The trimer axis is parallel to c. The two coordinate frames (black, pink) refer to obverse and reverse twinning. (b) An Ir_3O_{12} trimer with the three Ir sites M_i. The middle site M_2 is at the center of inversion and is crystallographically distinct from the outer sites M_1 and M_3. Black: Global coordinate system. Green and blue: Local coordinate systems for the outer and inner octahedra, respectively, with $(1,1,1)_{\mathrm{loc}}$ being parallel to the global c axis.

and different hole counts [18,19,42–45,48–55]. Shimoda *et al.* synthesized polycrystalline $Ba_4LnIr_3O_{12}$ with different Ln^{3+} and Ln^{4+} ions, giving rise to four and three t_{2g} holes per trimer, respectively [18]. Based on measurements of the magnetic susceptibility χ, the paramagnetic behavior of the Ln^{3+} compounds with four holes per trimer entirely results from the Ln^{3+} ions while the Ir trimers are found to be nonmagnetic [18]. In contrast, the three-hole trimers ($Ln = Ce^{4+}$, Pr^{4+}, Tb^{4+}) order antiferromagnetically at low temperature. An interesting variant is realized in $Ba_4BiIr_3O_{12}$ for which the highly unusual Bi^{4+} valence has been discussed in connection with a magnetoelastic effect [48,49]. Three-hole trimers are also realized in $Ba_5CuIr_3O_{12}$ [50–52] and $Ba_4Ir_3O_{10}$ [53–55]. In the latter, adjacent trimers are connected in corner-sharing geometry suggesting large exchange couplings, and a quantum spin liquid state persisting down to 0.2 K with a very large frustration parameter has been claimed [53]. RIXS data of $Ba_4Ir_3O_{10}$ have been interpreted in terms of a spinon continuum extending up to 0.2 eV [54]. However, also the occurrence of antiferromagnetic order below $T_N = 25$ K has been reported [55], while 2% Sr substitution yields $T_N = 130$ K [53]. Remarkably, very different points of view have been reported for these three-hole trimers. The physics of $Ba_4Ir_3O_{10}$ has been discussed in terms of exchange-coupled $j = \frac{1}{2}$ moments [53,54], while a molecular-orbital picture with a covalency-driven collapse of spin-orbit coupling has been claimed for $Ba_5CuIr_3O_{12}$ [51].

In $Ba_4NbIr_3O_{12}$ with nonmagnetic $4d^0$ Nb^{5+} ions, the average formal Ir valence amounts to 3.66 for the stoichiometric

compound, which corresponds to two t_{2g} holes per Ir trimer. Also, this compound has been discussed as a spin-liquid candidate [43–45]. Here, we address the quasimolecular structure via RIXS and exact diagonalization. We show how the **q**-dependent RIXS intensity entails the specific quasimolecular trimer character of a given excited state. Our central result is that the electronic structure of $Ba_4NbIr_3O_{12}$ qualitatively can be understood in a picture of quasimolecular trimer orbitals built from spin-orbit-entangled j states, in close analogy to the case of face-sharing dimers in $Ba_3MIr_2O_9$ [7–9]. For a single two-hole trimer, we find a nonmagnetic ground state for any realistic set of parameters.

The paper is organized as follows. Section II addresses experimental aspects such as crystal growth, characterization, and RIXS measurements. In Sec. III we present our RIXS data, while Sec. IV is devoted to the theoretical analysis of RIXS of two-hole trimers. We introduce the Hamiltonian and, for an intuitive picture, discuss the single-particle states. Furthermore, we analyze the generic properties of the RIXS response, highlighting the prominent role of inversion symmetry. Finally, we compare theory and experiment in Sec. V. Beyond the excitation spectrum, we address the $J = 0$ ground state in Sec. V A and the emergence of a small contribution to the magnetic susceptibility in an applied magnetic field in Sec. V C.

II. EXPERIMENTAL ASPECTS

We collected RIXS data on two different single crystals of $Ba_4Nb_{1-x}Ir_{3+x}O_{12}$. Sample A has been grown in Cologne, sample B in Dresden. The RIXS data measured on the two crystals are in excellent agreement with each other (see below). The growth of the Dresden crystal B has been described in Ref. [44]. For sample A, we first prepared polycrystalline $Ba_4NbIr_3O_{12}$ using conventional solid-state reaction. A stoichiometric mixture of $BaCO_3$, Nb_2O_5, and IrO_2 was ground and heated in an alumina crucible at 1100 °C for 48 h, similar to the method given in Ref. [43]. The resulting $Ba_4NbIr_3O_{12}$ was identified as being single phase by powder x-ray diffraction. Then, single crystals of $Ba_4Nb_{1-x}Ir_{3+x}O_{12}$ were grown using a flux method inspired by Ref. [44]. The prereacted polycrystalline compound was mixed with $BaCl_2 \cdot 2H_2O$ in a 1:30 molar ratio, heated in an alumina crucible to 1100 °C, and slowly cooled down to 950 °C at a rate of 1 °C/h. Remains of $BaCl_2$ were dissolved with distilled water.

The isostructural ruthenate $Ba_4Nb_{1-x}Ru_{3+x}O_{12}$ has been reported to change from metallic to insulating behavior as a function of the Nb concentration [47]. For the iridate $Ba_4Nb_{1-x}Ir_{3+x}O_{12}$ grown in Dresden, the resistivity reveals insulating behavior with an activation energy of 43 meV [44]. We thoroughly addressed the Nb-Ir ratio of our samples. For crystals from Dresden, energy-dispersive x-ray spectroscopy (EDX) shows a Nb-Ir ratio 1/3.3, i.e., $x \approx 0.1$, while the analysis of single-crystal x-ray diffraction points to $x \approx 0.2$ with both Nb^{5+} and excess Ir^{5+} ions occupying the $3a$ site [44] that connects adjacent trimers and shows 100 % Nb occupation in ideal $Ba_4NbIr_3O_{12}$ [see Fig. 1(a)]. The $5d^4$ Ir^{5+} ions are expected to yield nonmagnetic $J = 0$ moments [56–61]. For crystals grown in Cologne, the chemical composition and homogeneity have been determined using an electron beam microprobe (see Appendix A for details). The average Nb-Ir ratio is approximately 1/3.4, close to the value found on the Dresden crystals. In some crystals, the image of the backscattered electron detector (BSE) of the microprobe revealed well-separated Ir inclusions and intergrowths with $BaIrO_3$. We selected several crystals with mostly no inclusions or intergrowth and measured the Nb-Ir ratio via EDX. Sample A, studied in RIXS, shows a Nb-Ir ratio 0.97/3.06 that is very close to the nominal value $\frac{1}{3}$ of the stoichiometric compound $Ba_4NbIr_3O_{12}$. As discussed below, our RIXS results on samples A and B are fully equivalent and do not show any clear contribution of nonmagnetic $5d^4$ Ir^{5+} $J = 0$ ions on Nb sites that may arise in the case of Nb-Ir site disorder or off-stoichiometry.

At 300 K, $Ba_4Nb_{1-x}Ir_{3+x}O_{12}$ exhibits a trigonal crystal structure with space group $R\bar{3}m$ and lattice constants $a = 5.7733(6)$ Å and $c = 28.720(5)$ Å (sample A). The intratrimer Ir-Ir distance is $d = 2.54$ Å. The Ir_3O_{12} trimers are oriented parallel to c [see Fig. 1(a)]. Sample A (B) shows an area of about 0.6 mm × 0.3 mm (2 mm × 1 mm) perpendicular to the c axis and roughly 0.1 mm (0.3 mm) along c. On both samples, RIXS data were collected on the (001) surface with the (110) direction in the horizontal scattering plane. The quasimolecular trimer character gives rise to a periodic modulation of the RIXS intensity as a function of the transferred momentum **q**. The period depends on the Ir-Ir distance d. Since d is incommensurate with the lattice constant c, we use absolute units for **q** while still using reciprocal lattice units for $(h\ k\ l)$.

We performed Ir L_3-edge RIXS measurements at beam line ID20 at the ESRF at 300 K [62]. The synchrotron was operated with a ring current of about 65 mA (16-bunch mode), which is roughly $\frac{1}{3}$ of the maximum current. The beam line offers two equivalent spectrometers in Johann geometry with a Rowland circle diameter of 1 or 2 m [62]. With 1 m, the overall intensity of inelastically scattered photons is roughly a factor 4 larger compared to the 2 m version that offers a better energy resolution. To compensate for the reduced ring current that leads to a reduced photon flux, we used the 1 m Rowland circle spectrometer employing a diced Si(844) Johann crystal (1 m radius of curvature) with an aperture of 80 mm. The resonance behavior has been studied by collecting low-energy-resolution RIXS spectra ($\Delta E = 0.3$ eV) with the incident energy in the range from 11.211 to 11.222 keV using a Si(311) channel-cut monochromator (see Fig. 2). The advantage of the low-resolution setup is the high signal-to-noise ratio. For all other measurements, we employed a Si(844) backscattering monochromator and set the incident energy to 11.215 keV to resonantly maximize the RIXS intensity of intra-t_{2g} excitations. For these data, the overall energy resolution was $\Delta E = 63$ meV as estimated by the full width at half-maximum of elastic scattering from a piece of adhesive tape. The momentum resolution at, e.g., $(h\ k\ l) = (0.7\ 0\ 28.35)$ was $\delta_{hkl} = (0.18\ 0.18\ 0.8)$. The incident photons were π polarized in the horizontal scattering plane. All RIXS data have been corrected for self-absorption based on the scattering geometry [63]. Error bars for the integrated RIXS intensity denote the standard deviation and have been determined from the Poisson noise of the detector image.

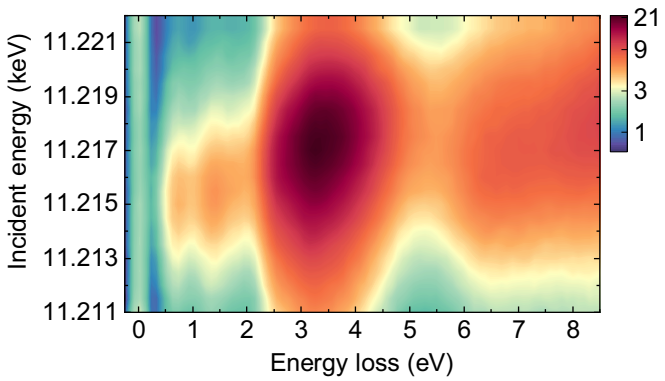

FIG. 2. Resonance map of the RIXS intensity of $Ba_4NbIr_3O_{12}$ (sample A) measured at 300 K with the low-resolution setup ($\Delta E = 0.3$ eV) at (0.7 0 36.7). The scattering angle 2θ was close to 90°. Excitations to e_g^σ state are peaking at an energy loss of about 3.5 eV for an incident energy $E_{\rm in} = 11.218$ keV. The intra-t_{2g} excitations at lower energy loss are resonantly enhanced around $E_{\rm in} = 11.215$ keV. The color is interpolated between adjacent data points. The color scale is logarithmic to highlight the intra-t_{2g} excitations.

III. RIXS RESULTS

The resonance behavior of the RIXS intensity is given in Fig. 2, which shows low-resolution RIXS spectra at (h k l) = (0.7 0 36.7) for incident energies in the range from 11.211 to 11.222 keV. The dominant RIXS feature is observed at an energy loss of about 3.5 eV. It peaks for an incident energy $E_{{\rm in},e_g} \approx 11.218$ keV and corresponds to excitations to e_g^σ states. The excitation energy of about 3.5 eV provides an estimate of the cubic crystal-field splitting 10 Dq. The RIXS peaks at still larger energy loss can be attributed to charge-transfer excitations. We focus on the intra-t_{2g} excitations with an energy loss below 2 eV. Their intensity is resonantly enhanced for $E_{{\rm in},t_{2g}} = 11.215$ keV. The two different resonance energies $E_{{\rm in},e_g}$ and $E_{{\rm in},t_{2g}}$ reflect the x-ray absorption step of the RIXS process, where a $2p$ core electron is promoted to either an e_g^σ or a t_{2g} orbital, respectively.

Figure 3(a) shows RIXS spectra of $Ba_4NbIr_3O_{12}$ measured with $E_{{\rm in},t_{2g}} = 11.215$ keV and 63 meV resolution for transferred momentum (0.7 0 l) at selected values of l. The data cover a very large range of l from 17.1 to 36.6, which is possible through the use of hard x-rays at the Ir L_3 edge. As discussed above (cf. Fig. 2), we attribute the inelastic features between about 0.5 and 2.2 eV to intra-t_{2g} excitations. Beyond inelastic features, the spectra in Fig. 3(a) also show the elastic line at zero loss. Since the data were collected with incident π polarization, the elastic line is suppressed for a scattering angle $2\theta = 90°$. The data with $l = 36.6$ are closest to this case and accordingly exhibit the smallest elastic line. In contrast, the small value of $2\theta = 40°$ for $l = 17.1$ gives rise to a large elastic line that dominates the data up to 0.4 eV.

Our main experimental result is the pronounced dependence of the RIXS intensity on l, i.e., on the component q_c of the transferred momentum parallel to the trimer axis. In fact, the RIXS intensity is modulated periodically as a function of l, as evident from the color map shown in Fig. 3(b). This provides strong evidence for the quasimolecular character of the excitations [7,8,10,29], as discussed in the Introduction and below. In particular, we can identify two different periodicities along l. In the range from about 1 to 2 eV, the data show a period $2l_0 = 11.3$ (or $2Q = 11.3 \times 2\pi/c$ in absolute units), while a different intensity modulation with half the period, $1Q \approx 5.67 \times 2\pi/c$, is observed around 0.5–0.8 eV [see Fig. 3(b)]. The two different periods can also be seen in Fig. 4, which shows the RIXS intensity as a function of l for integration over four different energy windows, as given in the plot. Note that the RIXS spectra in Fig. 3(a) have been measured at integer and half-integer values of Q, highlighting the features for minimum and maximum intensity of the two different modulations. Considering, e.g., the range from 1 to 1.5 eV and a transferred momentum of mQ, maximum intensity is

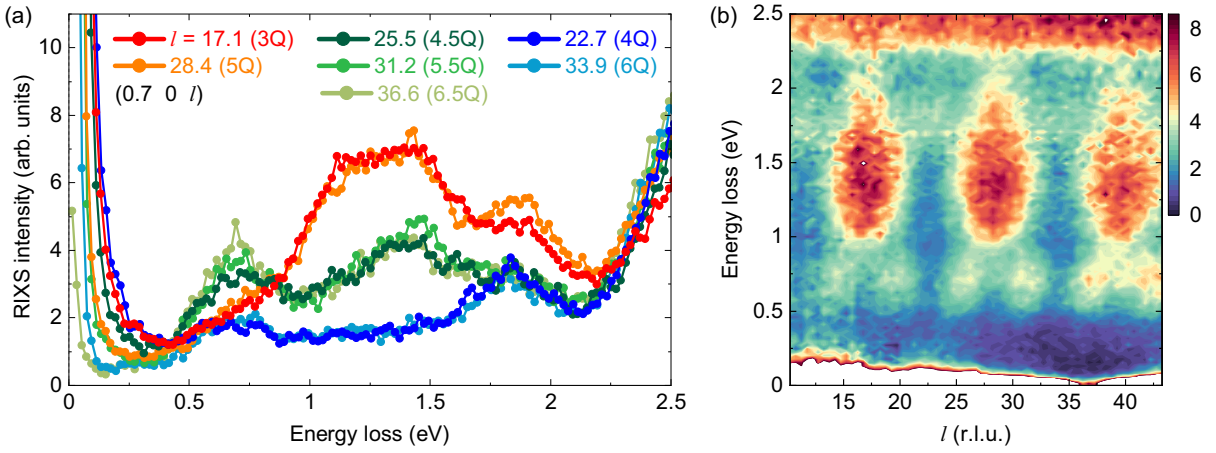

FIG. 3. (a) RIXS spectra of $Ba_4NbIr_3O_{12}$ (sample A) at (0.7 0 l) for selected values of l and (b) RIXS intensity map as a function of l at 300 K. The data do not show any dispersion as a function of the transferred momentum **q**. Instead, they reveal a pronounced, periodic intensity modulation with two periods, Q and $2Q$, where $Q = \pi/d \approx 5.67 \times 2\pi/c$ with the intradimer Ir-Ir distance d. The data in (b) were merged from measurements at (0.2 –0.2 l) for $10.25 \leqslant l \leqslant 30.25$ and at (0.7 0 l) for $20.25 \leqslant l \leqslant 43.25$. We used finite h and/or k to avoid enhanced elastic scattering close to a Bragg peak. The very different intensities of the elastic line below about 0.3 eV reflect the large differences in the scattering angle 2θ.

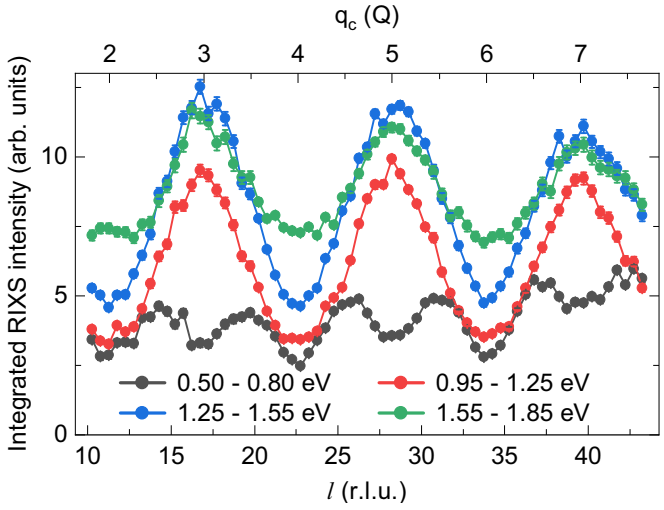

FIG. 4. Integrated RIXS intensity as a function of l, obtained by integrating the data shown in Fig. 3(b) for the integration ranges given in the plot. With increasing energy, the data have been shifted vertically by 0, 1, 2, and 3, respectively. The top scale uses $Q = \pi/d$ as unit for the component q_c of the transferred momentum. Two periodicities can be identified, $2Q = 11.3 \times 2\pi/c$ and half of this, $1Q$.

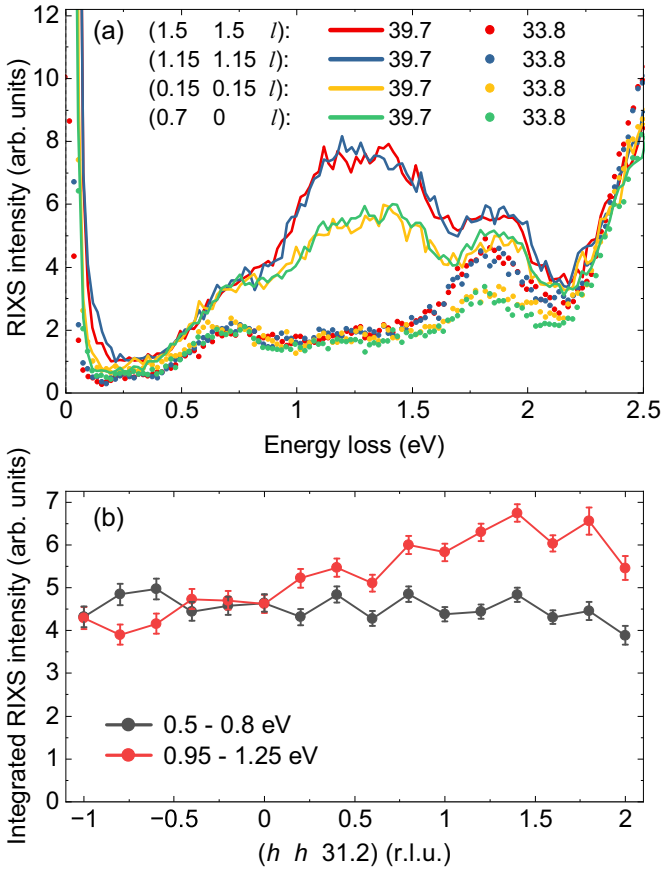

FIG. 5. Effect of a change of $\mathbf{q}$ perpendicular to c (sample A). (a) RIXS spectra at (h h l) and (0.7 0 l). For each, we compare two values of $l = 33.8$ (dotted) and 39.7 (solid line), equivalent to roughly $6Q$ and $7Q$, respectively. (b) Integrated RIXS intensity along (h h 31.2) for two different energy windows. The choice $l = 31.2$, equivalent to $5.5Q$, yields sizable intensity for all RIXS peaks [see Fig. 3(a)]. The quasimolecular character of the electronic excitations on a trimer causes a strong modulation as a function of l (cf. Fig. 4 and Sec. IV C). In contrast, the moderate, nonoscillatory intensity variation as a function of h for $h = k$ with constant l can be attributed to the polarization dependence. In the energy range 0.95 to 1.25 eV, the maximum intensity in (b) occurs for large h around 1.5, in agreement with the data in (a).

reached for odd m while the intensity minimum is reached for even m. With the lattice constant $c = 28.72$ Å, the long period $2Q$ corresponds to a real-space distance $d = 2\pi/2Q = 2.54$ Å. This agrees with the nearest-neighbor intratrimer Ir-Ir distance determined by x-ray diffraction, 2.54 Å. Accordingly, the short period $1Q$ corresponds to $2d$ in real space, equivalent to the distance between the two outer sites of a trimer. This period $1Q$ is a clear signature of a quasimolecular excitation that mainly involves the two outer trimer sites, as discussed in Sec. IV C.

Qualitatively, the overall features of our RIXS data of $Ba_3NbIr_3O_{12}$ are very similar to results obtained on the closely related dimer compounds $Ba_3MIr_2O_9$ with $M = Ce$ and In [7,8]. First, the spectra exhibit broad peaks with excitation energies that strongly differ from the RIXS response of other iridate Mott insulators with $j = \frac{1}{2}$ moments localized on individual sites [9,64–66]. Second, the inelastic features show a pronounced modulation of the RIXS intensity that depends on the component of $\mathbf{q}$ projected onto the trimer axis. In contrast to the strong $\mathbf{q}$ dependence of the intensity, the excitation energy is insensitive to $\mathbf{q}$. These properties reflect the localized, quasimolecular nature of the excitations, with charge carriers localized on a given cluster but fully delocalized over the sites of this cluster. The actual $\mathbf{q}$ dependence may serve as a fingerprint of the specific cluster shape. Dimers with Ir-Ir distance d host a sinusoidal interference pattern with period $2Q = 2\pi/d$ [7–9,29]. The three-dimensional shape of tetrahedral clusters allows for a more complex behavior [10]. The presence of two periods, $1Q$ and $2Q$, is characteristic for a linear trimer with Ir-Ir distances d and $2d$ (see Sec. IV C). Our RIXS data hence unambiguously demonstrate the quasimolecular character of the electronic structure of $Ba_4NbIr_3O_{12}$.

For a trimer running along the c axis, the RIXS intensity strongly depends on l. In contrast, h and k are expected to play a minor role. Also this is supported by experiment (see Fig. 5). Figure 5(a) shows RIXS spectra for different (h k l). For each set of h and k, data are given for $l = 33.8$ and 39.7. For $l_0 = 5.67$, these l values roughly correspond to $6l_0$ and $7l_0$ (or $6Q$ and $7Q$), respectively. For comparison, Fig. 5(b) depicts the integrated RIXS intensity in the energy ranges 0.5–0.8 eV and 0.95–1.25 eV for $l = 31.2$ or $5.5Q$. The insensitivity to h and k is particularly evident for the data in Fig. 5(a) with $6Q$, i.e., minimum intensity, and for the window 0.5–0.8 eV. Around 1–1.5 eV, the intensity moderately increases with h and k. We emphasize that this slow increase as a function of h and k strongly differs from the oscillating behavior as a function of l. This slow increase can be attributed to a polarization effect since the large change of $\mathbf{q}$ requires a corresponding change of the scattering geometry. Very similar polarization effects as a function of h and k have been observed in iridate dimer compounds [8].

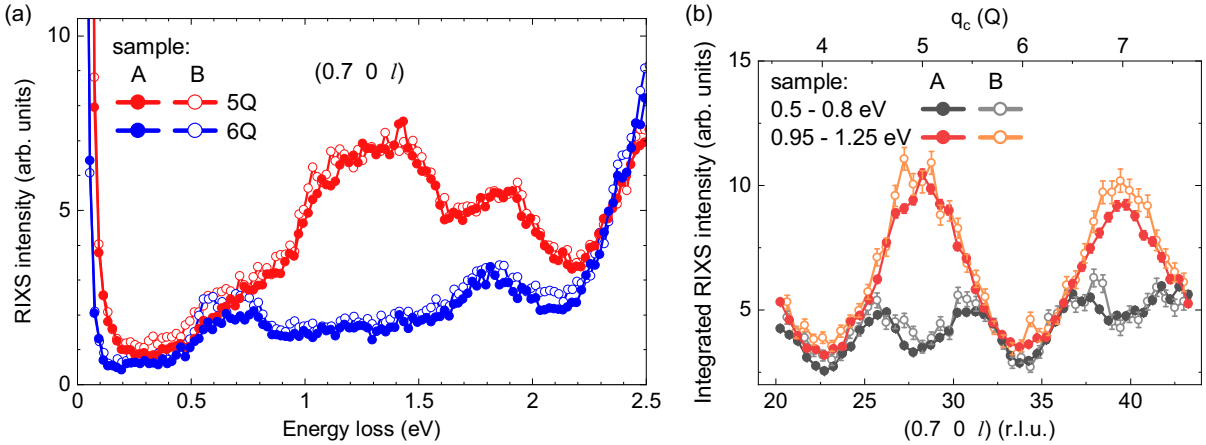

FIG. 6. Comparison of (a) RIXS spectra and (b) the **q**-dependent RIXS intensity of the two different samples A (full) and B (open symbols) (see Sec. II). The data agree very well with each other, pointing towards a negligible role of Nb-Ir disorder.

Finally, we address the possible role of Nb-Ir site disorder. We first consider a single $5d^4$ Ir^{5+} ion on a Nb^{5+} site (Wyckoff position $3a$), forming a local $J=0$ moment. These could be identified by observing two characteristic narrow peaks in the energy range up to $3/2\ \lambda$ [56–61], roughly 0.6 to 0.7 eV. Similarly, a single $5d^5$ Ir^{4+} ion would cause a sharp feature at $3/2\ \lambda$. The absence of such narrow peaks in our data suggests a minor role of Nb-Ir site disorder. This is supported by the **q** dependence of the RIXS intensity that reflects which Ir sites are involved in a given excitation. It thus can be used to detect signatures of disorder, e.g., excitations related to Ir ions located on the Nb $3a$ site that interact with Ir ions on trimer sites. This has been shown for the dimer compound $Ba_3Ti_{3-x}Ir_xO_9$ [9] with a sizable contribution of Ti-Ir site disorder. The Ti sites connect neighboring Ir_2O_9 dimers in the same way as the Nb $3a$ sites connect the trimers in $Ba_4NbIr_3O_{12}$ [see Fig. 1(a)]. Considering the projection onto the c axis, the Nb and Ir sites are displaced by 2.24 Å, which is smaller than the intratrimer Ir-Ir distance $d=2.54$ Å. Accordingly, Ir_{3a}-Ir pairs with one Ir ion on the Nb $3a$ site are expected to cause a modulation with a larger period $l_{\mathrm{Nb}}=12.8$. This is not present in our data. In addition, such pairs are also displaced perpendicular to c such that corresponding excitations would show a sinusoidal modulation as a function of h or k, as discussed below in Sec. IV C. Such a modulation indeed has been observed in $Ba_3Ti_{3-x}Ir_xO_9$ [9]. Figure 5(b) depicts the integrated RIXS intensity along (h h 31.2) for two different energy ranges. Along this direction, Ir_{3a}-Ir pairs would yield an intensity modulation following either $\sin^2[\pi(h\pm 31.2/12.8)]$ or $\cos^2[\pi(h\pm 31.2/12.8)]$ with a period of 1 in h, in close analogy to the case of $Ba_3Ti_{3-x}Ir_xO_9$ [9]. However, such modulation as a function of h is not observed in Fig. 5(b). We conclude that Nb-Ir site disorder is negligible for the discussion of our RIXS data. This is further supported by the comparison of data of the two different samples A and B, grown in Cologne and Dresden (see Sec. II). Figure 6 compares RIXS spectra of the two samples in Fig. 6(a) and the **q**-dependent RIXS intensity in Fig. 6(b). The data of the two samples agree very well with each other.

IV. THEORETICAL ANALYSIS

A. Hamiltonian for a single trimer

In the following, we address the RIXS response of $Ba_4NbIr_3O_{12}$ below 2 eV. Due to the large cubic crystal-field splitting 10 Dq (see Sec. III), we restrict the discussion to t_{2g} orbitals. For a trimer with two holes, the full Hamiltonian consists of spin-orbit coupling, noncubic crystal-field splitting, Coulomb repulsion and Hund's coupling [67], as well as hopping between neighboring sites,

$$H=\sum_i (H_{\mathrm{soc},i}+H_{\Delta,i}+H_{\mathrm{C},i})+H_t, \tag{1}$$

where i runs over the three trimer sites. The first two terms, $H_{\mathrm{soc},i}$ and $H_{\Delta,i}$, describe the single-ion physics in the case of a single t_{2g} hole per site [68]. The spin-orbit coupling term has the form

$$H_{\mathrm{soc},i}=\lambda\,\mathbf{L}_i\cdot\mathbf{S}_i, \tag{2}$$

where λ is the effective coupling constant, $\mathbf{L}_i$ the effective orbital momentum on site i, and $\mathbf{S}_i$ the spin. Iridium is a heavy atom with large $\lambda=0.4$–0.5 eV [7,64,65]. For an Ir site with a single t_{2g} hole, a positive λ splits the t_{2g} orbitals into a low-lying $j=\frac{1}{2}$ doublet and a $j=\frac{3}{2}$ quadruplet that is $3/2\ \lambda$ higher in energy. We use the global z axis as spin quantization axis [13] since the local coordinate systems for the IrO_6 octahedra have a different orientation for the middle and outer Ir sites [see Fig. 1(b)].

The second term of the Hamiltonian, the trigonal crystal-field splitting, is given by

$$H_{\Delta,i}=\Delta_i L_{z,i}^2-\overline{E}_{\Delta,i}, \tag{3}$$

where $L_{z,i}$ is the orbital momentum along the global z axis and $\overline{E}_{\Delta,i}$ denotes the average energy. For the trimer, a trigonal crystal-field splitting Δ_i arises for a corresponding distortion of the IrO_6 octahedra. However, finite Δ_i is also caused by the linear arrangement of the Ir neighbors even in the case of perfectly cubic octahedra [69]. The t_{2g} orbitals are split into a_{1g} and e_g^π orbitals with an energy gap Δ_i. Our convention in

the hole picture is such that the a_{1g} orbitals are lower in energy for positive Δ_i.

As the middle (m) and outer sites (o) are crystallographically distinct [see Fig. 1(b)], we allow for different crystal-field splittings Δ_m and Δ_o. In fact, *ab initio* simulations suggest that the two may differ substantially in magnitude and even have opposite signs [21]. In Eq. (3), we subtract the average energy $\overline{E}_{\Delta_m}$ or $\overline{E}_{\Delta_o}$ for each site to balance the energies around zero. This term is important for $\Delta_m \neq \Delta_o$. Without it, the relative energies of middle and outer sites become incorrect. For $\Delta_m = \Delta_o$, it only adds an overall energy constant.

Onsite Coulomb interactions are described by the third term in the Hamiltonian, Eq. (1), as follows [67]:

$$\begin{aligned} H_{\mathrm{C},i} = & U \sum_{\alpha} n_{i\alpha\uparrow} n_{i\alpha\downarrow} + \frac{1}{2}(U - 3J_H) \sum_{\sigma,\alpha\neq\alpha'} n_{i\alpha\sigma} n_{i\alpha'\sigma} \\ & + (U - 2J_H) \sum_{\alpha\neq\alpha'} n_{i\alpha\uparrow} n_{i\alpha'\downarrow} \\ & + (U - 2J_H) \left(15 - 5 \sum_{\alpha,\sigma} n_{i\alpha\sigma} \right) \\ & + J_H \sum_{\alpha\neq\alpha'} (c^{\dagger}_{i\alpha\uparrow} c^{\dagger}_{i\alpha\downarrow} c_{i\alpha'\downarrow} c_{i\alpha'\uparrow} - c^{\dagger}_{i\alpha\uparrow} c_{i\alpha\downarrow} c^{\dagger}_{i\alpha'\downarrow} c_{i\alpha'\uparrow}), \end{aligned}$$

where $c^{\dagger}_{i\alpha\sigma}$ ($c_{i\alpha\sigma}$) creates (annihilates) a hole at site M_i, with $i = 1,2,3$, of orbital type α with spin $\sigma = \uparrow, \downarrow$, and $n_{i\alpha\sigma} = c^{\dagger}_{i\alpha\sigma} c_{i\alpha\sigma}$ counts the number of holes. The intraorbital Coulomb repulsion is given by U, and J_H denotes Hund's coupling. The third line applies in the hole picture and takes care of the relative energies between different sites.

For the value of J_H, one has to distinguish different cases [70]. For a free ion, Hund's coupling can be expressed as $J^{\mathrm{free}}_{H,d} = (F^2 + F^4)/14$ if one considers the entire d shell, where F^2 and F^4 denote Slater integrals and the index "free" marks values without screening. For a t_{2g}-only model as used by us, $J^{\mathrm{free}}_{H} = (3/49)F^2 + (20/441)F^4$ applies [70]. The common choice of $F^4/F^2 \approx \frac{5}{8}$ results in $J^{\mathrm{free}}_{H} \approx 0.77\, J^{\mathrm{free}}_{H,d}$. Furthermore, screening causes a reduction of Hund's coupling by 20%–30% in a solid. Experimentally, the screened Hund's coupling can be determined from the multiplet energies of local excitations. The different values for the entire $5d$ shell and a t_{2g}-only model have recently been studied in $5d^4$ K_2OsCl_6 ($5d^3$ K_2ReCl_6), where $J_{H,d} = 0.43$ eV (0.46 eV) and $J_H = 0.28$ eV (0.34 eV) were reported [61,71]. For a t_{2g}-only model, RIXS studies of different $5d^4$ iridates find J_H in the range of 0.25 to 0.4 eV [56–60], while the RIXS results of $5d^4/5d^5$ Ir dimer compounds yield 0.30 to 0.33 eV [7,8]. In the following, we employ $J_H = 0.33$ eV but we find very similar results for $0.25\ \mathrm{eV} \leqslant J_H \leqslant 0.4$ eV.

Finally, the hopping of holes between neighboring Ir sites is described by the last term of the Hamiltonian,

$$H_t = \sum_{\langle i,j\rangle,\alpha,\alpha',\sigma} t^{\alpha\alpha'}_{ij} c^{\dagger}_{i\alpha\sigma} c_{j\alpha'\sigma}. \tag{4}$$

In face-sharing geometry, as a result of the threefold symmetry around the trigonal axis, direct Ir-Ir hopping and ligand-mediated hopping both are diagonal in the a_{1g}/e^{π}_{g} basis

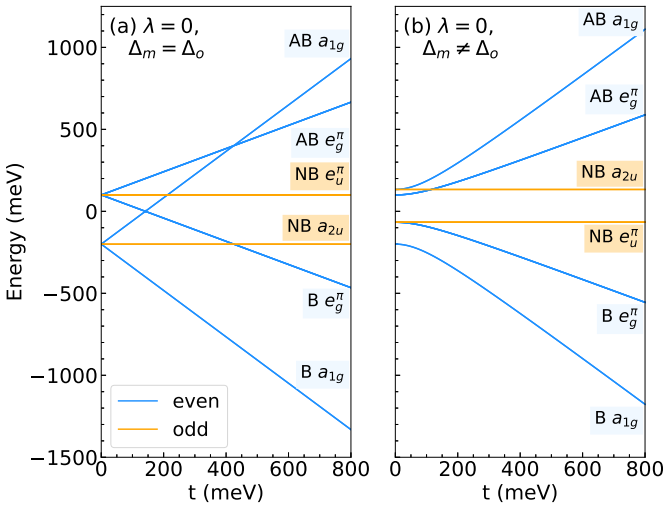

FIG. 7. Formation of quasimolecular B/NB/AB orbitals from single-site a_{1g} and e^{π}_{g} states as a function of $t = t_{a_{1g}}$ for $f = t_{e^{\pi}_{g}}/t_{a_{1g}} = -\frac{1}{2}$ in a single-particle picture with $\lambda = 0$. (a) $\Delta_m = \Delta_o = 0.3$ eV. (b) $\Delta_m = 0.3$ eV, $\Delta_o = -0.2$ eV. Blue (yellow) denotes even (odd) states.

[69]. In other words, the only nonzero hopping elements are those between the same a_{1g} or e^{π}_{g} orbitals on neighboring sites. Their respective hopping strength is denoted by $t_{a_{1g}}$ and $t_{e^{\pi}_{g}}$, respectively, with realistic values for their ratio $f = t_{e^{\pi}_{g}}/t_{a_{1g}}$ being close to $f = -\frac{1}{2}$ [13]. We will use $t = t_{a_{1g}}$ and f to parametrize the hopping.

B. Single-particle states

For an intuitive picture, we consider the noninteracting case $U = J_H = 0$, and discuss the formation of quasimolecular orbitals in two different limits $\Delta \gg \lambda$ vs $\Delta \ll \lambda$. First, we address the effect of hopping on the a_{1g} and e^{π}_{g} orbitals for $\lambda = 0$. Due to the very short Ir-Ir distance, we expect hopping to be large. Values of $t_{a_{1g}} = 0.5$–1.1 eV have been derived from the analysis of RIXS data of the face-sharing dimer compounds $Ba_3CeIr_2O_9$ and $Ba_3InIr_2O_9$ [7,8]. In the trimer, hopping yields bonding (B), nonbonding (NB), and antibonding (AB) orbitals. The energy of nonbonding states is not affected by t, while the shift of B/AB states in the simplest case, $\Delta_m = \Delta_o$, is linear in t [see Fig. 7(a)]. For $\Delta_m \neq \Delta_o$, the hopping Hamiltonian H_t does not commute with the crystal-field term H_{Δ}, which scrambles the order of states for small t and leads to a more complicated behavior [see Fig. 7(b)]. For realistic, large values of t, however, the qualitative behavior is the same in Figs. 7(a) and 7(b).

The opposite limit is achieved for $\Delta_m = \Delta_o = 0$, describing the effect of hopping on the spin-orbit entangled j states. In general, hopping mixes the $j = \frac{1}{2}$ and $\frac{3}{2}$ multiplets [8,13]. There is, however, a special value $f = -1$, for which H_t and H_{soc} commute such that j remains a good quantum number of the B/NB/AB states [see Fig. 8(a)]. Although $f = -1$ is not realized in $Ba_4NbIr_3O_{12}$, this case is helpful to simplify some of the discussion below. For $\Delta_m = \Delta_o = 0$ and $f = -1$, the quasimolecular states are B/NB/AB doublets built from $j = \frac{1}{2}$ states or B/NB/AB quartets made from $j = \frac{3}{2}$ states. Note that a further limit, considering exchange-coupled local

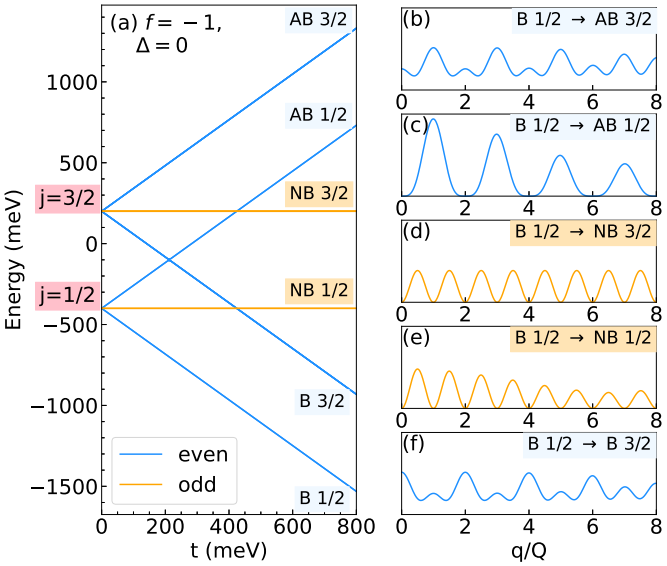

FIG. 8. Quasimolecular orbital picture for strong spin-orbit coupling and vanishing trigonal field $\Delta=0$. (a) Effect of hopping t on the spin-orbit entangled j states in a single-hole picture for $\lambda=0.4$ eV. The plot depicts the special case with $f=-1$, for which j remains a good quantum number of the B/NB/AB states. (b)–(f) RIXS intensity for a single hole per trimer with q along the trimer axis and $Q=\pi/d$. The five panels show the rich behavior of the q dependence for excitations from the bonding $j=\frac{1}{2}$ ground state to each of the excited states.

j moments, requires to consider finite U. However, two holes on three sites remain delocalized even for $t \ll U$ such that this limit cannot be realized here.

In the presence of inversion symmetry, it is easy to verify that the single-particle bonding and antibonding states of a trimer are even under inversion, while the nonbonding states are odd. A generic inversion-odd single-particle state can be written as

$$|\psi_o\rangle = \frac{1}{\sqrt{2}}(|m\rangle_1 - |m\rangle_3), \tag{5}$$

where $|m\rangle_i$ is a generic single-particle state on site M_i. The hopping amplitudes towards the middle site M_2 cancel, and hence the energy of an odd state does not depend on (nearest-neighbor) hopping, i.e., odd states are nonbonding. The odd nonbonding states built from single-site a_{1g} and e_g^π orbitals have a_{2u} and e_u^π character, respectively. In contrast a generic inversion-even state can be written as

$$|\psi_e\rangle = v|m\rangle_1 + u|n\rangle_2 + v|m\rangle_3, \tag{6}$$

where $|m\rangle$ and $|n\rangle$ are generic single-particle states and u and v are complex parameters with $|u|^2+2|v|^2=1$. This form of the even and odd states will prove useful in the next section to gain a better understanding of the RIXS intensities for the trimer system.

C. Generic properties of RIXS intensities for inversion-symmetric trimers

To put the RIXS response of trimers into perspective, we briefly recap the behavior of dimers. Coherent summation over resonant scattering processes on the two sites of a dimer yields a $\mathbf{q}$-dependent modulation of the RIXS intensity. This interference pattern can be described in terms of an inelastic version of Young's double-slit experiment [7,29]. In other words, RIXS probes the dynamical structure factor $S(\mathbf{q},\omega_0)$ of a dimer excitation at energy $\hbar\omega_0$ that exhibits a sinusoidal $\mathbf{q}$ dependence. In the presence of inversion symmetry, the RIXS intensity for a dimer is given by

$$I_{eo}^{\mathrm{dim}}(q) \sim \sin^2(qd/2), \quad I_{ee}^{\mathrm{dim}}(q) \sim \cos^2(qd/2), \tag{7}$$

where d is the distance between the two sites of a dimer, q denotes the component of $\mathbf{q}$ parallel to the dimer axis, and I_{eo}^{dim} refers to excitations on the dimer that flip the symmetry from even to odd or vice versa while I_{ee}^{dim} corresponds to excitations from even to even or from odd to odd states. The period of the interference pattern $2Q=2\pi/d$ measures the intradimer distance, while a $\cos^2(qd/2)$ or $\sin^2(qd/2)$ behavior reveals the symmetry and character of the states involved in the excitation. A trimer offers similar but richer behavior.

Before we consider RIXS on $Ba_4NbIr_3O_{12}$, let us first discuss some general properties of inversion-symmetric trimers. For direct RIXS processes with excitation energies that are smaller than the inverse core-hole lifetime $\Gamma \approx 3$ eV [72,73], we may employ the fast-collision approximation [32–35]. This allows for the factorization of the direct RIXS amplitude into a resonant prefactor and the dynamic structure factor. Considering a constant incident energy, we may ignore the resonant prefactor. In this case, the RIXS amplitude $A(\mathbf{q})$ is given by [34,35]

$$A(\mathbf{q}) \sim \langle\psi_f| \sum_{\mathbf{R}} e^{i\mathbf{q}\mathbf{R}}[D^\dagger(\epsilon_{\mathrm{out}}^*)D(\epsilon_{\mathrm{in}})]_{\mathbf{R}}|\psi_i\rangle, \tag{8}$$

where $\mathbf{R}=(0,0,0)$, $(0,0,\pm d)$ for the three sites of the trimer, D is the local dipole transition operator, $|\psi_i\rangle$ and $|\psi_f\rangle$ denote the initial and final state, respectively, and ϵ_{in} and ϵ_{out} denote the incident and outgoing polarization, respectively. The corresponding RIXS intensity is obtained as $I(\mathbf{q}) \sim |A(\mathbf{q})|^2$. In the experiment, ϵ_{in} was oriented within the horizontal scattering plane. For the total intensity, we sum the intensities for vertical and horizontal outgoing polarization ϵ_{out}. For $Ba_4NbIr_3O_{12}$, we additionally take into account that obverse and reverse twinning is common in rhombohedral structures. The two twins cannot be distinguished in, e.g., a Laue x-ray diffraction image. For the two-hole RIXS intensities discussed in Sec. V, we hence sum over the two possible trimer orientations, rotated by π around the c axis, that correspond to the two twin domains. This has only a minor effect on the result. It only affects the polarization and thus the slowly varying envelope of the interference pattern. Note that the single-hole RIXS intensities as depicted in Fig. 8 only consider one orientation.

For a dispersionless trimer excitation at energy $\hbar\omega_0$, the intensity $I(\mathbf{q}) \propto |A(\mathbf{q})|^2$ [cf. Eq. (8)] reflects the dynamical structure factor $S(\mathbf{q},\omega_0)$. We will argue for its form using the single-particle expressions in Eqs. (5) and (6), but the resulting Eqs. (9) and (11) are valid also for the many-body case (see Appendix B). With the generic single-particle states $|m\rangle_i$ and $|\tilde{m}\rangle_i$ on site i, the matrix elements $\langle\tilde{m}|D^\dagger D|m\rangle_i$ may be different for the inner site M_2 compared to the outer sites. On the equivalent outer sites M_1 and M_3, they have to be

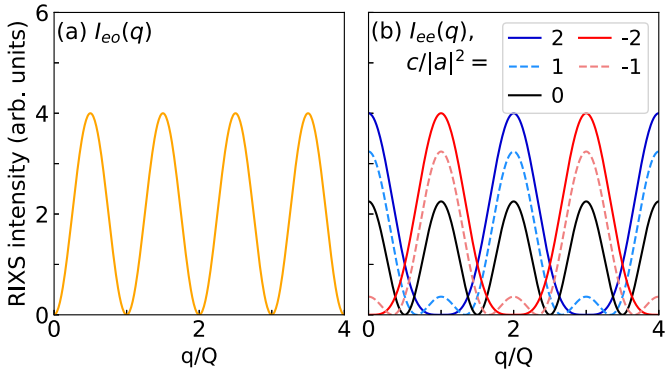

FIG. 9. Generic interference patterns for a trimer with inversion symmetry, carrying information on the character and symmetry of the states involved. Note that q is the component of $\mathbf{q}$ parallel to the trimer axis, with $Q=\pi/d$. (a) $|a_{eo}|^2\sin^2(qd)=|a_{eo}|^2\sin^2(\pi q/Q)$ behavior is characteristic for excitations from even to odd states or vice versa [see $I_{eo}(q)$ in Eq. (9)]. (b) The interference between inner and outer sites of the trimer yields a richer behavior for excitations from even to even or odd to odd states [see $I_{ee}(q)$ in Eq. (11)]. The plot shows $I_{ee}(q)$ for different $c/|a|^2$, illustrating the qualitatively different behavior of $|c|=2|a|^2$ (blue/red), $|c|=|a|^2$ (dashed blue/dashed red), and $c=0$ (black). To improve visibility, we have chosen $a=1$, 1.2, and 1.5 for $|c/a^2|=2$, 1, and 0, respectively. Here, we neglect the change of polarization with q that adds a slow envelope.

identical. However, the relative sign in the sum over sites in Eq. (8) is governed by the symmetry of the wave functions in the initial and final states, and the interference additionally depends on $\mathbf{q}$ via the phase factors $e^{i\mathbf{qR}}$. For an excitation that flips the symmetry from even to odd or from odd to even, the intensity is particularly simple. Since an odd state has no occupation on the middle site M_2, the amplitude contains only two terms,

$$A_{eo}(q)\sim\tfrac{v}{\sqrt{2}}[e^{iqd}\langle\tilde{m}|D^\dagger D|m\rangle_1-e^{-iqd}\langle\tilde{m}|D^\dagger D|m\rangle_3],$$

where q denotes the z component, parallel to the trimer axis. As the sites M_1 and M_3 are equivalent, their matrix elements are identical, which yields

$$I_{eo}(q)\sim|a_{eo}|^2\sin^2(qd). \tag{9}$$

This is valid also in the many-body case (see Appendix B). The parameter a_{eo} depends on the initial and final states but also on the scattering geometry and the corresponding polarization, which causes an effective $\mathbf{q}$ dependence of a_{eo}. For hard x-rays at the Ir L_3 edge, covering a large range of $\mathbf{q}$, $a_{eo}(\mathbf{q})$ serves as a slow envelope to the sinusoidal modulation. Neglecting this envelope, the intensity $I_{eo}(q)$ exhibits a period $Q=2\pi/2d$ since it is blind to the middle site and consequently shows the sinusoidal intensity modulation of an effective "dimer" with distance $2d$ [see Eq. (7) and Fig. 9(a)]. Intensity maxima occur for $q=(m+\frac{1}{2})Q$ with integer m. This agrees with the experimental result at low energies (see black curve in Fig. 4 and Sec. V).

For an even-to-even excitation, the RIXS intensity of a trimer is more abundant. Using the generic form of even states given in Eq. (6) and the equivalence of the matrix elements on the outer sites M_1 and M_3, the RIXS amplitude can be written as

$$\begin{aligned}A_{ee}(q)&\sim(e^{iqd}+e^{-iqd})\tilde{v}^*v\langle\tilde{m}|D^\dagger D|m\rangle_3+\tilde{u}^*u\langle\tilde{n}|D^\dagger D|n\rangle_2\\&\equiv a\cos(qd)+b,\end{aligned} \tag{10}$$

where $a\cos(qd)$ is the sum of the amplitudes on the outer sites while b is the amplitude on M_2. This implies

$$I_{ee}(q)\sim|a|^2\cos^2(qd)+c\cos(qd)+|b|^2 \tag{11}$$

where $c=(a^*b+b^*a)$ captures the interference between the outer sites and the middle site M_2. In this general form, $I_{ee}(q)$ applies to the many-body case for both even-to-even and odd-to-odd excitations (see Appendix B).

Note that $a\sim v\tilde{v}^*$ and $b\sim u\tilde{u}^*$ reflect the coefficients of the wave functions of initial and final states [see Eqs. (6) and (10)]. The rich structure of $I_{ee}(q)$ hence contains substantial information on these states. Again neglecting the slow q dependence of the envelope caused by polarization, $I_{ee}(q)$ in general has a period of $2Q=2\pi/d$, different from $I_{eo}(q)$. We distinguish three different cases: (i) $|c|\gg|a|^2$, (ii) $c=0$, and (iii) $0<|c|\ll|a|^2$. (i) $|c|\gg|a|^2$ implies that the interference term between middle and outer sites dominates the modulation, which requires a dominant occupation of the middle site. Beyond occupation, the interference term depends on the phases of the states and on the matrix elements, which are also sensitive to polarization effects. Using the trigonometric identities $2\sin^2(x/2)=1-\cos(x)$ and $2\cos^2(x/2)=1+\cos(x)$, one can find the limiting behavior of I_{ee} for large $|c|$. For $c\gg|a|^2$, the modulated part of the RIXS intensity roughly is given by $\cos^2(qd/2)$ and for $c\ll-|a|^2$ it becomes $\sin^2(qd/2)$. Qualitatively, this behavior persists even for small values of $|c|$ as long as $|c|/|a|^2\geqslant 2$ [see Fig. 9(b)]. The $\sin^2(qd/2)$-type modulation agrees with the experimental observation at high energies (see Fig. 4). (ii) A special case is achieved for $c=0$, i.e., vanishing interference between middle and outer sites. This gives rise to $\cos^2(qd)$ behavior, i.e., the system again mimics a dimer with site distance $2d$ and period $1Q$, similar to the case of I_{eo} but with different phase [see black curve in Fig. 9(b)]. (iii) Finally, $0<|c|\ll|a|^2$ corresponds to a small but finite interference term between the middle and outer sites, which yields secondary maxima. These still can be observed for, e.g., $c=|a|^2$ at $q=mQ$ with odd m [see dashed curves in Fig. 9(b)].

These results promise that the measured q-dependent RIXS intensity provides important information on the wave functions, as recently demonstrated for the tetrahedral clusters in $GaTa_4Se_8$ [10]. However, the situation is more complex when states with different symmetry are close in energy. Consider, e.g., the sum of RIXS intensities with $I_{eo}(q)\sim\sin^2(qd)$ and $I_{ee}(q)$ as given by Eq. (11). The latter contains a $\cos^2(qd)$ term that competes with $I_{eo}(q)$ such that the $\sin^2(qd)$ character becomes visible only for sufficient intensity. Also, this observation will be relevant for the comparison of our experimental and theoretical results (see Sec. V).

D. RIXS intensity for a single hole

As a simple example that showcases the features found in the previous section, we address a face-sharing trimer with a single hole for strong spin-orbit coupling, zero trigonal field $\Delta=0$, and hopping ratio $f=-1$. The energies are plotted

in Fig. 8(a) and have been discussed above. Bonding and antibonding states are even under inversion (blue), the nonbonding states are odd (yellow). Figures 8(b)–8(f) depict the q-dependent RIXS intensity for all possible excitations. First, the two excitations 8(d) and 8(e) from the even ground state to the odd nonbonding states stand out by showing $\sin^2(qd)$ behavior with period $1Q$, as described by $I_{eo}(q)$ [cf. Eq. (9)]. Second, excitation (c) to the antibonding $j = \frac{1}{2}$ state agrees with dominant $\sin^2(qd/2)$ behavior as discussed above for $I_{ee}(q)$ with $c \ll 0$, i.e., strong occupation of the middle site. Finally, excitations to $j = \frac{3}{2}$ [Figs. 8(b) and 8(f)] feature secondary maxima that are expected for $|c| < 2|a|^2$. This occurs, e.g., for small occupation of the middle site M_2, but in this case it is due to destructive interference. The finite background stems from summing the intensities for vertical and horizontal outgoing polarization that exhibit different q dependence. Note that the relative strength of main and secondary maxima changes with q, reflecting the slow change of prefactors upon changing the scattering geometry and thus polarization.

V. COMPARISON OF THEORY AND EXPERIMENT

A. Ground state of a single trimer

The compound $Ba_4NbIr_3O_{12}$ previously has been discussed as a spin-liquid candidate [43–45]. We therefore first discuss the ground state of a trimer with two holes. The Hamiltonian in Eq. (1) has seven parameters. We fix spin-orbit coupling $\lambda = 430$ meV and Hund's coupling $J_H = 330$ meV to realistic values for Ir oxides [7,64,65] (see also Sec. IV A). Large values are expected for the intraorbital Coulomb interaction, $U \approx 1$–2 eV, and for the hopping $t = t_{a_{1g}} = 0.5$–1 eV [7,8] due to the short Ir-Ir distance. The ratio $f = t_{e_g^\pi}/t_{a_{1g}}$ is expected to be negative, roughly $f = -\frac{1}{2}$ [13]. Finally, the trigonal crystal-field splitting may reach values as large as a few hundred meV and may differ substantially between the inner and outer sites, $\Delta_m \neq \Delta_o$ [21]. Given these physical constraints, the ground state of a single two-hole trimer is *always* a singlet and even under inversion, with the two holes filling a bonding orbital. This is intuitively evident in the noninteracting case depicted in Figs. 7 and 8, but is stable also in the presence of strong correlations [21], as discussed below. This already implies that a single trimer in zero magnetic field carries a vanishing quasimolecular moment, $J = 0$. The experimental observation of a q-dependent RIXS intensity, modulated with periods $1Q$ and $2Q$, firmly establishes that the quasimolecular picture is applicable to $Ba_4NbIr_3O_{12}$. This predicts a nonmagnetic ground state for $Ba_4NbIr_3O_{12}$ as long as defects and interactions between trimers can be neglected.

In polycrystalline $Ba_4NbIr_3O_{12}$, the magnetic susceptibility has been reported to follow the Curie-Weiss law with a small magnetic moment of 0.8 μ_B per trimer or 0.3 μ_B per Ir site [43,45]. Similar values have been found in single crystals [44]. It has been argued that this magnetic moment, even though small, is too large to be caused by defects [43]. From the refinement of powder x-ray diffraction data, 8%–10% of Nb-Ir site mixing have been claimed [45]. A possible spin-liquid behavior of $Ba_4NbIr_3O_{12}$ has been discussed on the basis of the small magnetic moment, the absence of long-range magnetic order down to 0.05 K, the specific heat, and μSR data [43–45]. Before discussing how a small but finite magnetic susceptibility may emerge from $J = 0$ trimers in an external magnetic field (cf. Sec. V C), we first address the excitations of $Ba_4NbIr_3O_{12}$.

B. Excitations

For the discussion of the low-energy excitations, we start by summarizing the main features in the experimental data. A trimer exhibits a large number of eigenstates, in particular at higher energies, and the average over different contributions washes out the characteristic features. We thus will focus on the excitations below about 1.5 eV, even though the overall behavior is similar up to 2 eV. (i) Up to 0.4 eV, the RIXS intensity is negligible. (ii) At low energies, 0.5–0.8 eV, there is a clear $\sin^2(qd)$ behavior with period $1Q$ (see Figs. 3 and 4). (iii) In the range 0.95–1.55 eV the dominant behavior is $\sin^2(qd/2)$ with period $2Q$. On top, the integrated RIXS intensity, in particular from 0.95 to 1.25 eV, exhibits shoulders at half-integer values of Q, indicating a small $\sin^2(qd)$ contribution (see Fig. 4).

Observation (ii) of a $\sin^2(qd)$ modulation with period $1Q$ at low energy is well suited to narrow down the relevant parameter regime. It agrees with $I_{eo}(q)$ [see Eq. (9)]. Since the ground state is even, theory should yield a dominant inversion-odd state in the range 0.5–0.8 eV and no states with substantial RIXS intensity below. In the same spirit, this observation may serve to answer the question which, if any, noninteracting limit offers a simple, intuitive starting point to understand the full, interacting system. For instance, consider the noninteracting case studied in Fig. 7 for vanishing spin-orbit coupling. A first excited state with odd symmetry (yellow) exists only for *small* hopping t and only if $\Delta_m \approx \Delta_o$ [see Fig. 7(a)]. However, the lowest excited state is even under inversion (blue) for realistic, larger values of t, in particular for the realistic case of opposite signs of Δ_m and Δ_o [see Fig. 7(b)]. Since this even-symmetry lowest excited state yields substantial RIXS intensity, the overall low-energy behavior of the noninteracting limit with $\lambda = 0$ disagrees with the experimental findings. In the following we will show that the correct low-energy behavior is obtained for realistic values of λ, highlighting the important role of spin-orbit coupling.

In addition to spin-orbit coupling, realistic hopping with $|t_{e_g^\pi}| < |t_{a_{1g}}|$, i.e., $0 > f > -1$, is an essential ingredient to get a qualitatively correct q dependence at low energies. To see this, we first consider the simple, idealized case $f = -1$ which does not mix states with $j = \frac{1}{2}$ and $\frac{3}{2}$. We address the noninteracting case for $\lambda = 430$ meV and vanishing trigonal crystal field (see Fig. 8). This scenario has the same problems as discussed above for the other limit, $\lambda = 0$ (cf. Fig. 7): the lowest excited state for not too small hopping t is even (blue curve) and thus exhibits the wrong symmetry. It gives a dominant $\cos^2(qd/2)$ behavior in the RIXS intensity [see Fig. 8(h)] in contrast to the experimental low-energy result $\sin^2(qd)$. This first excited state is the quasimolecular equivalent of the spin-orbit exciton, i.e., the excitation of one of the holes from the $j = \frac{1}{2}$ bonding to the $j = \frac{3}{2}$ bonding multiplet at energy $E = 3/2\lambda$. The discrepancy with experiment persists upon considering the trigonal crystal-field splitting and/or finite Coulomb interactions, even though the trigonal crystal field

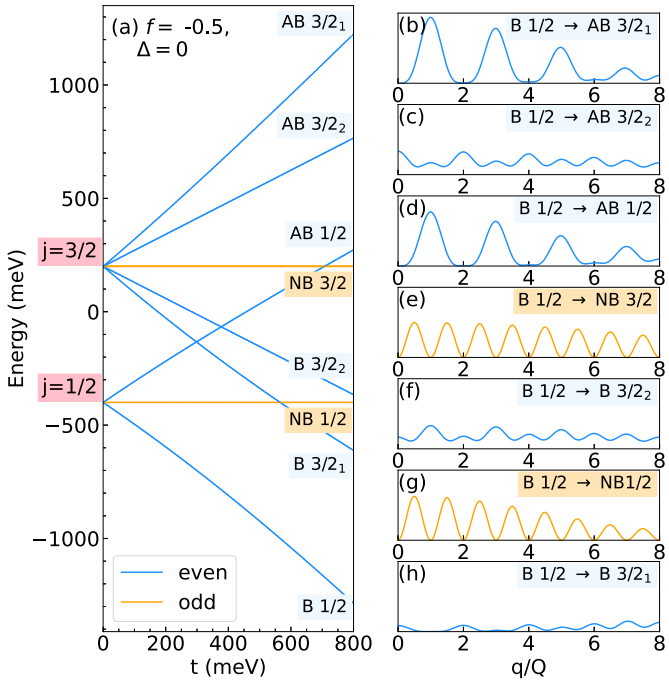

FIG. 10. Quasimolecular orbital picture for strong spin-orbit coupling and vanishing trigonal field. Same as Fig. 8 but for realistic $f = -0.5$. The corresponding mixing of $j = \frac{1}{2}$ and $\frac{3}{2}$ states lifts the degeneracy of bonding and antibonding $j = \frac{3}{2}$ quartets. (a) Effect of hopping t for $\lambda = 0.4$ eV. (b)–(h) RIXS intensity for a single hole per trimer. The panels show the q dependence for excitations from the bonding $j = \frac{1}{2}$ ground state to each of the excited states.

also mixes the $j = \frac{1}{2}$ and $\frac{3}{2}$ multiplets. The idealized case $f = -1$ hence fails to describe the dominant q dependence of the RIXS intensity.

However, the behavior is qualitatively different for realistic values of both $f = -\frac{1}{2}$ and $\lambda = 430$ meV (see Fig. 10). By mixing with the $j = \frac{1}{2}$ states, the $j = \frac{3}{2}$ multiplets split into two bonding doublets (blue), two antibonding doublets (blue), and a nonbonding quadruplet (yellow). For simplicity, we denote, e.g., the bonding doublets as bonding $j = \frac{3}{2}_1$ and $\frac{3}{2}_2$. Strictly speaking, j is not a good quantum number anymore, but most of the weight of a given wave function still lies in either $j = \frac{3}{2}$ or $\frac{1}{2}$ states. The essential point is that the lowest excitation to bonding $j = \frac{3}{2}_1$ carries nearly vanishing RIXS intensity [see Fig. 10(h)]. At the same time, the higher bonding branch $j = \frac{3}{2}_2$ remains above the lowest inversion-odd nonbonding state, as long as the hopping t does not become too large. Altogether, the $\sin^2(qd)$ behavior of the nonbonding branch [cf. Fig. 10(g)] dominates the RIXS intensity at low energy, in agreement with experiment.

In fact, this noninteracting scenario with strong spin-orbit coupling, large hopping $t \approx 0.8$ eV, and $f = -\frac{1}{2}$ already yields a qualitatively correct description of the three main experimental features. It has basically no RIXS intensity below 0.5 eV, a dominant $\sin^2(qd)$ modulation with period Q at low energies, and a dominant $\sin^2(qd/2)$ contribution with period $2Q$ at intermediate energies of about 1.5 eV. The latter originates from the excitation to antibonding $j = \frac{1}{2}$ states [see Figs. 10(a) and 10(d)]. Moreover, excitations to nonbonding $j = 3/2$ states add enhanced intensity at half-integer Q in the same intermediate energy range [see Fig. 10(e)], and this can be identified with the shoulders at $(m + \frac{1}{2})Q$ observed in our RIXS data (see Fig. 4).

For a quantitative comparison between theory and experiment, we have to go beyond the scenario plotted in Fig. 10 and include the trigonal crystal-field splitting as well as Coulomb interactions. Their effect on the two-hole energies is shown in Fig. 11. Figure 11(a) depicts the noninteracting case for $\Delta = 0$ with $f = -\frac{1}{2}$ and $\lambda = 430$ meV, as discussed above. It features an even ground state, and the lowest excited state for small t shows odd, nonbonding character (yellow). At $t = 800$ meV, the bonding $j = \frac{3}{2}_1$ state (blue dashed) is even lower in energy, but it carries very little RIXS intensity. At high energies, there are a multitude of states even in the noninteracting case. This makes it difficult to identify the dominant behavior, as mentioned above. Note that the states starting with an energy of $3\lambda = 1290$ meV at $t = 0$ have both holes in the $j = \frac{3}{2}$ multiplet. For $t = 0$, these states cannot be reached by the promotion of a single hole from the ground state in which both holes occupy $j = \frac{1}{2}$ states. This rule is not valid anymore for finite t and interactions, but the RIXS intensity of these states remains small.

In Fig. 11(b), the trigonal crystal-field splittings Δ_m and Δ_o simultaneously are tuned from zero on the left to $\Delta_m = -200$ meV and $\Delta_o = 300$ meV on the right. For these realistic values, the trigonal crystal field has hardly any effect on the low-energy states. Similarly, Fig. 11(c) shows the increase of Coulomb interactions from zero to $U = 1200$ meV and $J_H = 330$ meV. This causes a splitting of the multiplets and generically lowers the excitation energies. However, the qualitative behavior changes very little. We thus conclude that a substantial part of the excitation spectrum of the two-hole trimer can be motivated and discussed in a noninteracting picture as long as realistic values for λ, t, and f are considered. Despite the large value of U, this may not come as a surprise. In cluster Mott insulators, the main role of a repulsive U is to prevent charge fluctuations between different clusters, turning the entire system insulating. In other words, U suppresses the small hopping between clusters. Within a given cluster, however, the large hopping strongly competes with Coulomb correlations and charge carriers are fully delocalized over the cluster. Furthermore, correlations are less relevant for the present case with less holes than sites. Together, this intuitively explains the success of the noninteracting scenario for the discussion of a single trimer.

The q-dependent RIXS intensity for the interacting system is shown as a heat map in Fig. 11(d), and the corresponding RIXS spectra for selected q values are given in Fig. 12. Both plots use the parameter set that corresponds to the right end of Fig. 11(c). The most important qualitative features of the experimental data, in particular (i)–(iii) mentioned at the beginning of Sec. V B, are well reproduced. Note that the seven parameters in the Hamiltonian (1) span a large space, such that not all of them, in particular Δ_m and Δ_o, can be determined accurately. However, these results of the interacting model support the general outcome of the noninteracting case: the physics of $Ba_4NbIr_3O_{12}$ is governed by strong spin-orbit coupling λ of order 0.4 eV, large hopping $t_{a_{1g}}$ of order 0.8 eV, and $f = t_{e_g^\pi}/t_{a_{qg}} \approx -\frac{1}{2}$. Large hopping is required to

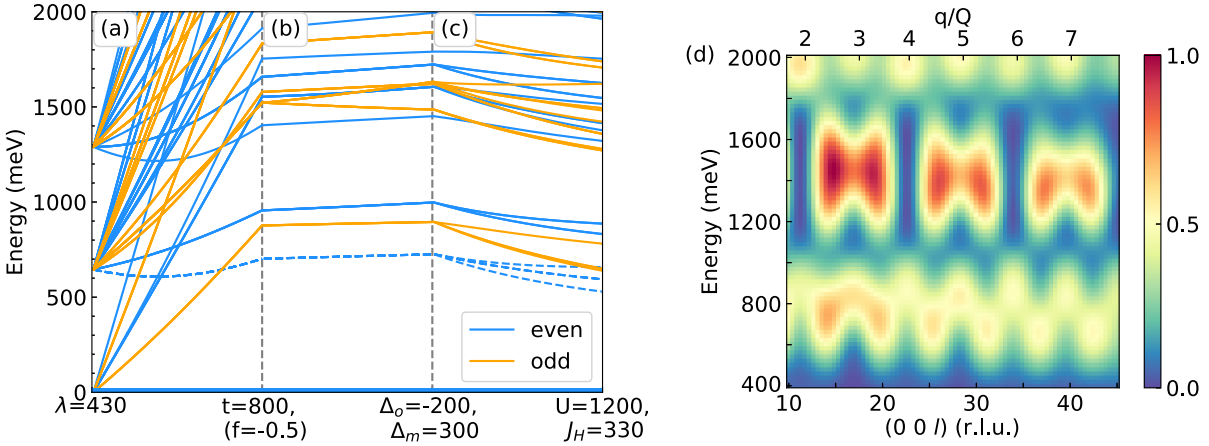

FIG. 11. Left: Energies of the two-hole eigenstates of a face-sharing trimer, relative to the ground state at zero. Blue (yellow) denotes states that are even (odd) upon inversion. The blue dashed lines refer to the bonding $j = \frac{3}{2}_1$ state which carries very little RIXS intensity. (a) Noninteracting case with spin-orbit coupling $\lambda = 0.43$ eV and vanishing trigonal crystal field $\Delta = 0$. Hopping $t = t_{a_{1g}}$ increases linearly from zero to 0.8 eV for fixed $f = t_{e_g^\pi}/t_{a_{1g}} = -\frac{1}{2}$. For $t = 0$, both holes are in a $j = \frac{1}{2}$ state in the ground state, and there are two possible excitation energies, $3/2\ \lambda$ and $3\ \lambda$, that correspond to one or two holes being excited to $j = \frac{3}{2}$, respectively. In (b), Δ_o and Δ_m are turned on simultaneously. In (c), Coulomb interactions are switched on, with U and J_H increasing up to 1.2 and 0.33 eV, respectively. The full parameter set at the very right reads as $\lambda = 0.43$ eV, $t = 0.8$ eV, $f = -\frac{1}{2}$, $\Delta_o = -0.2$ eV, $\Delta_m = 0.3$ eV, $U = 1.2$ eV, and $J_H = 0.33$ eV. The same parameters are used in (d), which shows the RIXS intensity on a color scale normalized to the maximum value.

achieve vanishing RIXS intensity at low energy, i.e., below 0.4 eV, and the combination with strong λ and $f \approx -\frac{1}{2}$ is necessary to reproduce the observed $1Q$-periodic intensity modulation of the low-energy RIXS peak. Accordingly, the ground state of a single trimer is well described by putting both holes in the quasimolecular bonding $j = \frac{1}{2}$ orbital, resulting in a total $J = 0$ state with even symmetry. Concerning the spatial distribution of the two holes, we first consider $U = J_H = \Delta_m = \Delta_o = 0$. In this simple case, we find one hole on the middle site while the outer sites carry half a hole each. For the realistic values of U, J_H, Δ_m, and Δ_o discussed above, these numbers change by less than 10%.

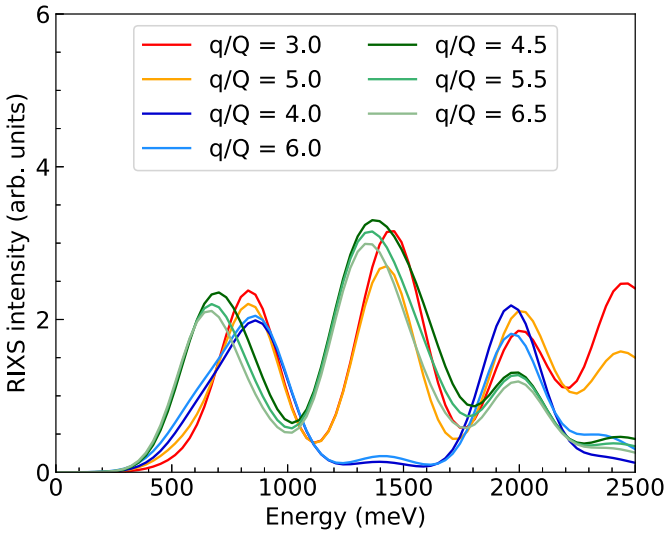

FIG. 12. Calculated RIXS spectra of intra-t_{2g} excitations of the two-hole trimer for different values of q/Q. The parameters are the same as used in Fig. 11(d), i.e., $\lambda = 0.43$ eV, $t = 0.8$ eV, $f = -\frac{1}{2}$, $\Delta_o = -0.2$ eV, $\Delta_m = 0.3$ eV, $U = 1.2$ eV, and $J_H = 0.33$ eV.

Our results challenge previously reported points of view on face-sharing iridate trimers. These have been discussed in terms of two limits $\lambda \gg t$ or $t \gg \lambda$ [21]. The first limit with extreme spin-orbit coupling considers local $j = \frac{1}{2}$ moments on individual Ir sites, where finite hopping yields exchange interactions between these local moments. The compound $Ba_4Ir_3O_{10}$ with three holes per trimer or one hole per Ir site has been discussed in this limit [53,54]. The opposite limit of extreme hopping $t \gg \lambda$ considers quasimolecular orbitals that are built from a_{1g} and e_g^π orbitals [21], i.e., it also assumes $\Delta \gg \lambda$. Ye *et al.* [51] claimed the covalency-driven collapse of strong spin-orbit coupling for $Ba_5CuIr_3O_{12}$ with three holes per trimer. Based on Raman scattering and density functional theory, they discussed the local $j = \frac{1}{2}$ scenario against a quasimolecular-orbital scenario where spin-orbit coupling was applied only to the bonding a_{1g} and e_g^π states (in the hole picture). Concerning $Ba_4NbIr_3O_{12}$, Bandyopadhyay *et al.* [45] discussed several properties in a $j = \frac{1}{2}$ scenario but at the same time interpreted the small magnetic moment and the suppressed bandwidth as support for a quasimolecular picture. Analyzing the Ir L_3 and L_2 white-line intensities in x-ray absorption (XAS), they claim that spin-orbit coupling is suppressed to a moderate value. However, this analysis of the branching ratio employs a single-site picture, which is not appropriate for the trimer compound $Ba_4NbIr_3O_{12}$, in particular not for a quantitative analysis. Our results highlight the quasimolecular nature of the trimer states but at the same time emphasize the important role of spin-orbit coupling, despite the large hopping. For a quantitative description, one has to treat spin-orbit coupling, hopping, Coulomb interactions, and the trigonal crystal field on equal footing. However, we have shown that a qualitative understanding can be achieved by considering quasimolecular orbitals built from spin-orbit-entangled j states but not from a_{1g} or e_g^π states for $\lambda = 0$.

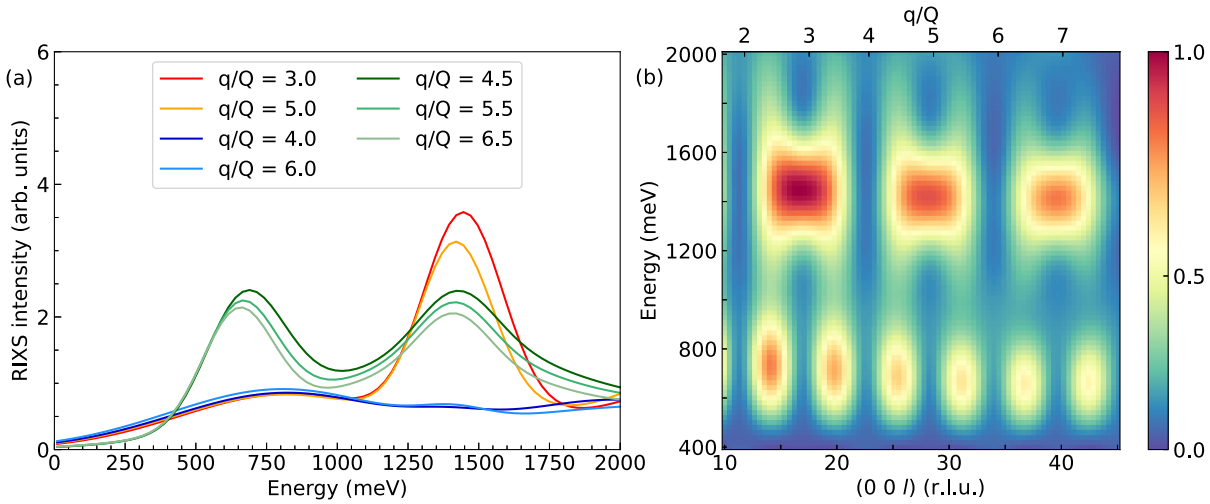

FIG. 13. (a) Calculated RIXS spectra and (b) q-dependent RIXS intensity for the same parameters as in Figs. 12 and 11(d). The single exception is the linewidth of excitations to $j = \frac{3}{2}$ type states, which here we choose to be 375 meV, i.e., three times larger than for excitations to $j = \frac{1}{2}$ states. Overall, this yields good agreement with the experimental result (cf. Fig. 3). We propose that the enhanced linewidth reflects the interaction with continuum states above the Mott gap.

Finally, we comment on the shortcomings of our theoretical approach. First, the RIXS data at 1–1.5 eV show a dominant $2Q$-periodic $\sin^2(qd/2)$ modulation and additionally weak shoulders at half-integer Q, i.e., a weak $\sin^2(qd)$ contribution (see Fig. 4). The former is well described by the excitation to the quasimolecular antibonding $j = \frac{1}{2}$ state [see Fig. 10(d)]. However, theory overestimates the intensity of the $1Q$-periodic features, i.e., the $\sin^2(qd)$ contribution of excitations to nonbonding $j = \frac{3}{2}$ states [cf. Figs. 10(e) and 11]. Second, just below 1 eV theory shows a predominant $\cos^2(qd) = \cos^2(\pi q/Q)$ behavior with maximum intensity for integer Q, out of phase with the $\sin^2(qd)$ modulation around 0.7 eV. In contrast, our experimental data show a clear minimum for $4Q$ and $6Q$ (see red and black curves in Fig. 4). Also, this shortcoming can be viewed as an overestimation of excitations to $j = \frac{3}{2}$ states, in this case to bonding orbitals [see Figs. 10(f) and 10(h)].

To find a possible reason for the overestimated intensity of excitations to $j = \frac{3}{2}$ states, we discuss the assumptions employed in our theoretical approach. First, we neglect the small admixture of e_g^σ orbitals. With the cubic crystal-field splitting 10 $Dq \approx 3.5$ eV, we expect this to have a minor effect on the intra-t_{2g} excitations below 2 eV (see Fig. 2). Second, we neglect the possible dynamics in the intermediate state of the RIXS process. This is very well justified for a single Ir site, where the Ir $2p^5t_{2g}^6$ intermediate state has a full t_{2g} shell. For a trimer, there are different intermediate states with one hole in the quasimolecular t_{2g} orbitals (and the second one in a $2p$ core state). However, the large width of a few eV of the RIXS resonance curve and its featureless line shape suggest that all intermediate states contribute equally to the RIXS amplitude. Using this assumption, the dynamics in the intermediate state can be neglected. Third, we consider a single trimer and ignore interaction effects with the electronic continuum above the Mott gap, i.e., *inter*trimer excitations. The actual size of the gap is not known well thus far. The activation energy Δ_{act} determined from the electrical resistivity may serve as a lower limit. Values of $\Delta_{\text{act}} = 0.05$ eV [43,44] and 0.22–0.25 eV [45] have been reported. Typically, the size of the Mott gap cannot be determined from RIXS at the transition-metal L edge [74]. With a $2p$ core hole in the intermediate state, the RIXS process in good approximation can be viewed as a coherent superposition of single-site scattering events [see Eq. (8)]. It is nevertheless possible that the RIXS spectra exhibit a weak, broad, and featureless contribution of intertrimer excitations across the Mott gap. In particular, the small RIXS intensity of the latter may be enhanced in the case of hybridization between intratrimer and intertrimer excitations. Our single-trimer theory predicts a nearly vanishing RIXS intensity just below 1.5 eV for $q = 4Q$ or $6Q$ (see Fig. 12). In contrast, the RIXS data between 1 and 1.5 eV show a weak background that indeed may indicate a finite contribution of intertrimer excitations (see blue curves in Fig. 3). A way to explain both the overestimated intensity of excitations to $j = \frac{3}{2}$ type of states and a finite continuum contribution is to assume a certain hybridization between such excitations to $j = \frac{3}{2}$ states and electronic continuum states. To mimic this, we empirically assume a linewidth of 375 meV for excitations to $j = \frac{3}{2}$ states, which is three times larger than for $j = \frac{1}{2}$. In this case, the calculated result in fact shows good agreement with the experimental data (see Figs. 13 and 3).

C. Magnetism vs $J = 0$

From our analysis of a single trimer, the ground state is very stable and given by a singlet. This raises the question of the origin of the Curie-Weiss contribution observed in the magnetic susceptibility $\chi(T)$, corresponding to a small magnetic moment of about 0.3 μ_B per Ir site [43–45]. Excitonic magnetism emerging from a nonmagnetic ground state has been discussed for, e.g., d^4 $J = 0$ systems [75,76]. It arises in the case of condensation of a magnetic excited state that exhibits large dispersion [75,77]. In other words, the system flips to an excited magnetic state on every site since the energy cost is overruled by the gain of exchange energy. Such

condensation yields an entirely different ground state, which we rule out for $Ba_4NbIr_3O_{12}$ based on the good agreement between our experimental and theoretical results. Moreover, excitonic magnetism requires strong intertrimer exchange interactions and a corresponding pronounced dispersion that, however, is absent in our RIXS data.

Furthermore, spin-orbit coupling causes Van Vleck paramagnetism in an external magnetic field since the magnetization operator mixes the zero-field eigenstates. This may give rise to the admixture of a magnetic state to the ground state, as discussed, e.g., for the $5d^4$ $J = 0$ ground state of K_2OsCl_6 [61]. We consider local excited states of individual, noninteracting trimers as well as excitations across the Mott gap that may admix states with different hole count via *inter*-trimer hopping. The lowest excitation energy of a single trimer amounts to about 0.5 eV, and a lower limit for intersite excitations is given by the activation energy 0.25 eV [45], as discussed above. Given these large excitation energies, the Van Vleck contribution to $\chi(T)$ is certainly small and nearly independent of temperature below 300 K. Altogether, we expect a small Van Vleck contribution in $\chi(T)$ of $Ba_4NbIr_3O_{12}$ but rule out that the trimers with two holes cause a finite Curie-Weiss contribution in a small magnetic field.

VI. CONCLUSION

In conclusion, we find that the RIXS spectra and in particular the momentum dependence of the RIXS intensity $I(\mathbf{q})$ of $Ba_4NbIr_3O_{12}$ yield clear fingerprints of the quasimolecular electronic structure of this trimer compound. In insulating $Ba_4NbIr_3O_{12}$, the two holes per trimer are delocalized in quasimolecular trimer orbitals. One characteristic feature of a trimer is the existence of two different periods in $I(\mathbf{q})$ that reflect the intratrimer Ir-Ir distances d and $2d$. Beyond the two periods, the presence of inversion symmetry for Ir_3O_{12} trimers in face-sharing geometry yields characteristic interference patterns in $I(\mathbf{q})$ that facilitate the interpretation of the RIXS spectra. This allows us to determine a realistic range of parameters. Remarkably, a noninteracting picture with strong spin-orbit coupling $\lambda \approx 0.4$ eV and large hopping $t_{a_{1g}} \approx 0.8$ eV with $t_{e_g^\pi}/t_{a_{1g}} \approx -\frac{1}{2}$ already describes the main qualitative features of the RIXS data. In this regime, a trigonal crystal field of up to a few hundred meV has only a small effect on the RIXS response and does not seem essential to understand the qualitative physics. Concerning Coulomb interactions, we employ $U = 1.2$ eV and $J_H = 0.33$ eV, but also these are not essential for a qualitative description of the properties of a single trimer. On a trimer, hopping wins against correlations, in particular for a hole count smaller than the number of Ir sites.

In the literature, the physics of $5d$ iridate trimers has been discussed in two limits, either extreme spin-orbit coupling with local $j = \frac{1}{2}$ moments or extreme hopping, i.e., a quasimolecular-orbital picture based on a_{1g} and e_g^π orbitals [21,45,51,53,54]. In the quasimolecular scenario, spin-orbit coupling has either been neglected or applied only to the bonding states [51]. We find that a quantitative description requires to consider spin-orbit coupling and hopping on the same footing and we show that the trimer physics of $Ba_4NbIr_3O_{12}$ can be understood very well in terms of quasimolecular states that are formed from spin-orbit-entangled j moments. This agrees with previous RIXS results on iridate dimers [7,8]. Remarkably, a different scenario has been found in RIXS on Ta tetrahedra in $GaTa_4Se_8$, where an intuitive picture is obtained by first considering hopping and then applying spin-orbit coupling only to the quasimolecular t_2 orbitals [10]. The choice of an appropriate intuitive model hence depends on the cluster shape and the relative size of electronic parameters. The essential role of spin-orbit coupling in these cluster Mott insulators promises a nontrivial character of the magnetic moments in, e.g., trimers with an odd number of holes. In general, theoretical investigations of exchange interactions between neighboring clusters are highly desirable.

For realistic parameters, we show that the ground state of a trimer with two holes is a nonmagnetic singlet that is even under inversion. Both holes occupy the bonding $j = \frac{1}{2}$ orbital, which yields a total $J = 0$. A nonmagnetic ground state has also been obtained in density-functional calculations for $Ba_4NbIr_3O_{12}$ [21]. Actually, the insulating character arises as soon as realistic spin-orbit coupling is included, i.e., even without correlations, which has been rationalized by the two holes filling the lowest cluster orbital [21]. This raises the question on the classification of $Ba_4NbIr_3O_{12}$ as either a cluster Mott insulator or a cluster-type band insulator. Our RIXS data show that the excited states can be assigned to a given trimer, supporting a significant role of intertrimer Coulomb interactions and a cluster Mott picture.

ACKNOWLEDGMENTS

Our research project on cluster Mott insulators to a large extent has been triggered by fruitful discussions with D. I. Khomskii, to whom we pay our sincere tribute. We acknowledge the European Synchrotron Radiation Facility (ESRF) for providing beam time at beam line ID20 under Proposal No. IH-HC-3879 and technical support. Furthermore, we acknowledge funding from the Deutsche Forschungsgemeinschaft (DFG, German Research Foundation) through Project No. 277146847-CRC 1238 (projects A02, B03) as well as from the European Union-Next Generation EU-PNRR-M4C2, investimento 1.1-Fondo PRIN 2022-Superlattices of relativistic oxides (Grant ID No. 2022L28H97, CUP D53D23002260006). A.S. and M.H. thank J. Attig for numerical support and acknowledge partial funding by the Knut and Alice Wallenberg Foundation as part of the Wallenberg Academy Fellows project.

DATA AVAILABILITY

The data shown in the figures are available on Zenodo [78].

APPENDIX A: SAMPLE CHARACTERIZATION

For crystals grown in Cologne, the chemical composition and homogeneity were determined with a JEOL JXA-8900RL Electronbeam Microprobe. On a polished planar surface, the Ba and Nb concentrations were measured using a PET crystal spectrometer with baryte and elemental Nb as standards. The

Ir concentration was measured using a LiF crystal spectrometer with an IrO_2 crystal as standard.

APPENDIX B: DETAILS ON THE RIXS INTENSITY

Here, we review how to derive Eq. (9). A generic state on the trimer can be written as

$$|\psi\rangle = \sum_{ijk} c_{ijk}|i;j;k\rangle, \tag{B1}$$

where i, j, k denote the basis states on the sites M_1, M_2, and M_3 (see Fig. 1). In general, i, j, k denote many-body states and need not have fixed particle number individually. Only the total particle number is fixed. How the single-particle orbitals transform under inversion depends on the material at hand. For the trimers in $Ba_4NbIr_3O_{12}$, the single-particle basis states, and consequently the many-particle ones as well, transform in a very simple way under inversion,

$$\hat{I}|i;j;k\rangle = |k;j;i\rangle. \tag{B2}$$

Thus, inversion constrains the coefficients c_{ijk} to

$$c_{ijk} = \pm c_{kji}, \tag{B3}$$

where the $+$ $(-)$ sign denotes even (odd) states under inversion. For instance, bonding and antibonding states are both inversion symmetric (even), while nonbonding states are antisymmetric (odd).

For a single trimer, the RIXS amplitude for generic initial and final states $|\psi_i\rangle$ and $|\psi_f\rangle$ reads as [cf. Eq. (8)]

$$\begin{aligned} A(\mathbf{q}) &\sim \sum_{\mathbf{R}} e^{i\mathbf{q}\mathbf{R}}\langle\psi_f|\left[D^\dagger(\epsilon_{\text{out}}^*)D(\epsilon_{\text{in}})\right]_{\mathbf{R}}|\psi_i\rangle \\ &= e^{iqd}\sum_{i,j,k}\sum_{i',j',k'}\tilde{c}^*_{i'j'k'}c_{ijk}\delta_{j,j'}\delta_{k,k'}\langle i'|D^\dagger D|i\rangle_1 \\ &\quad + e^{-iqd}\sum_{i,j,k}\sum_{i',j',k'}\tilde{c}^*_{i'j'k'}c_{ijk}\delta_{j,j'}\delta_{i,i'}\langle k'|D^\dagger D|k\rangle_3 \\ &\quad + \sum_{i,j,k}\sum_{i',j',k'}\tilde{c}^*_{i'j'k'}c_{ijk}\delta_{i,i'}\delta_{k,k'}\langle j'|D^\dagger D|j\rangle_2, \end{aligned} \tag{B4}$$

where the subscript of $|\ldots\rangle_m$ denotes the site. We can combine the terms in the second and third lines, using that the RIXS amplitudes for the outer sites are identical due to inversion symmetry, i.e., $\langle j|D^\dagger D|i\rangle_1 = \langle j|D^\dagger D|i\rangle_3$. To obtain a compact expression, we rename the dummy indices labeling the states on each site (e.g., in line three, we change indices as $k \to i$, $k' \to j$, $j = j' \to \alpha$, and $i = i' \to \beta$). This yields

$$\begin{aligned} A(\mathbf{q}) \sim \sum_{i,j,\alpha,\beta} &[(\tilde{c}^*_{j\alpha\beta}c_{i\alpha\beta}e^{iqd} + \tilde{c}^*_{\beta\alpha j}c_{\beta\alpha i}e^{-iqd})\langle j|D^\dagger D|i\rangle_1 \\ &+ \tilde{c}^*_{\alpha j\beta}c_{\alpha i\beta}\langle j|D^\dagger D|i\rangle_2]. \end{aligned} \tag{B5}$$

Note, that the RIXS amplitude on the middle site M_2 may differ from the ones on the outer sites and, thus, cannot be combined with the other two terms. This is, e.g., the case for a face-sharing trimer, where the middle octahedron is rotated by 180° around the global z axis compared to the outer ones.

If the initial and final states have different symmetry, one may use $\tilde{c}^*_{\beta\alpha j}c_{\beta\alpha i} = -c^*_{j\alpha\beta}c_{i\alpha\beta}$ to simplify the expression further,

$$A_{eo}(\mathbf{q}) \sim \sum_{i,j,\alpha,\beta}\tilde{c}^*_{j\alpha\beta}c_{i\alpha\beta}\underbrace{(e^{iqd} - e^{-iqd})}_{2i\sin(qd)}\langle j|D^\dagger D|i\rangle_1, \tag{B6}$$

where the contribution from the middle site vanishes under summation over α and β. The full intensity for an excitation that flips the symmetry is then given by

$$I_{eo}(q) \sim 4\,\sin^2(qd)\left|\sum_{i,j,\alpha\beta}\tilde{c}^*_{j\alpha\beta}c_{i\alpha\beta}\,\langle j|D^\dagger D|i\rangle_1\right|^2, \tag{B7}$$

as claimed in the main text [see Eq. (9)].

For excitations between states with the same symmetry, we also can combine the terms from the outer sites (now with a plus sign), but the contribution from the middle site will not vanish (the only difference is that $c_{\alpha j\alpha}$ is required to vanish for odd states),

$$\begin{aligned} A_{ee}(\mathbf{q}) &= \sum_{i,j,\alpha,\beta}\tilde{c}^*_{j\alpha\beta}c_{i\alpha\beta}\,2\,\cos(qd)\langle j|D^\dagger D|i\rangle_1 \\ &\quad + \tilde{c}^*_{\alpha j\beta}c_{\alpha i\beta}\,\langle j|D^\dagger D|i\rangle_2 \\ &= \cos(qd)\underbrace{\sum_{i,j,\alpha,\beta}2\tilde{c}^*_{j\alpha\beta}c_{i\alpha\beta}\langle j|D^\dagger D|i\rangle_1}_{a} \\ &\quad + \underbrace{\sum_{i,j,\alpha,\beta}\tilde{c}^*_{\alpha j\beta}c_{\alpha i\beta}\langle j|D^\dagger D|i\rangle_2}_{b}. \end{aligned} \tag{B8}$$

Note that a and b may have a different dependence on q, even in the case where the dipole matrix elements are the same for all three sites since the summation over the eigenstates may differ for outer and inner sites. From the amplitude in Eq. (B8), it immediately follows that the RIXS intensities for excitations between states with the same symmetry are given as claimed in Eq. (11),

$$I_{ee}(q) \sim |a|^2\cos^2(qd) + (a^*b + b^*a)\cos(qd) + |b|^2. \tag{B9}$$

[1] D. I. Khomskii and S. V. Streltsov, Orbital effects in Solids: Basics, recent progress, and opportunities, Chem. Rev. **121**, 2992 (2021).

[2] R. Pocha, D. Johrendt, and R. Pöttgen, Electronic and structural instabilities in GaV_4S_8 and $GaMo_4S_8$, Chem. Mater. **12**, 2882 (2000).

[3] M. M. Abd-Elmeguid, B. Ni, D. I. Khomskii, R. Pocha, D. Johrendt, X. Wang, and K. Syassen, Transition from Mott insulator to superconductor in $GaNb_4Se_8$ and $GaTa_4Se_8$ under high pressure, Phys. Rev. Lett. **93**, 126403 (2004).

[4] J. P. Sheckelton, J. R. Neilson, D. G. Soltan, and T. M. McQueen, Possible valence-bond condensation in the

frustrated cluster magnet $LiZn_2Mo_3O_8$, Nat. Mater. **11**, 493 (2012).

[5] G. Chen, H.-Y. Kee, and Y. B. Kim, Fractionalized charge excitations in a spin liquid on partially filled pyrochlore lattices, Phys. Rev. Lett. **113**, 197202 (2014).

[6] J.-P. Lv, G. Chen, Y. Deng, and Z. Y. Meng, Coulomb liquid phases of bosonic cluster Mott insulators on a pyrochlore lattice, Phys. Rev. Lett. **115**, 037202 (2015).

[7] A. Revelli, M. M. Sala, G. Monaco, P. Becker, L. Bohatý, M. Hermanns, T. C. Koethe, T. Fröhlich, P. Warzanowski, T. Lorenz, S. V. Streltsov, P. H. M. van Loosdrecht, D. I. Khomskii, J. van den Brink, and M. Grüninger, Resonant inelastic x-ray incarnation of Young's double-slit experiment, Sci. Adv. **5**, eaav4020 (2019).

[8] A. Revelli, M. Moretti Sala, G. Monaco, M. Magnaterra, J. Attig, L. Peterlini, T. Dey, A. A. Tsirlin, P. Gegenwart, T. Fröhlich, M. Braden, C. Grams, J. Hemberger, P. Becker, P. H. M. van Loosdrecht, D. I. Khomskii, J. van den Brink, M. Hermanns, and M. Grüninger, Quasimolecular electronic structure of the spin-liquid candidate $Ba_3InIr_2O_9$, Phys. Rev. B **106**, 155107 (2022).

[9] M. Magnaterra, M. Moretti Sala, G. Monaco, P. Becker, M. Hermanns, P. Warzanowski, T. Lorenz, D. I. Khomskii, P. H. M. van Loosdrecht, J. van den Brink, and M. Grüninger, RIXS interferometry and the role of disorder in the quantum magnet $Ba_3Ti_{3-x}Ir_xO_9$, Phys. Rev. Res. **5**, 013167 (2023).

[10] M. Magnaterra, J. Attig, L. Peterlini, M. Hermanns, M. H. Upton, J. Kim, L. Prodan, V. Tsurkan, I. Kézsmárki, P. H. M. van Loosdrecht, and M. Grüninger, Quasimolecular $J_{\text{tet}} = 3/2$ moments in the cluster Mott insulator $GaTa_4Se_8$, Phys. Rev. Lett. **133**, 046501 (2024).

[11] V. Jayakumar and C. Hickey, Elementary building blocks for cluster Mott insulators, arXiv:2310.01060.

[12] G. V. Chen and C. Wu, Multiflavor Mott insulators in quantum materials and ultracold atoms, npj Quantum Mater. **9**, 1 (2024).

[13] Y. Li, A. A. Tsirlin, T. Dey, P. Gegenwart, R. Valentí, and S. M. Winter, Soft and anisotropic local moments in 4*d* and 5*d* mixed-valence M_2O_9 dimers, Phys. Rev. B **102**, 235142 (2020).

[14] G. Jackeli and G. Khaliullin, Mott insulators in the strong spin-orbit coupling limit: From Heisenberg to a quantum compass and Kitaev models, Phys. Rev. Lett. **102**, 017205 (2009).

[15] S. Hwan Chun, J.-W. Kim, J. Kim, H. Zheng, C. C. Stoumpos, C. D. Malliakas, J. F. Mitchell, K. Mehlawat, Y. Singh, Y. Choi, T. Gog, A. Al-Zein, M. Moretti Sala, M. Krisch, J. Chaloupka, G. Jackeli, G. Khaliullin, and B. J. Kim, Direct evidence for dominant bond-directional interactions in a honeycomb lattice iridate Na_2IrO_3, Nat. Phys. **11**, 462 (2015).

[16] M. Magnaterra, K. Hopfer, C. J. Sahle, M. Moretti Sala, G. Monaco, J. Attig, C. Hickey, I. M. Pietsch, F. Breitner, P. Gegenwart, M. H. Upton, J. Kim, S. Trebst, P. H. M. van Loosdrecht, J. van den Brink, and M. Grüninger, RIXS observation of bond-directional nearest-neighbor excitations in the Kitaev material Na_2IrO_3, arXiv:2301.08340.

[17] Y. Doi and Y. Hinatsu, The structural and magnetic characterization of 6*H*-perovskite-type oxides $Ba_3LnIr_2O_9$ (Ln = Y, lanthanides), J. Phys.: Condens. Matter **16**, 2849 (2004).

[18] Y. Shimoda, Y. Doi, M. Wakeshima, and Y. Hinatsu, Synthesis and magnetic properties of 12L-perovskites $Ba_4LnIr_3O_{12}$ (Ln = lanthanides), J. Solid State Chem. **182**, 2873 (2009).

[19] Y. Shimoda, Y. Doi, M. Wakeshima, and Y. Hinatsu, Magnetic and electrical properties of quadruple perovskites with 12 layer structures $Ba_4LnM_3O_{12}$ (Ln = rare earths; M = Ru, Ir): The role of metal–metal bonding in perovskite-related oxides, J. Solid State Chem. **183**, 1962 (2010).

[20] D. Khomskii, K. Kugel, A. Sboychakov, and S. Streltsov, Role of local geometry in the spin and orbital structure of transition metal compounds, J. Exp. Theor. Phys. **122**, 484 (2016).

[21] E. V. Komleva, D. I. Khomskii, and S. V. Streltsov, Three-site transition-metal clusters: Going from localized electrons to molecular orbitals, Phys. Rev. B **102**, 174448 (2020).

[22] G. Cao, J. Crow, R. Guertin, P. Henning, C. Homes, M. Strongin, D. Basov, and E. Lochner, Charge density wave formation accompanying ferromagnetic ordering in quasi-one-dimensional $BaIrO_3$, Solid State Commun. **113**, 657 (2000).

[23] J. Zhao, L. Yang, Y. Yu, F. Li, R. Yu, and C. Jin, Structural and physical properties of the 6*M* $BaIrO_3$: A new metallic iridate synthesized under high pressure, Inorg. Chem. **48**, 4290 (2009).

[24] I. Terasaki, S. Ito, T. Igarashi, S. Asai, H. Taniguchi, R. Okazaki, Y. Yasui, K. Kobayashi, R. Kumai, H. Nakao, and Y. Murakami, Novel charge ordering in the trimer iridium oxide $BaIrO_3$, Crystals **6**, 27 (2016).

[25] R. Okazaki, S. Ito, K. Tanabe, H. Taniguchi, Y. Ikemoto, T. Moriwaki, and I. Terasaki, Spectroscopic signature of trimer Mott insulator and charge disproportionation in $BaIrO_3$, Phys. Rev. B **98**, 205131 (2018).

[26] T. Dey, M. Majumder, J. C. Orain, A. Senyshyn, M. Prinz-Zwick, S. Bachus, Y. Tokiwa, F. Bert, P. Khuntia, N. Büttgen, A. A. Tsirlin, and P. Gegenwart, Persistent low-temperature spin dynamics in the mixed-valence iridate $Ba_3InIr_2O_9$, Phys. Rev. B **96**, 174411 (2017).

[27] H.-S. Kim, J. Im, M. J. Han, and H. Jin, Spin-orbital entangled molecular j_{eff} states in lacunar spinel compounds, Nat. Commun. **5**, 3988 (2014).

[28] M. Y. Jeong, S. H. Chang, B. H. Kim, J.-H. Sim, A. Said, D. Casa, T. Gog, E. Janod, L. Cario, S. Yunoki, M. J. Han, and J. Kim, Direct experimental observation of the molecular $J_{\text{eff}} = 3/2$ ground state in the lacunar spinel $GaTa_4Se_8$, Nat. Commun. **8**, 782 (2017).

[29] Y. Ma and M. Blume, Interference of fluorescence x rays and coherent excitation of core levels, Rev. Sci. Instrum. **66**, 1543 (1995).

[30] F. Gel'mukhanov and H. Ågren, Resonant inelastic x-ray scattering with symmetry-selective excitation, Phys. Rev. A **49**, 4378 (1994).

[31] V. M. Katukuri, X. Lu, D. E. McNally, M. Dantz, V. N. Strocov, M. M. Sala, M. H. Upton, J. Terzic, G. Cao, O. V. Yazyev, and T. Schmitt, Charge ordering in Ir dimers in the ground state of $Ba_5AlIr_2O_{11}$, Phys. Rev. B **105**, 075114 (2022).

[32] J. Luo, G. T. Trammell, and J. P. Hannon, Scattering operator for elastic and inelastic resonant x-ray scattering, Phys. Rev. Lett. **71**, 287 (1993).

[33] J. van den Brink and M. van Veenendaal, Correlation functions measured by indirect resonant inelastic X-ray scattering, Europhys. Lett. **73**, 121 (2006).

[34] L. J. P. Ament, G. Khaliullin, and J. van den Brink, Theory of resonant inelastic x-ray scattering in iridium oxide compounds:

Probing spin-orbit-entangled ground states and excitations, Phys. Rev. B **84**, 020403(R) (2011).

[35] L. J. P. Ament, M. van Veenendaal, T. P. Devereaux, J. P. Hill, and J. van den Brink, Resonant inelastic x-ray scattering studies of elementary excitations, Rev. Mod. Phys. **83**, 705 (2011).

[36] F. Gel'mukhanov, M. Odelius, S. P. Polyutov, A. Föhlisch, and V. Kimberg, Dynamics of resonant x-ray and Auger scattering, Rev. Mod. Phys. **93**, 035001 (2021).

[37] J. Söderström, A. Ghosh, L. Kjellsson, V. Ekholm, T. Tokushima, C. Såthe, N. Velasquez, M. Simon, O. Björneholm, L. Duda, A. N. de Brito, M. Odelius, J.-C. Liu, J. Wang, V. Kimberg, M. Agåker, J.-E. Rubensson, and F. Gel'mukhanov, Parity violation in resonant inelastic soft x-ray scattering at entangled core holes, Sci. Adv. **10**, eadk3114 (2024).

[38] Z. Porter, P. M. Sarte, T. Petersen, M. H. Upton, L. Hozoi, and S. D. Wilson, Spin-orbit excitons and electronic configuration of the $5d^4$ insulator $Sr_3Ir_2O_7F_2$, Phys. Rev. B **106**, 115140 (2022).

[39] A. Revelli, M. Moretti Sala, G. Monaco, C. Hickey, P. Becker, F. Freund, A. Jesche, P. Gegenwart, T. Eschmann, F. L. Buessen, S. Trebst, P. H. M. van Loosdrecht, J. van den Brink, and M. Grüninger, Fingerprints of Kitaev physics in the magnetic excitations of honeycomb iridates, Phys. Rev. Res. **2**, 043094 (2020).

[40] T. Ren, Y. Shen, S. F. R. TenHuisen, J. Sears, W. He, M. H. Upton, D. Casa, P. Becker, M. Mitrano, M. P. M. Dean, and R. M. Konik, Witnessing quantum entanglement using resonant inelastic x-ray scattering, arXiv:2404.05850.

[41] L. T. Nguyen, T. Kong, and R. J. Cava, Trimers of MnO_6 octahedra and ferrimagnetism of $Ba_4NbMn_3O_{12}$, Mater. Res. Express **6**, 056108 (2019).

[42] L. T. Nguyen and R. J. Cava, Hexagonal perovskites as quantum materials, Chem. Rev. **121**, 2935 (2021).

[43] L. T. Nguyen and R. J. Cava, Trimer-based spin liquid candidate $Ba_4NbIr_3O_{12}$, Phys. Rev. Mater. **3**, 014412 (2019).

[44] G. S. Thakur, S. Chattopadhyay, T. Doert, T. Herrmannsdörfer, and C. Felser, Crystal growth of spin-frustrated $Ba_4Nb_{0.8}Ir_{3.2}O_{12}$: A possible spin liquid material, Cryst. Growth Des. **20**, 2871 (2020).

[45] A. Bandyopadhyay, S. Lee, D. T. Adroja, M. R. Lees, G. B. G. Stenning, P. Aich, L. Tortora, C. Meneghini, G. Cibin, A. Berlie, R. A. Saha, D. Takegami, A. Meléndez-Sans, G. Poelchen, M. Yoshimura, K. D. Tsuei, Z. Hu, T.-S. Chan, S. Chattopadhyay, G. S. Thakur *et al.*, Gapless dynamic magnetic ground state in the charge-gapped trimer iridate $Ba_4NbIr_3O_{12}$, Phys. Rev. Mater. **8**, 074405 (2024).

[46] A. Ali, H.-S. Kim, P. Yadav, S. Lee, D. Yoon, and S. Choi, Partial molecular orbitals in face-sharing $3d$ manganese trimer: Comparative studies on $Ba_4TaMn_3O_{12}$ and $Ba_4NbMn_3O_{12}$, Phys. Rev. Res. **6**, 013231 (2024).

[47] H. Zhao, Y. Zhang, P. Schlottmann, R. Nandkishore, L. E. DeLong, and G. Cao, Transition between heavy-fermion-strange-metal and quantum spin liquid in a $4d$-electron trimer lattice, Phys. Rev. Lett. **132**, 226503 (2024).

[48] W. Miiller, M. T. Dunstan, Z. Huang, Z. Mohamed, B. J. Kennedy, M. Avdeev, and C. D. Ling, Complex $5d$ magnetism in a novel $S = 1/2$ trimer system, the $12L$ hexagonal perovskite $Ba_4BiIr_3O_{12}$, Inorg. Chem. **52**, 12461 (2013).

[49] P. E. Blanchard, K. W. Chapman, S. M. Heald, M. Zbiri, M. R. Johnson, B. J. Kennedy, and C. D. Ling, Direct observation of pressure-driven valence electron transfer in $Ba_3BiRu_2O_9$, $Ba_3BiIr_2O_9$, and $Ba_4BiIr_3O_{12}$, Inorg. Chem. **55**, 5649 (2016).

[50] G. R. Blake, P. D. Battle, J. Sloan, J. F. Vente, J. Darriet, and F. Weill, Neutron diffraction study of the structures of $Ba_5CuIr_3O_{12}$ and $Ba_{16}Cu_3Ir_{10}O_{39}$, Chem. Mater. **11**, 1551 (1999).

[51] M. Ye, H.-S. Kim, J.-W. Kim, C.-J. Won, K. Haule, D. Vanderbilt, S.-W. Cheong, and G. Blumberg, Covalency-driven collapse of strong spin-orbit coupling in face-sharing iridium octahedra, Phys. Rev. B **98**, 201105(R) (2018).

[52] P. A. Volkov, C.-J. Won, D. I. Gorbunov, J. Kim, M. Ye, H.-S. Kim, J. H. Pixley, S.-W. Cheong, and G. Blumberg, Random singlet state in $Ba_5CuIr_3O_{12}$ single crystals, Phys. Rev. B **101**, 020406(R) (2020).

[53] G. Cao, H. Zheng, H. Zhao, Y. Ni, C. A. Pocs, Y. Zhang, F. Ye, C. Hoffmann, X. Wang, M. Lee, M. Hermele, and I. Kimchi, Quantum liquid from strange frustration in the trimer magnet $Ba_4Ir_3O_{10}$, npj Quantum Mater. **5**, 26 (2020).

[54] Y. Shen, J. Sears, G. Fabbris, A. Weichselbaum, W. Yin, H. Zhao, D. G. Mazzone, H. Miao, M. H. Upton, D. Casa, R. Acevedo-Esteves, C. Nelson, A. M. Barbour, C. Mazzoli, G. Cao, and M. P. M. Dean, Emergence of spinons in layered trimer iridate $Ba_4Ir_3O_{10}$, Phys. Rev. Lett. **129**, 207201 (2022).

[55] X. Chen, Y. He, S. Wu, Y. Song, D. Yuan, E. Bourret-Courchesne, J. P. C. Ruff, Z. Islam, A. Frano, and R. J. Birgeneau, Structural and magnetic transitions in the planar antiferromagnet $Ba_4Ir_3O_{10}$, Phys. Rev. B **103**, 224420 (2021).

[56] B. Yuan, J. P. Clancy, A. M. Cook, C. M. Thompson, J. Greedan, G. Cao, B. C. Jeon, T. W. Noh, M. H. Upton, D. Casa, T. Gog, A. Paramekanti, and Y.-J. Kim, Determination of Hund's coupling in $5d$ oxides using resonant inelastic x-ray scattering, Phys. Rev. B **95**, 235114 (2017).

[57] M. Kusch, V. M. Katukuri, N. A. Bogdanov, B. Büchner, T. Dey, D. V. Efremov, J. E. Hamann-Borrero, B. H. Kim, M. Krisch, A. Maljuk, M. M. Sala, S. Wurmehl, G. Aslan-Cansever, M. Sturza, L. Hozoi, J. van den Brink, and J. Geck, Observation of heavy spin-orbit excitons propagating in a non-magnetic background: The case of $(Ba, Sr)_2YIrO_6$, Phys. Rev. B **97**, 064421 (2018).

[58] A. Nag, S. Bhowal, A. Chakraborty, M. M. Sala, A. Efimenko, F. Bert, P. K. Biswas, A. D. Hillier, M. Itoh, S. D. Kaushik, V. Siruguri, C. Meneghini, I. Dasgupta, and S. Ray, Origin of magnetic moments and presence of spin-orbit singlets in Ba_2YIrO_6, Phys. Rev. B **98**, 014431 (2018).

[59] A. A. Aczel, Q. Chen, J. P. Clancy, C. de la Cruz, D. Reig-i-Plessis, G. J. MacDougall, C. J. Pollock, M. H. Upton, T. J. Williams, N. LaManna, J. P. Carlo, J. Beare, G. M. Luke, and H. D. Zhou, Spin-orbit coupling controlled ground states in the double perovskite iridates A_2BIrO_6 (A = Ba, Sr; B = Lu, Sc), Phys. Rev. Mater. **6**, 094409 (2022).

[60] A. de la Torre, B. Zager, J. R. Chamorro, M. H. Upton, G. Fabbris, D. Haskel, D. Casa, T. M. McQueen, and K. W. Plumb, Electronic ground state of two nonmagnetic pentavalent honeycomb iridates, Phys. Rev. Mater. **6**, 084406 (2022).

[61] P. Warzanowski, M. Magnaterra, P. Stein, G. Schlicht, Q. Faure, C. J. Sahle, T. Lorenz, P. Becker, L. Bohatý, M. Moretti Sala, G. Monaco, P. H. M. van Loosdrecht, and M. Grüninger, Electronic excitations in $5d^4 J = 0$ Os^{4+} halides studied by resonant

inelastic x-ray scattering and optical spectroscopy, Phys. Rev. B **108**, 125120 (2023).

[62] M. Moretti Sala, K. Martel, C. Henriquet, A. Al Zein, L. Simonelli, C. J. Sahle, H. Gonzalez, M.-C. Lagier, C. Ponchut, S. Huotari, R. Verbeni, M. Krisch, and G. Monaco, A high-energy-resolution resonant inelastic X-ray scattering spectrometer at ID20 of the European Synchrotron Radiation Facility, J. Synchrotron Rad. **25**, 580 (2018).

[63] M. Minola, G. Dellea, H. Gretarsson, Y. Y. Peng, Y. Lu, J. Porras, T. Loew, F. Yakhou, N. B. Brookes, Y. B. Huang, J. Pelliciari, T. Schmitt, G. Ghiringhelli, B. Keimer, L. Braicovich, and M. Le Tacon, Collective nature of spin excitations in superconducting cuprates probed by resonant inelastic x-ray scattering, Phys. Rev. Lett. **114**, 217003 (2015).

[64] H. Gretarsson, J. P. Clancy, X. Liu, J. P. Hill, E. Bozin, Y. Singh, S. Manni, P. Gegenwart, J. Kim, A. H. Said, D. Casa, T. Gog, M. H. Upton, H.-S. Kim, J. Yu, V. M. Katukuri, L. Hozoi, J. van den Brink, and Y.-J. Kim, Crystal-field splitting and correlation effect on the electronic structure of A_2IrO_3, Phys. Rev. Lett. **110**, 076402 (2013).

[65] A. Revelli, C. C. Loo, D. Kiese, P. Becker, T. Fröhlich, T. Lorenz, M. Moretti Sala, G. Monaco, F. L. Buessen, J. Attig, M. Hermanns, S. V. Streltsov, D. I. Khomskii, J. van den Brink, M. Braden, P. H. M. van Loosdrecht, S. Trebst, A. Paramekanti, and M. Grüninger, Spin-orbit entangled $j = 1/2$ moments in Ba_2CeIrO_6: A frustrated fcc quantum magnet, Phys. Rev. B **100**, 085139 (2019).

[66] P. Warzanowski, M. Magnaterra, C. J. Sahle, M. Moretti Sala, P. Becker, L. Bohatý, I. Císařová, G. Monaco, T. Lorenz, P. H. M. van Loosdrecht, J. van den Brink, and M. Grüninger, Spin-orbital-lattice entanglement in the ideal $j = 1/2$ compound K_2IrCl_6, Phys. Rev. B **110**, 195120 (2024).

[67] N. B. Perkins, Y. Sizyuk, and P. Wölfle, Interplay of many-body and single-particle interactions in iridates and rhodates, Phys. Rev. B **89**, 035143 (2014).

[68] M. Moretti Sala, S. Boseggia, D. F. McMorrow, and G. Monaco, Resonant x-ray scattering and the $j_{\text{eff}} = 1/2$ electronic ground state in iridate perovskites, Phys. Rev. Lett. **112**, 026403 (2014).

[69] K. I. Kugel, D. I. Khomskii, A. O. Sboychakov, and S. V. Streltsov, Spin-orbital interaction for face-sharing octahedra: Realization of a highly symmetric SU(4) model, Phys. Rev. B **91**, 155125 (2015).

[70] A. Georges, L. de' Medici, and J. Mravlje, Strong correlations from Hund's coupling, Annu. Rev. Condens. Matter Phys. **4**, 137 (2013).

[71] P. Warzanowski, M. Magnaterra, G. Schlicht, Q. Faure, C. J. Sahle, P. Becker, L. Bohatý, M. M. Sala, G. Monaco, M. Hermanns, P. H. M. van Loosdrecht, and M. Grüninger, Spin-orbit coupling in a half-filled t_{2g} shell: The case of $5d^3$ K_2ReCl_6, Phys. Rev. B **109**, 155149 (2024).

[72] J.-H. Choy, D.-K. Kim, S.-H. Hwang, G. Demazeau, and D.-Y. Jung, XANES and EXAFS studies on the Ir-O bond covalency in ionic iridium perovskites, J. Am. Chem. Soc. **117**, 8557 (1995).

[73] J. P. Clancy, N. Chen, C. Y. Kim, W. F. Chen, K. W. Plumb, B. C. Jeon, T. W. Noh, and Y.-J. Kim, Spin-orbit coupling in iridium-based $5d$ compounds probed by x-ray absorption spectroscopy, Phys. Rev. B **86**, 195131 (2012).

[74] E. Benckiser, L. Fels, G. Ghiringhelli, M. Moretti Sala, T. Schmitt, J. Schlappa, V. N. Strocov, N. Mufti, G. R. Blake, A. A. Nugroho, T. T. M. Palstra, M. W. Haverkort, K. Wohlfeld, and M. Grüninger, Orbital superexchange and crystal field simultaneously at play in YVO_3: Resonant inelastic x-ray scattering at the V L edge and the O K edge, Phys. Rev. B **88**, 205115 (2013).

[75] G. Khaliullin, Excitonic magnetism in Van Vleck–type d^4 Mott insulators, Phys. Rev. Lett. **111**, 197201 (2013).

[76] D. I. Khomskii, *Transition Metal Compounds* (Cambridge University Press, Cambridge, 2014).

[77] N. Kaushal, J. Herbrych, G. Alvarez, and E. Dagotto, Magnetization dynamics fingerprints of an excitonic condensate t_{2g}^4 magnet, Phys. Rev. B **104**, 235135 (2021).

[78] M. Magnaterra, A. Sandberg, H. Schilling, P. Warzanowski, L. Pätzold, E. Bergamasco, C. J. Sahle, B. Detlefs, K. Ruotsalainen, M. Moretti Sala, G. Monaco, P. Becker, Q. Faure, G. S. Thakur, M. Songvilay, C. Felser, P. van Loosdrecht, J. van den Brink, M. Hermanns, and M. Grüninger, Data for "Quasimolecular electronic structure of the trimer iridate $Ba_4NbIr_3O_{12}$", Zenodo (2025), doi: 10.5281/zenodo.14659272.

Chapter 6

Tetramers in $GaTa_4Se_8$

6.1 Quasimolecular $J_{\text{tet}} = 3/2$ Moments in the Cluster Mott Insulator $GaTa_4Se_8$

The lacunar spinel $GaTa_4Se_8$ attracted attention for the presence of a pressure-induced insulator-to-metal transition followed by topological superconductivity [127–131]. $GaTa_4Se_8$ was predicted to host a novel spin-orbit entangled quasimolecular state [133]. In Ref. [205], Jeong *et al.* performed RIXS measurements at the Ta L_3 and L_2 edges with the aim to determine the ground state. However, the interference effect has not been considered correctly, leading to a wrong peak assignment. In the following chapter, we present the results of our RIXS interferometry measurements on the tetrahedral cluster Mott insulator $GaTa_4Se_8$. These results are published in Pub. [3], which we reproduce in the following. This represents the first study of the RIXS interference effect on a tetrahedral cluster. Our results demonstrate that the RIXS modulation is highly sensitive to the detailed composition of the wavefunction. The wavefunction is determined by the competition of different hopping channels, which causes a mixing of the corresponding bonding and antibonding orbitals. Moreover, the mixing causes a renormalization of the effective spin-orbit coupling. This sensitivity proved crucial for the correct peak assignment and for understanding the quasimolecular electronic structure. In Chap. 6.2, we provide further insights into the quasimolecular orbitals of the tetrahedral cluster. Chapter 6.3 discusses the calculation of the RIXS intensity and the interference effects within the tetrahedron. Finally, Chap. 6.4 outlines the setup for calculating quasimolecular orbitals and RIXS intensity for the tetrahedron using Quanty.

Contribution

M. Magnaterra and M. Grüninger conceived the experiment. M. Magnaterra, M. H. Upton, Jungho Kim, and M. Grüninger carried out the experiment at beamline 27-ID at APS. M. Magnaterra analyzed the data. L. Prodan, V. Tsurkan, and I. Kézsmárki synthesized and characterized the single crystals used for the measurements. M. Magnaterra, J. Attig, L. Peterlini, M. Hermanns, and M. Grüninger performed the theoretical analysis and calculations. Central aspects of the interpretation have been worked out in discussions between M. Magnaterra, M. Hermanns, I. Kezsmarki, P. H. M. van Loosdrecht, and M. Grüninger. M. Magnaterra and M. Grüninger wrote the manuscript with input from all authors.

Editors' Suggestion

Quasimolecular $J_{\mathrm{tet}} = 3/2$ Moments in the Cluster Mott Insulator $GaTa_4Se_8$

M. Magnaterra,[1] J. Attig,[2] L. Peterlini,[2] M. Hermanns,[3] M. H. Upton,[4] Jungho Kim,[4] L. Prodan,[5] V. Tsurkan,[5,6] I. Kézsmárki,[5] P. H. M. van Loosdrecht,[1] and M. Grüninger[1]

[1]*Institute of Physics II, University of Cologne, 50937 Cologne, Germany*
[2]*Institute for Theoretical Physics, University of Cologne, 50937 Cologne, Germany*
[3]*Department of Physics, Stockholm University, AlbaNova University Center, SE-106 91 Stockholm, Sweden*
[4]*Advanced Photon Source, Argonne National Laboratory, Argonne, Illinois 60439, USA*
[5]*Experimental Physics V, Center for Electronic Correlations and Magnetism, University of Augsburg, Germany*
[6]*Institute of Applied Physics, Moldova State University, MD 2028, Chisinau, Republic of Moldova*

(Received 21 September 2023; revised 16 April 2024; accepted 7 June 2024; published 22 July 2024)

Quasimolecular orbitals in cluster Mott insulators provide a route to tailor exchange interactions, which may yield novel quantum phases of matter. We demonstrate the cluster Mott character of the lacunar spinel $GaTa_4Se_8$ using resonant inelastic x-ray scattering (RIXS) at the Ta L_3 edge. Electrons are fully delocalized over Ta_4 tetrahedra, forming quasimolecular $J_{\mathrm{tet}} = 3/2$ moments. The modulation of the RIXS intensity as function of the transferred momentum $\mathbf{q}$ allows us to determine the cluster wave function, which depends on competing intracluster hopping terms that mix states with different character. This mixed wave function is decisive for the macroscopic properties since it affects intercluster hopping and exchange interactions and furthermore renormalizes the effective spin-orbit coupling constant. The versatile wave function, tunable via intracluster hopping, opens a new perspective on the large family of lacunar spinels and cluster Mott insulators in general.

DOI: 10.1103/PhysRevLett.133.046501

With strong spin-orbit coupling, novel forms of quantum magnetism may emerge from unconventional magnetic moments that exhibit exotic exchange couplings. The Kitaev spin liquid is a prominent example [1,2]. Bond-directional Kitaev exchange has been realized in, e.g., $5d^5$ honeycomb iridates with spin-orbit-entangled $j = 1/2$ moments [3–7]. Another intriguing case is given by $5d^1$ $j = 3/2$ moments on an fcc lattice, e.g., in double perovskites. These moments experience bond-dependent multipolar interactions, giving rise to a rich phase diagram that includes multipolar order and a chiral quantum spin liquid with Majorana fermion excitations [8–11].

Exchange-coupled local moments exist in Mott insulators, where electrons are localized on individual sites. A new flavor is offered by cluster Mott insulators, which can be viewed as the electronic equivalent of a molecular crystal [12–17]. In these, electrons occupy quasimolecular orbitals that are delocalized over a cluster, e.g., a dimer or trimer, while intercluster charge fluctuations are suppressed by Coulomb repulsion. The emerging quasimolecular magnetic moments are the fundamental units determining the macroscopic low-energy properties. Importantly, the character of these moments can be tuned by internal degrees of freedom. One example is an Ir_2O_9 dimer with three holes as in the spin-liquid candidate $Ba_3InIr_2O_9$ [18]. With increasing intradimer hopping, the dimer moments change from $J_{\mathrm{dim}} = 1/2$ to $3/2$ [19,20]. In general, the quasimolecular wave function depends on competing intracluster hopping terms and is highly sensitive to the cluster shape. The ability to tune intracluster hopping via external or chemical pressure offers the promising perspective to tailor the moments and thereby the character and symmetry of intercluster exchange interactions with the aim to realize novel magnetic quantum phases of matter.

We focus on the transition-metal M_4 tetrahedra in the large family of lacunar spinels AM_4X_8 (M = V, Ti, Mo, Nb, Ta; A = Ga, Ge, Al; X = S, Se, Te) [12,21–24], see Fig. 1. With one electron in a quasimolecular t_2 orbital, ideal $J_{\mathrm{tet}} = 3/2$ moments forming an fcc lattice have been claimed to be realized in $5d$ $GaTa_4Se_8$ [25,26]. Remarkably, a cluster Mott character has also been proposed, mainly based on band-structure calculations, for the $4d$ and even the $3d$ compounds, where smaller hopping competes with larger on-site Coulomb repulsion U [12,13,24,25,27–33]. However, a direct experimental proof of quasimolecular electronic states in the lacunar spinels is still lacking. Such a quasimolecular character is particularly intriguing in light of the complex phase diagrams of the lacunar spinels, which include multiple multiferroic and skyrmion-lattice phases with, e.g., Néel-type skyrmions carrying electric polarization [34–37], (anti-)ferroelectric states with peculiar domain architectures [38–40], and magnetism tied to polar domain walls [41]. The $5d$ Ta compounds host a pressure-induced insulator-to-metal transition followed by topological superconductivity [13,42–44] and an avalanche-type dielectric breakdown of the Mott gap [45].

Here, we address the cluster wave function, which is the essential starting point for a comprehensive understanding of the lacunar spinels. We study $GaTa_4Se_8$ via resonant inelastic x-ray scattering (RIXS) at the Ta L_3 edge. RIXS directly probes the quasimolecular nature of, e.g., intra-t_2^1 excitations and pinpoints that the electrons are fully delocalized over a Ta_4 tetrahedron while correlations hardly affect the t_2^1 manifold. We find that the quasimolecular $J_{\mathrm{tet}} = 3/2$ wave function deviates from the idealized case assumed previously [25,26], since competing intracluster hopping terms mutually mix the corresponding bonding and antibonding orbitals. In $GaTa_4Se_8$, this mixing reduces the effective spin-orbit coupling constant ζ_{eff} by roughly $1/3$. Arising from strong hopping, the mixing is not a small perturbation and can be expected to affect the exchange interactions. Based on this mixing, the cluster wave function is sensitive to structural changes due to, e.g., external pressure or chemical substitution, which provides a new perspective on the entire family of lacunar spinels.

The delocalization of electrons over a cluster yields a characteristic modulation of the RIXS intensity $I(\mathbf{q})$ as function of the transferred momentum $\mathbf{q}$ [46,47]. This modulation reflects the dynamical structure factor $S(\mathbf{q}, \omega)$ and reveals the character and symmetry of electronic states. For a dimer, RIXS can be described as an inelastic version of Young's double-slit experiment [46]. The corresponding sinusoidal interference pattern has been observed recently in $Ba_3CeIr_2O_9$ and related dimer compounds [20,47,48]. Stunningly, a sinusoidal intensity modulation has also been found in the Kitaev material Na_2IrO_3 where it unravels the bond-directional nearest-neighbor character of the magnetic excitations [7,49]. Careful consideration of these interference effects is a prerequisite for the analysis of RIXS in cluster Mott insulators and provides a powerful tool to address the electronic states of $GaTa_4Se_8$.

Single crystals of $GaTa_4Se_8$ were grown by chemical vapor transport [50]. At 300 K, $GaTa_4Se_8$ shows the noncentrosymmetric cubic space group $F\bar{4}3m$ with lattice constant $a = 10.382$ Å [23], see Fig. 1. The short intratetrahedral Ta-Ta distance $d = 3.0$ Å suggests a quasimolecular character. The optical conductivity characterizes the lacunar spinels as narrow-gap insulators and reveals a Mott gap of 0.12 eV in $GaTa_4Se_8$ [45,51,52]. Experimental results for the magnetic moment per Ta_4 cluster yield 0.7–1.2 μ_B [23,53–55]. The magnetostructural transition at $T_{\mathrm{ms}} = 53$ K is accompanied by a strong drop in the magnetic susceptibility [53,55,56], but the crystal symmetry at low temperature is still under debate [24,55–57]. We first focus on cubic symmetry and then address the effect of distortions.

We measured RIXS at the Ta L_3 edge at Sector 27 at the Advanced Photon Source [58]. The incident energy 9.879 keV resonantly enhances excitations within the Ta t_{2g} orbitals [26]. We studied a (111) surface with the (110) and (001) directions in the horizontal scattering plane, using incident π polarization. An energy resolution $\Delta E = 76$ meV was achieved using a Si(440) four-bounce monochromator and a $R = 2$ m Si(066) spherical diced crystal analyzer. We measured RIXS spectra by scanning the energy loss at constant $\mathbf{q}$, see Fig. 2(a), and the intensity modulation by scanning $\mathbf{q}$ at constant energy loss, see Figs. 2(b), 2(c). We subtracted a constant background intensity that was determined by averaging over a range of negative energy loss. All data have been corrected for geometrical self-absorption [59]. We express $\mathbf{q}$ in reciprocal lattice units (r.l.u.). The $\mathbf{q}$ resolution equals $\Delta\mathbf{q} = (0.1\,0.1\,0.3)$.

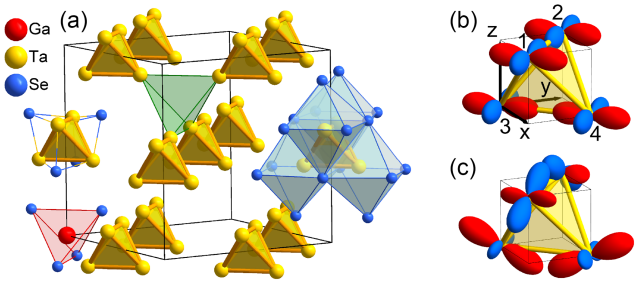

FIG. 1. (a) Simplified sketch of cubic $GaTa_4Se_8$ [23]. Not all Ga and Se ions are shown. The structure corresponds to a NaCl-like lattice of tetrahedral $(GaSe_4)^{-5}$ (red) and heterocubane $(Ta_4Se_4)^{+5}$ units. Tetrahedral Ta_4 clusters (yellow) arise from edge-sharing $TaSe_6$ octahedra (blue) and form an fcc lattice. The intracluster Ta-Ta distance $d = 3.0$ Å is much shorter than the intercluster one (4.3 Å, edges of green tetrahedron). (b) Bonding quasimolecular xy_b orbital, see Eq. (1). (c) $t_2(xy)$ orbital with sizable antibonding character, see Eq. (3) for $\alpha = 2$.

The RIXS spectra of $GaTa_4Se_8$ show three peaks A, B, and C at about 0.25, 0.62, and 1.2 eV, see Fig. 2(a). The peak energies hardly show any dispersion but the intensity strongly depends on $\mathbf{q}$, in agreement with the data of Jeong *et al.* [26]. This is a first indication of the local, quasimolecular character of the electronic states. For the peak assignment, we address the electronic structure of a single Ta_4 tetrahedron, starting with a noninteracting picture in the undistorted cubic case. Note that the RIXS data at 20 and 100 K, i.e., above and below the structural transition at 53 K, are very similar.

Because of the large cubic crystal-field splitting $10\,Dq \approx 3$ eV [26], it is sufficient to consider the Ta t_{2g} states. Direct σ-type hopping $t_\sigma \equiv t_{dd\sigma}$ of order 1 eV [25] yields bonding (b) and antibonding (ab) states at $\pm t_\sigma$. Adding π-type hopping $t_\pi \equiv t_{dd\pi}$ results in the quasimolecular orbitals a_1, e, and t_2 at low energy and further states at high energy, see Fig. 3(a). With 7 electrons per Ta_4 cluster, the ground state shows fully occupied a_1 and e orbitals plus a single electron in the t_2 states, $a_1^2 e^4 t_2^1$. The three t_2 orbitals are central to our discussion. Because of t_π, they are mixtures of bonding and antibonding states of t_σ, see Fig. 3(a). We will show the relevance of this mixture below but first follow the typical assumption where only the bonding ones are considered.

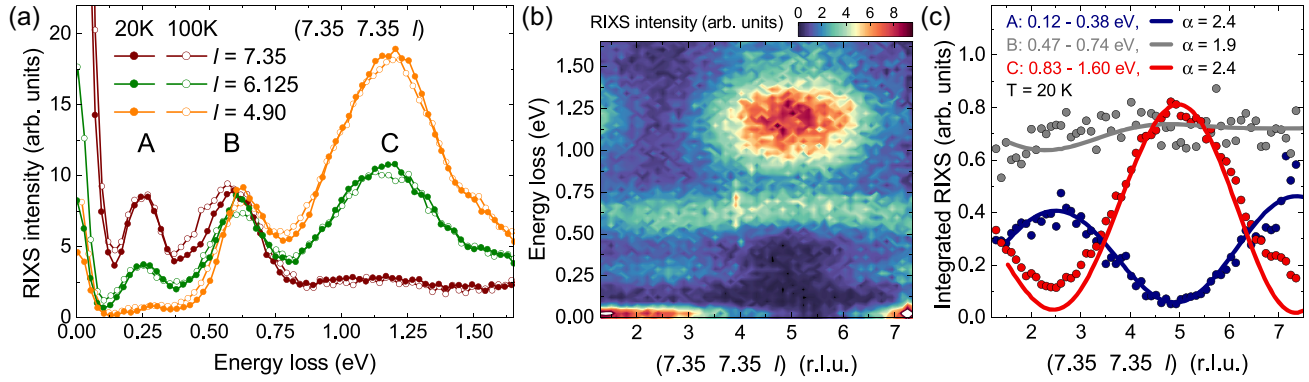

FIG. 2. RIXS data of $GaTa_4Se_8$ along $(7.35\,7.35\,l)$. (a) Spectra acquired at 20 and 100 K show the three peaks A, B, and C. Changing $\mathbf{q}$ strongly affects the intensity. (b) Color map of the RIXS intensity at 20 K. Independent of the cluster modulation, the elastic line is suppressed around $l = 5.4$ due to a scattering angle 2θ close to 90°. (c) Integrated intensity of peaks A, B, and C. Integration intervals are given in the panel. The data of peak C are scaled down by a factor 5 to facilitate comparison. Peaks A and C show dominant $\sin^2(\pi l/4.9)$ and $\cos^2(\pi l/4.9)$ behavior, respectively. Solid lines: Results of the single-particle model, where the intensity has been adapted to the experimental data. Very similar behavior of the $\mathbf{q}$-dependent intensity is observed at 100 K, see Supplemental Material [60].

This yields [cf. Fig. 1(b)]

$$xy_b = (xy_1 + xy_2 + xy_3 + xy_4)/2 \qquad (1)$$

and equivalent for yz_b and xz_b, where $i = 1$–4 denotes the Ta sites. Projecting spin-orbit coupling ζ onto the subspace of these t_2^1 states yields a cluster Hamiltonian that is fully equivalent to the single-site case [3], see Supplemental Material [60]. It shows a $J_{\text{tet}} = 3/2$ ground state and a $J_{\text{tet}} = 1/2$ excited state at 1.5ζ [25]. The latter, the so-called spin-orbit exciton, corresponds to peak A, while peaks B and C in this non-interacting scenario are assigned to excitations from e to J_{tet} states, i.e., from $e^4t_2^1$ to $e^3t_2^2$, see Fig. 3(a).

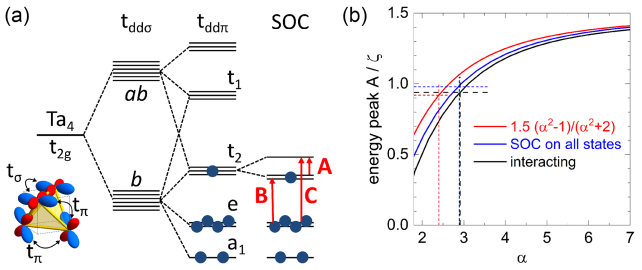

FIG. 3. (a) Single-particle energy levels of a Ta_4 tetrahedron. Intracluster hopping (see bottom left) yields quasimolecular orbitals and an $a_1^2e^4t_2^1$ ground state. Because of t_π, the t_2 orbitals show contributions of bonding (b) and antibonding (ab) states of t_σ. Spin-orbit coupling within the t_2^1 states forms a $J_{\text{tet}} = 3/2$ ground state. A, B, and C refer to the RIXS peaks, see Fig. 2. (b) The admixture of antibonding character renormalizes the energy of peak A, see Eq. (3). Red (blue): single-particle result for spin-orbit coupling within t_2 (all) states. Black: many-body cluster calculation using Quanty [63], see Supplemental Material [60]. Dashed lines: value of α derived from the $\mathbf{q}$ dependence and corresponding excitation energy.

This peak assignment is supported by quantum chemistry calculations [54] and is confirmed by the characteristic $\mathbf{q}$ dependence of the RIXS intensity. Figure 2(b) is a color plot for energies up to 1.6 eV for $\mathbf{q}$ along $(7.35\,7.35\,l)$, while Fig. 2(c) shows the corresponding integrated RIXS intensity of peaks A, B, and C together with results of a single-particle calculation (see below). Peak B hardly depends on $\mathbf{q}$, while A and C show a pronounced $\sin^2(\pi l/4.9)$ and $\cos^2(\pi l/4.9)$ behavior, respectively, reflecting the different symmetries of the corresponding states. The period $l_0 = 4.9$ points to a Ta-Ta distance of $a/4.9 \approx 2.12$ Å that agrees with the c-axis projection $d/\sqrt{2} \approx 2.12$ Å of the intratetrahedral Ta-Ta distance d. For $h = k = 7.35 = 1.5l_0$, spectra for $l = l_0$ and $l = 1.5l_0$ correspond to extrema of the intensity modulation, cf. Fig. 2(a).

The dominant $\sin^2(\pi l/4.9)$ behavior of peak A is a clear fingerprint of the quasimolecular intra-t_2^1 spin-orbit exciton. In general, the RIXS intensity for an excitation from the ground state $|0\rangle$ to a final state $|f\rangle$ is described by [65,66]

$$I_f(\mathbf{q},\omega) = \left|\langle f|\sum_\gamma e^{i\mathbf{q}\cdot\mathbf{R}_\gamma} D_\gamma^\dagger D_\gamma|0\rangle\right|^2 \delta(\hbar\omega - E_f) \qquad (2)$$

where E_f denotes the excitation energy and D_γ ($D_\gamma^\dagger$) is the local dipole operator for resonant scattering at the Ta site $\mathbf{R}_\gamma$. This coherent sum of local scattering processes is running over all $\mathbf{R}_\gamma$ from which the final state $|f\rangle$ can be reached. For the quasimolecular states in $GaTa_4Se_8$, this refers to the four Ta sites of a tetrahedron. For $\mathbf{q}$ along $(7.35\,7.35\,l) = (1.5l_0\,1.5l_0\,l)$, the physics is particularly simple if we stick to the contribution of bonding states to the quasimolecular t_2 orbitals, see Fig. 3(a), i.e., we employ Eq. (1) and the associated J_{tet} states for spin-orbit coupling within the t_2 states, as discussed above. In this case,

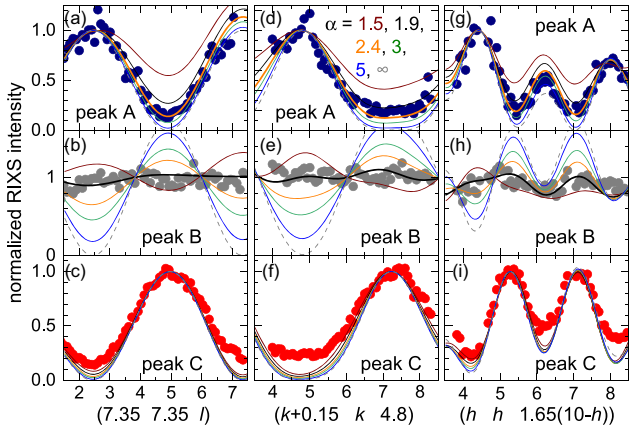

FIG. 4. Normalized RIXS intensity (symbols) along three $\mathbf{q}$ directions for peaks A, B, and C at 20 K with integration ranges as in Fig. 2. Lines: Results of the single-particle model for spin-orbit coupling within the t_2 states. Note that α is the only free parameter. For peaks A and B, best agreement is obtained for $\alpha = 2.4 \pm 0.3$ and 1.8–1.9, respectively. Dashed: Result for $\alpha = \infty$, neglecting antibonding states. For the normalization, an appropriate $\mathbf{q}$ point has been chosen for each panel.

$I_{B/C}(l) \propto \cos^2(\pi l/4.9)$ for all excitations from e to t_2, while only the spin-orbit exciton is expected to show $I_A(l) \propto \sin^2(\pi l/4.9)$, see dashed lines in Figs. 4(a)–4(c). This firmly supports our interpretation of peak A.

Our central goal is to determine the cluster wave function. Thus far, we considered only the bonding contributions to the t_2 orbitals, see Eq. (1), a common approximation [25,26] that, e.g., led to a different peak assignment in Ref. [26]. In this simple bonding picture, $I_C(l)$ describes the overall behavior of peak C but $I_B(l)$ does not explain the nearly $\mathbf{q}$-independent intensity of peak B. Furthermore, this approximation predicts the spin-orbit exciton at 1.5ζ, as for a single site, which is hard to reconcile with the energy of peak A at 0.25 eV. The equivalent excitation for weakly interacting Ta $5d^1$ ions has been observed in RIXS on Rb_2TaCl_6 at 0.4 eV [67], resulting in $\zeta \approx 0.27$ eV. Compared to 0.4 eV, the energy of peak A is about 40% smaller. As shown below, these critical issues are resolved by considering the admixture of antibonding character to the t_2 orbitals. With the intracluster hoppings t_σ and t_π, the eigenstate $t_2(xy)$ of the hopping Hamiltonian reads

$$t_2(xy) = [xy_b - (yz_{ab} - xz_{ab})/\alpha]/\sqrt{1 + (2/\alpha^2)} \quad (3)$$

with the antibonding orbitals $yz_{ab} = (yz_1 - yz_2 + yz_3 - yz_4)/2$ and $xz_{ab} = (xz_1 - xz_2 - xz_3 + xz_4)/2$. The approximation of Eq. (1) corresponds to $\alpha = \infty$. The mixing coefficient reads

$$\alpha = |t_\sigma/t_\pi| - 3/2 + \sqrt{(|t_\sigma/t_\pi| - 3/2)^2 + 2}. \quad (4)$$

Projecting spin-orbit coupling onto this t_2^1 subspace yields the same cluster Hamiltonian as above [60] but with renormalized coupling constant $\zeta_{\text{eff}} = \zeta \cdot (\alpha^2 - 1)/(\alpha^2 + 2)$. Accordingly, the peak assignment of Fig. 3(a) is still valid but α renormalizes in particular the energy of peak A, cf. Fig. 3(b), and changes the character of the quasimolecular J_{tet} states. Using Harrison's empirical d dependence of the Slater-Koster parameters [64], we find $|t_\sigma/t_\pi| = 1.5|V_{dd\sigma}/V_{dd\pi}| \approx 2.8$. This yields a first estimate $\alpha \approx 3.2$. Taking into account hopping t_{Se} via the Se ligands reduces α, for instance to $\alpha \approx 2$ for $t_{\text{Se}} \approx t_\pi$. The $t_2(xy)$ orbital for $\alpha = 2$ is depicted in Fig. 1(c).

Experimentally, the $\mathbf{q}$-dependent RIXS intensity is the ideal tool to determine the mixing coefficient α. Via the matrix elements in Eq. (2), RIXS is directly sensitive to the quasimolecular wave function and hence to the admixture of antibonding orbitals. We calculated the RIXS response in the single-particle picture for spin-orbit coupling within the t_2 states, taking into account polarization selection rules. Results for the normalized RIXS intensities of peaks A, B, and C along (7.35 7.35 l) and two further $\mathbf{q}$ directions are plotted in Fig. 4. Along (k+0.15 k 4.8), the dominant term for peak A is $\cos^4(\pi k/4.9)$ while a more complex behavior is observed along ($h\,h$ 1.65[10-h]). The single-particle picture captures the behavior of all three peaks surprisingly well. We emphasize that α is the only free parameter in Fig. 4, reflecting the dependence of the wave function on t_σ and t_π. These results unambiguously establish the quasimolecular cluster-Mott character of $GaTa_4Se_8$ and that the admixture of antibonding character is sizable, i.e., $1/\alpha$ is not small.

The single-particle picture is expected to work particularly well for the intra-t_2^1 excitation of the spin-orbit exciton, peak A. Peaks B and C with $e^3t_2^2$ final states will be more sensitive to interactions. Peak C is the least sensitive to α. The single-particle model reproduces the overall $\mathbf{q}$ dependence but fails to describe the minima quantitatively. To some extent, this may reflect a possible background contribution of excitations across the Mott gap at high energies. In contrast, peak B is highly sensitive to α. Its nearly constant behavior as a function of $\mathbf{q}$ is reproduced in a narrow window $\alpha = 1.8$–1.9. For peak A, excellent agreement is found for $\alpha = 2.4 \pm 0.3$.

These results for α fall in the range predicted above based on Harrison's rules. The precise value depends on details of the model concerning the range of spin-orbit coupling, distortions, subleading hopping terms, and correlations. Above, spin-orbit coupling was projected onto t_2 orbitals only. If we instead consider all orbitals, in particular, including e and t_1 [see Fig. 3(a)], peak A is best described for $\alpha = 2.9 \pm 0.4$. Furthermore, we discussed regular tetrahedra but the symmetry is lower than cubic below $T_{ms} = 53$ K. Recent x-ray and neutron results on the pair distribution function [57] point to dynamical local distortions up to temperatures far above T_{ms}. For

trigonally distorted tetrahedra, we find that RIXS is sensitive to the distortion if a single orientation can be studied while the average over different orientations is very close to the cubic case, see Supplemental Material [60]. The latter applies to both 20 and 100 K and validates our approach. However, a distortion of the tetrahedra with less than trigonal symmetry affects the value of α for which peak B is nearly independent of $\mathbf{q}$, see Ref. [60]. Note that different results were reported for the crystal symmetry at low temperature [24,55–57], impeding an even more precise determination of α at present.

In a cluster Mott insulator, electron-electron interactions suppress intercluster charge transport. Within a cluster, correlations compete with dominant hopping that delocalizes the electrons in quasimolecular orbitals. To study the effect on the RIXS response, we performed many-body calculations for a single tetrahedron using Quanty [63], see Supplemental Material [60]. Interactions yield a fanning out of the $a_1^2e^3t_2^2$ energy levels that is relevant to explain the width of peak C and the energies of B and C, supporting our peak assignment. For peak A, we find that electron-electron interactions have only a minor effect on both the energy and the $\mathbf{q}$-dependent intensity, in particular for comparison with the case where spin-orbit coupling is not restricted to t_2, see [60]. The many-body calculations thus support the overall picture of the single-particle model.

The renormalized energy of the spin-orbit exciton, peak A, provides an independent means to test our results for α. Figure 3(b) shows the single-particle result for spin-orbit coupling within t_2, $E_{\mathrm{SO}} = 1.5\zeta_{\mathrm{eff}} = 1.5\zeta(\alpha^2-1)/(\alpha^2+2)$. For comparison, the excitation energy is also given for spin-orbit coupling acting on all states and for the many-body cluster calculation. For the latter we change α by changing t_σ, cf. Eq. (4), with all other parameters fixed. The overall behavior is very similar. For all three cases, the dashed lines denote the value of α that best describes the $\mathbf{q}$ dependence. This yields an excitation energy of 0.9–1.0ζ and hence $\zeta \approx 0.27$–0.30 eV, in very good agreement with both quantum chemistry calculations [54] and the value 0.27 eV reported for $5d^1$ Rb_2TaCl_6 [67].

In conclusion, our results establish $GaTa_4Se_8$ as a fascinating example of a cluster Mott insulator. The valence electrons are fully delocalized over a Ta_4 tetrahedron, while intercluster charge fluctuations are suppressed. A thorough analysis of the modulated RIXS intensity $I(\mathbf{q})$ reveals the quasimolecular wave function, which is the essential starting point for exploring the physics of cluster Mott insulators. The spin-orbit exciton, an excitation within the t_2^1 manifold, is particularly well described in a single-particle scenario that is coined by competing hopping terms, t_σ and t_π. This competition shapes the wave function, renormalizes the effective spin-orbit coupling constant by roughly $1/3$, and hence affects the nature of the quasimolecular magnetic moment. We expect that this is decisive for intercluster exchange coupling, calling for future theoretical investigations. In general, the mixing coefficient α also depends on $t_{dd\delta}$ and on the indirect hopping via ligands. Therefore, it is reasonable to assume that α can be tuned in the lacunar spinels by external pressure and chemical substitution, and one may speculate that even temperature may tip the balance in certain cases. Our results on the quasimolecular character, the particular role of antibonding states, and the tunability of the wave function are relevant for many of the open questions on the large family of lacunar spinels.

Acknowledgments—We thank D. I. Khomskii and J. van den Brink for fruitful discussions and A. Revelli for experimental support. We gratefully acknowledge the Advanced Photon Source (APS) for providing beam time and technical support. APS is a U.S. Department of Energy (DOE) Office of Science user facility operated for the DOE Office of Science by Argonne National Laboratory under Contract No. DE-AC02-06CH11357. Furthermore, we acknowledge funding from the Deutsche Forschungsgemeinschaft (DFG, German Research Foundation) via Projects No. 277146847 (CRC 1238, projects B03, C03), 492547816 (TRR 360), and 437124857 (KE 2370/3-1). V. T. acknowledges the support via project ANCD 20.80009.5007.19 (Moldova). M. H. acknowledges partial funding by the Knut and Alice Wallenberg Foundation as part of the Wallenberg Academy Fellows project.

[1] A. Kitaev, Anyons in an exactly solved model and beyond, Ann. Phys. (Amsterdam) **321**, 2 (2006).

[2] M. Hermanns, I. Kimchi, and J. Knolle, Physics of the Kitaev model: Fractionalization, dynamic correlations, and material connections, Annu. Rev. Condens. Matter Phys. **9**, 17 (2018).

[3] G. Jackeli and G. Khaliullin, Mott insulators in the strong spin-orbit coupling limit: From Heisenberg to a quantum compass and Kitaev models, Phys. Rev. Lett. **102**, 017205 (2009).

[4] J. G. Rau, E. K.-H. Lee, and H.-Y. Kee, Spin-orbit physics giving rise to novel phases in correlated systems: Iridates and related materials, Annu. Rev. Condens. Matter Phys. **7**, 195 (2016).

[5] S. Trebst and C. Hickey, Kitaev materials, Phys. Rep. **950**, 1 (2022).

[6] S. H. Chun, J.-W. Kim, J. Kim, H. Zheng, C. C. Stoumpos, C. D. Malliakas, J. F. Mitchell, K. Mehlawat, Y. Singh, Y. Choi, T. Gog, A. Al-Zein, M. Moretti Sala, M. Krisch, J. Chaloupka, G. Jackeli, G. Khaliullin, and B. J. Kim, Direct evidence for dominant bond-directional interactions in a honeycomb lattice iridate Na_2IrO_3, Nat. Phys. **11**, 462 (2015).

[7] M. Magnaterra, K. Hopfer, C. J. Sahle, M. Moretti Sala, G. Monaco, J. Attig, C. Hickey, I.-M. Pietsch, F. Breitner, P. Gegenwart, M. H. Upton, J. Kim, S. Trebst, P. H. M. van Loosdrecht, J. van den Brink, and M. Grüninger, RIXS

observation of bond-directional nearest-neighbor excitations in the Kitaev material Na_2IrO_3, arXiv:2301.08340.
[8] G. Chen, R. Pereira, and L. Balents, Exotic phases induced by strong spin-orbit coupling in ordered double perovskites, Phys. Rev. B **82**, 174440 (2010).
[9] W. M. H. Natori, E. C. Andrade, E. Miranda, and R. G. Pereira, Chiral spin-orbital liquids with nodal lines, Phys. Rev. Lett. **117**, 017204 (2016).
[10] J. Romhányi, L. Balents, and G. Jackeli, Spin-orbit dimers and noncollinear phases in d^1 cubic double perovskites, Phys. Rev. Lett. **118**, 217202 (2017).
[11] A. Mansouri Tehrani, J.-R. Soh, J. Pásztorová, M. E. Merkel, I. Živković, H. M. Rønnow, and N. A. Spaldin, Charge multipole correlations and order in Cs_2TaCl_6, Phys. Rev. Res. **5**, L012010 (2023).
[12] R. Pocha, D. Johrendt, and R. Pöttgen, Electronic and structural instabilities in GaV_4S_8 and $GaMo_4S_8$, Chem. Mater. **12**, 2882 (2000).
[13] M. M. Abd-Elmeguid, B. Ni, D. I. Khomskii, R. Pocha, D. Johrendt, X. Wang, and K. Syassen, Transition from Mott insulator to superconductor in $GaNb_4Se_8$ and $GaTa_4Se_8$ under high pressure, Phys. Rev. Lett. **93**, 126403 (2004).
[14] J. P. Sheckelton, J. R. Neilson, D. G. Soltan, and T. M. McQueen, Possible valence-bond condensation in the frustrated cluster magnet $LiZn_2Mo_3O_8$, Nat. Mater. **11**, 493 (2012).
[15] G. Chen, H.-Y. Kee, and Y. B. Kim, Fractionalized charge excitations in a spin liquid on partially filled pyrochlore lattices, Phys. Rev. Lett. **113**, 197202 (2014).
[16] J.-P. Lv, G. Chen, Y. Deng, and Z. Y. Meng, Coulomb liquid phases of bosonic cluster Mott insulators on a pyrochlore lattice, Phys. Rev. Lett. **115**, 037202 (2015).
[17] D. I. Khomskii and S. V. Streltsov, Orbital effects in solids: Basics, recent progress, and opportunities, Chem. Rev. **121**, 2992 (2021).
[18] T. Dey, M. Majumder, J. C. Orain, A. Senyshyn, M. Prinz-Zwick, S. Bachus, Y. Tokiwa, F. Bert, P. Khuntia, N. Büttgen, A. A. Tsirlin, and P. Gegenwart, Persistent low-temperature spin dynamics in the mixed-valence iridate $Ba_3InIr_2O_9$, Phys. Rev. B **96**, 174411 (2017).
[19] Y. Li, A. A. Tsirlin, T. Dey, P. Gegenwart, R. Valentí, and S. M. Winter, Soft and anisotropic local moments in 4*d* and 5*d* mixed-valence M_2O_9 dimers, Phys. Rev. B **102**, 235142 (2020).
[20] A. Revelli, M. Moretti Sala, G. Monaco, M. Magnaterra, J. Attig, L. Peterlini, T. Dey, A. A. Tsirlin, P. Gegenwart, T. Fröhlich, M. Braden, C. Grams, J. Hemberger, P. Becker, P. H. M. van Loosdrecht, D. I. Khomskii, J. van den Brink, M. Hermanns, and M. Grüninger, Quasimolecular electronic structure of the spin-liquid candidate $Ba_3InIr_2O_9$, Phys. Rev. B **106**, 155107 (2022).
[21] H. Barz, New ferromagnetic molybdenum spinels, Mater. Res. Bull. **8**, 983 (1973).
[22] H. Yaich, J. Jegaden, M. Potel, M. Sergent, A. Rastogi, and R. Tournier, Nouveaux chalcogénures et chalcohalogénures à clusters tétraédriques Nb_4 ou Ta_4, J. Less-Common Met. **102**, 9 (1984).
[23] R. Pocha, D. Johrendt, B. Ni, and M. M. Abd-Elmeguid, Crystal structures, electronic properties, and pressure-induced superconductivity of the tetrahedral cluster compounds $GaNb_4S_8$, $GaNb_4Se_8$, and $GaTa_4Se_8$, J. Am. Chem. Soc. **127**, 8732 (2005).
[24] K. Geirhos, S. Reschke, S. Ghara, S. Krohns, P. Lunkenheimer, and I. Kézsmárki, Optical, dielectric, and magnetoelectric properties of ferroelectric and antiferroelectric lacunar spinels, Phys. Status Solidi (b) **259**, 2100160 (2022).
[25] H.-S. Kim, J. Im, M. Han, and H. Jin, Spin-orbital entangled molecular j_{eff} states in lacunar spinel compounds, Nat. Commun. **5**, 3988 (2014).
[26] M. Y. Jeong, S. H. Chang, B. H. Kim, J.-H. Sim, A. Said, D. Casa, T. Gog, E. Janod, L. Cario, S. Yunoki, M. J. Han, and J. Kim, Direct experimental observation of the molecular $J_{\mathrm{eff}} = 3/2$ ground state in the lacunar spinel $GaTa_4Se_8$, Nat. Commun. **8**, 782 (2017).
[27] D. Johrendt, Crystal and electronic structure of the tetrahedral V_4 cluster compounds GeV_4Q_8 (Q = S, Se), Z. Anorg. Allg. Chem. **624**, 952 (1998).
[28] S. A. Nikolaev and I. V. Solovyev, Microscopic theory of electric polarization induced by skyrmionic order in GaV_4S_8, Phys. Rev. B **99**, 100401(R) (2019).
[29] H. Lee, M. Y. Jeong, J.-H. Sim, H. Yoon, S. Ryee, and M. J. Han, Charge density functional plus U calculation of lacunar spinel GaM_4Se_8 (M = Nb, Mo, Ta, and W), Europhys. Lett. **125**, 47005 (2019).
[30] H.-S. Kim, K. Haule, and D. Vanderbilt, Molecular Mott state in the deficient spinel GaV_4S_8, Phys. Rev. B **102**, 081105(R) (2020).
[31] R. L. Dally, W. D. Ratcliff, II, L. Zhang, H.-S. Kim, M. Bleuel, J. W. Kim, K. Haule, D. Vanderbilt, S.-W. Cheong, and J. W. Lynn, Magnetic phase transitions and spin density distribution in the molecular multiferroic system GaV_4S_8, Phys. Rev. B **102**, 014410 (2020).
[32] L. Hozoi, M. S. Eldeeb, and U. K. Rößler, V_4 tetrahedral units in AV_4X_8 lacunar spinels: Near degeneracy, charge fluctuations, and configurational mixing within a valence space of up to 21 *d* orbitals, Phys. Rev. Res. **2**, 022017(R) (2020).
[33] T. Petersen, P. Bhattacharyya, U. K. Rößler, and L. Hozoi, Resonating holes vs molecular spin-orbit coupled states in group-5 lacunar spinels, Nat. Commun. **14**, 5218 (2023).
[34] I. Kézsmárki, S. Bordács, P. Milde, E. Neuber, L. M. Eng, J. S. White, H. M. Rønnow, C. D. Dewhurst, M. Mochizuki, K. Yanai, H. Nakamura, D. Ehlers, V. Tsurkan, and A. Loidl, Néel-type skyrmion lattice with confined orientation in the polar magnetic semiconductor GaV_4S_8, Nat. Mater. **14**, 1116 (2015).
[35] E. Ruff, S. Widmann, P. Lunkenheimer, V. Tsurkan, I. K. S. Bordács, and A. Loidl, Multiferroicity and skyrmions carrying electric polarization in GaV_4S_8, Sci. Adv. **1**, e15009 (2015).
[36] S. Bordács, A. Butykai, B. G. Szigeti, J. S. White, R. Cubitt, A. O. Leonov, S. Widmann, D. Ehlers, H.-A. K. von Nidda, V. Tsurkan, A. Loidl, and I. Kézsmárki, Equilibrium Skyrmion lattice ground state in a polar easy-plane magnet, Sci. Rep. **7**, 7584 (2017).
[37] A. Butykai, K. Geirhos, D. Szaller, L. F. Kiss, L. Balogh, M. Azhar, M. Garst, L. DeBeer-Schmitt, T. Waki, Y. Tabata, H. Nakamura, I. Kézsmárki, and S. Bordács, Squeezing the periodicity of Néel-type magnetic modulations by enhanced

Dzyaloshinskii-Moriya interaction of 4d electrons, npj Quantum Mater. **7**, 26 (2022).

[38] S. Ghara, K. Geirhos, L. Kuerten, P. Lunkenheimer, V. Tsurkan, M. Fiebig, and I. Kézsmárki, Giant conductivity of mobile non-oxide domain walls, Nat. Commun. **12**, 3975 (2021).

[39] K. Geirhos, J. Langmann, L. Prodan, A. A. Tsirlin, A. Missiul, G. Eickerling, A. Jesche, V. Tsurkan, P. Lunkenheimer, W. Scherer, and I. Kézsmárki, Cooperative cluster Jahn-Teller effect as a possible route to antiferroelectricity, Phys. Rev. Lett. **126**, 187601 (2021).

[40] L. Puntigam, M. Altthaler, S. Ghara, L. Prodan, V. Tsurkan, S. Krohns, I. Kézsmárki, and D. M. Evans, Strain driven conducting domain walls in a Mott insulator, Adv. Electron. Mater. **8**, 2200366 (2022).

[41] K. Geirhos, B. Gross, B. G. Szigeti, A. Mehlin, S. Philipp, J. S. White, R. Cubitt, S. Widmann, S. Ghara, P. Lunkenheimer, V. Tsurkan, E. Neuber, D. Ivaneyko, P. Milde, L. M. Eng, A. O. Leonov, S. Bordács, M. Poggio, and I. Kézsmárki, Macroscopic manifestation of domain-wall magnetism and magnetoelectric effect in a Néel-type Skyrmion host, npj Quantum Mater. **5**, 44 (2020).

[42] M. J. Park, G. Sim, M. Y. Jeong, A. Mishra, M. J. Han, and S. Lee, Pressure-induced topological superconductivity in the spin–orbit Mott insulator $GaTa_4Se_8$, npj Quantum Mater. **5**, 41 (2020).

[43] H. Deng, J. Zhang, M. Y. Jeong, D. Wang, Q. Hu, S. Zhang, R. Sereika, T. Nakagawa, B. Chen, X. Yin, H. Xiao, X. Hong, J. Ren, M. J. Han, J. Chang, H. Weng, Y. Ding, H.-Q. Lin, and H.-K. Mao, Metallization of quantum material $GaTa_4Se_8$ at high pressure, J. Phys. Chem. Lett. **12**, 5601 (2021).

[44] M. Y. Jeong, S. H. Chang, H. J. Lee, J.-H. Sim, K. J. Lee, E. Janod, L. Cario, A. Said, W. Bi, P. Werner, A. Go, J. Kim, and M. J. Han, $J_{\mathrm{eff}} = \frac{3}{2}$ metallic phase and unconventional superconductivity in $GaTa_4Se_8$, Phys. Rev. B **103**, L081112 (2021).

[45] V. Guiot, L. Cario, E. Janod, B. Corraze, V. Ta Phuoc, M. Rozenberg, P. Stoliar, T. Cren, and D. Roditchev, Avalanche breakdown in $GaTa_4Se_{8-x}Te_x$ narrow-gap Mott insulators, Nat. Commun. **4**, 1722 (2013).

[46] Y. Ma and M. Blume, Interference of fluorescence x-rays and coherent excitation of core levels, Rev. Sci. Instrum. **66**, 1543 (1995).

[47] A. Revelli, M. Moretti Sala, G. Monaco, P. Becker, L. Bohatý, M. Hermanns, T. C. Koethe, T. Fröhlich, P. Warzanowski, T. Lorenz, S. V. Streltsov, P. H. M. van Loosdrecht, D. I. Khomskii, J. van den Brink, and M. Grüninger, Resonant inelastic x-ray incarnation of Young's double-slit experiment, Sci. Adv. **5**, eaav4020 (2019).

[48] M. Magnaterra, M. Moretti Sala, G. Monaco, P. Becker, M. Hermanns, P. Warzanowski, T. Lorenz, D. I. Khomskii, P. H. M. van Loosdrecht, J. van den Brink, and M. Grüninger, RIXS interferometry and the role of disorder in the quantum magnet $Ba_3Ti_{3-x}Ir_xO_9$, Phys. Rev. Res. **5**, 013167 (2023).

[49] A. Revelli, M. Moretti Sala, G. Monaco, C. Hickey, P. Becker, F. Freund, A. Jesche, P. Gegenwart, T. Eschmann, F. L. Buessen, S. Trebst, P. H. M. van Loosdrecht, J. van den Brink, and M. Grüninger, Fingerprints of Kitaev physics in the magnetic excitations of honeycomb iridates, Phys. Rev. Res. **2**, 043094 (2020).

[50] M. Winkler, L. Prodan, V. Tsurkan, P. Lunkenheimer, and I. Kézsmárki, Antipolar transitions in $GaNb_4Se_8$ and $GaTa_4Se_8$, Phys. Rev. B **106**, 115146 (2022).

[51] V. Ta Phuoc, C. Vaju, B. Corraze, R. Sopracase, A. Perucchi, C. Marini, P. Postorino, M. Chligui, S. Lupi, E. Janod, and L. Cario, Optical conductivity measurements of $GaTa_4Se_8$ under high pressure: Evidence of a bandwidth-controlled insulator-to-metal Mott transition, Phys. Rev. Lett. **110**, 037401 (2013).

[52] S. Reschke, F. Meggle, F. Mayr, V. Tsurkan, L. Prodan, H. Nakamura, J. Deisenhofer, C. A. Kuntscher, and I. Kézsmárki, Lattice dynamics and electronic excitations in a large family of lacunar spinels with a breathing pyrochlore lattice structure, Phys. Rev. B **101**, 075118 (2020).

[53] S. Kawamoto, T. Higo, T. Tomita, S. Suzuki, Z. M. Tian, K. Mochitzuki, A. Matsuo, K. Kindo, and S. Nakatsuji, Frustrated magnetism in a Mott insulator based on a transition metal chalcogenide, J. Phys. Conf. Ser. **683**, 012025 (2016).

[54] T. Petersen, L. Prodan, V. Tsurkan, H.-A. Krug von Nidda, I. Kézsmárki, U. K. Rößler, and L. Hozoi, How correlations and spin–orbit coupling work within extended orbitals of transition-metal tetrahedra of $4d/5d$ lacunar spinels, J. Phys. Chem. Lett. **13**, 1681 (2022).

[55] H. Ishikawa, T. Yajima, A. Matsuo, Y. Ihara, and K. Kindo, Nonmagnetic ground states and a possible quadrupolar phase in 4d and 5d lacunar spinel selenides GaM_4Se_8 (M = Nb, Ta), Phys. Rev. Lett. **124**, 227202 (2020).

[56] S. Jakob, Strukturen, Magnetismus und Phasenumwandlungen der Mott-Isolatoren $Ga(M_{4-x}M'_x)Q_8$ und $(M_{4-x}M'_x)Q_4I_4$ (M, M' = Mo, Nb, Ta; Q = S, Se; x = 0–4), Ph.D. thesis, Ludwig-Maximilians-Universität München, 2007, https://edoc.ub.uni-muenchen.de/7765/.

[57] T.-H. Yang, S. Kawamoto, T. Higo, S. G. Wang, M. B. Stone, J. Neuefeind, J. P. C. Ruff, A. M. M. Abeykoon, Y.-S. Chen, S. Nakatsuji, and K. W. Plumb, Bond ordering and molecular spin-orbital fluctuations in the cluster Mott insulator $GaTa_4Se_8$, Phys. Rev. Res. **4**, 033123 (2022).

[58] Y. Shvyd'ko, J. Hill, C. Burns, D. Coburn, B. Brajuskovic, D. Casa, K. Goetze, T. Gog, R. Khachatryan, J.-H. Kim, C. Kodituwakku, M. Ramanathan, T. Roberts, A. Said, H. Sinn, D. Shu, S. Stoupin, M. Upton, M. Wieczorek, and H. Yavas, MERIX—Next generation medium energy resolution inelastic x-ray scattering instrument at the APS, J. Electron Spectrosc. Relat. Phenom. **188**, 140 (2013).

[59] M. Minola, G. Dellea, H. Gretarsson, Y. Y. Peng, Y. Lu, J. Porras, T. Loew, F. Yakhou, N. B. Brookes, Y. B. Huang, J. Pelliciari, T. Schmitt, G. Ghiringhelli, B. Keimer, L. Braicovich, and M. Le Tacon, Collective nature of spin excitations in superconducting cuprates probed by resonant inelastic x-ray scattering, Phys. Rev. Lett. **114**, 217003 (2015).

[60] See Supplemental Material at http://link.aps.org/supplemental/10.1103/PhysRevLett.133.046501, which includes Refs. [57,61–64], for additional information about spin-orbit coupling on the cluster, the role of noncubic distortions, and the cluster calculations in the interacting many-body picture.

[61] S. Sugano, Y. Tanabe, and H. Kamimura, *Multiplets of Transition-Metal Ions in Crystals* (Academic, New York, 1970).

[62] N. B. Perkins, Y. Sizyuk, and P. Wölfle, Interplay of many-body and single-particle interactions in iridates and rhodates, Phys. Rev. B **89**, 035143 (2014).

[63] M. W. Haverkort, Quanty for core level spectroscopy—excitons, resonances and band excitations in time and frequency domain, J. Phys. Conf. Ser. **712**, 012001 (2016).

[64] W. A. Harrison, *Electronic Structure and the Properties of Solids: The Physics of the Chemical Bond* (Dover, New York, 1989).

[65] L. J. P. Ament, G. Khaliullin, and J. van den Brink, Theory of resonant inelastic x-ray scattering in iridium oxide compounds: Probing spin-orbit-entangled ground states and excitations, Phys. Rev. B **84**, 020403(R) (2011).

[66] L. J. P. Ament, M. van Veenendaal, T. P. Devereaux, J. P. Hill, and J. van den Brink, Resonant inelastic x-ray scattering studies of elementary excitations, Rev. Mod. Phys. **83**, 705 (2011).

[67] H. Ishikawa, T. Takayama, R. K. Kremer, J. Nuss, R. Dinnebier, K. Kitagawa, K. Ishii, and H. Takagi, Ordering of hidden multipoles in spin-orbit entangled $5d^1$ Ta chlorides, Phys. Rev. B **100**, 045142 (2019).

Supplementary Information
Quasimolecular $J_{\rm tet}$ = 3/2 moments in the cluster Mott insulator $GaTa_4Se_8$

M. Magnaterra,[1] J. Attig,[2] L. Peterlini,[2] M. Hermanns,[3] M. H. Upton,[4] Jungho Kim,[4]
L. Prodan,[5] V. Tsurkan,[5,6] I. Kézsmárki,[5] P.H.M. van Loosdrecht,[1] and M. Grüninger[1]

[1]*Institute of Physics II, University of Cologne, 50937 Cologne, Germany*
[2]*Institute for Theoretical Physics, University of Cologne, 50937 Cologne, Germany*
[3]*Department of Physics, Stockholm University, AlbaNova University Center, SE-106 91 Stockholm, Sweden*
[4]*Advanced Photon Source, Argonne National Laboratory, Argonne, Illinois 60439, USA*
[5]*Experimental Physics V, Center for Electronic Correlations and Magnetism, University of Augsburg, Germany*
[6]*Institute of Applied Physics, Moldova State University, MD 2028, Chisinau, R. of Moldova*

(Dated: September 21, 2023; revised: April 16, 2024)

I. SPIN-ORBIT COUPLING ON THE CLUSTER

Before addressing the tetrahedral cluster, we start by considering a single site in cubic symmetry with the three t_{2g} orbitals $X = yz$, $Y = zx$, and $Z = xy$. Applying spin-orbit coupling $H_{\rm SOC} = \zeta \vec{l}\,\vec{s}$ to the single electron configuration t_{2g}^1 couples $|X\uparrow\rangle$, $|Y\uparrow\rangle$, and $|Z\downarrow\rangle$ as well as $|X\downarrow\rangle$, $|Y\downarrow\rangle$, and $|Z\uparrow\rangle$ [1], which is described by the two Hamiltonians

$$H_{X\uparrow,Y\uparrow,Z\downarrow} = \begin{pmatrix} 0 & i & -1 \\ -i & 0 & i \\ -1 & -i & 0 \end{pmatrix} \frac{\zeta}{2} \tag{S1}$$

$$H_{X\downarrow,Y\downarrow,Z\uparrow} = \begin{pmatrix} 0 & -i & 1 \\ i & 0 & i \\ 1 & -i & 0 \end{pmatrix} \frac{\zeta}{2} \tag{S2}$$

where the indices denote the basis states. Altogether, this yields a $j = 3/2$ ground state and a $j = 1/2$ excited state at $3/2\,\zeta$.

For the four Ta sites of a tetrahedron, we consider hopping t_σ and t_π between the $4 \times 3\,t_{2g}$ orbitals as well as spin-orbit coupling on each of the four sites. Then we transform to the quasimolecular basis states of the hopping Hamiltonian, see Fig. 3a) of the main text. For the single-particle model, we project spin-orbit coupling to the quasimolecular t_2 states. (For comparison, we also consider the case of spin-orbit coupling acting on all states. These exceptions are clearly marked in the main text.) This is a reasonable approximation as long as the energy difference between the quasimolecular states is large. In spirit, it is analogous to neglecting the e_g orbitals in the discussion of a single site. We find a Hamiltonian that is equivalent to the single-site case,

$$H_{X_{\rm tet}\uparrow,Y_{\rm tet}\uparrow,Z_{\rm tet}\downarrow} = \begin{pmatrix} 0 & i & -1 \\ -i & 0 & i \\ -1 & -i & 0 \end{pmatrix} \frac{\zeta}{2}\,\frac{\alpha^2-1}{\alpha^2+2} \tag{S3}$$

$$H_{X_{\rm tet}\downarrow,Y_{\rm tet}\downarrow,Z_{\rm tet}\uparrow} = \begin{pmatrix} 0 & -i & 1 \\ i & 0 & i \\ 1 & -i & 0 \end{pmatrix} \frac{\zeta}{2}\,\frac{\alpha^2-1}{\alpha^2+2} \tag{S4}$$

with

$$|X_{\rm tet}\sigma\rangle = \beta \left(\frac{-1}{\alpha},1,\frac{1}{\alpha},\quad \frac{1}{\alpha},1,\frac{1}{\alpha},\quad \frac{-1}{\alpha},1,\frac{-1}{\alpha},\quad \frac{1}{\alpha},1,\frac{-1}{\alpha}\right)_\sigma$$
$$|Y_{\rm tet}\sigma\rangle = \beta \left(\frac{1}{\alpha},\frac{1}{\alpha},1,\quad \frac{-1}{\alpha},\frac{1}{\alpha},1,\quad \frac{-1}{\alpha},\frac{-1}{\alpha},1,\quad \frac{1}{\alpha},\frac{-1}{\alpha},1\right)_\sigma$$
$$|Z_{\rm tet}\sigma\rangle = \beta \left(1,\frac{-1}{\alpha},\frac{1}{\alpha},\quad 1,\frac{1}{\alpha},\frac{-1}{\alpha},\quad 1,\frac{-1}{\alpha},\frac{-1}{\alpha},\quad 1,\frac{1}{\alpha},\frac{1}{\alpha}\right)_\sigma$$

where

$$\beta = \frac{1}{2\sqrt{1+(2/\alpha^2)}}\,. \tag{S5}$$

These states are expressed in the basis xy_1, yz_1, zx_1, xy_2, yz_2, zx_2, ..., where the index i = 1-4 denotes the site within the Ta_4 cluster. Note that $|Z_{\rm tet}\sigma\rangle = t_2(xy)_\sigma$ as defined in Eq. (3) of the main text. The $J_{\rm tet} = 3/2$ eigenstates of Eqs. (S3) and (S4) are given by

$$\left|\frac{3}{2},\frac{3}{2}\right\rangle = \frac{-1}{\sqrt{2}}\left[|X_{\rm tet}\uparrow\rangle + i|Y_{\rm tet}\uparrow\rangle\right], \tag{S6}$$
$$\left|\frac{3}{2},\frac{-3}{2}\right\rangle = \frac{1}{\sqrt{2}}\left[|X_{\rm tet}\downarrow\rangle - i|Y_{\rm tet}\downarrow\rangle\right], \tag{S7}$$
$$\left|\frac{3}{2},\frac{1}{2}\right\rangle = \frac{-1}{\sqrt{6}}\left[|X_{\rm tet}\downarrow\rangle + i|Y_{\rm tet}\downarrow\rangle - 2|Z_{\rm tet}\uparrow\rangle\right], \tag{S8}$$
$$\left|\frac{3}{2},\frac{-1}{2}\right\rangle = \frac{1}{\sqrt{6}}\left[|X_{\rm tet}\uparrow\rangle - i|Y_{\rm tet}\uparrow\rangle + 2|Z_{\rm tet}\downarrow\rangle\right], \tag{S9}$$

while the $J_{\rm tet} = 1/2$ states read

$$\left|\frac{1}{2},\frac{1}{2}\right\rangle = \frac{-1}{\sqrt{3}}\left[|X_{\rm tet}\downarrow\rangle + i|Y_{\rm tet}\downarrow\rangle + |Z_{\rm tet}\uparrow\rangle\right], \tag{S10}$$
$$\left|\frac{1}{2},\frac{-1}{2}\right\rangle = \frac{-1}{\sqrt{3}}\left[|X_{\rm tet}\uparrow\rangle - i|Y_{\rm tet}\uparrow\rangle - |Z_{\rm tet}\downarrow\rangle\right]. \tag{S11}$$

The corresponding single-site states of Eqs. (S1) and (S2) are obtained by replacing $X_{\rm tet}$ by $X = yz$ and equivalent for $Y_{\rm tet}$ and $Z_{\rm tet}$ [1, 2]. For a Ta_4 cluster, the central role of α is to shape these basis states, as described above and in Eq. (3), and to renormalize the energy scale, see Eqs. (S3) and (S4) and Fig. 3b) in the main text. The energy normalization factor approaches 1 in the limit $\alpha = \infty$.

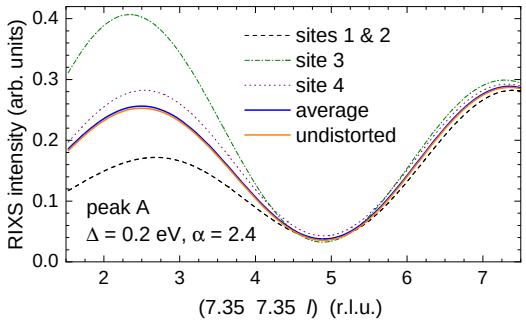

FIG. S1. RIXS intensity of peak A for $\mathbf{q}$ along (7.35 7.35 l) for a distorted tetrahedron with $\Delta = 0.2$ eV and $\alpha = 2.4$. For this $\mathbf{q}$ direction, the results for distortions with either site 1 or 2 as unique site are identical. The average over the four different orientations of the distortion (solid blue line) is hard to distinguish from the undistorted case (solid orange line).

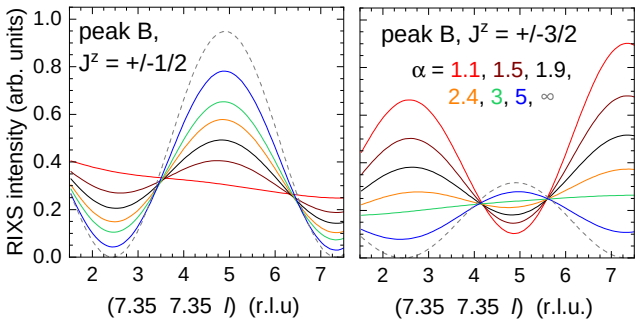

FIG. S2. The α dependence of the RIXS intensities of the two different contributions to peak B. Left (right): Excitations from an e orbital to $J_{\rm tet} = 3/2$ with $J^z = \pm 1/2$ ($\pm 3/2$).

II. EFFECT OF NON-CUBIC DISTORTIONS

In cubic symmetry, all Ta-Ta edges of the regular tetrahedron are of equal length $d = 3.0$ Å. However, the symmetry is lower than cubic below $T_{ms} = 53$ K. Furthermore, recent x-ray and neutron results on the pair distribution function [3] point to dynamical local distortions up to temperatures far above T_{ms}. These dynamical distortions are of similar size as the static distortions at low temperature. RIXS averages over different orientations of the dynamical distortions above T_{ms} and different domains below T_{ms}. Even within a single domain, different tetrahedra within the unit cell show different orientations [3]. For a single tetrahedron, we approximate the distorted case by three short and three long bonds with 3.0 ± 0.04 Å, where the long bonds meet at one Ta site [3]. We implement such a trigonal distortion of the tetrahedron via the size of σ-type hopping, for which we assume $t_\sigma \mp \Delta/2$. With $t_\sigma \propto 1/d^5$ [4], we estimate $\Delta/t_\sigma \approx 0.13$. Below we use $\Delta = 0.2$ eV, which somewhat overestimates the effect of a trigonal distortion.

As in the cubic case, we employ the single-particle picture and first calculate the eigenstates of the hopping Hamiltonian for a single, distorted tetrahedron. Then we apply spin-orbit coupling within the t_2^1 states. The distortion splits the $J_{\rm tet} = 3/2$ quartet into two doublets, in close analogy to the single-site case. We calculate RIXS for the four equivalent orientations of the distortion and finally average over the four curves. Figure S1 shows the result for peak A along (7.35 7.35 l) for $\Delta = 0.2$ eV and $\alpha = 2.4$. We find clear differences for different orientations of the distortion. RIXS thus would be sensitive to the distortion if a single orientation of the distortion could be measured. However, the average over the four distorted results is very close to the RIXS response of the undistorted case. This is a plausible explanation for our RIXS data being very similar at 20 K and 100 K and validates the description of the data in terms of a cubic model.

Peak B corresponds to excitations from e to $J_{\rm tet} = 3/2$ states. The $J_{\rm tet} = 3/2$ quartet contains states with $J^z = \pm 1/2$ and $J^z = \pm 3/2$, and these show a different $\mathbf{q}$ dependence, see Fig. S2. In particular a nearly $\mathbf{q}$-independent behavior is observed for $\alpha \approx 1.1$ for $J^z = \pm 1/2$ but for $\alpha \approx 3$ for $J^z = \pm 3/2$. The trigonal distortion considered above mixes these two states with equal weight, and hence has little effect on the $\mathbf{q}$ dependence. However, a distortion of lower symmetry may cause preferential occupation of, e.g., $J^z = \pm 1/2$ in the ground state, which will partially block the corresponding contribution. In this case, a $\mathbf{q}$-independent behavior is expected for a larger value of α up to $\alpha = 2.2$. It is plausible that such a low-symmetry distortion may describe the behavior of peaks A and B for the same value of α.

III. ELECTRON-ELECTRON INTERACTIONS

Beyond the calculations within the single-particle model, we also performed many-body cluster calculations using Quanty [5]. For the seven t_{2g} electrons on a Ta_4 tetrahedron, we consider the model Hamiltonian $\mathrm{H} = \mathrm{H}_t + \mathrm{H}_\zeta + \mathrm{H}_{e-e}$ that takes into account hopping t_σ and t_π, spin-orbit coupling ζ, and electron-electron interactions, i.e., on-site Coulomb repulsion U and Hund's coupling J_H. We first diagonalize H_t and then consider the lower nine (a_1, e, t_2, and t_1) out of 12 quasimolecular orbitals, see Fig. 3a) of the main text.

Taking into account electron-electron interactions is in particular necessary in order to correctly reproduce the excitation energies of peaks B and C as well as the width of peak C. Figure S3 shows the low-energy excitation energies of a Ta_4 tetrahedron, in particular for intra-t_2 and e-to-t_2 excitations. The first panel on the left depicts the effect of hopping t_σ and t_π for a fixed ratio $|t_\sigma/t_\pi| \approx 2.6$, i.e., $\alpha = 2.9$, while the second panel introduces spin-orbit coupling ζ. Both panels employ $\mathrm{H}_{e-e} = 0$, i.e., the non-interacting scenario. For $\zeta = 0$, the ground state configuration is within the $a_1^2 e^4 t_2^1$ manifold, while the lowest excited states correspond to $a_1^2 e^3 t_2^2$. Finite ζ yields a $J_{\rm tet} = 3/2$ ground state and a $J_{\rm tet} = 1/2$ doublet at an energy of roughly ζ, i.e., the excitation energy is reduced from the expectation $1.5\,\zeta$ for $\alpha = \infty$, see Fig. 3b) of the main text. Figure 3b) also shows that the renormalization is slightly different compared to our single-particle calculations and that the normalization depends on the set of orbitals to which spin-orbit coupling is restricted. At higher energy, ζ

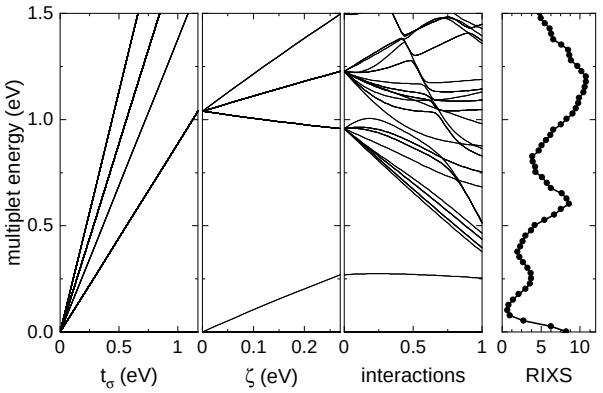

FIG. S3. Excitation energies of a single Ta_4 tetrahedron (left) compared to a RIXS spectrum (right). The plot focuses on the low-energy sector, in particular on intra-t_2 and e-to-t_2 excitations. First panel: effect of hopping t_σ for fixed $|t_\sigma/t_\pi| \approx 2.6$, i.e., $\alpha = 2.9$. Beyond the $a_1^2e^4t_2^1$ ground state manifold at zero energy it shows, with increasing energy, the states $a_1^2e^3t_2^2$, $a_1^2e^4t_2^0t_1^1$, $a_1^2e^2t_2^3$, and $a_1^2e^3t_2^1t_1^1$. Second panel: finite ζ lifts the degeneracy of the $a_1^2e^3t_2^2$ states at about 1 eV while the $a_1^2e^4t_2^1$ ground state is split into $J_{\rm tet} = 3/2$ and 1/2 with an excitation energy of about ζ. Third panel: Electron-electron interactions are necessary to correctly describe the excitation energies of peaks B and C. The scale 0 to 1 encodes the linear increase from $J_H = U = 0$ to $J_H = 0.4$ eV and $U = 1.75$ eV.

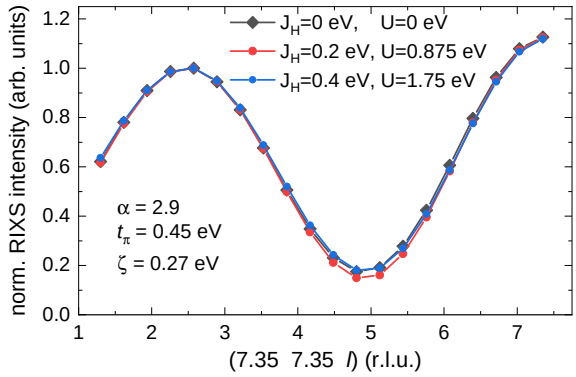

FIG. S4. Effect of electron-electron interactions on the **q** dependence of the normalized RIXS intensity of peak A along (7.35 7.35 l) for $\alpha = 2.9$.

splits the $a_1^2e^3t_2^2$ manifold into three energy levels that, in the absence of electron-electron interactions, can be distinguished according to the occupation of the t_2 states: $J^2_{3/2}$, $J^1_{3/2}$ $J^1_{1/2}$, and $J^2_{1/2}$. Note that the latter state cannot be reached from a $J^1_{3/2}$ ground state in a single-particle scenario. The two lower branches hence correspond to peaks B and C. Electron-electron interactions cause a fanning out of energies for the $a_1^2e^3t_2^2$ states but have little effect on the low-energy $a_1^2e^4t_2^1$ states, i.e., $J_{\rm tet} = 3/2$ and 1/2. Based on the RIXS peak energies and the **q** dependence, we employ $\alpha = 2.9$, $t_\pi = 0.45$ eV, $t_\sigma \approx 1.17$ eV, $\zeta = 0.27$ eV, $U = 1.75$ eV, and $J_H = 0.4$ eV. These parameters have also been used for Fig. 3b) of the main text, where α has been changed by varying t_σ.

The single-particle model offers a very good description of peak A, the excitation from $J_{\rm tet} = 3/2$ to 1/2 within the $a_1^2e^4t_2^1$ manifold. This result is stable against the addition of electron-electron interactions. For $\alpha = 2.9$, Fig. S4 compares the **q**-dependent intensity of peak A along (7.35 7.35 l) for vanishing, intermediate, and sizable electron-electron interactions. For all three curves, spin-orbit coupling acts within the lower nine quasimolecular orbitals, i.e., a_1, e, t_2, and t_1. The behavior is very similar, and we conclude that electron-electron interactions have only a minor effect on peak A.

IV. RIXS INTENSITY

Finally, we provide further information on the RIXS intensity. Figure 2c) in the main text shows the integrated RIXS intensity of peaks A, B, and C for **q** along (7.35 7.35 l) at 20 K in comparison to results of the single-particle model. Figure S5 highlights that the **q** dependence of the intensity is very similar at 20 K and 100 K.

The color maps in Fig. S6 depict the RIXS intensity at 20 K for **q** along (k+0.15 k 4.8) and (h h 1.65(10-h)). The data in Fig. 4d)-i) in the main text show the corresponding integrated intensity with integration ranges as given in Fig. S5.

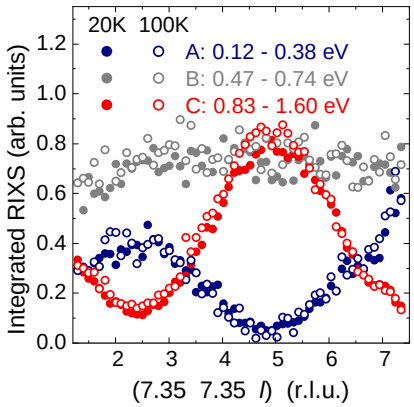

FIG. S5. Integrated intensity of peaks A, B, and C at 20 K (full symbols) and 100 K (open), cf. Fig. 2c) in the main text. Integration intervals are given in the figure. The data of peak C are scaled down by a factor 5 to facilitate comparison.

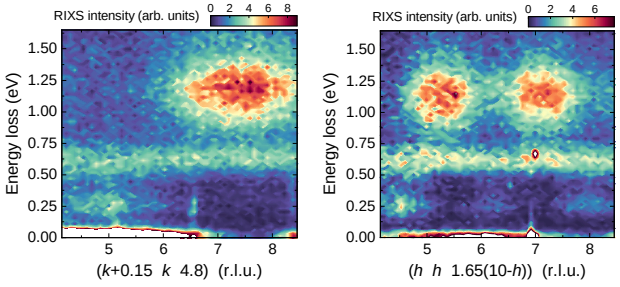

FIG. S6. Color maps of the RIXS intensity at 20 K, cf. Fig. 4 in the main text.

[1] S. Sugano, Y. Tanabe, and H. Kamimura, *Multiplets of Transition-Metal Ions in Crystals* (Academic, New York, 1970).
[2] N. B. Perkins, Y. Sizyuk, and P. Wölfle, Interplay of many-body and single-particle interactions in iridates and rhodates, Phys. Rev. B **89**, 035143 (2014).
[3] T.-H. Yang, S. Kawamoto, T. Higo, S. G. Wang, M. B. Stone, J. Neuefeind, J. P. C. Ruff, A. M. M. Abeykoon, Y.-S. Chen, S. Nakatsuji, and K. W. Plumb, Bond ordering and molecular spin-orbital fluctuations in the cluster Mott insulator $GaTa_4Se_8$, Phys. Rev. Res. **4**, 033123 (2022).
[4] W. A. Harrison, *Electronic Structure and the Properties of Solids: The Physics of the Chemical Bond* (Dover, 1989).
[5] M. W. Haverkort, Quanty for core level spectroscopy - excitons, resonances and band excitations in time and frequency domain, J. Phys. Conf. Ser. **712**, 012001 (2016).

6.2 Tetrahedral quasimolecular orbitals

In the previous chapter, we have seen how, in the cluster Mott insulator $GaTa_4Se_8$, the formation of tetrahedral quasimolecular orbitals is crucial for understanding the electronic structure of this material. We showed, in particular, how the balance of the strength of different hopping paths determines the mixing of bonding and antibonding quasimolecular orbitals. This was shown to be crucial for understanding the RIXS spectra and the intensity modulation. Additionally, it was shown to result in a renormalization of the spin-orbit coupling. The correct modeling of the quasimolecular orbitals is important. In the following, we present further insights into the modeling of the tetrahedral molecular wavefunctions and the calculation of the RIXS intensity. As shown in Fig. 1(a) of Chap. 6.1, the Ta ions are found in an octahedral environment. From the RIXS experiments [205], we observe that the e_g orbitals are at about 3 eV, so $10Dq \approx 3\,\text{eV}$. In the following, we neglect the e_g orbitals and restrict the calculations to the t_{2g} orbitals. A Ta_4 cluster is formed by four edge-sharing $TaSe_6$ octahedra and the quasimolecular orbitals arise from the hopping between the local t_{2g} orbitals of the Ta ions. The same edge-sharing geometry is present in the Kitaev materials discussed in Chap. 4. However, in that case, the M-L-M bond angle is greater than 90° (see Fig. 4.1), while in $GaTa_4Se_8$ the bond angle is about 72°. This results in the fact that, in Na_2IrO_3, the direct t_3 hopping is reduced, and the hopping through the ligands is dominant, while in $GaTa_4Se_8$, t_3 is the dominant hopping path [3] [205].

The hopping matrix between the orbital degrees of freedom of the four sites in the $\{yz_1, zx_1, xy_1, yz_2, \ldots, xy_4\}$ basis, where the subscript identifies the site number as defined in Fig. 1(b) of Chap. 6.1, reads

$$H_{tetra} = \begin{pmatrix} 0 & T_{12} & T_{13} & T_{14} \\ T_{21} & 0 & T_{23} & T_{24} \\ T_{31} & T_{32} & 0 & T_{34} \\ T_{41} & T_{42} & T_{43} & 0 \end{pmatrix}, \tag{6.1}$$

where $T_{ij} = T_{ji}^*$ are the matrices describing the hopping between the sites number $i, j = 1, 2, 3, 4$. For example, using the definition of the geometry as in Fig. 1(b) of Chap. 6.1, the hopping matrix T_{12} between sites 1 and 2 can be calculated starting from the analytical expressions in Ref. [260] as

$$T_{12} = \begin{pmatrix} \frac{1}{2}(V_{dd\pi} + V_{dd\delta}) & \frac{1}{2}(-V_{dd\pi} + V_{dd\delta}) + t_{dd}^p & 0 \\ \frac{1}{2}(-V_{dd\pi} + V_{dd\delta}) + t_{dd}^p & \frac{1}{2}(V_{dd\pi} + V_{dd\delta}) & 0 \\ 0 & 0 & \frac{3}{4}V_{dd\sigma} + \frac{1}{4}V_{dd\delta} \end{pmatrix}, \tag{6.2}$$

where V_{dd} are the direct interatomic matrix elements between d orbitals and t_{dd}^p is the hopping mediated by the p orbitals of the ligands. In Chap. 6.1, we neglected $V_{dd\delta}$ and t_{dd}^p which means considering only $t_\pi = \frac{1}{2}V_{dd\pi}$ and $t_\sigma = \frac{3}{4}V_{dd\sigma}$ hoppings. To remain more general here we allow $\frac{1}{2}(V_{dd\pi} + V_{dd\delta})$ and $\frac{1}{2}(V_{dd\pi} - V_{dd\delta}) - t_{dd}^p$ to be different and call them respectively t_1 and t_2. Furthermore, we employ $t_3 = \frac{3}{4}V_{dd\sigma} + \frac{1}{4}V_{dd\delta}$. Which orbitals are connected by which hopping changes for different sites, such that in the geometry defined

in Fig. 1(b) of Chap. 6.1, we can write the hopping matrices as

$T_{12}:$	yz_2	zx_2	xy_2
yz_1	t_1	$-t_2$	0
zx_1	$-t_2$	t_1	0
xy_1	0	0	$-t_3$

$T_{13}:$	yz_3	zx_3	xy_3
yz_1	t_1	0	t_2
zx_1	0	$-t_3$	0
xy_1	t_2	0	t_1

$T_{14}:$	yz_4	zx_4	xy_4
yz_1	$-t_3$	0	$-t_2$
zx_1	0	t_1	0
xy_1	$-t_2$	0	$-t_1$

$T_{23}:$	yz_3	zx_3	xy_3
yz_2	$-t_3$	0	0
zx_2	0	t_1	t_2
xy_2	0	t_2	t_1

$T_{24}:$	yz_4	zx_4	xy_4
yz_2	t_1	0	$-t_2$
zx_2	0	$-t_3$	0
xy_2	$-t_2$	0	t_1

$T_{34}:$	yz_4	zx_4	xy_4
yz_3	t_1	t_2	0
zx_3	t_2	t_1	0
xy_3	0	0	$-t_3$

(6.3)

One can see that the dominant hopping t_3 connects the yz orbitals of sites 1-4 and 2-3, the zx orbitals of sites 1-3 and 2-4, and the xy orbitals of 1-2 and 3-4. So, if we consider only the t_3 hopping we form bonding (b) and antibonding (ab) orbitals at an energy $\pm t_3$ that can be written as

$$\begin{aligned}
yz_{b\pm} &= [(yz_1 + yz_4) \pm (yz_2 + yz_3)]/2 \\
yz_{ab\pm} &= [(yz_1 - yz_4) \pm (yz_2 - yz_3)]/2 \\
zx_{b\pm} &= [(zx_1 + zx_3) \pm (zx_2 + zx_4)]/2 \\
zx_{ab\pm} &= [(zx_1 - zx_3) \pm (zx_2 - zx_4)]/2 \\
xy_{b\pm} &= [(xy_1 + xy_2) \pm (xy_3 + xy_4)]/2 \\
xy_{ab\pm} &= [(xy_1 - xy_2) \pm (xy_3 - xy_4)]/2.
\end{aligned} \tag{6.4}$$

In this basis the hopping matrix H_{tetra} becomes block diagonal such that we can rewrite the individual blocks as

	yz_{b-}	zx_{b-}	xy_{b-}
yz_{b-}	$-t_3 - 2t_1$	t_2	$-t_2$
zx_{b-}	t_2	$-t_3 - 2t_1$	t_2
xy_{b-}	$-t_2$	t_2	$-t_3 - 2t_1$

	yz_{ab-}	zx_{ab-}	xy_{b+}
yz_{ab-}	t_3	t_2	t_2
zx_{ab-}	t_2	t_3	$-t_2$
xy_{b+}	t_2	$-t_2$	$-t_3 + 2t_1$

	yz_{b+}	zx_{ab+}	xy_{ab+}
yz_{b+}	$-t_3 + 2t_1$	$-t_2$	t_2
zx_{ab+}	$-t_2$	t_3	t_2
xy_{ab+}	t_2	t_2	t_3

	yz_{ab+}	zx_{b+}	xy_{ab-}
yz_{ab+}	t_3	$-t_2$	$-t_2$
zx_{b+}	$-t_2$	$-t_3 + 2t_1$	$-t_2$
xy_{ab-}	$-t_2$	$-t_2$	t_3

(6.5)

Note that if t_2 is zero the matrices are diagonal which means that there is no mixing between bonding and antibonding states. The first matrix has the eigenvalues

$$\begin{aligned}
E_{a_1} &= -t_3 - 2t_1 - 2t_2 \\
E_e &= -t_3 - 2t_1 + t_2.
\end{aligned} \tag{6.6}$$

Each of the other three matrices has the eigenvalues

$$\begin{aligned} E_{t_{2b}} &= t_1 - t_2/2 - \sqrt{4(t_3 - t_1)(t_3 - t_1 - t_2) + 9t_2^2} \\ E_{t_{2ab}} &= t_1 - t_2/2 + \sqrt{4(t_3 - t_1)(t_3 - t_1 - t_2) + 9t_2^2} \\ E_{t_1} &= t_3 + t_2. \end{aligned} \tag{6.7}$$

The eigenstates can be written as

$$\begin{aligned} a_1 &= (yz_{b-} - zx_{b-} + xy_{b-})/\sqrt{3} \\ e_\alpha &= (zx_{b-} + xy_{b-})/\sqrt{2} \\ e_\beta &= (-2yz_{b-} - zx_{b-} + xy_{b-})/\sqrt{6} \\ t_{2b\alpha} &= (\alpha\, yz_{b+} + zx_{ab+} - xy_{ab+})/\sqrt{2+\alpha^2} \\ t_{2b\beta} &= (yz_{ab+} + \alpha\, zx_{b+} + xy_{ab-})/\sqrt{2+\alpha^2} \\ t_{2b\gamma} &= (-yz_{ab-} + zx_{ab-} + \alpha\, xy_{b+})/\sqrt{2+\alpha^2} \\ t_{2ab\alpha} &= (-2yz_{b+} + \alpha\, zx_{ab+} - \alpha\, xy_{ab+})/\sqrt{4+2\alpha^2} \\ t_{2ab\beta} &= (-\alpha\, yz_{ab+} + 2zx_{b+} - \alpha\, xy_{ab-})/\sqrt{4+2\alpha^2} \\ t_{2ab\gamma} &= (-\alpha\, yz_{ab-} + \alpha\, zx_{ab-} - 2xy_{b+})/\sqrt{4+2\alpha^2} \\ t_{1\alpha} &= (zx_{ab+} + xy_{ab+})/\sqrt{2} \\ t_{1\beta} &= (yz_{ab+} - xy_{ab-})/\sqrt{2} \\ t_{1\gamma} &= (yz_{ab-} + zx_{ab-})/\sqrt{2}. \end{aligned} \tag{6.8}$$

where we introduced the parameter

$$\alpha = \frac{t_3 - t_1}{2} - \frac{1}{2} + \frac{1}{2t_2}\sqrt{4(t_3 - t_1)(t_3 - t_1 - t_2) + 9t_2^2}, \tag{6.9}$$

that describes the mixing of the states with t_2 symmetry. These quasimolecular wavefunctions are represented in Fig. 6.1, plotting the angular density of the projection of the wavefunctions onto the single-site basis states. In Fig. 6.1 the effect of the hopping on the 12 t_{2g} orbitals of the Ta_4 tetrahedral cluster is shown. The lines represent single electron energy levels and are Kramers doublets. The dominant hopping t_3 splits the levels in six bonding (b) and six antibonding (ab) orbitals leading to the eigenstates written in Eq. (6.4). The hopping t_1 splits the bonding orbitals in two triplets, $b+$ and $b-$. The levels are further split by t_2 leading to the tetrahedral quasimolecular orbitals a, e, t_2, t_2, and t_1[1], where the letters refer to the irreducible representations of the T_d symmetry group. The stoichiometry nominally gives $Ga^{3+}(Ta_4)^{13+}(Se_8)^{16-}$, which results in a fractional valence for Ta of 3.25+ and 7 electrons per Ta_4 tetrahedron. In a single-electron picture, this results in a complete filling of the a and e orbitals and one single electron in the lowest t_2 orbital. In the following, we are going to see how the RIXS intensity can be well described by single-electron calculations. Expressions in Eq. (6.8) show that as α tends to infinity, either due to t_3 becoming very large or t_2 approaching zero, the t_{2b} states simplify to purely $b+$ orbitals.

[1]Note that in Chap. 6.1 the labels of the highest two quasimolecular orbitals are exchanged

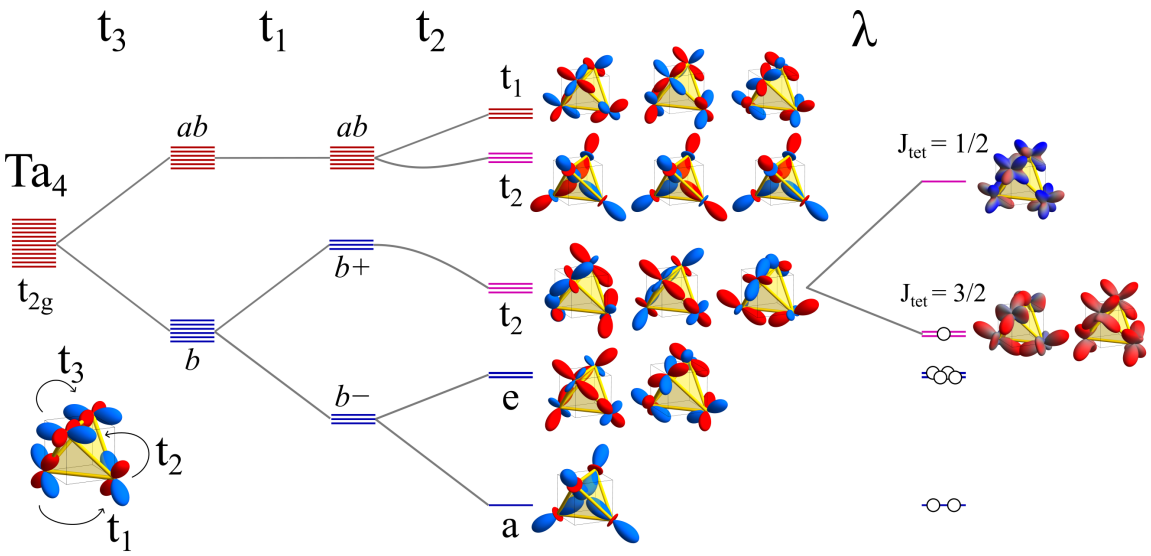

Figure 6.1: Sketch of the energy levels of the tetrahedral quasimolecular orbitals in $GaTa_4Se_8$ as a function of the hopping parameters t_3, t_1, and t_2 and the effect of the spin-orbit coupling on the t_2 quasimolecular orbitals. The density plots show the angular density of the projection of the orbitals over each local t_{2g} single-site basis states. For the spin-orbit entangled states on the very right-hand side, the color represents the spin-up (red) and spin-down (blue) components. For the other orbitals the color represents the phase of the wavefunction.

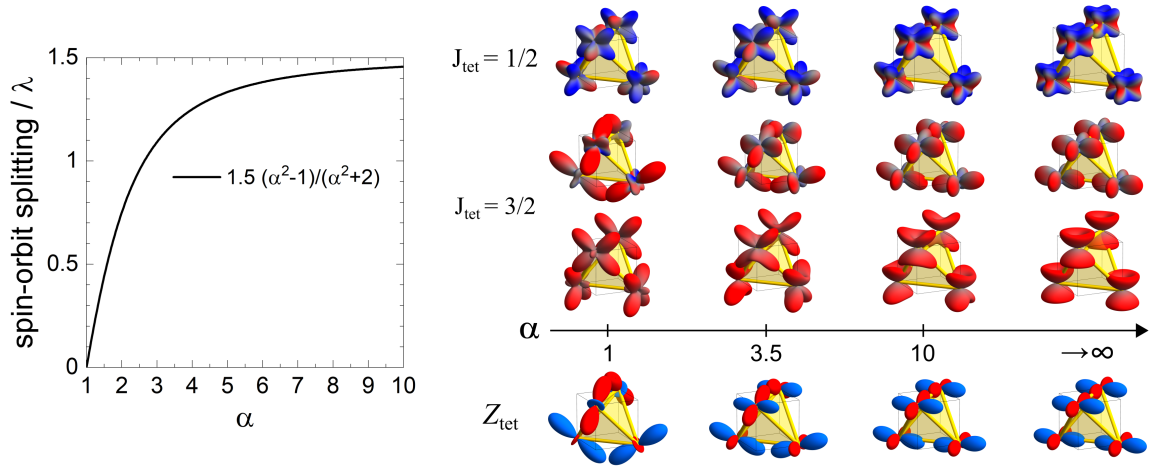

Figure 6.2: *Left*: dependence of the splitting between the J_{tet}=3/2 and the 1/2 states in units of λ as a function of α. *Right*: at the bottom angular density of the Z_{tet} orbital as a function of α where the color represents the phase of the wavefunction. On top the $J_{\text{tet}} = 3/2$ and 1/2 states are shown as a function of α where the color represents the spin component.

These $b+$ orbitals are the bonding combinations of one type of the single-site t_{2g} orbitals, see Eq. 6.4. So, yz_{b+}, zx_{b+}, and xy_{b+} are analogous to a single site t_{2g} shell and we can call these quasimolecular orbitals in a similar way as X_{tet}, Y_{tet}, and Z_{tet}.

In the t_{2g} basis $\{yz_1, zx_1, xy_1, yz_2, \ldots, xy_4\}$, for each Ta site, the spin-orbit Hamiltonian with quantization along z applies as in Eq. (2.10). We want to restrict the discussion to the lowest t_2 quasimolecular orbitals $\{X_{\text{tet}}\uparrow,\ X_{\text{tet}}\downarrow,\ Y_{\text{tet}}\uparrow,\ Y_{\text{tet}}\downarrow,\ Z_{\text{tet}}\uparrow,\ Z_{\text{tet}}\downarrow\}$. In this basis we obtain the spin-orbit coupling Hamiltonian

$$H_{so,t_2} = \begin{pmatrix} 0 & 0 & i & 0 & 0 & -1 \\ 0 & 0 & 0 & -i & 1 & 0 \\ -i & 0 & 0 & 0 & 0 & i \\ 0 & i & 0 & 0 & i & 0 \\ 0 & 1 & 0 & -i & 0 & 0 \\ -1 & 0 & -i & 0 & 0 & 0 \end{pmatrix} \frac{\zeta}{2}\frac{\alpha^2-1}{\alpha^2+2}. \tag{6.10}$$

By comparing with Eq. 2.17, we can see the similarity to the single-site Hamiltonian, however renormalized by the factor $(\alpha^2-1)/(\alpha^2+2)$. The t_2 orbitals split into a lower $J_{\text{tet}} = 3/2$ quartet and an upper $J_{\text{tet}} = 1/2$ doublet. Both the eigenstates and the eigenvalues of this Hamiltonian depend on the mixing parameter α. The eigenstates are analogous to the single-site ones written in Eq. (2.18) but with the quasimolecular orbitals instead of the single-site ones. The eigenvalues are also written in the Supplementary Information of Chap. 6.1 in Eq. (S6)-(S11).

The dependence of the spin-orbit splitting on α is shown in Fig. 6.2. For $\alpha \to \infty$, the spin-orbit splitting is 1.5λ, as in the single-site case. As α decreases, the spin-orbit splitting also decreases, eventually reaching the point of being suppressed at $\alpha = 1$. At the bottom right of Fig. 6.2, the angular density of the Z_{tet} orbital is plotted as a function of α. For $\alpha \to \infty$, the quasimolecular orbital Z_{tet} is composed of local xy orbitals on each site with the same phase. The color indicates the phase of the wavefunction. For the J_{tet} states, the color instead represents the spin component. As $\alpha \to \infty$, these states are composed of the single-site $j = 1/2$ and $j = 3/2$ states, as shown in Fig. 2.2. As α decreases, the mixing with the antibonding states increases, which affects the shape of the quasimolecular magnetic moments. This is determined by the balance of the different hopping channels, represented by α, see Eq. 6.9.

6.3 RIXS interference on a tetrahedron

We see in the following how the RIXS modulation can be calculated for the tetrahedral quasimolecular orbitals in a single-electron picture. In particular, we demonstrate how the modulation is sensitive to the phase of the quasimolecular wavefunctions and their dependence on the mixing parameter α. First, we make some general considerations on the modulation expected for a tetrahedron. We define the positions of the Ta ions as $\mathbf{R}_1 = (0,0,0)$, $\mathbf{R}_2 = (-1,1,0)d/\sqrt{2}$, $\mathbf{R}_3 = (-1,0,-1)d/\sqrt{2}$, and $\mathbf{R}_4 = (0,1,-1)d/\sqrt{2}$, where $d = 3.0\,\text{Å}$ is the distance between the Ta ions. This geometry is defined in Fig. 1(b) of Chap. 6.1, with the origin set at site 1. We use $\mathbf{q}$ in absolute units $1/\text{Å}$ and h, k, and l in

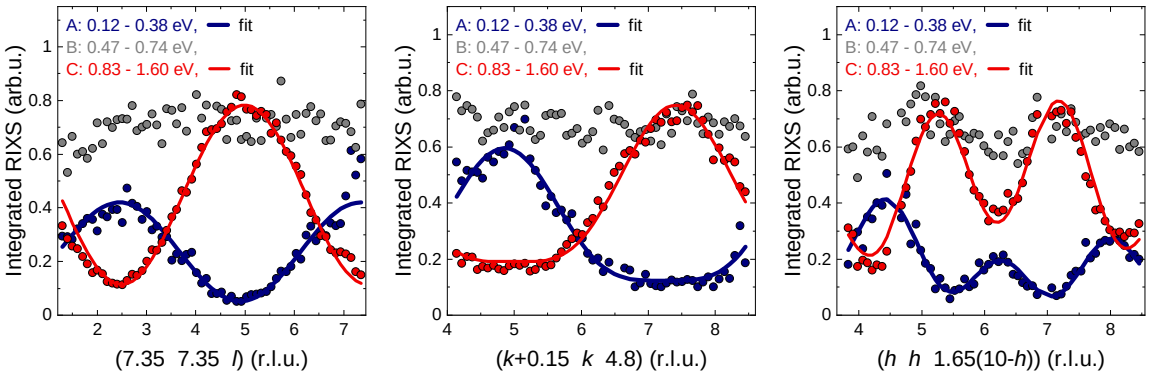

Figure 6.3: Integrated RIXS intensity of $GaTa_4Se_8$ along (7.35 7.35 l), ($k + 0.15$ k 4.8), and (h h $1.65(10 - h)$). For the integrals of peak A and peak C the fits of the modulation are also plot. For peak A it corresponds to a structure factor with coefficients $f_a = (1, 1, 1, 1)$ while peak C to $f_b = (1, 1, -1, -1)$.

r.l.u.. With the cubic lattice constant $a = 10.38$ Å, the structure factor for the tetrahedron is

$$F = \sum_{i=1}^{4} f_i \, e^{i\mathbf{q}\cdot\mathbf{R}_i} = f_1 + f_2 \, e^{i(-h+k)\frac{d}{\sqrt{2}}\frac{2\pi}{a}} + f_3 \, e^{i(-h-l)\frac{d}{\sqrt{2}}\frac{2\pi}{a}} + f_4 \, e^{i(k-l)\frac{d}{\sqrt{2}}\frac{2\pi}{a}}, \qquad (6.11)$$

where we introduced the coefficients $f = (f_1, f_2, f_3, f_4)$. The complex exponential factors are related to the optical path difference between the different sites, while the coefficients contain the information about the phase of the quasimolecular wavefunctions. The RIXS intensity modulation (neglecting the polarization dependence) is proportional to $I_{RIXS} \propto |F|^2$. In Fig. 6.3 we show the experimental integrated RIXS intensity along (7.35 7.35 l), ($k + 0.15$ k 4.8), and (h h $1.65(10 - h)$) and the fits. The integrated RIXS intensity of peaks A and C can de described very well by the function $a|F|^2 + b$ where a is a scaling factor and b an offset. The modulation of the intensity of peak A is described very well by the coefficients $f_a = (1, 1, 1, 1)$ while the modulation of peak C is described by $f_b = (1, 1, -1, -1)$. With $\sqrt{2}a/d \approx 4.9 = l_0$ and $7.35 = 1.5l_0$, the modulation along the (7.35 7.35 l) direction is equal to $\sin^2(\pi l/4.9)$ for f_a and $\cos^2(\pi l/4.9)$ for f_b. Instead, along the ($k + 0.15$ k 4.8) direction the modulation is $\sin^4(\pi k/4.9)$ for f_a and $\cos^4(\pi k/4.9)$ for f_b. Along (h h $1.65(10 - h)$) the modulation is more complicated being equal to $1 + \cos^2(2\pi h/4.9) \pm 2\cos(2\pi h/4.9)\cos(2\pi 1.65(10 - h)/4.9)$ for f_a and f_b. But in any case the experimental modulation can be very well described by the structure factor of the tetrahedron. To understand the origin of the different modulations we look at the quasimolecular wavefunctions.

To illustrate the calculation of the modulation of peak A, we consider the excitation from the $J_{\text{tet}} = 3/2$ quartet to the $J_{\text{tet}} = 1/2$ doublet. This involves eight excitation paths, each corresponding to a transition from one of the quartet states to one of the doublet states. Due to the complexity of the expressions, not all derivations are shown explicitly. We want to perform single-electron calculations. To use the matrix elements M in Eq. (3.14), which are derived for a single hole in the t_{2g} shell, we need to switch the initial and final states. Thus, if we excite an electron from the $J_{\text{tet}} = 3/2$ to the $J_{\text{tet}} = 1/2$ state, we can use the expressions derived in Chap. 3.3 with the $J_{\text{tet}} = 1/2$ state as the initial state and the

$J_{\text{tet}} = 3/2$ state as the final state. Since the local coordinate axes are the same for all sites, the matrix elements are identical across sites, and can differ only in phase. By examining the bonding and antibonding orbitals in Eq. (6.4), we introduce the coefficients $f_a = (1,1,1,1)$ for yz_{b+}, zx_{b+}, and xy_{b+}; $f_b = (1,1,-1,-1)$ for yz_{ab+}, zx_{ab+}, and xy_{b-}; $f_c = (1,-1,1,-1)$ for yz_{ab-}, zx_{b-}, and xy_{ab+}; and $f_d = (1,-1,-1,1)$ for yz_{b-}, zx_{ab-}, and xy_{ab-}. We can summarize the multiplication of these coefficients in the following table

	f_a	f_b	f_c	f_d
f_a	f_a	f_b	f_c	f_d
f_b	f_b	f_a	f_d	f_c
f_c	f_c	f_d	f_a	f_b
f_d	f_d	f_c	f_b	f_a

(6.12)

We can then reduce the basis to a single-site t_{2g} basis $\{X\uparrow, X\downarrow, Y\uparrow, Y\downarrow, Z\uparrow, Z\downarrow\}$ and express the wavefunctions in terms of these coefficients. Using the definitions of the $J_{\text{tet}} = 1/2$ and $J_{\text{tet}} = 3/2$ wavefunctions in Eq. (S6)-(S11) of the Supplementary Information of Chap. 6.1 and the coefficients above, we can rewrite them as

$$\begin{aligned}
|\tfrac{1}{2}, +\tfrac{1}{2}\rangle &= (f_c,\ -if_b - f_a\alpha,\ -f_d,\ -f_b - if_a\alpha,\ -f_a\alpha,\ f_c - if_d)/(2\sqrt{3}\sqrt{2+\alpha^2}),\\
|\tfrac{3}{2}, +\tfrac{3}{2}\rangle &= (-if_b - f_a\alpha,\ 0,\ -f_b - if_a\alpha,\ 0,\ f_c - if_d,\ 0)/(2\sqrt{2}\sqrt{2+\alpha^2}).
\end{aligned} \tag{6.13}$$

The calculation of the excitation paths $\langle \frac{3}{2}, +\frac{3}{2}| \otimes |\frac{1}{2}, +\frac{1}{2}\rangle$ yields

$$\frac{1}{\sqrt{6}(4\alpha^2+8)}
\begin{pmatrix}
-\alpha f_c + if_d & \left(\alpha^2+1\right) f_a & \alpha f_d - if_c \\
0 & 0 & 0 \\
-f_d + i\alpha f_c & 2\alpha f_b - i\left(\alpha^2-1\right) f_a & f_c - i\alpha f_d \\
0 & 0 & 0 \\
f_a + if_b & -\alpha f_c + f_c - i(\alpha+1) f_d & -f_b + (-i) f_a \\
0 & 0 & 0
\end{pmatrix}$$

$$\begin{pmatrix}
2\alpha f_b + i\left(\alpha^2-1\right) f_a & \alpha(\alpha f_a - if_b) & -\alpha f_c + f_c + i(\alpha+1) f_d \\
0 & 0 & 0 \\
\left(\alpha^2+1\right) f_a & \alpha(f_b - i\alpha f_a) & (\alpha-1) f_d + i(\alpha+1) f_c \\
0 & 0 & 0 \\
(\alpha-1) f_d - i(\alpha+1) f_c & -(\alpha(f_c + if_d)) & 2f_a \\
0 & 0 & 0
\end{pmatrix}. \tag{6.14}$$

When α is dominant, the excitation paths simplify to

$$\begin{pmatrix}
0 & f_a & 0 & if_a & f_a & 0 \\
0 & 0 & 0 & 0 & 0 & 0 \\
0 & -if_a & 0 & f_a & -if_a & 0 \\
0 & 0 & 0 & 0 & 0 & 0 \\
0 & 0 & 0 & 0 & 0 & 0 \\
0 & 0 & 0 & 0 & 0 & 0
\end{pmatrix}, \tag{6.15}$$

showing that only the coefficients f_a contribute. This results from the fact that, for $\alpha \to \infty$, the excitation paths involve only quasimolecular orbitals with the same phase, i.e., the bonding $b+$ orbitals. For smaller values of α, the bonding and antibonding states are mixed, resulting in excitation paths where the phase changes according to the coefficients f_b, f_c, and f_d. Each path is then multiplied by the respective matrix elements of Eq. (3.14) and summed in amplitude. The intensity is proportional to the square of the amplitude. The modulation arises from the structure factor and the coefficients via Eq. (6.11). To obtain the intensity of peak A, we sum the intensities of the excitations from the other quartet states to the doublet states in all the 8 combinations. The result and its dependence on α are shown in Fig. 4(a), (d), and (g) of Chap. 6.1.

For peaks B and C, we calculate the excitations of an electron from the e states to the $J_{\text{tet}} = 3/2$ and $J_{\text{tet}} = 1/2$ states, respectively. Using the matrix elements derived in Chap. 3.3, we consider moving a hole from the $J_{\text{tet}} = 3/2$ or $J_{\text{tet}} = 1/2$ states to the e states. This calculation is more complex because, even for dominant α, it involves, in general, a combination of f_a, f_b, f_c, and f_d coefficients. However, for peak C, the calculation leads to a dominant f_b behavior, as shown in Fig. 4(c), (f), and (i) of Chap. 6.1. Interestingly, the modulation of peak B also shows a dominant f_b behavior for large α. However, it also contains the coefficients f_a, which instead becomes dominant for small α. So, the modulation of peak B transitions from dominant f_b at large α to dominant f_a at small α, passing through a range of α for which the modulation is quite constant. This behavior is shown in Fig. 4(b), (e), and (h) of Chap. 6.1.

6.4 Calculation of quasimolecular orbitals with Quanty

We used Quanty [247, 261] to check the correctness of the calculations described in the previous section and to calculate the effect of electron-electron interactions on the quasimolecular orbitals and the RIXS intensity. Many tutorials and descriptions of the functions used here can be found on the Quanty website [262]. In this section, we report the specific physics-related problems we encountered and the solutions we found for the calculation of the quasimolecular orbitals. To calculate RIXS at the L_3 edge of a Ta tetrahedron in Quanty, we need four sites, each with a p and a d shell. The skeleton of the code for a single Ta site was created with Crispy [263]. We use 64 basis states, numbered from 0 to 63. They are ordered as described below, where `Dn` and `Up` refer to the spin-down and spin-up states, respectively.

```
Ta1_2p_Dn = {0,2,4};  Ta1_2p_Up = {1,3,5}
Ta2_2p_Dn = {6,8,10}; Ta2_2p_Up = {7,9,11}
Ta3_2p_Dn = {12,14,16}; Ta3_2p_Up = {13,15,17}
Ta4_2p_Dn = {18,20,22}; Ta4_2p_Up = {19,21,23}

Ta1_5d_Dn = {24, 26, 28, 30, 32}; Ta1_5d_Up = {25, 27, 29, 31, 33}
Ta2_5d_Dn = {34, 36, 38, 40, 42}; Ta2_5d_Up = {35, 37, 39, 41, 43}
Ta3_5d_Dn = {44, 46, 48, 50, 52}; Ta3_5d_Up = {45, 47, 49, 51, 53}
Ta4_5d_Dn = {54, 56, 58, 60, 62}; Ta4_5d_Up = {55, 57, 59, 61, 63}
```

All the operators are written in second quantization in terms of annihilation and creation operators on these basis states. For example, we can create the creation and annihilation

operators on a certain basis state as

```
-- total number of basis states
NFermions = 64
-- creation and annihilation operators on basis state 0
Op_C0 = NewOperator("Cr", NFermions, 0)
Op_A0 = NewOperator("An", NFermions, 0)
-- creation and annihilation operator on basis state 1
Op_C1 = NewOperator("Cr", NFermions, 1)
Op_A1 = NewOperator("An", NFermions, 1)
-- print in the terminal the information about the operators
print(Op_C0)
print(Op_A1)
-- print in the terminal the result of the multiplication and summation of
  some operators with some factors
print((3-1*I)*Op_C0*Op_A1 + (-2+4*I)*Op_C1*Op_A0)
```

Executing this script gives the following output in the terminal:

```
Operator: Creation operator on site 0
QComplex         =          0 (Real==0 or Complex==1 or Mixed==2)
MaxLength        =          1 (largest number of product of lader operators)
NFermionic modes =         64 (Number of fermionic modes (site, spin, orbital,
   ...) in the one particle basis)
NBosonic modes   =          0 (Number of bosonic modes (phonon modes, ...) in
  the one particle basis)

Operator of Length   1
QComplex      =          0 (Real==0 or Complex==1)
N             =          1 (number of operators of length   1)
C  0 | 1.00000000000000E+000


Operator: Annihilation operator on site 1
QComplex         =          0 (Real==0 or Complex==1 or Mixed==2)
MaxLength        =          1 (largest number of product of lader operators)
NFermionic modes =         64 (Number of fermionic modes (site, spin, orbital,
   ...) in the one particle basis)
NBosonic modes   =          0 (Number of bosonic modes (phonon modes, ...) in
  the one particle basis)

Operator of Length   1
QComplex      =          0 (Real==0 or Complex==1)
N             =          1 (number of operators of length   1)
A  1 | 1.00000000000000E+000


Operator: Operator
QComplex         =          1 (Real==0 or Complex==1 or Mixed==2)
MaxLength        =          2 (largest number of product of lader operators)
NFermionic modes =         64 (Number of fermionic modes (site, spin, orbital,
   ...) in the one particle basis)
NBosonic modes   =          0 (Number of bosonic modes (phonon modes, ...) in
  the one particle basis)
```

```
Operator of Length   2
QComplex      =          1 (Real==0 or Complex==1)
N             =          2 (number of operators of length   2)
C  0 A  1 | 3.00000000000000E+000 -1.00000000000000E+000
C  1 A  0 | -2.00000000000000E+000 4.00000000000000E+000
```

We aim to create the Hamiltonian that describes the tetrahedron in the ground state. This requires constructing four single-site Hamiltonians that include the spin-orbit coupling and the electron-electron interaction. Since we will restrict the calculation to the t_{2g} orbitals, we can omit for simplicity the creation of the crystal field Hamiltonian. Next, we need to construct the hopping Hamiltonian. As the $2p$ shells are fully occupied in the ground state, we can skip creating the Hamiltonian for these states. Quanty provides built-in functions to create these operators.

```
-- spin-orbit coupling operator
zeta = 0.27
Hso_5d_1 = zeta*NewOperator('ldots', NFermions, Ta1_5d_Up, Ta1_5d_Dn)

-- electron-electron interaction operators with input parameters JH and U,
  converted into F0, F2, and F4
JH = 0.4
U = 1.75

F2 = JH*1323/121
F4 = F2*2/3
F0 = U - (F2 + F4)*4/49
F0_5d_5d_1 = F0*NewOperator('U', NFermions, Ta1_5d_Up, Ta1_5d_Dn, {1, 0, 0})
F2_5d_5d_1 = F2*NewOperator('U', NFermions, Ta1_5d_Up, Ta1_5d_Dn, {0, 1, 0})
F4_5d_5d_1 = F4*NewOperator('U', NFermions, Ta1_5d_Up, Ta1_5d_Dn, {0, 0, 1})
Hee_5d_1 = F0_5d_5d_1 + F2_5d_5d_1 + F4_5d_5d_1
```

With this code, we can create the single-site Hamiltonian for the Ta site number 1. Similarly, the other three single-site Hamiltonians `Hso_5d_2`, `Hso_5d_3`, `Hso_5d_4`, `Hee_5d_2`, `Hee_5d_3`, and `Hee_5d_4` can be created by substituting the appropriate basis state numbers. Then, we want to create the hopping Hamiltonian, using the hopping matrix T_{12} between the Ta_1 and Ta_2 sites as an example. For a given hopping matrix T, we create the operator

$$H_t = \sum_{i,j} T_{ij}\, c^\dagger_{i\sigma}\, c_{j\sigma} + \text{c.c.} \tag{6.16}$$

where $c^\dagger_{i\sigma}$ is the creation operator of an electron with spin σ on site i, and $c_{j\sigma}$ is the annihilation operator of an electron with spin σ on site j. The summation runs over the basis states of the two sites. We define a function `hopping_Hamiltonian(NFermions, Orb1, Orb2, T)` to create this operator. The function takes as input the total number of basis states, the basis states of the two sites, and the hopping matrix.

```
-- value of the hopping parameters
t1 = 0.45
t2 = 0.45
t3 = 1.17
-- hopping matrix between Ta1 and Ta2 in the cubic basis: {x2y2, z2, yz, xz, xy}
T12 = {{ 0,  0,  0,  0,  0 },
```

```
       { 0, 0,  0,  0,  0 },
       { 0, 0, t1,-t2,  0 },
       { 0, 0,-t2, t1,  0 },
       { 0, 0,  0,  0,-t3 }}

-- helper function to create the hopping hamiltonian between two orbitals
function hopping_Hamiltonian(NFermions, Orb1, Orb2, T)
    Ht = 0
    for ii = 1, #Orb1 do
        for jj = 1, #Orb2 do
            Op_C1 = NewOperator("Cr", NFermions, Orb1[ii])
            Op_A1 = NewOperator("An", NFermions, Orb1[ii])
            Op_C2 = NewOperator("Cr", NFermions, Orb2[jj])
            Op_A2 = NewOperator("An", NFermions, Orb2[jj])

            Ht = Ht + T[ii][jj]*Op_C1*Op_A2 + Conjugate(T[ii][jj])*Op_C2*Op_A1
        end
    end
    return Ht
end

Ht12 = hopping_Hamiltonian(NFermions, Ta1_5d_Up, Ta2_5d_Up, T12) +
       hopping_Hamiltonian(NFermions, Ta1_5d_Dn, Ta2_5d_Dn, T12)
```

Analogously, we create the other hopping matrices `Ht13`, `Ht14`, `Ht23`, `Ht24`, and `Ht34`. (The same result can be obtained using the built-in `Matrix` object and the function `ToOperator`, but it requires the full 64×64 matrix as input.) For simplicity of their expressions, the hopping Hamiltonians were created assuming that the basis states are the cubic basis states. However, the default Quanty operators for the d shells, such as the spin-orbit coupling and electron-electron interaction operators, are created using the $l = 2$ spherical harmonics basis, ordered from $m_l = -2$ to $+2$ with alternating spin-down and spin-up. So, we need to change the basis of the spin-orbit and electron-electron interaction Hamiltonians before summing them with the hopping Hamiltonian. We can use the built-in function `YtoKMatrix` to create the matrix that changes the basis from spherical harmonics to the cubic basis, following the same definitions as in Eq. (2.1) for the d orbitals and Eq. (2.4) for the p orbitals. Then, we apply the basis transformation using the `Rotate(M,R)` function, which performs $R^* \cdot M \cdot R^T$. The basis of each p and d shell will change from the spherical harmonics to $\{x\downarrow, x\uparrow, y\downarrow, y\uparrow, z\downarrow, z\uparrow\}$ for the p shell and to $\{x^2-y^2\downarrow, x^2-y^2\uparrow, z^2\downarrow, z^2\uparrow, yz\downarrow, yz\uparrow, zx\downarrow, zx\uparrow, xy\downarrow, xy\uparrow\}$ for each d shell.

```
M_cubic = YtoKMatrix({"p","p","p","p","d","d","d","d","d"})
Hso_1234 = Hso_5d_1 + Hso_5d_2 + Hso_5d_3 + Hso_5d_4
Hee_1234 = Hee_5d_1 + Hee_5d_2 + Hee_5d_3 + Hee_5d_4
H_so_ee_cubic = Rotate( Hso_1234 + Hee_1234, M_cubic)

Ht_1234 = Ht12 + Ht13 + Ht14 + Ht23 + Ht24 + Ht34
Hgs_cubic= Hso_ee_cubic + Ht_1234
```

For example, we can verify that the spin-orbit coupling Hamiltonian is the standard one by printing the operator in matrix form

```
  print(Matrix.Sub(
```

```
          OperatorToMatrix(
            Rotate(Hso_5d_1*2/zeta, M_cubic)),
          29, 6, 29, 6))
```

where `OperatorToMatrix` converts the operator into a 64×64 matrix, and `Matrix.Sub` extracts the 6×6 submatrix corresponding to the t_{2g} orbitals of site 1. These start at position 29: 24 p orbitals, 4 e_g orbitals, and 1 because Lua uses 1-based array indexing. The result, in units of $\frac{\lambda}{2}$, is the following:

```
{ { 0   ,  0   , -1 I ,  0   ,  0   ,  1   } ,
  { 0   ,  0   ,  0   ,  1 I , -1   ,  0   } ,
  { 1 I ,  0   ,  0   ,  0   ,  0   ,  1 I } ,
  { 0   , -1 I ,  0   ,  0   ,  1 I ,  0   } ,
  { 0   , -1   ,  0   , -1 I ,  0   ,  0   } ,
  { 1   ,  0   , -1 I ,  0   ,  0   ,  0   } }
```

which corresponds to Eq. (2.17), apart from the switching of the order of down and up states. In our case, we can use the z quantization axis. If we want to change the quantization axis, to simulate, e.g., a face-sharing geometry as described in Chap. 2.2.3, we can use the rotation matrix as in Eq. (2.16). It is important to note that the order of the up and down states used in Quanty differs from the one used in Eq. (2.16). We can create the spin-orbit coupling matrix in Eq. (2.16) as a function of the polar angle θ and the azimuthal angle ϕ, and then use the function `Rotate` to apply the rotation to the spin-orbit coupling Hamiltonian created in Quanty. We do this using the function

```
function OperatorSpinOrbitThetaPhi(NF, OrbDn, OrbUp, theta, phi)
-- theta and phi in radians
  alphap =  math.exp(-1*I*phi) * math.cos(theta/2)
  alpham = -math.exp(-1*I*phi) * math.sin(theta/2)
  betap = math.sin(theta/2)
  betam = math.cos(theta/2)
  abMat = {{betam, alpham},
           {betap, alphap}}

  rotMat = ZeroMatrix(NF,NF)
  for i = 1, #OrbDn do
    rotMat = insertMatrix( rotMat, abMat, OrbDn[i]+1, OrbDn[i]+1)
  end

  Hso = NewOperator("ldots", NF, OrbUp, OrbDn)
  Hso_thetaphi = Rotate(Hso, rotMat);

  return Hso_thetaphi
end
```

where we used the functions

```
-- Creates a zero-initialized matrix with specified size (nrows x ncolumns).
function ZeroMatrix(nrows, ncolumns)
    local matrix = {}
    for i = 1, nrows do
        matrix[i] = {}
        for j = 1, ncolumns do
            matrix[i][j] = 0
```

```
        end
    end
    return matrix
end

-- Inserts a submatrix into a larger matrix
-- at a specified starting row and column.
function insertMatrix(matrix, submatrix, startRow, startCol)
    for i = 1, #submatrix do
        for j = 1, #submatrix[1] do
            matrix[startRow+i-1][startCol+j-1] = submatrix[i][j]
        end
    end
end
```

We now want to restrict the calculation to the t_{2g} orbitals. There are multiple ways to achieve this. One approach is to set restrictions when calculating the eigenstates using the `Eigensystem` function with the `Restrictions` option. The restrictions are specified as a table containing the number of fermions, the number of bosons, and the restrictions themselves. The restrictions are represented as a string of 64 characters, where each character corresponds to a basis state. A "1" indicates that the restriction applies to that basis state, while a "0" means it does not. The string is followed by the minimum and maximum number of fermions allowed in the basis states marked by "1". In the cubic basis, the e_g states correspond to the following basis state numbers: 24, 25, 26, 27 for site 1; 34, 35, 36, 37 for site 2; 44, 45, 46, 47 for site 3; 54, 55, 56, 57 for site 4. To calculate the eigenstates, we also need the Hamiltonian (`Hgs_t2g`), the initial vector (`initial_vector`), and the number of eigenstates (`NPsis`) to compute. Note that the number of electrons occupying the basis states is not specified during the creation of the Hamiltonian. Instead, it is defined in the initial vector, where we specify the number of electrons present in the system. This is done similarly to the restrictions, using a string of 64 characters followed by the number of electrons in the basis states marked by "1". The number has to be specified for each basis state. In the ground state, the $2p$ states are fully occupied with 24 electrons, 7 electrons are shared among the 4 t_{2g} shells, and 0 electrons occupy the e_g states.

```
Neg_min = 0
Neg_max = 0
restriction_eg = { 64, 0,
  {'000000 000000 000000 000000 1111000000 1111000000 1111000000 1111000000',
    Neg_min, Neg_max}}

initial_vector = { 64, 0,
  {'111111 111111 111111 111111 0000000000 0000000000 0000000000 0000000000',
    24, 24},
  {'000000 000000 000000 000000 0000111111 0000111111 0000111111 0000111111',
    7,  7},
  {'000000 000000 000000 000000 1111000000 1111000000 1111000000 1111000000',
    0,  0}}
NPsis = 10
eigenstates = Eigensystem( Hgs_cubic, initial_vector, NPsis,
                           {{'Restrictions', restriction_eg}})
```

In this case, we do not want any electrons in the e_g states, so we set the minimum (`Neg_min`) and maximum (`Neg_max`) number of electrons in the e_g states to 0. Using these restrictions, it is possible to allow, for example, at most only 1 electron in the e_g states by changing `Neg_max` to 1. This way, we could calculate the corrections to the ground state from the configurations with 1 electron in the e_g states while neglecting the much higher energy configurations with 2 electrons in the e_g states, which would have a negligible contribution.

Another way to restrict the e_g states, since we are going to neglect them completely, is to remove the e_g basis states entirely, thus reducing the dimension of the Hilbert space. We can do this by creating a 48×64 ($r \times c$) matrix and using the function `Rotate`. We do not want to modify the $2p$ states, so their part will simply be a 24×24 identity matrix. For each of the d shells, we want to remove the first 4 basis states and keep the last 6. We achieve this with a 6×10 matrix, as shown in the code here:

```
M_t2g = ZeroMatrix(48, 64)
insertMatrix(M_t2g, Matrix.ToTable(Matrix.Identity(24)), 1, 1)
M_restr_t2g = {{ 0, 0, 0, 0, 1, 0, 0, 0, 0, 0},
               { 0, 0, 0, 0, 0, 1, 0, 0, 0, 0},
               { 0, 0, 0, 0, 0, 0, 1, 0, 0, 0},
               { 0, 0, 0, 0, 0, 0, 0, 1, 0, 0},
               { 0, 0, 0, 0, 0, 0, 0, 0, 1, 0},
               { 0, 0, 0, 0, 0, 0, 0, 0, 0, 1}}
insertMatrix(M_t2g, M_restr_t2g, 25, 25)
insertMatrix(M_t2g, M_restr_t2g, 31, 35)
insertMatrix(M_t2g, M_restr_t2g, 37, 45)
insertMatrix(M_t2g, M_restr_t2g, 43, 55)

Hgs_t2g = Rotate(Hgs_cubic, M_t2g)
```

If we now want to calculate the eigenvectors, we can use the same `Eigensystem` function as before, but without the restrictions on the e_g states. Since our basis now consists of only 48 fermionic states, the initial vector needs to be modified accordingly.

```
initial_vector = {48, 0,
 {'111111 111111 111111 111111 000000 000000 000000 000000', 24, 24},
 {'000000 000000 000000 000000 111111 111111 111111 111111',  7,  7}}
eigenstates = Eigensystem( Hgs_t2g, initial_vector, NPsis)
```

We want to perform an additional basis transformation to rotate the Hamiltonian into the tetrahedral quasimolecular orbital basis defined in Eq. (6.8). This can be achieved similarly to the previous transformation by constructing a matrix that transforms the cubic basis into the tetrahedral basis and applying the `Rotate` function. The upper-left 24×24 block of the matrix, corresponding to the p basis states, remains an identity matrix since these states are not modified. The lower-right 24×24 block represents the transformation of the t_{2g} orbitals into the tetrahedral quasimolecular orbitals. In the resulting basis, the states are ordered as $\{a_1\downarrow, a_1\uparrow, e_\alpha\downarrow, e_\alpha\uparrow, e_\beta\downarrow, \ldots, t_{1\gamma}\uparrow\}$, following the sequence in Eq. (6.8), with alternating spin-down and spin-up components.

```
function scaleList(list, multiplier)
-- returns the list with each element scaled by the multiplier
    for i = 1, #list do
        list[i] = list[i] * multiplier
```

```
    end
    return list
end

alp = (t3-t1)/t2 - 0.5 + 1/(2*t2)*math.sqrt(4*(t3-t1)*(t3-t1-t2)+9*t2*t2)
c1 = 1/(2*math.sqrt(3))
c2 = 1/(2*math.sqrt(2))
c3 = 1/(2*math.sqrt(6))
c4 = 1/(2*math.sqrt(2+alp*alp))
c5 = 1/(2*math.sqrt(4+2*alp*alp))
c6 = 1/math.sqrt(8)

a1 = scaleList({ 1,-1, 1,-1, 1, 1,-1,-1,-1, 1, 1,-1},c1)
ea = scaleList({ 0, 1, 1, 0,-1, 1, 0, 1,-1, 0,-1,-1},c2)
eb = scaleList({-2,-1, 1, 2, 1, 1, 2,-1,-1,-2, 1,-1},c3)
t2ba = scaleList({alp,  1, -1,alp,  1,  1,alp, -1, -1,alp, -1,  1},c4)
t2bb = scaleList({  1,alp,  1,  1,alp, -1, -1,alp, -1, -1,alp,  1},c4)
t2bc = scaleList({ -1,  1,alp,  1, -1,alp, -1, -1,alp,  1,  1,alp},c4)
t2aba = scaleList({  -2,alp,-alp,  -2, alp,alp,  -2,-alp,-alp, -2,-alp, alp},c5)
t2abb = scaleList({-alp,  2,-alp,-alp,  2, alp, alp,   2, alp,alp,   2,-alp},c5)
t2abc = scaleList({-alp,alp,  -2, alp,-alp, -2,-alp,-alp,  -2,alp, alp,  -2},c5)
t1a = scaleList({ 0, 1, 1, 0, 1,-1, 0,-1, 1, 0,-1,-1},c6)
t1b = scaleList({ 1, 0,-1, 1, 0, 1,-1, 0, 1,-1, 0,-1},c6)
t1c = scaleList({ 1, 1, 0,-1,-1, 0, 1,-1, 0,-1, 1, 0},c6)

M_MO = Matrix.AddSpin{a1, ea, eb, t2ba, t2bb, t2bc, t2aba, t2abb, t2abc, t1a,
    t1b, t1c}

rot_MO = ZeroMatrix(48, 48)
insertMatrix(rot_MO, Matrix.ToTable(Matrix.Identity(24)), 1, 1)
insertMatrix(rot_MO, M_MO, 25, 25)

Hgs_MO = Rotate(Hgs_t2g, rot_MO)
```

In the quasimolecular orbital basis, we could restrict the effect of the spin-orbit coupling to only the lowest t_2 molecular orbitals. To achieve this, we can use the `Rotate` function with a projection matrix. This matrix is initialized with all zeros, except for a 6×6 identity matrix positioned at row 31 and column 31. The starting position accounts for 24 p orbitals, 2 a_1 orbitals, 4 e orbitals, and the 1-based indexing used in Lua. This would ensure that only the lowest t_2 orbitals are affected by the spin-orbit coupling.

```
Hso_1234_cubic = Rotate(Hso_1234, M_cubic) -- spherical to cubic basis
Hso_1234_t2g = Rotate(Hso_1234_cubic, M_t2g) -- t2g restriction
Hso_1234_MO = Rotate(Hso_1234_t2g, rot_MO) -- t2g to MO basis

-- projection matrix for the t2 orbitals
M_so_t2 = ZeroMatrix(48, 48)
insertSublist(M_so_t2, Matrix.ToTable(Matrix.Identity(6)), 31, 31)

Hso_1234_MO_t2 = Rotate(Hso_1234_MO, M_so_t2) -- restriction of so to t2
```

After transforming the basis to the quasimolecular orbitals, we can apply restrictions to speed up the calculation. For example, we can restrict the calculation to the lowest 12

quasimolecular orbitals or allow only a single electron in the uppermost antibonding t_2 quasimolecular orbitals. This would reduce the size of the Hilbert space from $\binom{24}{7} = 346104$ to respectively $\binom{12}{7} = 792$ and $\binom{12}{7} + \binom{12}{6}\,6 = 6336$. These restrictions can be implemented using the same approach described earlier for the e_g states.

```
restriction_t2t1 = { 48, 0,
  {'000000 000000 000000 000000 00 0000 000000 111111 000000', 0, 1},
  {'000000 000000 000000 000000 00 0000 000000 000000 111111', 0, 0}}

initial_vector = { 48, 0,
  {'111111 111111 111111 111111 00 0000 000000 000000 000000', 24, 24},
  {'000000 000000 000000 000000 11 1111 111111 000000 000000',  7,  7},
  {'000000 000000 000000 000000 00 0000 000000 111111 111111',  0,  0}}
NPsis = 10
eigenstates = Eigensystem(Hgs_MO, initial_vector, NPsis,
                                  {{'Restrictions', restriction_t2t1}})
```

To analyze the eigenstates, we can calculate the expectation values of various operators for these wavefunctions. This can be done using the function `Braket(Psi, Operator, Psi)` or simply by doing the product `Psi*Operator*Psi`. In the following, we calculate the expectation values of the Hamiltonian to obtain the eigenvalues and, as an example, the number operator for each molecular orbital shell to determine the orbital occupation.

```
Na = NewOperator("Number",48, {24,25}, {24,25}, {1,1})
Ne = NewOperator("Number",48, {26,27,28,29}, {26,27,28,29}, {1,1,1,1})
Nt2b = NewOperator("Number",48, {30,31,32,33,34,35},
                                {30,31,32,33,34,35}, {1,1,1,1,1,1})
Nt2ab = NewOperator("Number",48, {36,37,38,39,40,41},
                                 {36,37,38,39,40,41}, {1,1,1,1,1,1})
Nt1 = NewOperator("Number",48, {42,43,44,45,46,47},
                               {42,43,44,45,46,47}, {1,1,1,1,1,1})
Na.Name = "Na"; Ne.Name = "Ne"; Nt2b.Name = "Nt2b";
Nt2ab.Name = "Nt2ab"; Nt1.Name = "Nt1"; H_1234_MO.Name = "H_MO"

Egs = eigenstates[1]*H_1234_MO*eigenstates[1] -- ground state energy
PrintExpectationValues(eigenstates,{H_1234_MO-Egs, Na, Ne, Nt2b, Nt2ab, Nt1})
```

Where `NewOperator("Number",NF, {i,k}, {j,l}, {a,b})` creates the operator $a\,c_i^\dagger c_j + b\,c_k^\dagger c_l$. The function `PrintExpectationValues(psiList, opList)` prints the expectation values of a list of operators on the eigenstates on the terminal giving the following output:

```
          H_MO     Na       Ne       Nt2b     Nt2ab    Nt1
  1       0        1.9862   3.829    1.1567   0.0281   0
  2       0        1.9862   3.829    1.1567   0.0281   0
  3       0        1.9862   3.829    1.1567   0.0281   0
  4       0        1.9862   3.829    1.1567   0.0281   0
  5       0.2573   1.985    3.7944   1.1811   0.0394   0
  6       0.2573   1.985    3.7944   1.1811   0.0394   0
  7       0.5022   1.9896   2.9323   2.0531   0.025    0
  8       0.5022   1.9896   2.9323   2.0531   0.025    0
  9       0.5256   1.9897   2.9215   2.0627   0.026    0
  10      0.5256   1.9897   2.9215   2.0627   0.026    0
```

From the eigenvalues we recognize the quartet ground state and the doublet first excited state at $\approx 250\,\mathrm{meV}$. From the expectation values of the number operators, we see that the first six eigenstates correspond to an electronic configuration close to $a_1^2\, e^4\, t_2^1\, t_2^0$. At higher energies, we find states with configurations predominantly close to $a_1^2\, e^3\, t_2^2\, t_2^0$. To analyze the eigenstates in more detail, we can save them to a file and analyze their composition.

```
print(eigenstates[1])
eigenstates[1].Print({{"file", "eigenstate_1.txt"}})
```

The output is a list of the Slater determinants that constitute the wavefunction and their coefficients.

```
WaveFunction: Wave Function
QComplex         =          1 (Real==0 or Complex==1)
N                =       6334 (Number of basis functions used to discribe psi)
NFermionic modes =         48 (Number of fermions in the one particle basis)
NBosonic modes   =          0 (Number of bosons in the one particle basis)

####   pre-factor        pre-factor        Determinant
   1 -4.2075706678E-06  2.8025293719E-06  111111111111111111111111010101010101010000000000
   2  2.7984526989E-06  4.0582600176E-06  111111111111111111111111010101010101000100000000
   3  8.9561740677E-06  4.2354369819E-06  111111111111111111111111010111010100000000000000
   4  1.0161618865E-04  4.8058094489E-05  111111111111111111111111000111011100000000000000
   5  3.1891479050E-05 -3.1997850585E-05  111111111111111111111111010101111001000000000000
...
6333  3.5522166748E-03 -6.6468439231E-03  111111111111111111111111111100100010000000000000
6334 -5.6889048569E-02 -6.0344871599E-02  111111111111111111111111111110100000000000000000
```

The Slater determinants are represented as strings of, in this case, 48 characters, where "1" indicates that the basis state is occupied and "0" that it is empty. We can analyze this file to understand the composition of the wavefunction in terms of electronic configurations. For the parameters $t_3 = 1.17$, $t_2 = t_1 = 0.45$, $\lambda = 0.27$, $J_H = 0.4$, and $U = 1.75$ we find that the ground state $J_{\mathrm{tet}} = 3/2$ wavefunctions and the first excited states $J_{\mathrm{tet}} = 1/2$ wavefunctions are composed of the following electronic configurations:

Configuration	$J_{\mathrm{tet}} = 3/2$	$J_{\mathrm{tet}} = 1/2$
$a_1^2\ e^4\ t_2^1\ t_2^0$	88.4 %	84.8 %
$a_1^2\ e^2\ t_2^3\ t_2^0$	5.2 %	6.1 %
$a_1^2\ e^3\ t_2^2\ t_2^0$	2.9 %	4.4 %
$a_1^2\ e^3\ t_2^1\ t_2^1$	1.3 %	1.2 %
$a_1^1\ e^3\ t_2^2\ t_2^1$	1.2 %	1.2 %
$a_1^2\ e^4\ t_2^0\ t_2^1$	0.2 %	1.4 %
...	< 0.2 %	< 0.2 %

(6.17)

The leading configuration of $J_{\mathrm{tet}} = 3/2$ and $J_{\mathrm{tet}} = 1/2$ is $a_1^2\ e^4\ t_2^1\ t_2^0$, with respectively weights of 88.4 % and 84.8 %. The main effect of the electron-electron interactions J_H and U is to mix into the ground and excited states the configuration $a_1^2\ e^2\ t_2^3\ t_2^0$, contributing approximately 5.2 % and 6.1 % weight, respectively. This is in agreement with the results of quantum chemistry calculations in Ref. [264], see Table 6 in the Supplementary Information. The effect of electron-electron interactions on the eigenvalues is shown in Fig. S3 of the Supplementary Information of Chap. 6.1, while their effect on the spin-orbit splitting is shown in Fig. 3 of Chap. 6.1.

In the following, we examine the impact of electron-electron interactions on the RIXS modulation. It is important to note that the configuration $a_1^2\ e^2\ t_2^3\ t_2^0$ in the $J_{\text{tet}} = 1/2$ state cannot be reached by the RIXS process from the leading configuration $a_1^2\ e^4\ t_2^1\ t_2^0$ of the $J_{\text{tet}} = 3/2$ ground state. So, we intuitively expect only a minor effect on the RIXS amplitude. Additionally, all the other configurations that also involve a change in the orbital occupation of more than one electron at a time are inaccessible from the leading configuration of the $J_{\text{tet}} = 3/2$ ground state. We now show how to set up the calculation of the RIXS intensity using Quanty. We use the function `CreateResonantSpectra`

```
CreateResonantSpectra(
  H_intermediate,                    -- intermediate state hamiltonian
  H_final,                           -- final state hamiltonian
  D_in,                              -- absorption transition operator
  D_out,                             -- fluorescence transition operator
  Psi,                               -- ground state
{{'restrictions1', restr_interm},    -- restrictions intermediate states
 {'restrictions2', restr_final},     -- restrictions final states
 {'Emin1', Emin1}, {'Emax1', Emax1},-- energy range of the resonance energy
 {'NE1', NE1},                       -- number of points of the resonance energy
 {'Gamma1', Gamma1},                 -- broadening of the intermediate state
 {'Emin2', Emin2}, {'Emax2', Emax2},-- energy loss range in eV
 {'NE2', NE2},                       -- number of points in the spectrum
 {'Gamma2', Gamma2},                 -- broadening of the spectrum
})
```

that calculates the RIXS intensity as a third order Green's function or susceptibility (χ_3) [265] according to

$$I(\omega_{in}, \mathbf{q}, \omega_{out}) = -\frac{1}{\pi}\text{Im}\left\langle \Psi_i \right| D_{in}^{\dagger} \frac{1}{\omega_{in} - H_m + i\Gamma_1} D_{out}^{\dagger} \frac{1}{\omega_{out} - H_f + i\Gamma_2} D_{out} \frac{1}{\omega_{in} - H_m + i\Gamma_1} D_{in} \left| \Psi_i \right\rangle \quad (6.18)$$

where Ψ_i is the inital wavefunction, ω_{in}, the resonance energy, corresponds to `E1`, ω_{out}, the emission energy, to `E2`, H_m to `H_intermediate`, and H_f to `H_final`.

We need to create the intermediate state Hamiltonian. To describe the d shells, we can use the same Hamiltonian as for the initial state. Now, we need to include a Hamiltonian to describe the p shell as well. The most significant term is the strong spin-orbit coupling of the p shell. This is important to split the L_3 and L_2 edges, which determines the RIXS polarization selection rules. We can create the spin-orbit coupling operator for the intermediate state in the same manner as we did for the ground state. In the intermediate state, there is also an interaction between the core hole and the valence electrons. However, given that the broadening of the intermediate state for the L_3 edge of Ir is approximately 4-5 eV, this interaction does not have a substantial effect. Therefore, for the sake of simplicity, we will not discuss it further. Again, Crispy [263] can be used to easily generate the code for the intermediate state Hamiltonian. For the final state Hamiltonian we use the same as the ground state Hamiltonian.

Next, we need the transition operators. We want to create the operators

$$\begin{aligned}\hat{D}_{in} &= \sum_{i=1,2,3,4} e^{\mathbf{k}_{in}\cdot\mathbf{R}_i}\ \epsilon_{in}\cdot\hat{\mathbf{r}}_i \\ \hat{D}_{out} &= \sum_{i=1,2,3,4} e^{\mathbf{k}_{out}\cdot\mathbf{R}_i}\ \epsilon_{out}\cdot\hat{\mathbf{r}}_i\end{aligned} \tag{6.19}$$

We can create the dipole transition operator by expanding it in renormalized spherical harmonics C_{l,m_l}:

$$\epsilon\cdot\hat{\mathbf{r}} = (\epsilon_x + i\epsilon_y)C_{1,-1} + (-\epsilon_x + i\epsilon_y)C_{1,1} + \epsilon_z C_{1,0} \tag{6.20}$$

where ϵ_x, ϵ_y, and ϵ_z are the components of the polarization vector.

```
t = math.sqrt(1/2)
Dx_1 = NewOperator('CF', 64, Ta1_5d_Up, Ta1_5d_Dn, Ta1_2p_Up, Ta1_2p_Dn,
        {{1, -1, t    }, {1, 1, -t    }})
Dy_1 = NewOperator('CF', 64, Ta1_5d_Up, Ta1_5d_Dn, Ta1_2p_Up, Ta1_2p_Dn,
        {{1, -1, t * I}, {1, 1,  t * I}})
Dz_1 = NewOperator('CF', 64, Ta1_5d_Up, Ta1_5d_Dn, Ta1_2p_Up, Ta1_2p_Dn,
        {{1,  0, 1    }                })
Dx_dag_1 = NewOperator('CF', 64, Ta1_2p_Up, Ta1_2p_Dn, Ta1_5d_Up, Ta1_5d_Dn,
        {{1, -1, t    }, {1, 1, -t    }})
Dy_dag_1 = NewOperator('CF', 64, Ta1_2p_Up, Ta1_2p_Dn, Ta1_5d_Up, Ta1_5d_Dn,
        {{1, -1, t * I}, {1, 1,  t * I}})
Dz_dag_1 = NewOperator('CF', 64, Ta1_2p_Up, Ta1_2p_Dn, Ta1_5d_Up, Ta1_5d_Dn,
        {{1,  0, 1    }                })
```

In this way, we created the operators for the absorption and the emission of the photon of site 1, which have to be weighted by the respective polarization components. In the same way we can create the operators for the other sites. These operators are defined in the spherical harmonics basis, so we need to transform them into the quasimolecular orbital basis before performing the calculation. Fundamental for our purposes, to account for the interference effect between the RIXS amplitudes scattered at the four sites, each operator must be weighted by the corresponding complex exponential factor before being summed.

```
d = 3; l = d/sqrt(2);
R1 = { 0, 0, 0 }
R2 = {-l, l, 0 }
R3 = {-l, 0,-l }
R4 = { 0, l,-l }

kin_R1 = R1[1]*kin[1] + R1[2]*kin[2] + R1[3]*kin[3];
kout_R1 = R1[1]*kout[1] + R1[2]*kout[2] + R1[3]*kout[3];

ein_r_1 = e_in[1]*Dx_1 + e_in[2]*Dy_1 + e_in[3]*Dz_1
eouth_r_1 = e_out_h[1]*Dx_dag_1 + e_out_h[2]*Dy_dag_1 + e_out_h[3]*Dz_dag_1

D_in_1    = math.exp(I*kin_R1)*ein_r_1
D_out_1_h = math.exp(I*kout_R1)*eouth_r_1
```

Here, $\mathbf{k}_{in}$ and $\mathbf{k}_{out}$ are in units of $1/\text{Å}$ and defined in the same reference frame as the position of the ions $\mathbf{R}_i$. The RIXS transition operators of the other three sites are created in the same way. Then, we sum them to obtain the total transition operator

```
D_in = D_in_1 + D_in_2 + D_in_3 + D_in_4
D_out_h = D_out_1_h + D_out_2_h + D_out_3_h + D_out_4_h
```

Next, we need the ground state wavefunction from which the RIXS spectrum is calculated. As with the calculation of the eigenstates, we can apply restrictions to both the intermediate Hamiltonian and the final Hamiltonian.

In Quanty, the energies are relative and not absolute. To find the correct resonance energy for the calculation, we need to determine the energy difference between the ground state of the initial Hamiltonian and that of the intermediate Hamiltonian. This requires calculating the ground state eigenstate of the intermediate Hamiltonian and its energy. We can compute it by evaluating the expectation value of the intial and intermediate Hamiltonian on their respective ground states.

```
initial_state_interm = { 48, 0,
        {'111111 111111 111111 111111 00 0000 000000 000000 000000', 23, 23},
        {'000000 000000 000000 000000 11 1111 111111 000000 000000',  8,  8}}
Psis_m = Eigensystem(H_int_MO, initial_state_interm, 1,
                             {{'Restrictions', restriction_t2t1}})
E0m = Psi_m * H_int_MO * Psis_m
E0 = Psi_gs * H_gs_MO * Psi_gs
DeltaE = E0m - E0

Emin1 = -3 + DeltaE
Emax1 =  7 + DeltaE
NE1 = 10
Gamma1 = 5.0
```

In this way, we are in resonance with the L_3 edge, as the states with a core hole in the $p_{3/2}$ are lower in energy than the $p_{1/2}$ states. To be in resonance with the L_2 edge, we need to increase `Emin1` and `Emax1` by 1254 eV, using a spin-orbit coupling constant for the p shell of 836 eV. However, this code cannot reproduce the resonance map of $GaTa_4Se_8$ because we restricted the calculation to the t_{2g} orbitals. Thus, we can calculate the RIXS intensity at a single resonance energy selected to resonate with the t_{2g} states. The broadening due to the core-hole lifetime (`Gamma1`) is set to 5 eV. The last parameters we need are the energy loss range and the final broadening of the spectrum, which are straightforward to define.

To simulate an experimental spectrum we need additionaly to sum the spectra in intensity for the outgoing vertical polarization and the outgoing horizontal polarization. Additionally, we sum in intensity over all the degenerate ground states by varying the ground state eigenstate used in the calculation.

We have seen how to set up a Quanty script to perform calculations on a tetrahedron. We were particularly interested in studying the effect of the electron-electron interaction. As shown in Table (6.17), in the ground state, the main effect is to mix in the configuration $a_1^2\,e^2\,t_2^3\,t_2^0$. The leading configuration of the $J_{\text{tet}} = 3/2$ state is $a_1^2\,e^4\,t_2^1\,t_2^0$, with a weight of 88.4 %. This indicates that it can be well described by a single electron in the t_2 shell. As a result, single-electron calculations provide a good approximation to the many-body calculations. The effect of the electron-electron interaction on the modulation of the RIXS intensity of peak A is shown in Fig. S4 of the Supplementary Information of Chap. 6.1. As expected, it has only a minor effect.

Chapter 7

Conclusions and Outlook

We have seen how RIXS interference effects can be exploited to gain valuable information about bond-directional excitations in Kitaev materials and the quasimolecular wavefunctions in cluster Mott insulators containing, e.g., dimers, trimers, and tetramers.

We consider strongly correlated electron systems, in particular Mott insulators with localized magnetic moments, and highlight the important roles of orbitals and spin-orbit coupling. The directionality of the orbital interactions can, due to spin-orbit coupling, translate into anisotropic exchange interactions. Particularly interesting is the case of $j = 1/2$ magnetic moments, which are realized, for example, in the transition metal Ir^{4+} in an octahedral coordination with t_{2g}^5 electronic configuration. Specifically, IrO_6 octahedra placed in an edge-sharing geometry in a honeycomb lattice can, in the ideal case, realize the Kitaev Hamiltonian. This Hamiltonian is characterized by bond-directional nearest-neighbor magnetic interactions, which lead to exchange frustration and, in the ideal case, to a quantum spin liquid ground state. Experiments demonstrating the bond-directional character of the magnetic excitations were still missing.

Strong hopping in cluster Mott insulators lead to the delocalization of electrons over a cluster, such as a dimer, trimer, or tetramer, forming localized quasimolecular magnetic moments. We describe the hopping in the cases of edge-, corner-, and face-sharing ML_6 octahedra. The quasimolecular electronic structure of these systems is not well studied even though these materials might provide a source of exotic physics, given their higher complexity.

RIXS is a powerful technique to study the electronic structure of materials. Spin and orbital excitations can be measured to obtain information about their energy and the dependence on the exchanged momentum. Due to the coherence of the RIXS scattering process, the RIXS intensity exhibits a characteristic periodic modulation as a function of the exchanged momentum when the electrons are delocalized over a cluster forming quasimolecular wavefunctions. This arises from the interference of the RIXS amplitude scattered by the different atoms within the cluster. The RIXS interference effect has been predicted in Refs. [194,195] using the example of a dimer molecule. The experimental realization of RIXS interference in dimers such as $Ba_3CeIr_2O_9$ [197] and $Ba_3InIr_2O_9$ [6] has been discussed in the PhD thesis of A. Revelli [175], where also a first analysis of the data of $Ba_3Ti_{3-x}Ir_xO_9$ [1] can be found. We investigate for the first time the RIXS interference effects in trimers and tetramers, demonstrating the applicability of this technique to more complex systems. We

show in particular how the RIXS modulation contains very useful information about the composition and the symmetry of the quasimolecular wavefunctions.

Bond-directional excitations in the Kitaev materials Na_2IrO_3 and α-Li_2IrO_3

In Ref. [188], Revelli *et al.* observed a modulation of the RIXS intensity also in the magnetic excitations of the Kitaev materials Na_2IrO_3 and α-Li_2IrO_3. These magnetic excitations were observed to persist up to temperatures much higher than the ordering temperature, suggesting that they are not excitations of the ordered state. The observation of the modulation demonstrated the nearest-neighbor character of the magnetic excitations. In Kitaev materials, the bond-directional nearest-neighbor character of the magnetic interactions is of fundamental importance. In the ideal case, these magnetic interactions give rise to a quantum spin-liquid ground state. A system with bond-directional magnetic interactions is expected to exhibit bond-directional magnetic excitations, i.e., spin excitations that are magnetically inequivalent even for crystallographically equivalent directions. We use the honeycob lattice as an example. Crystallographically, it exhibits a three-fold rotation symmetry on each lattice site. For bond-directional excitations, however, different bond directions correspond to excitations of different spin components, such that a certain spin excitation can live only on the corresponding bond, breaking the crystallographic equivalence. However, proving the bond-directional character of the magnetic excitations is difficult. Chun *et al.* [193] showed the presence of dominant bond-directional interactions by measuring the polarization dependence of the REXS intensity in Na_2IrO_3. Their investigation focused on the diffuse scattering related to residual magnetic Bragg peak intensity observed above the magnetic ordering temperature. This diffuse scattering originates from short-range magnetic correlations. Through the analysis of the polarization dependence of the intensity, they provided evidence for dominant anisotropic bond-directional interactions. Instead, we focus on showing the presence of dominant bond-directional interactions via the study of the magnetic excitations not related to magnetic order. We show in particular how to observe the bond-directional character of the magnetic excitations using RIXS at the Ir L_3 edge in the Kitaev materials Na_2IrO_3 and α-Li_2IrO_3. This is based on the simultaneous determination of the spin component involved in the excitation (thanks to the RIXS polarization dependence) and the spatial orientation of the bond involved (thanks to the characteristic modulation of the RIXS intensity from each bond). This technique provides a tool to search for signatures of bond-directional interactions in the magnetic excitations and could be applied in the case of a real spin liquid.

In particular, in the RIXS spectra of Na_2IrO_3 and α-Li_2IrO_3, we observe two distinct features that can be distinguished by their polarization dependence: a low-energy excitation at 10 meV and 15 meV, and a high-energy excitation at 45 meV and 35 meV, in Na_2IrO_3 and α-Li_2IrO_3, respectively. Based on their polarization dependence, we identify the low-energy excitation as a spin-conserving excitation and the high-energy excitation as a spin-flip excitation. These excitations do not show strong dispersion, but the main effect as a function of the exchanged momentum is a pronounced periodic modulation of the RIXS intensity. We measure the RIXS intensity over a broad range of reciprocal space above and below the ordering temperature. We find that a simple model based on independent bonds was able

to describe many features of the RIXS data.

We present a model based on a single dimer described by the $JK\Gamma\Gamma'$ Hamiltonian. We explain how the wavefunctions split into $|0\rangle = (i|\uparrow\uparrow\rangle + |\downarrow\downarrow\rangle)/\sqrt{2}$, $|1\rangle = (-i|\uparrow\uparrow\rangle + |\downarrow\downarrow\rangle)/\sqrt{2}$, $|2\rangle = (|\downarrow\uparrow\rangle - |\uparrow\downarrow\rangle)/\sqrt{2}$, and $|3\rangle = (|\downarrow\uparrow\rangle + |\uparrow\downarrow\rangle)/\sqrt{2}$. In particular, if only $K \neq 0$, we have two doublets, $|0\rangle$-$|1\rangle$ and $|2\rangle$-$|3\rangle$, split by $K/4$. These doublets are further split, respectively, by Γ and J, where a positive sign of the parameter lowers the energy of $|0\rangle$ and of $|2\rangle$. The excitations among these states give rise to a peculiar polarization dependence that affects the RIXS intensity modulation. We propose as the ground state for both Na_2IrO_3 and α-Li_2IrO_3 the $|0\rangle$ state, obtained in this simple model from a positive sign of Γ. The spin-conserving excitation is then the transition from the $|0\rangle$ state to the $|1\rangle$ state. In Na_2IrO_3, the spin-flip excitation is the transition from the $|0\rangle$ state to the $|3\rangle$ state. Instead, in α-Li_2IrO_3, the spin-flip excitations can be explained by the superposition of the excitations from the $|0\rangle$ state to the $|2\rangle$ and $|3\rangle$ states. We speculate about the sign of J in Na_2IrO_3 and α-Li_2IrO_3 based on the observation or absence of the excitation to the $|3\rangle$ state, suggesting a positive sign of J in Na_2IrO_3 and a negative sign in α-Li_2IrO_3.

Further investigations of Na_2IrO_3 and α-Li_2IrO_3 using L_3 edge RIXS experiments with higher resolution at selected $\mathbf{q}$ points, chosen based on the presented model to maximize the intensity difference between the excitations, could help to identify the three excitations separately. The approach presented can be extended to other materials to search for signatures of bond-directional behavior in the electronic excitations. In Ref. [192], de la Torre *et al.* claim the observation of a momentum-independent continuum in $H_3LiIr_2O_6$. However, their analysis is restricted to $\mathbf{q}$ points close to the Brillouin zone center. It would be interesting to see if, by measuring over an extended region of the Brillouin zone and using a geometry that highlights the polarization dependence, one could observe a dependence of the RIXS intensity of the continuum on the momentum. We have seen that the comparison of different X_γ points is particularly effective in revealing the bond-directional character. However, it has been proposed that these samples do not show magnetic order because of the presence of disorder, rather than the realization of a spin-liquid ground state.

Another interesting Kitaev material is β-Li_2IrO_3, which has a hyperhoneycomb structure. The 3D spatial arrangement of the bonds leads to a more complex RIXS modulation. However, we could try to identify the same magnetic excitations as in Na_2IrO_3 and α-Li_2IrO_3, and see if they show a bond-directional character. Unlike in Na_2IrO_3 and α-Li_2IrO_3, in β-Li_2IrO_3 the Γ term is proposed to be negative [266–268], so the state $|1\rangle$ would be the ground state. We know how to distinguish the $|0\rangle$ and the $|1\rangle$ ground states based on the different polarization dependence of the spin-flip excitations. We can check from the data and the comparison with our model whether we would reach the same conclusion.

In Ref. [175], it is shown that the orbital excitations also exhibit a RIXS modulation. Their study could reveal something interesting about these unusual orbital excitations.

The simple model used was able to describe many of the features of the RIXS data and provided very useful insight into the nature of the excitations in Kitaev materials. However, it is undoubtedly a very simplified model. It would be interesting to extend the model and consider, for example, a hexagon, and see if the same conclusions can be drawn.

Quasimolecular electronic structure of the trimer system $Ba_4NbIr_3O_{12}$

In cluster Mott insulators, we show how the modulation of the RIXS intensity contains very useful information about the quasimolecular wavefunctions.

In the compound $Ba_4NbIr_3O_{12}$, which contains Ir_3O_{12} trimers, we observe a rich set of intra-t_{2g} quasimolecular excitations in the range 0.5–2 eV. These excitations exhibit a strong periodic modulation of the RIXS intensity as a function of exchanged momentum. In particular, the modulation is present when varying the exchanged momentum along the axis of the trimer, while it is absent when varying $\mathbf{q}$ in the directions perpendicular to the trimer. A peculiarity of a trimer system is the observation of two different modulation periods, $2\pi/d$ and $2\pi/2d$, where d is the distance between nearest-neighbor Ir ions inside the trimer. Our theoretical analysis reveals that the RIXS modulation is sensitive to the symmetry of the quasimolecular wavefunctions. In a trimer with inversion symmetry, the states can be even or odd under inversion. In a single-electron (or hole) picture, the even symmetry is characteristic of bonding and antibonding quasimolecular wavefunctions, while the odd symmetry is characteristic of the non-bonding ones. In particular, the odd (non-bonding) states are characterized by having no weight on the central Ir ion. This means that an excitation involving these states will involve only the two outer Ir ions, having vanishing RIXS amplitude on the central Ir ion. This results in a RIXS intensity modulation whose period depends on the distance between the two outer Ir ions, which is $2d$. Thus, from the study of the RIXS modulation, we obtain information about the symmetry of the quasimolecular wavefunctions involved, aiding in peak assignment. The theoretical analysis also shows that the experimental data are consistent with a non-magnetic $J = 0$ singlet ground state, in agreement with previous theoretical calculations [259]. In $Ba_4NbIr_3O_{12}$, behavior compatible with a spin liquid has been claimed [106–108]. Our results, however, show that the trimer ground state is non-magnetic, which suggests looking for an explanation in possible Nb-Ir site disorder. Nevertheless, the trimer excitations seem to dominate the RIXS spectra, and disorder does not appear to be necessary to explain the data.

Overall, our results represent the first experimental RIXS study of the quasimolecular electronic structure of a quasimolecular trimer compound. Our theoretical analysis also presents general features of trimer quasimolecular wavefunctions and the resulting RIXS modulation. This will serve as a solid basis for future studies of similar systems. It would be interesting, for example, to study other trimer systems with a different number of electrons per trimer. An odd number of electrons (or holes) per trimer should result in a quasimolecular magnetic ground state. In the structure $Ba_4AM_3O_{12}$, the choice of the A ion determines the number of electrons per trimer. Another option is to change the M ion to a $4d$ or $3d$ element, such as Ru or Mn. By going from $5d$ to $4d$ and $3d$, the hopping between the t_{2g} orbitals is expected to decrease, while the electron-electron interaction increases. An interesting question is whether the quasimolecular picture still holds or whether a localized picture is more appropriate. Moreover, systems with interacting magnetic trimers could be studied to observe the effects of interactions between quasimolecular magnetic moments. For example, the systems $Ba_4Ir_3O_{10}$ [81, 82] and $Ba_7Ir_6O_{19}$ [83] contain trimers that are connected to each other, leading to strong inter-trimer interactions. Trimers also exist in a different planar geometry, forming a triangle as in the breathing kagome lattice

$A_xB_y\mathrm{Mo_3O_8}$ [84–88]. The different cluster symmetries lead to different properties of the quasimolecular wavefunctions and the resulting RIXS modulation. However, the Mo L_3 edge is in the tender-RIXS range, making it more difficult to measure a full period of the modulation.

From the theoretical side, the effect of mixing with the e_g orbitals in dimers and trimers might be investigated. In a trigonal geometry, the e_g orbitals are mixed with the t_{2g} orbitals. This might be relevant for obtaining a better description of the RIXS spectral weight, as suggested in [202].

Spin-orbit-entangled quasimolecular moments in $\mathrm{GaTa_4Se_8}$

We present a study of the lacunar spinel $\mathrm{GaTa_4Se_8}$, which hosts spin-orbit-entangled quasimolecular wavefunctions on $\mathrm{Ta_4}$ tetrahedra. By measuring RIXS at the Ta L_3 edge we identify three distinct peaks, labeled A, B, and C, at approximately 0.25, 0.62, and 1.2 eV, respectively. As a function of the exchanged momentum, they display a pronounced periodic modulation of the RIXS intensity. For example, along (7.35 7.35 l), peak A shows a $\cos^2$ modulation, while peak C shows a $\sin^2$ modulation. Peak B, in contrast, remains almost constant. We demonstrate that the modulations observed for peaks A and C along (7.35 7.35 l), ($k + 0.15$ k 4.8), and (h h $1.65(10 - h)$) are consistent with the structure factor of a tetrahedron. We model the quasimolecular wavefunctions of the $\mathrm{Ta_4}$ tetrahedra to calculate and understand the RIXS modulation. The hopping within the tetrahedron can be described by two parameters, t_σ and t_π. The strongest hopping is the direct $t_\sigma \approx 1\,\mathrm{eV}$, which splits the levels into bonding and antibonding states. The inclusion of t_π give rise to quasimolecular orbitals with a_1, e, t_2, t_2, and t_1 symmetry. With seven electrons per tetrahedron, the ground state, in a single-particle picture, is the configuration $a_1^2\,e^4\,t_2^1$. This is split by spin-orbit coupling into a $J_{\mathrm{tet}} = 3/2$ quartet and a $J_{\mathrm{tet}} = 1/2$ doublet. Notably, we find that the relative strength of the two hopping parameters, described by a parameter α, determines the exact shape of the quasimolecular wavefunctions. In particular, there is significant mixing between the bonding and antibonding states originating from t_σ. We show that this mixing has a noticeable effect on both the RIXS modulation and the effective spin-orbit splitting. We demonstrate that the experimental RIXS modulation can be reproduced and understood within a single-electron picture. Peak A is identified as the spin-orbit exciton, corresponding to the excitation from the ground state $J_{\mathrm{tet}} = 3/2$ to the excited state $J_{\mathrm{tet}} = 1/2$. Overall, we show that the RIXS modulation contains a wealth of information that allows us to achieve a precise modeling of the tetrahedral quasimolecular wavefunction.

We find that the ground state can be described mainly as the $J_{\mathrm{tet}} = 3/2$ quartet. This system should therefore be prone to a quasimolecular Jahn-Teller distortion. A reduction in the symmetry of the tetrahedron, for example by making the bond lengths within the tetrahedron inequivalent, would lead to a splitting of the quartet into two Kramers doublets. In fact, there appears to be a dynamical quasimolecular Jahn-Teller distortion in $\mathrm{GaTa_4Se_8}$, as pair distribution function studies have found that the bond lengths differ even at ambient temperature [269]. However, if the splitting is small, the two doublets at finite temperature may remain almost equally populated. For a small splitting, this is valid down to low

temperatures. If one of the two is favored and the system acquires a quasimolecular orbital ordering at very low temperature, it should be possible to distinguish the two doublets based on the RIXS spectra and the RIXS modulation. However, the presence of different domains might make the analysis difficult and inconclusive.

We have seen how the RIXS modulation is sensitive to the quasimolecular wavefunction. It would be interesting to perform measurements under pressure and possibly follow the change in the quasimolecular wavefunction that gives rise to the superconducting phase by measuring the RIXS modulation at selected $\mathbf{q}$ points guided by our results.

Lacunar spinels can also be formed with tetrahedra containing $4d$ or $3d$ transition-metal elements. The $4d$ compounds are still predicted to show quasimolecular character, but according to quantum chemistry calculations, lacunar spinels with $3d$ transition metals, with smaller hopping and stronger electron-electron interactions, are better described in a resonating site-centered picture that, however, still preserves the tetrahedral symmetry [264]. RIXS interferometry could reveal whether the quasimolecular picture still holds or whether a localized picture is more appropriate.

In conclusion, we present a method to identify the bond-directional character of magnetic excitations using RIXS in Kitaev materials and related systems with dominant bond-directional interactions. We solidify RIXS interferometry as a powerful technique for investigating the electronic structure of cluster Mott insulators. We go beyond the dimer case, demonstrating the applicability of RIXS interferometry to more complex systems such as trimers and tetramers. In particular, we show that the RIXS modulation provides valuable information about the symmetry and composition of quasimolecular wavefunctions. The materials we studied belong to families of compounds with intriguing magnetic properties, where exotic physics arises from the presence of quasimolecular magnetic moments. These systems are not well studied, and further theoretical studies are highly desirable to investigate the exchange interactions between quasimolecular magnetic moments. To achieve accurate modeling, a precise understanding of the quasimolecular wavefunctions is an essential starting point.

Publications

The following is the list of publications to which I contributed during my PhD. These are cited in the text as "Pub.". The manuscript [2] and the publications [3] and [4] are reproduced in Chaps. 4, 5, and 6, respectively.

[1] **M. Magnaterra**, M. Moretti Sala, G. Monaco, P. Becker, M. Hermanns, P. Warzanowski, T. Lorenz, D. I. Khomskii, P. H. M. van Loosdrecht, J. van den Brink, and M. Grüninger, *RIXS interferometry and the role of disorder in the quantum magnet* $Ba_3Ti_{3-x}Ir_xO_9$, Phys. Rev. Res. **5**, 013167 (2023). 12, 13, 14, 37, 39, 41, 47, 127

[2] **M. Magnaterra**, K. Hopfer, C. J. Sahle, M. M. Sala, G. Monaco, J. Attig, C. Hickey, I. M. Pietsch, F. Breitner, P. Gegenwart, M. H. Upton, J. Kim, S. Trebst, P. H. M. van Loosdrecht, J. van den Brink, and M. Grüninger, *RIXS observation of bond-directional nearest-neighbor excitations in the Kitaev material* Na_2IrO_3, arXiv:2301.08340 (2023). 11, 13, 14, 47

[3] **M. Magnaterra**, J. Attig, L. Peterlini, M. Hermanns, M. H. Upton, J. Kim, L. Prodan, V. Tsurkan, I. Kézsmárki, P. H. M. van Loosdrecht, and M. Grüninger, *Quasimolecular* $J_{tet} = 3/2$ *Moments in the Cluster Mott Insulator* $GaTa_4Se_8$, Phys. Rev. Lett. **133**, 046501 (2024). 8, 13, 14, 27, 93, 107

[4] **M. Magnaterra**, A. Sandberg, H. Schilling, P. Warzanowski, L. Pätzold, E. Bergamasco, C. J. Sahle, B. Detlefs, K. Ruotsalainen, M. Moretti Sala, G. Monaco, P. Becker, Q. Faure, G. S. Thakur, M. Songvilay, C. Felser, P. H. M. van Loosdrecht, J. van den Brink, M. Hermanns, and M. Grüninger, *Quasimolecular electronic structure of the trimer iridate* $Ba_4NbIr_3O_{12}$, Phys. Rev. B **111**, 085122 (2025). 13, 14, 73

The following are additional publications as a co-author:

[5] I. Vergara, **M. Magnaterra**, P. Warzanowski, J. Attig, S. Kunkemöller, D. I. Khomskii, M. Braden, M. Hermanns, and M. Grüninger, *Spin-orbit coupling and crystal-field splitting in Ti-doped* Ca_2RuO_4 *studied by ellipsometry*, Phys. Rev. B **106**, 085103 (2022).

[6] A. Revelli, M. Moretti Sala, G. Monaco, **M. Magnaterra**, J. Attig, L. Peterlini, T. Dey, A. A. Tsirlin, P. Gegenwart, T. Fröhlich, M. Braden, C. Grams, J. Hemberger, P. Becker, P. H. M. van Loosdrecht, D. I. Khomskii, J. van den Brink, M. Hermanns, and M. Grüninger, *Quasimolecular electronic structure of the spin-liquid candidate* $Ba_3InIr_2O_9$, Phys. Rev. B **106**, 155107 (2022). 7, 12, 47, 127

[7] P. Warzanowski, **M. Magnaterra**, P. Stein, G. Schlicht, Q. Faure, C. J. Sahle, T. Lorenz, P. Becker, L. Bohatý, M. Moretti Sala, G. Monaco, P. H. M. van Loosdrecht, and M. Grüninger, *Electronic excitations in* $5d^4$ $J = 0$ Os^{4+} *halides studied by resonant inelastic x-ray scattering and optical spectroscopy*, Phys. Rev. B **108**, 125120 (2023). 25

[8] P. Warzanowski, **M. Magnaterra**, G. Schlicht, Q. Faure, C. J. Sahle, P. Becker, L. Bohatý, M. M. Sala, G. Monaco, M. Hermanns, P. H. M. van Loosdrecht, and M. Grüninger, *Spin-orbit coupling in a half-filled* t_{2g} *shell: The case of* $5d^3$ K_2ReCl_6, Phys. Rev. B **109**, 155149 (2024). 25

[9] P. Warzanowski, **M. Magnaterra**, C. J. Sahle, M. Moretti Sala, P. Becker, L. Bohatý, I. Císařová, G. Monaco, T. Lorenz, P. H. M. van Loosdrecht, J. van den Brink, and M. Grüninger, *Spin orbital lattice entanglement in the ideal* $j = \frac{1}{2}$ *compound* K_2IrCl_6, Phys. Rev. B **110**, 195120 (2024). 22

Bibliography

[10] P. W. Anderson, *More Is Different*, Science **177**, 393–396 (1972). 1

[11] E. Dagotto, *Complexity in Strongly Correlated Electronic Systems*, Science **309**, 257–262 (2005). 2

[12] Y. Tokura, M. Kawasaki, and N. Nagaosa, *Emergent functions of quantum materials*, Nature Physics **13**, 1056–1068 (2017). 2

[13] J. Hubbard, *Electron correlations in narrow energy bands*, Proceedings of the Royal Society of London. Series A. Mathematical and Physical Sciences **276**, 238–257 (1963). 3

[14] D. Khomskii, *Transition metal compounds*, Cambridge University Press, Cambridge (2014). 3, 4, 18, 19, 24, 25

[15] M. Imada, A. Fujimori, and Y. Tokura, *Metal-insulator transitions*, Rev. Mod. Phys. **70**, 1039–1263 (1998). 3

[16] N. F. Mott and R. Peierls, *Discussion of the paper by de Boer and Verwey*, Proceedings of the Physical Society **49**, 72 (1937). 3

[17] J. B. Goodenough, *Theory of the Role of Covalence in the Perovskite-Type Manganites* $[La, M(II)]MnO_3$, Phys. Rev. **100**, 564–573 (1955). 4

[18] J. Kanamori, *Theory of the Magnetic Properties of Ferrous and Cobaltous Oxides, II*, Progress of Theoretical Physics **17**, 197–222 (1957). 4

[19] J. B. Goodenough, *An interpretation of the magnetic properties of the perovskite-type mixed crystals* $La_{1-x}Sr_xCoO_{3-\lambda}$, Journal of Physics and Chemistry of Solids **6**, 287–297 (1958). 4

[20] J. Kanamori, *Superexchange interaction and symmetry properties of electron orbitals*, Journal of Physics and Chemistry of Solids **10**, 87–98 (1959). 4

[21] J. B. Goodenough, *Magnetism and the chemical bond*, John Wiley And Sons (1963). 4

[22] Y. Tokura and N. Nagaosa, *Orbital Physics in Transition-Metal Oxides*, Science **288**, 462–468 (2000). 4, 25

[23] S. V. Streltsov and D. I. Khomskii, *Orbital physics in transition metal compounds: new trends*, Physics-Uspekhi **60**, 1121 (2017). 4, 25

[24] D. I. Khomskii and S. V. Streltsov, *Orbital Effects in Solids: Basics, Recent Progress, and Opportunities*, Chemical Reviews **121**, 2992–3030 (2021). 4, 6, 25, 60

[25] D. I. Khomskii, *Review—Orbital Physics: Glorious Past, Bright Future*, ECS Journal of Solid State Science and Technology **11**, 054004 (2022). 4, 25

[26] H. A. Jahn, E. Teller, and F. G. Donnan, *Stability of polyatomic molecules in degenerate electronic states - I—Orbital degeneracy*, Proceedings of the Royal Society of London. Series A - Mathematical and Physical Sciences **161**, 220–235 (1937). 4

[27] D. I. Khomskii, *Role of Orbitals in the Physics of Correlated Electron Systems*, Physica Scripta **72**, CC8 (2005). 4

[28] K. I. Kugel and D. I. Khomskii, *Superexchange Ordering of Degenerate Orbitals and Magnetic Structure of Dielectrics with Jahn-Teller Ions*, JETP Letters-USSR **15**, 446 (1972). 4

[29] K. I. Kugel and D. I. Khomskii, *Crystal structure and magnetic properties of substances with orbital degeneracy*, Zh. Eksp. Teor. Fiz. **64**, 1429–1439 (1973). 4

[30] K. I. Kugel and D. I. Khomskii, *The Jahn-Teller effect and magnetism: transition metal compounds*, Soviet Physics Uspekhi **25**, 231 (1982). 4

[31] Z. Nussinov and J. van den Brink, *Compass models: Theory and physical motivations*, Rev. Mod. Phys. **87**, 1–59 (2015). 4

[32] G. Khaliullin and S. Maekawa, *Orbital Liquid in Three-Dimensional Mott Insulator: $LaTiO_3$*, Phys. Rev. Lett. **85**, 3950–3953 (2000). 4

[33] S. V. Streltsov and D. I. Khomskii, *Orbital-dependent singlet dimers and orbital-selective Peierls transitions in transition-metal compounds*, Phys. Rev. B **89**, 161112 (2014). 4

[34] A. Krajewska, A. N. Yaresko, J. Nuss, S. Bette, A. S. Gibbs, M. Blankenhorn, R. E. Dinnebier, D. P. Sari, I. Watanabe, J. Bertinshaw, H. Gretarsson, K. Ishii, D. Matsumura, T. Tsuji, M. Isobe, B. Keimer, H. Takagi, and T. Takayama, *Nearly linear orbital molecules on a pyrochlore lattice*, Science Advances **10**, eadn3880 (2024). 4

[35] W. Witczak-Krempa, G. Chen, Y. B. Kim, and L. Balents, *Correlated Quantum Phenomena in the Strong Spin-Orbit Regime*, Annual Review of Condensed Matter Physics **5**, 57–82 (2014). 4

[36] J. G. Rau, E. K.-H. Lee, and H.-Y. Kee, *Spin-Orbit Physics Giving Rise to Novel Phases in Correlated Systems: Iridates and Related Materials*, Annual Review of Condensed Matter Physics **7**, 195–221 (2016). 4

[37] R. Schaffer, E. Kin-Ho Lee, B.-J. Yang, and Y. B. Kim, *Recent progress on correlated electron systems with strong spin–orbit coupling*, Reports on Progress in Physics **79**, 094504 (2016). 4

[38] G. Khaliullin, *Orbital Order and Fluctuations in Mott Insulators*, Progress of Theoretical Physics Supplement **160**, 155–202 (2005). 4

[39] B. J. Kim, H. Jin, S. J. Moon, J.-Y. Kim, B.-G. Park, C. S. Leem, J. Yu, T. W. Noh, C. Kim, S.-J. Oh, J.-H. Park, V. Durairaj, G. Cao, and E. Rotenberg, *Novel $J_{eff} = 1/2$ Mott State Induced by Relativistic Spin-Orbit Coupling in Sr_2IrO_4*, Phys. Rev. Lett. **101**, 076402 (2008). 4, 9

[40] S. J. Moon, H. Jin, W. S. Choi, J. S. Lee, S. S. A. Seo, J. Yu, G. Cao, T. W. Noh, and Y. S. Lee, *Temperature dependence of the electronic structure of the $J_{eff} = \frac{1}{2}$ Mott insulator Sr_2IrO_4 studied by optical spectroscopy*, Phys. Rev. B **80**, 195110 (2009). 4

[41] H. Gretarsson, J. P. Clancy, X. Liu, J. P. Hill, E. Bozin, Y. Singh, S. Manni, P. Gegenwart, J. Kim, A. H. Said, D. Casa, T. Gog, M. H. Upton, H.-S. Kim, J. Yu, V. M. Katukuri, L. Hozoi, J. van den Brink, and Y.-J. Kim, *Crystal-Field Splitting and Correlation Effect on the Electronic Structure of A_2IrO_3*, Phys. Rev. Lett. **110**, 076402 (2013). 4, 9, 10

[42] S. V. Streltsov and D. I. Khomskii, *Jahn-Teller Effect and Spin-Orbit Coupling: Friends or Foes?*, Phys. Rev. X **10**, 031043 (2020). 5

[43] M. Vojta, *Frustration and quantum criticality*, Reports on Progress in Physics **81**, 064501 (2018). 5

[44] P. Anderson, *Resonating valence bonds: A new kind of insulator?*, Materials Research Bulletin **8**, 153–160 (1973). 5

[45] P. Fazekas and P. W. Anderson, *On the ground state properties of the anisotropic triangular antiferromagnet*, The Philosophical Magazine: A Journal of Theoretical Experimental and Applied Physics **30**, 423–440 (1974). 5

[46] G. Jackeli and G. Khaliullin, *Mott Insulators in the Strong Spin-Orbit Coupling Limit: From Heisenberg to a Quantum Compass and Kitaev Models*, Phys. Rev. Lett. **102**, 017205 (2009). 5

[47] A. Kitaev, *Anyons in an exactly solved model and beyond*, Annals of Physics **321**, 2–111 (2006). 5

[48] L. Savary and L. Balents, *Quantum spin liquids: a review*, Reports on Progress in Physics **80**, 016502 (2016). 5

[49] L. Balents, *Spin liquids in frustrated magnets*, Nature **464**, 199–208 (2010). 5

[50] C. Broholm, R. J. Cava, S. A. Kivelson, D. G. Nocera, M. R. Norman, and T. Senthil, *Quantum spin liquids*, Science **367**, eaay0668 (2020). 5

[51] S. M. Winter, A. A. Tsirlin, M. Daghofer, J. van den Brink, Y. Singh, P. Gegenwart, and R. Valentí, *Models and materials for generalized Kitaev magnetism*, Journal of Physics: Condensed Matter **29**, 493002 (2017). 5, 60, 69

[52] M. Hermanns, I. Kimchi, and J. Knolle, *Physics of the Kitaev Model: Fractionalization, Dynamic Correlations, and Material Connections*, Annual Review of Condensed Matter Physics **9**, 17–33 (2018). 5

[53] H. Takagi, T. Takayama, G. Jackeli, G. Khaliullin, and S. E. Nagler, *Concept and realization of Kitaev quantum spin liquids*, Nature Reviews Physics **1**, 264–280 (2019). 5

[54] S. Trebst and C. Hickey, *Kitaev materials*, Physics Reports **950**, 1–37 (2022). 5, 10, 11

[55] Y. Matsuda, T. Shibauchi, and H.-Y. Kee, *Kitaev Quantum Spin Liquids*, arXiv:2501.05608 (2025). 5

[56] Y. Singh, S. Manni, J. Reuther, T. Berlijn, R. Thomale, W. Ku, S. Trebst, and P. Gegenwart, *Relevance of the Heisenberg-Kitaev Model for the Honeycomb Lattice Iridates A_2IrO_3*, Phys. Rev. Lett. **108**, 127203 (2012). 5

[57] M. Abramchuk, C. Ozsoy-Keskinbora, J. W. Krizan, K. R. Metz, D. C. Bell, and F. Tafti, *Cu_2IrO_3: A New Magnetically Frustrated Honeycomb Iridate*, Journal of the American Chemical Society **139**, 15371–15376 (2017). 5

[58] K. Kitagawa, T. Takayama, Y. Matsumoto, A. Kato, R. Takano, Y. Kishimoto, S. Bette, R. Dinnebier, G. Jackeli, and H. Takagi, *A spin-orbital-entangled quantum liquid on a honeycomb lattice*, Nature **554**, 341–345 (2018). 5

[59] T. Takayama, A. Gibbs, K. Kitagawa, Y. Matsumoto, K. Ishii, A. Kato, R. Takano, S. Bette, R. Dinnebier, and H. Takagi, *Robust quantum spin liquid state in the presence of giant magnetic isotope effect in $D_3LiIr_2O_6$*, npj Quantum Materials **10**, 7 (2025). 5

[60] L. T. Nguyen and R. J. Cava, *Hexagonal Perovskites as Quantum Materials*, Chemical Reviews **121**, 2935–2965 (2021). 6, 7, 27

[61] L. T. Nguyen, *Frustrated Magnetism in Hexagonal Perovskites as Quantum Spin Liquid Candidates*, Ph.D. thesis, Princeton University (2021). 6

[62] Y. Doi, K. Matsuhira, and Y. Hinatsu, *Crystal Structures and Magnetic Properties of 6H-Perovskites $Ba_3MRu_2O_9$ (M=Y, In, La, Sm, Eu, and Lu)*, Journal of Solid State Chemistry **165**, 317–323 (2002). 6

[63] Y. Doi and Y. Hinatsu, *Magnetic and calorimetric studies on $Ba_3LnRu_2O_9$ (Ln = Gd, Ho–Yb) with 6H-perovskite structure*, J. Mater. Chem. **12**, 1792–1795 (2002). 6

[64] D. Ziat, A. A. Aczel, R. Sinclair, Q. Chen, H. D. Zhou, T. J. Williams, M. B. Stone, A. Verrier, and J. A. Quilliam, *Frustrated spin-$\frac{1}{2}$ molecular magnetism in the mixed-valence antiferromagnets $Ba_3MRu_2O_9$ (M = In, Y, Lu)*, Phys. Rev. B **95**, 184424 (2017). 6

[65] Q. Chen, S. Fan, K. M. Taddei, M. B. Stone, A. I. Kolesnikov, J. Cheng, J. L. Musfeldt, H. Zhou, and A. A. Aczel, *Large Positive Zero-Field Splitting in the Cluster Magnet $Ba_3CeRu_2O_9$*, Journal of the American Chemical Society **141**, 9928–9936 (2019). 6

[66] S. A. J. Kimber, M. S. Senn, S. Fratini, H. Wu, A. H. Hill, P. Manuel, J. P. Attfield, D. N. Argyriou, and P. F. Henry, *Charge Order at the Frontier between the Molecular and Solid States in $Ba_3NaRu_2O_9$*, Phys. Rev. Lett. **108**, 217205 (2012). 6

[67] T. Sakamoto, Y. Doi, and Y. Hinatsu, *Crystal structures and magnetic properties of 6H-perovskite-type oxides $Ba_3MIr_2O_9$ (M=Mg, Ca, Sc, Ti, Zn, Sr, Zr, Cd and In)*, Journal of Solid State Chemistry **179**, 2595–2601 (2006). 6

[68] Y. Doi and Y. Hinatsu, *The structural and magnetic characterization of 6H-perovskite-type oxides $Ba_3LnIr_2O_9$ (Ln = Y, lanthanides)*, Journal of Physics: Condensed Matter **16**, 2849 (2004). 6

[69] S.-J. Kim, M. D. Smith, J. Darriet, and H.-C. zur Loye, *Crystal growth of new perovskite and perovskite related iridates: $Ba_3LiIr_2O_9$, $Ba_3NaIr_2O_9$, and $Ba_{3.44}K_{1.56}Ir_2O_{10}$*, Journal of Solid State Chemistry **177**, 1493–1500 (2004). 6

[70] Y. Doi and Y. Hinatsu, *Studies on magnetic susceptibility and specific heat for 6H-perovskite-type oxides $Ba_3LnIr_2O_9$ (Ln=La, Nd, Sm-Yb)*, Journal of Solid State Chemistry **177**, 3239–3244 (2004). 6

[71] T. Dey, R. Kumar, A. V. Mahajan, S. D. Kaushik, and V. Siruguri, *Unconventional magnetism in the spin-orbit-driven Mott insulators $Ba_3MIr_2O_9$ ($M = Sc, Y$)*, Phys. Rev. B **89**, 205101 (2014). 6

[72] C. Garg, D. Roy, M. Lonsky, P. Manuel, A. Cervellino, J. Müller, M. Kabir, and S. Nair, *Evolution of the structural, magnetic, and electronic properties of the triple perovskite $Ba_3CoIr_2O_9$*, Phys. Rev. B **103**, 014437 (2021). 6

[73] J. Terzic, J. C. Wang, F. Ye, W. H. Song, S. J. Yuan, S. Aswartham, L. E. DeLong, S. V. Streltsov, D. I. Khomskii, and G. Cao, *Coexisting charge and magnetic orders in the dimer-chain iridate $Ba_5AlIr_2O_{11}$*, Phys. Rev. B **91**, 235147 (2015). 6

[74] S. V. Streltsov, G. Cao, and D. I. Khomskii, *Suppression of magnetism in $Ba_5AlIr_2O_{11}$: Interplay of Hund's coupling, molecular orbitals, and spin-orbit interaction*, Phys. Rev. B **96**, 014434 (2017). 6

[75] L. T. Nguyen, T. Kong, and R. J. Cava, *Trimers of MnO_6 octahedra and ferrimagnetism of $Ba_4NbMn_3O_{12}$*, Materials Research Express **6**, 056108 (2019). 6

[76] Y. Shimoda, Y. Doi, M. Wakeshima, and Y. Hinatsu, *Magnetic and electrical properties of quadruple perovskites with 12 layer structures $Ba_4LnM_3O_{12}$ (Ln=rare earths; M=Ru, Ir): The role of metal-metal bonding in perovskite-related oxides*, Journal of Solid State Chemistry **183**, 1962–1969 (2010). 6

[77] L. T. Nguyen, T. Halloran, W. Xie, T. Kong, C. L. Broholm, and R. J. Cava, *Geometrically frustrated trimer-based Mott insulator*, Phys. Rev. Mater. **2**, 054414 (2018). 6

[78] Y. Shimoda, Y. Doi, M. Wakeshima, and Y. Hinatsu, *Synthesis and magnetic properties of 12L-perovskites $Ba_4LnIr_3O_{12}$ (Ln=lanthanides)*, Journal of Solid State Chemistry **182**, 2873–2879 (2009). 6

[79] W. Miiller, M. T. Dunstan, Z. Huang, Z. Mohamed, B. J. Kennedy, M. Avdeev, and C. D. Ling, *Complex 5d Magnetism in a Novel S = 1/2 Trimer System, the 12L Hexagonal Perovskite $Ba_4BiIr_3O_{12}$*, Inorganic Chemistry **52**, 12461–12467 (2013). 6

[80] G. S. Thakur, S. Chattopadhyay, T. Doert, T. Herrmannsdörfer, and C. Felser, *Crystal Growth of Spin-frustrated $Ba_4Nb_{0.8}Ir_{3.2}O_{12}$: A Possible Spin Liquid Material*, Crystal Growth & Design **20**, 2871–2876 (2020). 6

[81] J. Wilkens and H. Müller-Buschbaum, *Zur Kenntnis von $Ba_4Ir_3O_{10}$*, Zeitschrift für anorganische und allgemeine Chemie **592**, 79–83 (1991). 6, 130

[82] G. Cao, H. Zheng, H. Zhao, Y. Ni, C. A. Pocs, Y. Zhang, F. Ye, C. Hoffmann, X. Wang, M. Lee, M. Hermele, and I. Kimchi, *Quantum liquid from strange frustration in the trimer magnet $Ba_4Ir_3O_{10}$*, npj Quantum Materials **5**, 26 (2020). 6, 7, 130

[83] C. Lang and H. Müller-Buschbaum, *About a new oxoiridat (IV): $Ba_7Ir_6O_{19}$*, Monatshefte für Chemie/Chemical Monthly **120**, 705–710 (1989). 6, 130

[84] Y. Wang, G. L. Pascut, B. Gao, T. A. Tyson, K. Haule, V. Kiryukhin, and S.-W. Cheong, *Unveiling hidden ferrimagnetism and giant magnetoelectricity in polar magnet $Fe_2Mo_3O_8$*, Scientific reports **5**, 12268 (2015). 6, 131

[85] T. Kurumaji, S. Ishiwata, and Y. Tokura, *Diagonal magnetoelectric susceptibility and effect of Fe doping in the polar ferrimagnet $Mn_2Mo_3O_8$*, Phys. Rev. B **95**, 045142 (2017). 6, 131

[86] S. V. Streltsov, D.-J. Huang, I. Solovyev, and D. I. Khomskii, *Ordering of Fe and Zn ions and the magnetic properties of $FeZnMo_3O_8$*, JETP Letters **109**, 786–789 (2019). 6, 131

[87] I. V. Solovyev and S. V. Streltsov, *Microscopic toy model for magnetoelectric effect in polar $Fe_2Mo_3O_8$*, Phys. Rev. Mater. **3**, 114402 (2019). 6, 131

[88] S. V. Streltsov, D. Takegami, R. Nakamura, P. P. Kovaleva, A. I. Poteryaev, S. A. Nikolaev, H.-H. Xu, Y. Sui, M. Yoshimura, K.-D. Tsuei, N. L. Saini, D. I. Khomskii, and T. Mizokawa, *Beyond a cluster-Mott state in the breathing kagome lattice of $LiZn_2Mo_3O_8$*, Phys. Rev. B **111**, 085124 (2025). 6, 131

[89] H. Barz, *New ferromagnetic molybdenum spinels*, Materials Research Bulletin **8**, 983–988 (1973). 6

[90] H. Yaich, J. Jegaden, M. Potel, M. Sergent, A. Rastogi, and R. Tournier, *Nouveaux chalcogénures et chalcohalogénures à clusters tétraédriques Nb_4 ou Ta_4*, Journal of the Less Common Metals **102**, 9–22 (1984). 6

[91] H. B. Yaich, J. Jegaden, M. Potel, R. Chevrel, M. Sergent, A. Berton, J. Chaussy, A. Rastogi, and R. Tournier, *Nouveaux chalcogenures mixtes $GaMo_4(XX')_8$ (X =S, Se, Te)a'clusters tetraedriques Mo_4*, Journal of Solid State Chemistry **51**, 212–217 (1984). 6

[92] R. Pocha, D. Johrendt, and R. Pöttgen, *Electronic and Structural Instabilities in GaV_4S_8 and $GaMo_4S_8$*, Chemistry of Materials **12**, 2882–2887 (2000). 6

[93] R. Pocha, D. Johrendt, B. Ni, and M. M. Abd-Elmeguid, *Crystal Structures, Electronic Properties, and Pressure-Induced Superconductivity of the Tetrahedral Cluster Compounds $GaNb_4S_8$, $GaNb_4Se_8$, and $GaTa_4Se_8$*, Journal of the American Chemical Society **127**, 8732–8740 (2005). 6

[94] S. Reschke, F. Meggle, F. Mayr, V. Tsurkan, L. Prodan, H. Nakamura, J. Deisenhofer, C. A. Kuntscher, and I. Kézsmárki, *Lattice dynamics and electronic excitations in a large family of lacunar spinels with a breathing pyrochlore lattice structure*, Phys. Rev. B **101**, 075118 (2020). 6, 7

[95] K. Geirhos, S. Reschke, S. Ghara, S. Krohns, P. Lunkenheimer, and I. Kézsmárki, *Optical, Dielectric, and Magnetoelectric Properties of Ferroelectric and Antiferroelectric Lacunar Spinels*, physica status solidi (b) **259**, 2100160 (2022). 6, 7

[96] V. Jayakumar and C. Hickey, *Elementary Building Blocks for Cluster Mott Insulators*, arXiv:2310.01060 (2023). 7

[97] A. Nag, S. Middey, S. Bhowal, S. K. Panda, R. Mathieu, J. C. Orain, F. Bert, P. Mendels, P. G. Freeman, M. Mansson, H. M. Ronnow, M. Telling, P. K. Biswas, D. Sheptyakov, S. D. Kaushik, V. Siruguri, C. Meneghini, D. D. Sarma, I. Dasgupta, and S. Ray, *Origin of the Spin-Orbital Liquid State in a Nearly $J = 0$ Iridate $Ba_3ZnIr_2O_9$*, Phys. Rev. Lett. **116**, 097205 (2016). 7

[98] T. Dey, M. Majumder, J. C. Orain, A. Senyshyn, M. Prinz-Zwick, S. Bachus, Y. Tokiwa, F. Bert, P. Khuntia, N. Büttgen, A. A. Tsirlin, and P. Gegenwart, *Persistent low-temperature spin dynamics in the mixed-valence iridate $Ba_3InIr_2O_9$*, Phys. Rev. B **96**, 174411 (2017). 7

[99] W.-J. Lee, S.-H. Do, S. Yoon, S. Lee, Y. S. Choi, D. J. Jang, M. Brando, M. Lee, E. S. Choi, S. Ji, Z. H. Jang, B. J. Suh, and K.-Y. Choi, *Putative spin liquid in the triangle-based iridate $Ba_3IrTi_2O_9$*, Phys. Rev. B **96**, 014432 (2017). 7

[100] H. Man, M. Halim, H. Sawa, M. Hagiwara, Y. Wakabayashi, and S. Nakatsuji, *Spin-orbital entangled liquid state in the copper oxide $Ba_3CuSb_2O_9$*, Journal of Physics: Condensed Matter **30**, 443002 (2018). 7

[101] S. Kundu, A. Shahee, A. Chakraborty, K. M. Ranjith, B. Koo, J. Sichelschmidt, M. T. F. Telling, P. K. Biswas, M. Baenitz, I. Dasgupta, S. Pujari, and A. V. Mahajan, *Gapless Quantum Spin Liquid in the Triangular System $Sr_3CuSb_2O_9$*, Phys. Rev. Lett. **125**, 267202 (2020). 7

[102] A. Bandyopadhyay, S. Lee, D. T. Adroja, G. B. G. Stenning, A. Berlie, M. R. Lees, R. A. Saha, D. Takegami, A. Meléndez-Sans, G. Poelchen, M. Yoshimura, K. D. Tsuei, Z. Hu, C.-W. Kao, Y.-C. Huang, T.-S. Chan, and K.-Y. Choi, *Quantum spin liquid ground state in the trimer rhodate $Ba_4NbRh_3O_{12}$*, Phys. Rev. B **109**, 184403 (2024). 7

[103] H. Zhao, Y. Zhang, P. Schlottmann, R. Nandkishore, L. E. DeLong, and G. Cao, *Transition between Heavy-Fermion-Strange-Metal and Quantum Spin Liquid in a 4d-Electron Trimer Lattice*, Phys. Rev. Lett. **132**, 226503 (2024). 7

[104] T. Dey, A. V. Mahajan, P. Khuntia, M. Baenitz, B. Koteswararao, and F. C. Chou, *Spin-liquid behavior in $J_{eff} = \frac{1}{2}$ triangular lattice compound $Ba_3IrTi_2O_9$*, Phys. Rev. B **86**, 140405 (2012). 7

[105] R. Kumar, D. Sheptyakov, P. Khuntia, K. Rolfs, P. G. Freeman, H. M. Rønnow, T. Dey, M. Baenitz, and A. V. Mahajan, *$Ba_3M_xTi_{3-x}O_9$ (M = Ir, Rh): A family of 5d/4d-based diluted quantum spin liquids*, Phys. Rev. B **94**, 174410 (2016). 7

[106] L. T. Nguyen and R. J. Cava, *Trimer-based spin liquid candidate $Ba_4NbIr_3O_{12}$*, Phys. Rev. Mater. **3**, 014412 (2019). 7, 73, 130

[107] G. S. Thakur, S. Chattopadhyay, T. Doert, T. Herrmannsdörfer, and C. Felser, *Crystal Growth of Spin-frustrated $Ba_4Nb_{0.8}Ir_{3.2}O_{12}$: A Possible Spin Liquid Material*, Crystal Growth & Design **20**, 2871–2876 (2020). 7, 73, 130

[108] A. Bandyopadhyay, S. Lee, D. T. Adroja, M. R. Lees, G. B. G. Stenning, P. Aich, L. Tortora, C. Meneghini, G. Cibin, A. Berlie, R. A. Saha, D. Takegami, A. Meléndez-Sans, G. Poelchen, M. Yoshimura, K. D. Tsuei, Z. Hu, T.-S. Chan, S. Chattopadhyay, G. S. Thakur, and K.-Y. Choi, *Gapless dynamic magnetic ground state in the charge-gapped trimer iridate $Ba_4NbIr_3O_{12}$*, Phys. Rev. Mater. **8**, 074405 (2024). 7, 73, 130

[109] Y. Li, A. A. Tsirlin, T. Dey, P. Gegenwart, R. Valentí, and S. M. Winter, *Soft and anisotropic local moments in 4d and 5d mixed-valence M_2O_9 dimers*, Phys. Rev. B **102**, 235142 (2020). 7, 28, 29

[110] G. Chen, H.-Y. Kee, and Y. B. Kim, *Cluster Mott insulators and two Curie-Weiss regimes on an anisotropic kagome lattice*, Phys. Rev. B **93**, 245134 (2016). 7

[111] G. Chen and P. A. Lee, *Emergent orbitals in the cluster Mott insulator on a breathing kagome lattice*, Phys. Rev. B **97**, 035124 (2018). 7

[112] S. Nikolaev, I. Solovyev, and S. Streltsov, *Quantum spin liquid and cluster Mott insulator phases in the Mo_3O_8 magnets*, npj Quantum Materials **6**, 25 (2021). 7

[113] Y. Haraguchi, C. Michioka, M. Imai, H. Ueda, and K. Yoshimura, *Spin-liquid behavior in the spin-frustrated Mo_3 cluster magnet $Li_2ScMo_3O_8$ in contrast to magnetic ordering in isomorphic $Li_2InMo_3O_8$*, Phys. Rev. B **92**, 014409 (2015). 7

[114] A. Akbari-Sharbaf, R. Sinclair, A. Verrier, D. Ziat, H. D. Zhou, X. F. Sun, and J. A. Quilliam, *Tunable Quantum Spin Liquidity in the 1/6th-Filled Breathing Kagome Lattice*, Phys. Rev. Lett. **120**, 227201 (2018). 7

[115] K. Iida, H. Yoshida, H. Okabe, N. Katayama, Y. Ishii, A. Koda, Y. Inamura, N. Murai, M. Ishikado, R. Kadono, and R. Kajimoto, *Quantum magnetisms in uniform triangular lattices $Li_2AMo_3O_8$ (A= In, Sc)*, Scientific Reports **9**, 1826 (2019). 7

[116] J. P. Sheckelton, J. R. Neilson, D. G. Soltan, and T. M. McQueen, *Possible valence-bond condensation in the frustrated cluster magnet $LiZn_2Mo_3O_8$*, Nature materials **11**, 493–496 (2012). 7

[117] L. Cario, B. Corraze, and E. Janod, *Physics and Chemistry of Chalcogenide Quantum Materials with Lacunar Spinel Structure*, Chemistry of Materials **37**, 532–550 (2025). 7

[118] I. Kézsmárki, S. Bordács, P. Milde, E. Neuber, L. M. Eng, J. S. White, H. M. Rønnow, C. D. Dewhurst, M. Mochizuki, K. Yanai, H. Nakamura, D. Ehlers, V. Tsurkan, and A. Loidl, *Néel-type skyrmion lattice with confined orientation in the polar magnetic semiconductor GaV_4S_8*, Nature materials **14**, 1116–1122 (2015). 7

[119] Z. Wang, E. Ruff, M. Schmidt, V. Tsurkan, I. Kézsmárki, P. Lunkenheimer, and A. Loidl, *Polar Dynamics at the Jahn-Teller Transition in Ferroelectric GaV_4S_8*, Phys. Rev. Lett. **115**, 207601 (2015). 7

[120] E. Ruff, S. Widmann, P. Lunkenheimer, V. Tsurkan, S. Bordács, I. Kézsmárki, and A. Loidl, *Multiferroicity and skyrmions carrying electric polarization in GaV_4S_8*, Science Advances **1**, e1500916 (2015). 7

[121] S. Bordács, A. Butykai, B. G. Szigeti, J. S. White, R. Cubitt, A. O. Leonov, S. Widmann, D. Ehlers, H.-A. K. von Nidda, V. Tsurkan, A. Loidl, and I. Kézsmárki, *Equilibrium skyrmion lattice ground state in a polar easy-plane magnet*, Scientific reports **7**, 7584 (2017). 7

[122] Á. Butykai, K. Geirhos, D. Szaller, L. F. Kiss, L. Balogh, M. Azhar, M. Garst, L. DeBeer-Schmitt, T. Waki, Y. Tabata, H. Nakamura, I. Kézsmárki, and S. Bordács, *Squeezing the periodicity of Néel-type magnetic modulations by enhanced Dzyaloshinskii-Moriya interaction of 4d electrons*, npj Quantum Materials **7**, 26 (2022). 7

[123] S. Ghara, K. Geirhos, L. Kuerten, P. Lunkenheimer, V. Tsurkan, M. Fiebig, and I. Kézsmárki, *Giant conductivity of mobile non-oxide domain walls*, Nature Communications **12**, 3975 (2021). 7

[124] L. Puntigam, M. Altthaler, S. Ghara, L. Prodan, V. Tsurkan, S. Krohns, I. Kézsmárki, and D. M. Evans, *Strain Driven Conducting Domain Walls in a Mott Insulator*, Advanced Electronic Materials **8**, 2200366 (2022). 7

[125] K. Geirhos, B. Gross, B. G. Szigeti, A. Mehlin, S. Philipp, J. S. White, R. Cubitt, S. Widmann, S. Ghara, P. Lunkenheimer, V. Tsurkan, E. Neuber, D. Ivaneyko, P. Milde, L. M. Eng, A. O. Leonov, S. Bordács, M. Poggio, and I. Kézsmárki, *Macroscopic manifestation of domain-wall magnetism and magnetoelectric effect in a Néel-type skyrmion host*, npj Quantum Materials **5**, 44 (2020). 7

[126] K. Geirhos, J. Langmann, L. Prodan, A. A. Tsirlin, A. Missiul, G. Eickerling, A. Jesche, V. Tsurkan, P. Lunkenheimer, W. Scherer, and I. Kézsmárki, *Cooperative Cluster Jahn-Teller Effect as a Possible Route to Antiferroelectricity*, Phys. Rev. Lett. **126**, 187601 (2021). 7

[127] M. M. Abd-Elmeguid, B. Ni, D. I. Khomskii, R. Pocha, D. Johrendt, X. Wang, and K. Syassen, *Transition from Mott Insulator to Superconductor in $GaNb_4Se_8$ and $GaTa_4Se_8$ under High Pressure*, Phys. Rev. Lett. **93**, 126403 (2004). 8, 93

[128] V. Ta Phuoc, C. Vaju, B. Corraze, R. Sopracase, A. Perucchi, C. Marini, P. Postorino, M. Chligui, S. Lupi, E. Janod, and L. Cario, *Optical Conductivity Measurements of $GaTa_4Se_8$ Under High Pressure: Evidence of a Bandwidth-Controlled Insulator-to-Metal Mott Transition*, Phys. Rev. Lett. **110**, 037401 (2013). 8, 93

[129] M. J. Park, G. Sim, M. Y. Jeong, A. Mishra, M. J. Han, and S. Lee, *Pressure-induced topological superconductivity in the spin–orbit Mott insulator $GaTa_4Se_8$*, NPJ Quantum Materials **5**, 41 (2020). 8, 93

[130] H. Deng, J. Zhang, M. Y. Jeong, D. Wang, Q. Hu, S. Zhang, R. Sereika, T. Nakagawa, B. Chen, X. Yin, H. Xiao, X. Hong, J. Ren, M. J. Han, J. Chang, H. Weng, Y. Ding, H.-Q. Lin, and H.-k. Mao, *Metallization of Quantum Material $GaTa_4Se_8$ at High Pressure*, The Journal of Physical Chemistry Letters **12**, 5601–5607 (2021). 8, 93

[131] M. Y. Jeong, S. H. Chang, H. J. Lee, J.-H. Sim, K. J. Lee, E. Janod, L. Cario, A. Said, W. Bi, P. Werner, A. Go, J. Kim, and M. J. Han, *$J_{eff} = \frac{3}{2}$ metallic phase and unconventional superconductivity in $GaTa_4Se_8$*, Phys. Rev. B **103**, L081112 (2021). 8, 93

[132] V. Guiot, L. Cario, E. Janod, B. Corraze, V. Ta Phuoc, M. Rozenberg, P. Stoliar, T. Cren, and D. Roditchev, *Avalanche breakdown in $GaTa_4Se_{8-x}Te_x$ narrow-gap Mott insulators*, Nature communications **4**, 1722 (2013). 8

[133] H.-S. Kim, J. Im, M. J. Han, and H. Jin, *Spin-orbital entangled molecular j_{eff} states in lacunar spinel compounds*, Nature communications **5**, 3988 (2014). 8, 27, 93

[134] L. J. P. Ament, M. van Veenendaal, T. P. Devereaux, J. P. Hill, and J. van den Brink, *Resonant inelastic x-ray scattering studies of elementary excitations*, Rev. Mod. Phys. **83**, 705–767 (2011). 8, 31, 32, 33

[135] F. M. de Groot, M. W. Haverkort, H. Elnaggar, A. Juhin, K.-J. Zhou, and P. Glatzel, *Resonant inelastic X-ray scattering*, Nature Reviews Methods Primers **4**, 45 (2024). 8, 31, 32, 33

[136] M. Mitrano, S. Johnston, Y.-J. Kim, and M. P. M. Dean, *Exploring Quantum Materials with Resonant Inelastic X-Ray Scattering*, Phys. Rev. X **14**, 040501 (2024). 8, 10, 31, 32

[137] M. Lundberg and P. Wernet, *Resonant Inelastic X-ray Scattering (RIXS) Studies in Chemistry: Present and Future*, 2315–2366, Springer, Cham (2020). 8, 31

[138] F. Gel'mukhanov, M. Odelius, S. P. Polyutov, A. Föhlisch, and V. Kimberg, *Dynamics of resonant x-ray and Auger scattering*, Rev. Mod. Phys. **93**, 035001 (2021). 8, 31

[139] O. Thomas, *Resonant inelastic X-ray scattering in energy materials research and beyond*, Nature Reviews Clean Technology 1–1 (2025). 8, 31

[140] M. Z. Hasan, E. D. Isaacs, Z.-X. Shen, L. L. Miller, K. Tsutsui, T. Tohyama, and S. Maekawa, *Electronic Structure of Mott Insulators Studied by Inelastic X-ray Scattering*, Science **288**, 1811–1814 (2000). 9

[141] C.-C. Kao, W. A. L. Caliebe, J. B. Hastings, and J.-M. Gillet, *X-ray resonant Raman scattering in NiO: Resonant enhancement of the charge-transfer excitations*, Phys. Rev. B **54**, 16361–16364 (1996). 9

[142] L. Braicovich, C. Dallera, G. Ghiringhelli, N. B. Brookes, J. B. Goedkoop, and M. A. van Veenendaal, *X-ray $L_{2,3}$ resonant Raman scattering from NiO: Spin flip and intermediate-state relaxation*, Phys. Rev. B **55**, R15989–R15992 (1997). 9

[143] F. M. F. de Groot, P. Kuiper, and G. A. Sawatzky, *Local spin-flip spectral distribution obtained by resonant x-ray Raman scattering*, Phys. Rev. B **57**, 14584–14587 (1998). 9

[144] P. Abbamonte, C. A. Burns, E. D. Isaacs, P. M. Platzman, L. L. Miller, S. W. Cheong, and M. V. Klein, *Resonant Inelastic X-Ray Scattering from Valence Excitations in Insulating Copper Oxides*, Phys. Rev. Lett. **83**, 860–863 (1999). 9

[145] Y. J. Kim, J. P. Hill, C. A. Burns, S. Wakimoto, R. J. Birgeneau, D. Casa, T. Gog, and C. T. Venkataraman, *Resonant Inelastic X-Ray Scattering Study of Charge Excitations in La_2CuO_4*, Phys. Rev. Lett. **89**, 177003 (2002). 9

[146] G. Ghiringhelli, N. B. Brookes, E. Annese, H. Berger, C. Dallera, M. Grioni, L. Perfetti, A. Tagliaferri, and L. Braicovich, *Low Energy Electronic Excitations in the Layered Cuprates Studied by Copper L_3 Resonant Inelastic X-Ray Scattering*, Phys. Rev. Lett. **92**, 117406 (2004). 9

[147] M. Dean, *Insights into the high temperature superconducting cuprates from resonant inelastic X-ray scattering*, Journal of Magnetism and Magnetic Materials **376**, 3–13 (2015). 9

[148] J. P. Hill, G. Blumberg, Y.-J. Kim, D. S. Ellis, S. Wakimoto, R. J. Birgeneau, S. Komiya, Y. Ando, B. Liang, R. L. Greene, D. Casa, and T. Gog, *Observation of a 500 meV Collective Mode in $La_{2-x}Sr_xCuO_4$ and Nd_2CuO_4 Using Resonant Inelastic X-Ray Scattering*, Phys. Rev. Lett. **100**, 097001 (2008). 9

[149] L. Braicovich, J. van den Brink, V. Bisogni, M. M. Sala, L. J. P. Ament, N. B. Brookes, G. M. De Luca, M. Salluzzo, T. Schmitt, V. N. Strocov, and G. Ghiringhelli, *Magnetic Excitations and Phase Separation in the Underdoped $La_{2-x}Sr_xCuO_4$ Superconductor Measured by Resonant Inelastic X-Ray Scattering*, Phys. Rev. Lett. **104**, 077002 (2010). 9

[150] G. Ghiringhelli and L. Braicovich, *Magnetic excitations of layered cuprates studied by RIXS at Cu L_3 edge*, Journal of Electron Spectroscopy and Related Phenomena **188**, 26–31 (2013). 9

[151] K. Ishii, I. Jarrige, M. Yoshida, K. Ikeuchi, J. Mizuki, K. Ohashi, T. Takayama, J. Matsuno, and H. Takagi, *Momentum-resolved electronic excitations in the Mott insulator Sr_2IrO_4 studied by resonant inelastic x-ray scattering*, Phys. Rev. B **83**, 115121 (2011). 9

[152] J. Kim, D. Casa, M. H. Upton, T. Gog, Y.-J. Kim, J. F. Mitchell, M. van Veenendaal, M. Daghofer, J. van den Brink, G. Khaliullin, and B. J. Kim, *Magnetic Excitation Spectra of Sr_2IrO_4 Probed by Resonant Inelastic X-Ray Scattering: Establishing Links to Cuprate Superconductors*, Phys. Rev. Lett. **108**, 177003 (2012). 9

[153] J. Kim, M. Daghofer, A. Said, T. Gog, J. Van den Brink, G. Khaliullin, and B. Kim, *Excitonic quasiparticles in a spin–orbit Mott insulator*, Nature communications **5**, 4453 (2014). 9

[154] J. Wen, S.-L. Yu, S. Li, W. Yu, and J.-X. Li, *Experimental identification of quantum spin liquids*, npj Quantum Materials **4**, 12 (2019). 9

[155] J. Knolle and R. Moessner, *A Field Guide to Spin Liquids*, Annual Review of Condensed Matter Physics **10**, 451–472 (2019). 9

[156] T.-H. Han, J. S. Helton, S. Chu, D. G. Nocera, J. A. Rodriguez-Rivera, C. Broholm, and Y. S. Lee, *Fractionalized excitations in the spin-liquid state of a kagome-lattice antiferromagnet*, Nature **492**, 406–410 (2012). 9

[157] T.-H. Han, M. R. Norman, J.-J. Wen, J. A. Rodriguez-Rivera, J. S. Helton, C. Broholm, and Y. S. Lee, *Correlated impurities and intrinsic spin-liquid physics in the kagome material herbertsmithite*, Phys. Rev. B **94**, 060409 (2016). 9

[158] J. D. Thompson, P. A. McClarty, D. Prabhakaran, I. Cabrera, T. Guidi, and R. Coldea, *Quasiparticle Breakdown and Spin Hamiltonian of the Frustrated Quantum Pyrochlore $Yb_2Ti_2O_7$ in a Magnetic Field*, Phys. Rev. Lett. **119**, 057203 (2017). 9

[159] M. Songvilay, J. Robert, S. Petit, J. A. Rodriguez-Rivera, W. D. Ratcliff, F. Damay, V. Balédent, M. Jiménez-Ruiz, P. Lejay, E. Pachoud, A. Hadj-Azzem, V. Simonet,

and C. Stock, *Kitaev interactions in the Co honeycomb antiferromagnets $Na_3Co_2SbO_6$ and $Na_2Co_2TeO_6$*, Phys. Rev. B **102**, 224429 (2020). 9

[160] C. Kim, J. Jeong, G. Lin, P. Park, T. Masuda, S. Asai, S. Itoh, H.-S. Kim, H. Zhou, J. Ma, and J.-G. Park, *Antiferromagnetic Kitaev interaction in $J_eff = 1/2$ cobalt honeycomb materials $Na_3Co_2SbO_6$ and $Na_2Co_2TeO_6$*, Journal of Physics: Condensed Matter **34**, 045802 (2021). 9

[161] T. Halloran, F. Desrochers, E. Z. Zhang, T. Chen, L. E. Chern, Z. Xu, B. Winn, M. Graves-Brook, M. B. Stone, A. I. Kolesnikov, Y. Qiu, R. Zhong, R. Cava, Y. B. Kim, and C. Broholm, *Geometrical frustration versus Kitaev interactions in $BaCo_2(AsO_4)_2$*, Proceedings of the National Academy of Sciences **120**, e2215509119 (2023). 9

[162] Y. Gu, Y. Gu, F. Liu, S. Ohira-Kawamura, N. Murai, and J. Zhao, *Signatures of Kitaev Interactions in the van der Waals Ferromagnet VI_3*, Phys. Rev. Lett. **132**, 246702 (2024). 9

[163] A. Banerjee, C. A. Bridges, J.-Q. Yan, A. A. Aczel, L. Li, M. B. Stone, G. E. Granroth, M. D. Lumsden, Y. Yiu, J. Knolle, S. Bhattacharjee, D. L. Kovrizhin, R. Moessner, D. A. Tennant, D. G. Mandrus, and S. E. Nagler, *Proximate Kitaev quantum spin liquid behaviour in a honeycomb magnet*, Nature materials **15**, 733–740 (2016). 9

[164] A. Banerjee, J. Yan, J. Knolle, C. A. Bridges, M. B. Stone, M. D. Lumsden, D. G. Mandrus, D. A. Tennant, R. Moessner, and S. E. Nagler, *Neutron scattering in the proximate quantum spin liquid α-$RuCl_3$*, Science **356**, 1055–1059 (2017). 9, 11

[165] S.-H. Do, S.-Y. Park, J. Yoshitake, J. Nasu, Y. Motome, Y. S. Kwon, D. T. Adroja, D. J. Voneshen, K. Kim, T.-H. Jang, J.-H. Park, K.-Y. Choi, and S. Ji, *Majorana fermions in the Kitaev quantum spin system α-$RuCl_3$*, Nature Physics **13**, 1079–1084 (2017). 9

[166] M. Braden, X. Wang, A. Bertin, P. Steffens, and Y. Su, *Direct evidence for anisotropic magnetic interaction in α-$RuCl_3$ from polarized inelastic neutron scattering*, arXiv:2409.08854 (2024). 9

[167] S. K. Choi, R. Coldea, A. N. Kolmogorov, T. Lancaster, I. I. Mazin, S. J. Blundell, P. G. Radaelli, Y. Singh, P. Gegenwart, K. R. Choi, S.-W. Cheong, P. J. Baker, C. Stock, and J. Taylor, *Spin Waves and Revised Crystal Structure of Honeycomb Iridate Na_2IrO_3*, Phys. Rev. Lett. **108**, 127204 (2012). 9, 69

[168] S. Choi, S. Manni, J. Singleton, C. V. Topping, T. Lancaster, S. J. Blundell, D. T. Adroja, V. Zapf, P. Gegenwart, and R. Coldea, *Spin dynamics and field-induced magnetic phase transition in the honeycomb Kitaev magnet $\alpha-Li_2IrO_3$*, Phys. Rev. B **99**, 054426 (2019). 9

[169] T. Halloran, Y. Wang, M. Li, I. Rousochatzakis, P. Chauhan, M. B. Stone, T. Takayama, H. Takagi, N. P. Armitage, N. B. Perkins, and C. Broholm, *Magnetic excitations and interactions in the Kitaev hyperhoneycomb iridate $\beta-Li_2IrO_3$*, Phys. Rev. B **106**, 064423 (2022). 9

[170] T. Halloran, Y. Wang, K. W. Plumb, M. B. Stone, B. Winn, M. K. Graves-Brook, J. A. Rodriguez-Rivera, Y. Qiu, P. Chauhan, J. Knolle, R. Moessner, N. P. Armitage, T. Takayama, H. Takagi, and C. Broholm, *Continuum of magnetic excitations in the Kitaev honeycomb iridate $D_3LiIr_2O_6$*, npj Quantum Materials **10**, 1–7 (2025). 9

[171] H. Suzuki, H. Liu, J. Bertinshaw, K. Ueda, H. Kim, S. Laha, D. Weber, Z. Yang, L. Wang, H. Takahashi, K. Fürsich, M. Minola, B. V. Lotsch, B. J. Kim, H. Yavaş, M. Daghofer, J. Chaloupka, G. Khaliullin, H. Gretarsson, and B. Keimer, *Proximate ferromagnetic state in the Kitaev model material α-$RuCl_3$*, Nature communications **12**, 4512 (2021). 10

[172] H. Gretarsson, H. Fujihara, F. Sato, H. Gotou, Y. Imai, K. Ohgushi, B. Keimer, and H. Suzuki, *$J=\frac{1}{2}$ pseudospins and $d-p$ hybridization in the Kitaev spin liquid candidates RuX_3 ($X=Cl$, Br, I)*, Phys. Rev. B **109**, L180413 (2024). 10

[173] P. Warzanowski, N. Borgwardt, K. Hopfer, J. Attig, T. C. Koethe, P. Becker, V. Tsurkan, A. Loidl, M. Hermanns, P. H. M. van Loosdrecht, and M. Grüninger, *Multiple spin-orbit excitons and the electronic structure of α-$RuCl_3$*, Phys. Rev. Res. **2**, 042007 (2020). 10

[174] A. de la Torre, B. Zager, F. Bahrami, M. DiScala, J. R. Chamorro, M. H. Upton, G. Fabbris, D. Haskel, D. Casa, T. M. McQueen, F. Tafti, and K. W. Plumb, *Enhanced hybridization in the electronic ground state of the intercalated honeycomb iridate $Ag_3LiIr_2O_6$*, Phys. Rev. B **104**, L100416 (2021). 10

[175] A. Revelli, *RIXS interferometry on cluster Mott insulators and Kitaev materials*, Ph.D. thesis, Universität zu Köln (2022). 10, 13, 37, 68, 127, 129

[176] B. W. Lebert, S. Kim, B. H. Kim, S. H. Chun, D. Casa, J. Choi, S. Agrestini, K. Zhou, M. Garcia-Fernandez, and Y.-J. Kim, *Nonlocal features of the spin-orbit exciton in Kitaev materials*, Phys. Rev. B **108**, 155122 (2023). 10, 68

[177] J. P. Clancy, H. Gretarsson, J. A. Sears, Y. Singh, S. Desgreniers, K. Mehlawat, S. Layek, G. K. Rozenberg, Y. Ding, M. H. Upton, D. Casa, N. Chen, J. Im, Y. Lee, R. Yadav, L. Hozoi, D. Efremov, J. van den Brink, and Y.-J. Kim, *Pressure-driven collapse of the relativistic electronic ground state in a honeycomb iridate*, npj Quantum Materials **3**, 35 (2018). 10

[178] T. Takayama, A. Krajewska, A. S. Gibbs, A. N. Yaresko, H. Ishii, H. Yamaoka, K. Ishii, N. Hiraoka, N. P. Funnell, C. L. Bull, and H. Takagi, *Pressure-induced collapse of the spin-orbital Mott state in the hyperhoneycomb iridate $\beta - Li_2IrO_3$*, Phys. Rev. B **99**, 125127 (2019). 10

[179] G. Fabbris, E. H. T. Poldi, S. Sinha, J. Lim, T. Elmslie, J. H. Kim, A. Said, M. Upton, M. Abramchuk, F. Bahrami, C. Kenney-Benson, C. Park, G. Shen, Y. K. Vohra, R. J. Hemley, J. J. Hamlin, F. Tafti, and D. Haskel, *Electronic structure of the honeycomb iridate Cu_2IrO_3 at high pressure*, Phys. Rev. B **111**, 075153 (2025). 10

[180] A. Ruiz, N. P. Breznay, M. Li, I. Rousochatzakis, A. Allen, I. Zinda, V. Nagarajan, G. Lopez, Z. Islam, M. H. Upton, J. Kim, A. H. Said, X.-R. Huang, T. Gog, D. Casa, R. J. Birgeneau, J. D. Koralek, J. G. Analytis, N. B. Perkins, and A. Frano, *Magnon-spinon dichotomy in the Kitaev hyperhoneycomb $\beta-Li_2IrO_3$*, Phys. Rev. B **103**, 184404 (2021). 10, 11

[181] J. Kim, T.-K. Choi, E. Mercer, L. T. Schmidt, J. Park, S.-Y. Park, D. Jang, S. H. Chang, A. Said, S. H. Chun, K. J. Lee, S. W. Lee, H. Jeong, H. Jeong, C. Lee, K.-Y. Choi, F. Bahrami, F. Tafti, M. Claassen, and A. de la Torre, *Signatures of Floquet Engineering in the proximal Kitaev Quantum Spin Liquid $H_3LiIr_2O_6$ by tr-RIXS*, arXiv preprint arXiv:2412.03777 (2024). 10

[182] G. B. Halász, N. B. Perkins, and J. van den Brink, *Resonant Inelastic X-Ray Scattering Response of the Kitaev Honeycomb Model*, Phys. Rev. Lett. **117**, 127203 (2016). 10

[183] G. B. Halász, B. Perreault, and N. B. Perkins, *Probing Spinon Nodal Structures in Three-Dimensional Kitaev Spin Liquids*, Phys. Rev. Lett. **119**, 097202 (2017). 10

[184] G. B. Halász, S. Kourtis, J. Knolle, and N. B. Perkins, *Observing spin fractionalization in the Kitaev spin liquid via temperature evolution of indirect resonant inelastic x-ray scattering*, Phys. Rev. B **99**, 184417 (2019). 10

[185] W. M. H. Natori and J. Knolle, *Dynamics of a Two-Dimensional Quantum Spin-Orbital Liquid: Spectroscopic Signatures of Fermionic Magnons*, Phys. Rev. Lett. **125**, 067201 (2020). 10

[186] A. Scheie, P. Laurell, A. M. Samarakoon, B. Lake, S. E. Nagler, G. E. Granroth, S. Okamoto, G. Alvarez, and D. A. Tennant, *Witnessing entanglement in quantum magnets using neutron scattering*, Phys. Rev. B **103**, 224434 (2021). 10

[187] H. Gretarsson, J. P. Clancy, Y. Singh, P. Gegenwart, J. P. Hill, J. Kim, M. H. Upton, A. H. Said, D. Casa, T. Gog, and Y.-J. Kim, *Magnetic excitation spectrum of Na_2IrO_3 probed with resonant inelastic x-ray scattering*, Phys. Rev. B **87**, 220407 (2013). 10

[188] A. Revelli, M. Moretti Sala, G. Monaco, C. Hickey, P. Becker, F. Freund, A. Jesche, P. Gegenwart, T. Eschmann, F. L. Buessen, S. Trebst, P. H. M. van Loosdrecht, J. van den Brink, and M. Grüninger, *Fingerprints of Kitaev physics in the magnetic excitations of honeycomb iridates*, Phys. Rev. Research **2**, 043094 (2020). 10, 11, 13, 47, 68, 128

[189] J. G. Vale, C. D. Dashwood, E. Paris, L. S. I. Veiga, M. Garcia-Fernandez, A. Nag, A. Walters, K.-J. Zhou, I.-M. Pietsch, A. Jesche, P. Gegenwart, R. Coldea, T. Schmitt, and D. F. McMorrow, *High-resolution resonant inelastic x-ray scattering study of the electron-phonon coupling in honeycomb $\alpha-Li_2IrO_3$*, Phys. Rev. B **100**, 224303 (2019). 10

[190] J. Kim, J. Chaloupka, Y. Singh, J. W. Kim, B. J. Kim, D. Casa, A. Said, X. Huang, and T. Gog, *Dynamic Spin Correlations in the Honeycomb Lattice Na_2IrO_3 Measured by Resonant Inelastic x-Ray Scattering*, Phys. Rev. X **10**, 021034 (2020). 10, 11, 71

[191] S. H. Chun, P. P. Stavropoulos, H.-Y. Kee, M. Moretti Sala, J. Kim, J.-W. Kim, B. J. Kim, J. F. Mitchell, and Y.-J. Kim, *Optical magnons with dominant bond-directional exchange interactions in the honeycomb lattice iridate α-Li_2IrO_3*, Phys. Rev. B **103**, L020410 (2021). 10, 11, 71

[192] A. de la Torre, B. Zager, F. Bahrami, M. H. Upton, J. Kim, G. Fabbris, G.-H. Lee, W. Yang, D. Haskel, F. Tafti, and K. W. Plumb, *Momentum-independent magnetic excitation continuum in the honeycomb iridate $H_3LiIr_2O_6$*, Nature Communications **14**, 5018 (2023). 10, 129

[193] S. Hwan Chun, J.-W. Kim, J. Kim, H. Zheng, C. C. Stoumpos, C. D. Malliakas, J. F. Mitchell, K. Mehlawat, Y. Singh, Y. Choi, T. Gog, A. Al-Zein, M. M. Sala, M. Krisch, J. Chaloupka, G. Jackeli, G. Khaliullin, and B. J. Kim, *Direct evidence for dominant bond-directional interactions in a honeycomb lattice iridate Na_2IrO_3*, Nature Physics **11**, 462–466 (2015). 11, 63, 128

[194] F. Gel'mukhanov and H. Ågren, *Resonant inelastic x-ray scattering with symmetry-selective excitation*, Phys. Rev. A **49**, 4378–4389 (1994). 12, 37, 127

[195] Y. Ma and M. Blume, *Interference of fluorescence x-rays and coherent excitation of core levels*, Review of Scientific Instruments **66**, 1543–1545 (1995). 12, 37, 127

[196] Y. Ma, *X-ray absorption, emission, and resonant inelastic scattering in solids*, Phys. Rev. B **49**, 5799–5805 (1994). 12

[197] A. Revelli, M. M. Sala, G. Monaco, P. Becker, L. Bohatý, M. Hermanns, T. C. Koethe, T. Fröhlich, P. Warzanowski, T. Lorenz, S. V. Streltsov, P. H. M. van Loosdrecht, D. I. Khomskii, J. van den Brink, and M. Grüninger, *Resonant inelastic x-ray incarnation of Young's double-slit experiment*, Science Advances **5**, eaav4020 (2019). 12, 37, 47, 127

[198] B. Yuan, B. H. Kim, Q. Chen, D. Dobrowolski, M. Azmanska, G. M. Luke, S. Fan, V. Bisogni, J. Pelliciari, and J. P. Clancy, *Exploring a New Regime of Molecular Orbital Physics in 4d Cluster Magnets with Resonant Inelastic X-Ray Scattering*, Phys. Rev. Lett. **134**, 106504 (2025). 12, 13

[199] A. Nag, S. Bhowal, M. M. Sala, A. Efimenko, I. Dasgupta, and S. Ray, *Hopping-Induced Ground-State Magnetism in 6H Perovskite Iridates*, Phys. Rev. Lett. **123**, 017201 (2019). 12

[200] Y. Wang, R. Wang, J. Kim, M. H. Upton, D. Casa, T. Gog, G. Cao, G. Kotliar, M. P. M. Dean, and X. Liu, *Direct Detection of Dimer Orbitals in $Ba_5AlIr_2O_{11}$*, Phys. Rev. Lett. **122**, 106401 (2019). 12

[201] V. M. Katukuri, X. Lu, D. E. McNally, M. Dantz, V. N. Strocov, M. M. Sala, M. H. Upton, J. Terzic, G. Cao, O. V. Yazyev, and T. Schmitt, *Charge ordering in Ir dimers in the ground state of $Ba_5AlIr_2O_{11}$*, Phys. Rev. B **105**, 075114 (2022). 12

[202] T. Ren, Y. Shen, S. F. R. TenHuisen, J. Sears, W. He, M. H. Upton, D. Casa, P. Becker, M. Mitrano, M. P. M. Dean, and R. M. Konik, *Witnessing Quantum Entanglement Using Resonant Inelastic X-ray Scattering*, arXiv:2404.05850 (2024). 12, 13, 131

[203] S. Hayashida, H. Gretarsson, P. Puphal, M. Isobe, E. Goering, Y. Matsumoto, J. Nuss, H. Takagi, M. Hepting, and B. Keimer, *Magnetic ground state of the dimer-based hexagonal perovskite $Ba_3ZnRu_2O_9$*, Phys. Rev. B **111**, 104418 (2025). 12

[204] Y. Shen, J. Sears, G. Fabbris, A. Weichselbaum, W. Yin, H. Zhao, D. G. Mazzone, H. Miao, M. H. Upton, D. Casa, R. Acevedo-Esteves, C. Nelson, A. M. Barbour, C. Mazzoli, G. Cao, and M. P. M. Dean, *Emergence of Spinons in Layered Trimer Iridate $Ba_4Ir_3O_{10}$*, Phys. Rev. Lett. **129**, 207201 (2022). 13

[205] M. Y. Jeong, S. H. Chang, B. H. Kim, J.-H. Sim, A. Said, D. Casa, T. Gog, E. Janod, L. Cario, S. Yunoki, M. J. Han, and J. Kim, *Direct experimental observation of the molecular $J_{eff}= 3/2$ ground state in the lacunar spinel $GaTa_4Se_8$*, Nature Communications **8**, 782 (2017). 13, 93, 107

[206] M. Y. Jeong, S. H. Chang, H. J. Lee, J.-H. Sim, K. J. Lee, E. Janod, L. Cario, A. Said, W. Bi, P. Werner, A. Go, J. Kim, and M. J. Han, *$J_{eff} = \frac{3}{2}$ metallic phase and unconventional superconductivity in $GaTa_4Se_8$*, Phys. Rev. B **103**, L081112 (2021). 13

[207] D. J. Newman and B. K. C. Ng, *Crystal Field Handbook*, Cambridge University Press, Cambridge (2000). 17

[208] E. Pavarini, *Crystal-field theory, tight-binding method and jahn-teller effect*, Correlated electrons: from models to materials **2**, 6–2 (2012). 17

[209] S. V. Streltsov, F. V. Temnikov, K. I. Kugel, and D. I. Khomskii, *Interplay of the Jahn-Teller effect and spin-orbit coupling: The case of trigonal vibrations*, Phys. Rev. B **105**, 205142 (2022). 19

[210] B.-J. Yang and Y. B. Kim, *Topological insulators and metal-insulator transition in the pyrochlore iridates*, Phys. Rev. B **82**, 085111 (2010). 20

[211] M. Moretti Sala, S. Boseggia, D. F. McMorrow, and G. Monaco, *Resonant X-Ray Scattering and the j_{eff}=1/2 Electronic Ground State in Iridate Perovskites*, Phys. Rev. Lett. **112**, 026403 (2014). 21

[212] S. Boseggia, *Magnetic order and excitations in perovskite iridates studied with resonant X-ray scattering techniques*, Ph.D. thesis, UCL (University College London) (2015). 21, 23

[213] S. Sugano, T. Yukito, and K. Hiroshi, *Multiplets of transition-metal ions in crystals*, Academic Press, New York (2012). 22

[214] H. Ishikawa, T. Takayama, R. K. Kremer, J. Nuss, R. Dinnebier, K. Kitagawa, K. Ishii, and H. Takagi, *Ordering of hidden multipoles in spin-orbit entangled $5d^1$ Ta chlorides*, Phys. Rev. B **100**, 045142 (2019). 22

[215] A. Revelli, C. C. Loo, D. Kiese, P. Becker, T. Fröhlich, T. Lorenz, M. Moretti Sala, G. Monaco, F. L. Buessen, J. Attig, M. Hermanns, S. V. Streltsov, D. I. Khomskii, J. van den Brink, M. Braden, P. H. M. van Loosdrecht, S. Trebst, A. Paramekanti, and M. Grüninger, *Spin-orbit entangled $j = \frac{1}{2}$ moments in Ba_2CeIrO_6: A frustrated fcc quantum magnet*, Phys. Rev. B **100**, 085139 (2019). 22

[216] N. B. Perkins, Y. Sizyuk, and P. Wölfle, *Interplay of many-body and single-particle interactions in iridates and rhodates*, Phys. Rev. B **89**, 035143 (2014). 23, 24

[217] M. Haverkort, *Spin and orbital degrees of freedom in transition metal oxides and oxide thin films studied by soft x-ray absorption spectroscopy*, Ph.D. thesis, Universität zu Köln (2005). 24, 25

[218] J. Kanamori, *Electron Correlation and Ferromagnetism of Transition Metals*, Progress of Theoretical Physics **30**, 275–289 (1963). 24

[219] A. Georges, L. d. Medici, and J. Mravlje, *Strong Correlations from Hund's Coupling*, Annual Review of Condensed Matter Physics **4**, 137–178 (2013). 24, 25

[220] R. E. Watson, *Iron Series Hartree-Fock Calculations*, Phys. Rev. **118**, 1036–1045 (1960). 25

[221] B. Yuan, J. P. Clancy, A. M. Cook, C. M. Thompson, J. Greedan, G. Cao, B. C. Jeon, T. W. Noh, M. H. Upton, D. Casa, T. Gog, A. Paramekanti, and Y.-J. Kim, *Determination of Hund's coupling in 5d oxides using resonant inelastic x-ray scattering*, Phys. Rev. B **95**, 235114 (2017). 25

[222] M. Kusch, V. M. Katukuri, N. A. Bogdanov, B. Büchner, T. Dey, D. V. Efremov, J. E. Hamann-Borrero, B. H. Kim, M. Krisch, A. Maljuk, M. M. Sala, S. Wurmehl, G. Aslan-Cansever, M. Sturza, L. Hozoi, J. van den Brink, and J. Geck, *Observation of heavy spin-orbit excitons propagating in a nonmagnetic background: The case of $(Ba, Sr)_2YIrO_6$*, Phys. Rev. B **97**, 064421 (2018). 25

[223] A. Nag, S. Bhowal, A. Chakraborty, M. M. Sala, A. Efimenko, F. Bert, P. K. Biswas, A. D. Hillier, M. Itoh, S. D. Kaushik, V. Siruguri, C. Meneghini, I. Dasgupta, and S. Ray, *Origin of magnetic moments and presence of spin-orbit singlets in Ba_2YIrO_6*, Phys. Rev. B **98**, 014431 (2018). 25

[224] A. A. Aczel, Q. Chen, J. P. Clancy, C. dela Cruz, D. Reig-i Plessis, G. J. MacDougall, C. J. Pollock, M. H. Upton, T. J. Williams, N. LaManna, J. P. Carlo, J. Beare, G. M. Luke, and H. D. Zhou, *Spin-orbit coupling controlled ground states in the double perovskite iridates A_2BIrO_6 (A = Ba, Sr; B = Lu, Sc)*, Phys. Rev. Mater. **6**, 094409 (2022). 25

[225] E. M. Pärschke, W.-C. Chen, R. Ray, and C.-C. Chen, *Evolution of electronic and magnetic properties of Sr_2IrO_4 under strain*, npj Quantum Materials **7**, 90 (2022). 26

[226] S. M. Winter, Y. Li, H. O. Jeschke, and R. Valentí, *Challenges in design of Kitaev materials: Magnetic interactions from competing energy scales*, Phys. Rev. B **93**, 214431 (2016). 26, 27, 59, 60, 61, 67, 71

[227] K. Foyevtsova, H. O. Jeschke, I. I. Mazin, D. I. Khomskii, and R. Valentí, *Ab initio analysis of the tight-binding parameters and magnetic interactions in Na_2IrO_3*, Phys. Rev. B **88**, 035107 (2013). 27, 59

[228] I. I. Mazin, S. Manni, K. Foyevtsova, H. O. Jeschke, P. Gegenwart, and R. Valentí, *Origin of the insulating state in honeycomb iridates and rhodates*, Phys. Rev. B **88**, 035115 (2013). 27, 59

[229] V. M. Katukuri, S. Nishimoto, V. Yushankhai, A. Stoyanova, H. Kandpal, S. Choi, R. Coldea, I. Rousochatzakis, L. Hozoi, and J. v. d. Brink, *Kitaev interactions between $j = 1/2$ moments in honeycomb Na_2IrO_3 are large and ferromagnetic: insights from ab initio quantum chemistry calculations*, New Journal of Physics **16**, 013056 (2014). 27, 59

[230] K. I. Kugel, D. I. Khomskii, A. O. Sboychakov, and S. V. Streltsov, *Spin-orbital interaction for face-sharing octahedra: Realization of a highly symmetric SU(4) model*, Phys. Rev. B **91**, 155125 (2015). 28

[231] A. Kotani and S. Shin, *Resonant inelastic x-ray scattering spectra for electrons in solids*, Rev. Mod. Phys. **73**, 203–246 (2001). 31, 32

[232] Schülke, Winfried, *Electron Dynamics by Inelastic X-ray Scattering*, Oxford University Press (2007). 31, 33

[233] F. De Groot and A. Kotani, *Core level spectroscopy of solids*, CRC press (2008). 31, 33

[234] L. J. P. Ament, *Resonant inelastic x-ray scattering studies of elementary excitations*, Ph.D. thesis, Univertsiteit Leiden (2010). 31, 33, 43

[235] A. Thompson, D. Attwood, Y. Liu, M. Howells, E. Gullikson, J. Kortright, A. Robinson, J. Underwood, K.-J. Kim, J. Kirz, I. Lindau, P. Pianetta, H. Winick, G. Williams, and J. Scofield, *X-Ray Data Booklet*, Lawrence Berkeley National Laboratory (2009). 31

[236] L. J. P. Ament, G. Ghiringhelli, M. M. Sala, L. Braicovich, and J. van den Brink, *Theoretical Demonstration of How the Dispersion of Magnetic Excitations in Cuprate Compounds can be Determined Using Resonant Inelastic X-Ray Scattering*, Phys. Rev. Lett. **103**, 117003 (2009). 32

[237] P. Willmott, *An introduction to synchrotron radiation: techniques and applications*, John Wiley & Sons (2019). 32

[238] J. Als-Nielsen and D. McMorrow, *Elements of modern X-ray physics*, John Wiley & Sons (2011). 32

[239] J. Stöhr, *The Nature of X-Rays and Their Interactions with Matter*, Springer (2023). 32

[240] P. Kirkpatrick and A. V. Baez, *Formation of Optical Images by X-Rays*, J. Opt. Soc. Am. **38**, 766–774 (1948). 33

[241] H. A. Rowland, *On concave gratings for optical purposes*, American Journal of Science **3**, 87–98 (1883). 33

[242] H. H. Johann, *Die erzeugung lichtstarker röntgenspektren mit hilfe von konkavkristallen*, Zeitschrift für Physik **69**, 185–206 (1931). 33

[243] R. Verbeni, M. Kocsis, S. Huotari, M. Krisch, G. Monaco, F. Sette, and G. Vanko, *Advances in crystal analyzers for inelastic X-ray scattering*, Journal of Physics and Chemistry of Solids **66**, 2299–2305 (2005). 33

[244] S. Huotari, G. Vankó, F. Albergamo, C. Ponchut, H. Graafsma, C. Henriquet, R. Verbeni, and G. Monaco, *Improving the performance of high-resolution X-ray spectrometers with position-sensitive pixel detectors*, Journal of Synchrotron Radiation **12**, 467–472 (2005). 33

[245] S. Huotari, F. Albergamo, G. Vankó, R. Verbeni, and G. Monaco, *Resonant inelastic hard x-ray scattering with diced analyzer crystals and position-sensitive detectors*, Review of Scientific Instruments **77**, 053102 (2006). 33

[246] C. Ponchut, J. M. Rigal, J. Clément, E. Papillon, A. Homs, and S. Petitdemange, *MAXIPIX, a fast readout photon-counting X-ray area detector for synchrotron applications*, Journal of Instrumentation **6**, C01069 (2011). 33

[247] M. W. Haverkort, *Quanty for core level spectroscopy - excitons, resonances and band excitations in time and frequency domain*, Journal of Physics: Conference Series **712**, 012001 (2016). 36, 114

[248] J. P. Clancy, N. Chen, C. Y. Kim, W. F. Chen, K. W. Plumb, B. C. Jeon, T. W. Noh, and Y.-J. Kim, *Spin-orbit coupling in iridium-based 5d compounds probed by x-ray absorption spectroscopy*, Phys. Rev. B **86**, 195131 (2012). 36

[249] M. Moretti Sala, C. Henriquet, L. Simonelli, R. Verbeni, and G. Monaco, *High energy-resolution set-up for Ir L_3 edge RIXS experiments*, Journal of Electron Spectroscopy and Related Phenomena **188**, 150–154 (2013). 37

[250] M. Moretti Sala, K. Martel, C. Henriquet, A. Al Zein, L. Simonelli, C. J. Sahle, H. Gonzalez, M.-C. Lagier, C. Ponchut, S. Huotari, R. Verbeni, M. Krisch, and G. Monaco, *A high-energy-resolution resonant inelastic X-ray scattering spectrometer at ID20 of the European Synchrotron Radiation Facility*, Journal of Synchrotron Radiation **25**, 580–591 (2018). 37

[251] T. Sakamoto, Y. Doi, and Y. Hinatsu, *Crystal structures and magnetic properties of 6H-perovskite-type oxides $Ba_3MIr_2O_9$ (M=Mg, Ca, Sc, Ti, Zn, Sr, Zr, Cd and In)*, Journal of Solid State Chemistry **179**, 2595–2601 (2006). 40

[252] P. Marra, K. Wohlfeld, and J. van den Brink, *Unraveling Orbital Correlations with Magnetic Resonant Inelastic X-Ray Scattering*, Phys. Rev. Lett. **109**, 117401 (2012). 42

[253] P. Marra, *Theoretical approach to direct resonant inelastic x-ray scattering on magnets and superconductors*, Ph.D. thesis, Technische Universität Dresden (2016). 42

[254] L. J. P. Ament, G. Khaliullin, and J. van den Brink, *Theory of resonant inelastic x-ray scattering in iridium oxide compounds: Probing spin-orbit-entangled ground states and excitations*, Phys. Rev. B **84**, 020403 (2011). 43

[255] H. Matsuura and M. Ogata, *A Poor Man's Derivation of Quantum Compass–Heisenberg Interaction: Superexchange Interaction in J-J Coupling Scheme*, Journal of the Physical Society of Japan **83**, 093701 (2014). 60

[256] S. Kim, E. Horsley, C. S. Nelson, J. P. C. Ruff, and Y.-J. Kim, *Re-investigation of moment direction in a Kitaev material α-RuCl3*, Journal of Physics: Condensed Matter **37**, 215601 (2025). 63

[257] S. C. Williams, R. D. Johnson, F. Freund, S. Choi, A. Jesche, I. Kimchi, S. Manni, A. Bombardi, P. Manuel, P. Gegenwart, and R. Coldea, *Incommensurate counter-rotating magnetic order stabilized by Kitaev interactions in the layered honeycomb* $\alpha-Li_2IrO_3$, Phys. Rev. B **93**, 195158 (2016). 68, 69

[258] F. Ye, S. Chi, H. Cao, B. C. Chakoumakos, J. A. Fernandez-Baca, R. Custelcean, T. F. Qi, O. B. Korneta, and G. Cao, *Direct evidence of a zigzag spin-chain structure in the honeycomb lattice: A neutron and x-ray diffraction investigation of single-crystal* Na_2IrO_3, Phys. Rev. B **85**, 180403 (2012). 69

[259] E. V. Komleva, D. I. Khomskii, and S. V. Streltsov, *Three-site transition-metal clusters: Going from localized electrons to molecular orbitals*, Phys. Rev. B **102**, 174448 (2020). 73, 130

[260] W. A. Harrison, *Electronic structure and the properties of solids: the physics of the chemical bond*, Courier Corporation, Dover (1989). 107

[261] K. Ackermann, K. Arnold, M. Braß, C. Cardot, R. Green, S. Heinze, P. Hill, Y. Lu, S. Macke, M. Retegan, S. Shokri, M. Tagliavini, A. Zacinskis, and M. W. Haverkort, *QUANTY, a quantum many-body scripting toolkit*, SciPost Physics Codebases (2024). 114

[262] M. W. Haverkort *et al.*, *Quanty - a quantum many body script language* (2019), https://www.quanty.org/doku.php?id=index.html&rev=1560456998 (accessed 19-March-2025). 114

[263] M. Retegan, *mretegan/crispy: v0.8.0* (2024), https://doi.org/10.5281/zenodo.13845266 (accessed 19-March-2025). 114, 124

[264] T. Petersen, P. Bhattacharyya, U. K. Rößler, and L. Hozoi, *Resonating holes vs molecular spin-orbit coupled states in group-5 lacunar spinels*, Nature Communications **14**, 5218 (2023). 123, 132

[265] M. W. Haverkort, *Theory of Resonant Inelastic X-Ray Scattering by Collective Magnetic Excitations*, Phys. Rev. Lett. **105**, 167404 (2010). 124

[266] I. Rousochatzakis and N. B. Perkins, *Magnetic field induced evolution of intertwined orders in the Kitaev magnet β-Li_2IrO_3*, Phys. Rev. B **97**, 174423 (2018). 129

[267] S. Ducatman, I. Rousochatzakis, and N. B. Perkins, *Magnetic structure and excitation spectrum of the hyperhoneycomb Kitaev magnet β-Li_2IrO_3*, Phys. Rev. B **97**, 125125 (2018). 129

[268] M. Li, I. Rousochatzakis, and N. B. Perkins, *Unconventional magnetic field response of the hyperhoneycomb Kitaev magnet β-Li_2IrO_3*, Phys. Rev. Res. **2**, 013065 (2020). 129

[269] T.-H. Yang, S. Kawamoto, T. Higo, S. G. Wang, M. B. Stone, J. Neuefeind, J. P. C. Ruff, A. M. M. Abeykoon, Y.-S. Chen, S. Nakatsuji, and K. W. Plumb, *Bond ordering and molecular spin-orbital fluctuations in the cluster Mott insulator $GaTa_4Se_8$*, Phys. Rev. Res. **4**, 033123 (2022). 131